Computational investigation of excited state processes in ESIPT-based systems and vinylene-linked thiophene-pyrrole

A thesis submitted by

Ibanrishisha Mawa

to

Indian Institute of Technology Guwahati

in fulfillment of the requirements for the degree of

Doctor of Philosophy

Department of Chemistry

Indian Institute of Technology Guwahati

Guwahati 781039

INDIA

January 2024

Computational investigation of excited state processes in ESIPT-based systems and vinylene-linked thiophene-pyrrole

Doctoral Thesis

Author:

Ibanrishisha Mawa

Roll No. 176122008

Supervisor:

Dr. Aditya N. Panda

Department of Chemistry

Indian Institute of Technology Guwahati

Guwahati 781039

INDIA

January 2024

Declaration

I, Ibanrishisha Mawa, declare that this thesis titled, "*Computational investigation of excited state processes in ESIPT-based systems and vinylene-linked thiophene-pyrrole*" and the work presented in it are my own. I confirm that this work was done by me during the period from July 2017 to August 2023 in candidature for the degree of Doctor of Philosophy at Indian Institute of Technology Guwahati under the guidance and supervision of Dr. Aditya N. Panda, Professor, Department of Chemistry. Any part of this thesis has not previously been submitted for a degree or any other qualification at this Institution or any other university/institution. Where I have consulted the published work of others, this is always clearly attributed. I have acknowledged all main sources of help.

Signed:

Ibanrishisha Mawa

Date:

Certificate

This is to certify that the thesis titled "*Computational investigation of excited state processes in ESIPT-based systems and vinylene-linked thiophene-pyrrole*" submitted for the award of degree of Doctor of Philosophy by **Ibanrishisha Mawa** is the record of research work carried out by her during the period July 2017 to August 2023 under my guidance and supervision. This work has not formed the basis for the award of any degree, diploma, associateship, fellowship or other titles in this Institution or in any other university/institution.

Signed:

Dr. Aditya N. Panda

Professor

Date:

Acknowledgements

First and foremost, I would like to thank God the Almighty for His promises and divine protection that has brought me safe thus far.

I take this opportunity to express my gratitude to everyone who has helped me with my academic endeavours. I want to start by expressing my sincere gratitude to my supervisor, Prof. Aditya Narayan Panda for letting me work under his guidance and for being an excellent mentor. I would like to thank him for the immense knowledge he has imparted to me and for his continuous support and encouragement. His patience, rigour and integrity will have a lasting impression on me. I consider it a blessing that I worked under his direction. I will always be appreciative that I joined his group.

I would like to thank my doctoral committee members, **Prof. Sandip Paul**, **Prof. Mohd. Qureshi**, and **Prof. Ashish Kumar Gupta** for their insightful comments, valuable suggestions and encouragements.

I would like to acknowledge the financial support from Indian Institute of Technology, Guwahati. I am very thankful to the Department of Chemistry for giving me the opportunity to work as a research scholar in this department. I acknowledge the computational facility from Param-Ishan, IIT Guwahati.

I thank my labmates Mohd. Shavez, Bishwanath, Palak and Derreck for their helpful discussions, suggestions, and cooperation in the lab.

I would like to extend my sincere gratitude to my sisters namely Pheni, Wanri, Adeline, Tympang, Hame, Sheeba, Christy akka, Nengneithem, Pampi, Bweny, Vise, Chelsi, Phida, Naphi, Iba, Zhonei, Rebecca, Tekoki, Cher, Ribha and to my brothers namely Arban, Vara, Prem, Charakho, Ryan for their support and companionship throughout my PhD years.

I am thankful to all my friends from school, college and IITG

Last but not the least, I would like to convey my special thanks to my family members especially my parents and my brother for their unwavering support and encouragement.

Synopsis

The interaction of light with matter has long been an exciting field of research both from experimental and theoretical perspectives. Upon light absorption, the molecule is excited to higher electronic states, initiating a variety of excited state processes, which are classified as photophysical and photochemical processes. Photophysical processes are of two types: radiative transition such as fluorescence and phosphorescence, and non-radiative transition such as internal conversion and intersystem crossing. Photochemical process include photoinduced chemical reactions like photosynthesis, photoisomerization and photolysis. These kind of processes are observed in our everyday life such as the vision process in retinal chromophores, vitamin D production in human on exposure to sunlight and mutation during DNA replication, etc. The application part of systems undergoing photoinduced processes are realized in the design and development of certain materials such as optoelectronic devices. Therefore unveiling the mechanism of these processes at an atomistic scale is of utmost importance as it would add to our understanding and also assist in designing materials with better performance. In this thesis, the excited state processes encompassing the excited state proton transfer, *cis-trans* isomerization and the non-radiative relaxation pathways are explored using state-of-the-art computational tools. For excited state proton transfer studies, two different systems are considered viz. 1-hydroxy-2-acetonaphthone (HAN) and nitrile-substituted 2-(oxazolinyl)-phenols. HAN was chosen based on the unsettled issues regarding the proton transfer process and the existence of other competitive channels. For the nitrile-substituted 2-(oxazolinyl)-phenols, two regiomers are considered based on their distinct emission properties in the solution and in the aggregated forms. In addition, the *cis-trans* photoisomerization in the vinylene-linked thiophene-pyrrole are also explored. Considering the computational cost for the dynamics study in the excited state, we have employed single-reference method such as time-dependent density functional theory (TDDFT) and algebraic diagrammatic construction scheme of second order (ADC(2)). However, multi-reference studies were also incorporated in our study wherever the single-reference methods fail. The chapter-wise outline of the thesis are provided below.

Chapter 1: Introduction

Chapter 1 gives a brief description of the photophysical and photochemical processes that occurs upon light absorption. Excited state proton transfer and *cis-trans* photoisomerization are discussed specifically with few examples. The aim and scope of the present work are also discussed at the end of the chapter.

Chapter 2: Methodology

This chapter discusses the basic concepts and mathematical formulation of the methods used in the study of excited state processes. It includes the Schrödinger equation, the fundamental equation in quantum mechanics which gives information about the state of the system. The basic ideas of the Hartree-Fock theory which forms the basis of several sophisticated approximation are also discussed. Single reference method such as Density functional theory (DFT), TDDFT, second-order Møller-Plesset perturbation theory (MP2) and ADC(2) are included. Multireference method like complete active space self-consistent field (CASSCF) is discussed. For dynamics study, mixed quantum-classical method such as trajectory surface hopping is also discussed.

high energy barrier.

Chapter 4: Excited state processes in nitrile-sub

phenols in gas and implicit solvents

Chapter 3: Excited-state processes in 1-hydroxy-2-acetonaphthone at ADC(2) and CASSCF levels

In this chapter, the underlying mechanisms of oxazol

Dimethyl-4,5-dihydrooxazol-2-yl)-3-hydroxybenzonitrile (1-C

dihydrooxazol-2-yl)-4-hydroxybenzonitrile (2-CN), which are

vent phase and highly emissive in the crystalline form are pr

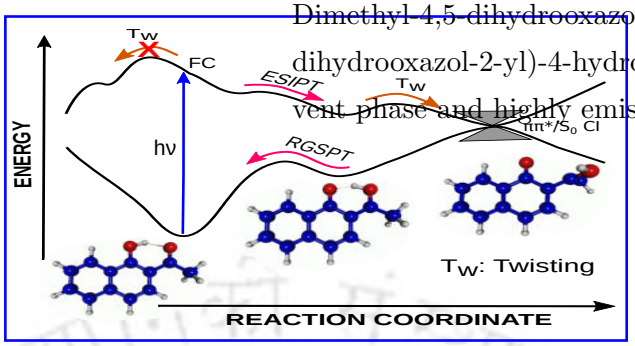

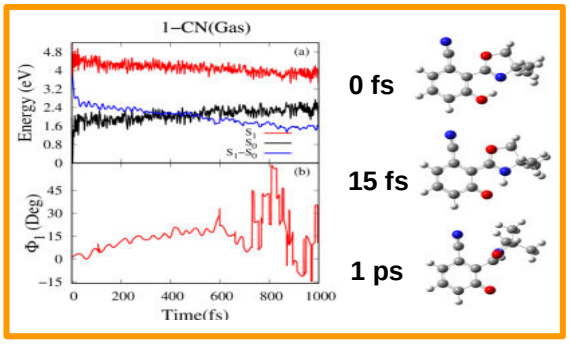

the ground and excited state properties of these two regiomers in gas phase, and in two solvents of different polarities. A systematic computational study comprising of static calculations at density functional theory (DFT) and ab initio, and non-adiabatic ab initio dynamics at DFT levels are performed. Proton transfer process in the S_1 state is thermodynamically favored in the gas as well as in solvents. Our dynamics simulation at TDDFT level predicts an average proton transfer time of $\sim$ 11-15 fs. Following proton transfer, a non-radiative channel driven by inter-ring torsional motion is identified from the keto structures. This pathway was found to be accessible and more probable in the gas and CH due to small barriers in comparison to barrier in MeOH.

Chapter 5: E/Z photoisomerization pathway in 1-(2-Pyrrolyl)-2 -(2-Thienyl) ethylene

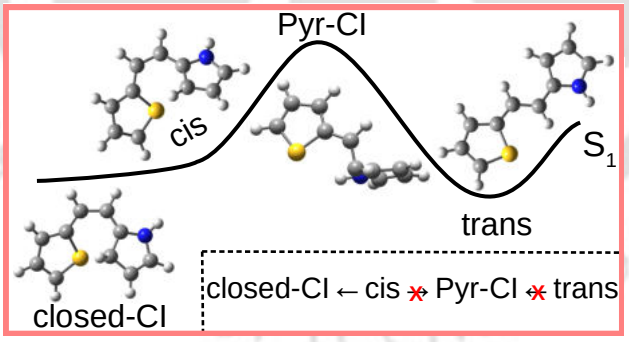

In this chapter, we have explored the various possibilities of excited state relaxation mechanism in vinylene-linked thiophene-pyrrole system. Simple vinylene-linked systems like stilbene has been widely studied in understanding its photochemistry. However, effect of substitution on the vinylene-linked by five-membered heterocyclic rings, thiophene and pyrrole has not been reported. Therefore, in the present study our aim is to illustrate the photoinduced processes in vinylene-linked thiophene pyrrole system. We have carried out computational studies at the RI-MP2/RI-ADC(2)/cc-pVTZ level where several possible conformations of the studied system are explored in the ground

and excited state. The conical intersection structures which acts a funnel in dissipating excess energy non-radiatively are also obtained. These are classified into two classes: closed ring and twisted-pyramidalized structures. The relaxations via the former CIs are found to be accessible from the *cis* isomers. However, the latter CIs are inaccessible due to high energy barriers along the linear interpolation internal coordinate paths.

Chapter 6: Summary and conclusions

The last chapter of the thesis gives an overview of the present work and the scope for future work. In the first work of HAN, we are able to show the proton transfer process through potential energy plots and dynamics simulation and correlate with the experimental results. In addition, other competitive channels are also shown. In the second work of ESIPT-based systems: 1-CN and 2-CN, we are able to explain the low quantum yield of these systems in the solution phase due to the easily accessible non-radiative pathway. In the third work of vinylene-linked thiophene-pyrrole system, the relaxation mechanism from the *cis* and *trans* are shown.

Published articles:

1. Mawa, I.; Panda, A. N. Insights into the Excited State Processes in 1-hydroxy-2-acetonaphthone at ADC(2) and CASSCF Levels *J. Phys. Chem. A* **2021**, 125(14), 3015-3024
2. Mawa, I.; Panda, A. N. Excited state processes in nitrile-substituted 2-(oxazolinyl)-phenols in gas and implicit solvents: A computational study *Chem. Phys. Lett.* **2022**, 806, 139969
3. Mawa, I.; Panda, A. N. Theoretical Investigation of The E/Z Photoisomerization Pathway in 1-(2-Pyrrolyl)-2 -(2-Thienyl) Ethylene *J. Phys. Chem. A* **2023**, 127(27), 5673-5682

Attended Conferences:

1. Poster presentation in Theoretical Chemistry Symposium 2021, IISER Kolkata
2. Poster presentation in Chemical Research Society of India 28th National Symposium in Chemistry 2022, IIT Guwahati
3. Oral presentation in Frontiers in Chemical Sciences 2022, IIT Guwahati

Contents

List of Figures

List of Tables

Abbreviations

ϵ	epsilon
θ	theta
ω	omega
Ω	Omega
π	pi
Ψ	Psi
ψ	psi
μ	mu
λ	lambda
ϕ	Uppercase phi
φ	Lowercase phi
ν	nu
χ	chi
∇	operator
Å	Angstrom
%	Percentage
E_{g}	Excitation energy
E^{1}_{abs}	First excitation energy
λ_{em}	Emission energy
HF	Hartree-Fock
MP	Møller-Plesset
MO	Molecular orbital
BO	Born-Oppenheimer
TD	Time dependent
DFT	Density functional theory
CAM	Coulomb-attenuating method
GGA	Generalized gradient approximation
HOMO	Highest occupied molecular orbital

LUMO	Lowest unoccupied molecular orbital
PT	Proton transfer
f_{osc}	Oscillator strength
lc	long-range corrected
UV	Ultraviolet
LE	Locally excited
NTO	Natural transition orbital
ADC(2)	Second order algebraic diagrammatic construction
CC2	Second order coupled-cluster
ω_{CT}	Charge transfer
ISC	Intersystem crossing
IC	Internal conversion
ESIPT	Excited state intramolecular proton transfer
MCSCF	Multiconfiguration self-consistent field
CASSCF	Complete active space self consistent field
CASPT2	Complete active space second-order perturbation
CI	Conical intersection
MECI	Minimum energy conical intersection

Chapter 1

Introduction

The interactions of light with matter have long been an exciting field of research.[1–4] The absorption of a photon by a molecule results in an electronic excitation leading to a sequence of processes including photochemical and photophysical processes. These two processes are competitive in nature depending on their effectiveness. Photochemical process refers to the state where chemical structures change in the course of the reaction such as photodissociation, photolysis, photoionization, photoinduced isomerization, photosynthesis. However, in photophysical process the structure retains its identity. The Jablonski diagram shown in Figure 1.1 is commonly used to display these processes,

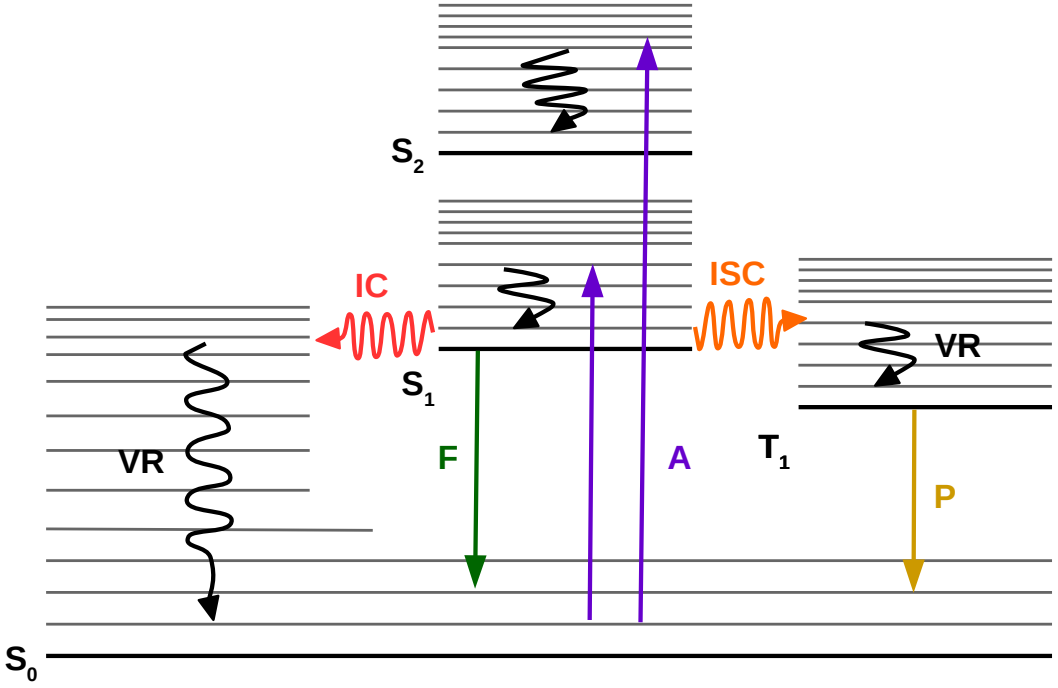

FIGURE 1.1: Jablonski diagram. A: Absorption; F: Fluorescence; P:Phosphorescence; IC: Internal Conversion; ISC: Intersystem Crossing, VR: Vibrational Relaxation; Radiative processes are represented by straight arrows and non radiative by wavy arrows.

which include radiative and non-radiative transitions. Radiative transition is referred to as either fluorescence or phosphorescence where the excess energy is dissipated via light

emission. Fluorescence corresponds to spin-allowed transition while phosphorescence to spin-forbidden transition. Non-radiative transition such as internal conversion happens between states of the same multiplicity and intersystem crossing takes place between states of different multiplicities. As shown in Figure 1.1, the molecule is excited to a higher vibrational level of the electronically excited state such as S_1 or S_2 via light absorption of certain wavelength. The excess vibrational energy gets dissipated rapidly via vibrational relaxation(VR) to the ground vibrational level. In the solvent phase, this energy is released in the form of heat via collision with the solvent molecules. From the lowest vibrational level in the S_1 state, the molecule relaxes by fluorescence to S_0 or it can undergo intersystem crossing (ISC) to the triplet state T_1 followed by VR and phosphorescence to the S_0 state. Another pathway for relaxation is the ISC from T_1 to higher vibrational level of S_0 followed by VR. The understanding of these processes is essential as these affect our everyday life. In particular, the photosynthesis process which involves the conversion of solar energy into chemical energy through an electron transfer reaction plays an important role in the existence and the evolution of life. Vision, which is one of the most important senses of observation, is caused by a simple cis-trans isomerization process. These physical phenomena have drawn considerable interest in the experimental and computational community because of the dependence of all life forms on the sun's visible and ultraviolet radiation. Out of the various photoinduced processes, in the present thesis we are focussing on excited state intramolecular proton transfer(ESIPT) and cis-trans isomerization.

1.1 Excited state intramolecular proton transfer

One of the important processes that happens after excitation in many systems is the proton transfer. In the year 1955, Weller first reported the process of ESIPT in salicylic acid.[5] The photoinduced proton transfer has been well known for its fundamental role in biological and chemical processes. It has been one among many other photochemical reactions that has grasped the attention of researchers because of its broad and beneficial application in the area of material science, such as organic light emitting diodes, fluorescent imaging probes, molecular switches, UV photostabilizers, chemical

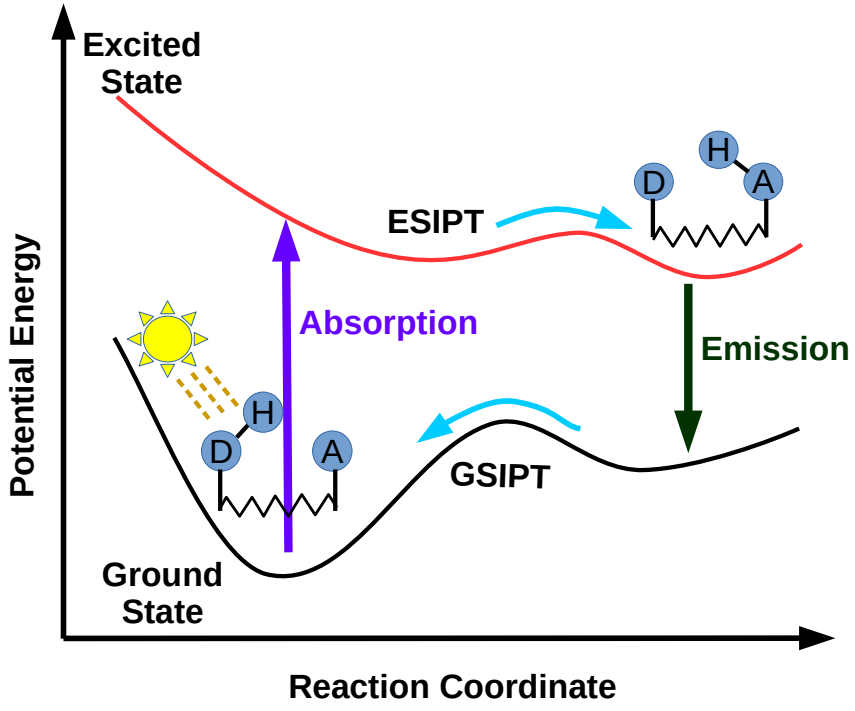

FIGURE 1.2: Schematic illustration of the ESIPT process. D: proton donor; A: proton acceptor.

sensors and so on.[6–10] Besides the technological applications, the importance and significance extend to biological systems where the structure and the biological functions of biomolecules were determined by the ESIPT processes. In the year 2008, the application of ESIPT process in green fluorescent protein was highlighted where the Nobel Prize in Chemistry was awarded to Osamu Shimomura, Martin Chalfie and Roger Y. Tsien.[11–13] Therefore, the study of such kind of process is essential in understanding the underlying mechanism of the biochemical reaction in nature which includes the binding of protein and ligand, mutation during DNA replication, and so on.[14–17] The presence of hydrogen bonding between the proton donor and proton accepting group is essential for ESIPT. ESIPT is an ultrafast process which takes place in femtosecond timescale and is monitored experimentally using femtosecond techniques and computationally by molecular dynamics. The process usually takes place in molecules with a delocalized π electron. The presence of acidic and basic groups in the molecular structure is responsible for the occurrence of the process where upon electromagnetic radiation, the acidity and the basicity of the functional groups are enhanced. In the course of light absorption by the π electronic system, the molecule is excited to a higher electronic state as a result of the

HOMO to LUMO electronic transition. In most cases, the topography of the PES in the ground and excited state is different. In the ground state, the enol form is typically the most stable structure and the proton-transferred conformer, keto is the most stable structure in the excited state. Schematic energy diagram of ESIPT mechanism shown in Figure 1.2 illustrates the four-level photocycle, which includes the excitation of the enol form followed by tautomerization yielding keto form, light emission, and reverse proton transfer in the ground state, giving back the initial enol form. A plethora of studies has been reported for single proton transfer[18–25] due to its simplicity when compared to a complicated double proton transfer process. The complexity of double proton transfer lies in the reaction mechanisms where two possibilities are expected.[26–33] In the concerted mechanism, the two protons are transferred at the same time and in the stepwise mechanism, only one proton is transferred at a time leading to zwitterion formation. The presence of more than one proton transfer process in a molecule leads to the existence of many stable structures in the excited state thus resulting in the design of fine molecular photomemories.[27] However, the role of water or polar solvents as mediator between the donor and acceptor group via a relay mechanism results in an intramolecular proton transfer.[34,35] Since this area of research has been widely explored over the last five decades including a large number of ESIPT systems ranging from simple to complex behavior, covering all of it is beyond the scope of this work. In the paragraph below, two of the widely studied systems which have had significant contribution to the understanding of excited state processes, and scientific and technological applications are discussed.

Salicylic acid, as mentioned above, is the system where ESIPT was first observed by Weller. The theoretical explanation of ESIPT process was delivered by Kasha.[36] Since then, extensive studies including experimental and computational calculations had been performed,[37–43] being one of the smallest molecules which showed ESIPT. The fluorescence in salicylic acid and its derivatives in the ultraviolet and visible range from the S_1 state was long known.[44–46] It showed dual emission, and the emission in the long wavelength region was found to be from the proton-transferred tautomer. The existence of a double well potential in the excited state was proposed by Weller,[47,48] corresponding to the enol-keto equilibrium. In contrast, the experimental results based on electronic

spectroscopy of jet-cooled salicylic acid showed a single well potential attributed to the keto form, which was found to be dependent on the excitation energy.[38,49–51] Ab initio calculation was then carried out by Sobolewski et al.,[39,52] which suggested the presence of a single minimum in the S_1 state where the hydrogen atom was dislocated. A comparative study of different computational methods was made by Aquino et al.[40,41] showing two shallow minima in the excited state separated by a small barrier at the TDDFT level of theory and one minimum in the keto side at CC2 level of theory. In 2017, a full dimensional photodynamic study of salicylic acid was carried out by Tim Raeker and Bernd Hartke[43] to explore the deactivation mechanism. Floating-occupation configuration interaction (FOCI) method implemented in MOPAC was employed for the calculation. The presence of two hydroxyl groups complicates the excited state process. ESIPT followed by 180° rotation of the carboxyl group resulted in a so-called "wrong isomer" where the proton being transferred back in the ground state was different from the initial one. The deactivation pathway that had been reported previously was through fluorescence, but the low fluorescence quantum yield suggested the existence of a radiationless pathway. In their studies, a new relaxation mechanism was suggested which had not been reported earlier where the system relaxed to the ground state through internal conversion via twisting motion around the C=C double bond.

Experimental and theoretical calculations had shown that ESIPT process followed by rapid internal conversion was the reason behind the photostability of indigo (Ind).[53–55] Confusion still remained regarding the mechanism of proton transfer: (a)whether it was concerted which involve both the two groups or a single proton transfer (SPT) or (b) whether it was inter or intramolecular processes or (c) was there any torsional rotation around the C-C bond joining the two rings. In the case of indigo, keto was found to be the more stable geometry in the ground state where the ESPT process transformed the excited-keto to the excited-enol form. TDDFT calculation[55,56] showed that back proton transfer was taking place in the ground state only and no such transfer happened in the singlet excited state. From the experimental results obtained for indigo carmine, SPT was found to be possible which was then followed by reverse proton transfer in the excited state within 0.5 ps.[57] In 2017, Pina et al.[58] aimed at clarifying the confusion existed between experimental and theoretical findings mentioned above. Investigation

of the ESPT process in indigo and mono-hexyl indigo were carried out experimentally and computationally. Comparison of the processes taking place in both indigo and N-hexylindigo was made. It was inferred that SPT was taking place in both indigo and its derivatives, and both inter and intramolecular PT were taking place while intra was found to be more feasible in dried non-protic solvents. For both indigo and N-hexylindigo, ESPT occurred around 2.7-12.6 ps giving enol form which then relaxed to the ground state at around 33-130 ps through a non-radiative transition.

As mentioned above, in systems showing ESIPT, such as salicylic acid and indigo, radiationless transitions play an important role in the relaxation mechanisms, which are attributed to the process's ultrafast nature. At the beginning of the last century, the presence of metastable states was known, but their significance in the photoinduced process was not recognized.[59] With the advancement in technology and the development of time-resolved laser spectroscopy, the existence of non-radiative transitions was realized in many molecular reactions and mostly in polyatomic molecular systems.[60,61] From the quantum chemical point of view, these types of transitions could not be explained based on the BO approximation. However, the concept of potential energy surface based on BO approximation, which separates the nuclear and the electronic motion, has been successfully applied in elucidating the mechanism of certain photochemical reactions. The breakdown of BO approximation for non-radiative transition is due to the coupling of the nuclear and electronic motions. The region in which the the electronic states become close to each other and where the non-adiabatic coupling between these states become non-vanishing is called the region/seam of conical intersection. This concept of conical intersection was first discussed by Hund in 1927,[62] which was mathematically formulated by Neumann and Wigner.[63] Since then, the theoretical research and efforts to locate conical intersections have advanced with the implementation in several quantum chemistry packages, indicating the crucial role of the conical intersection in the photoinduced chemical reactions.[64,65]

1.2 Photoisomerization

Another common type of photoreactions is cis-trans isomerization which have been widely studied for many olefins[66,67], azomethines[68,69] and azo compounds.[70,71] The isomerization around the central double bond is a fundamental step in which photon energy is utilized resulting in mechanical motion. It is one of the important process in photobiological systems such as retinal chromophore where cis-trans isomerization is responsible for the vision.[72,73] Technologically, molecule undergoing photoisomerization process can be used in photoswitches,[74,75] photoprotection,[76,77] photoreceptor proteins,[78,79] molecular motors[80,81] and so on. Therefore, studying this kind of phenomenon has been of great interest.[82] In the designs and applications of photosystems that require safe and efficient dissipation of absorbed energy, photoisomerization is one of the commonly selected photoinduced reactions. This is due to the efficient non-radiative relaxation process via internal conversion giving back the initial isomer or the photoisomer.

There are several pathways by which the molecule can undergo isomerization[83] such as the breaking of double bond via homolytic or heterolytic process, and the decrease in the double bond character by resonance. The homolytic rupture of a double bond is basically observed in several kinds of reactions such as heterogeneous hydrogenation, radical reactions that is initiated by radical generators, paramagnetic molecule-catalyzed reactions and so on. The heterolytic cleavage of a double bond is observed in chemical reactions with reactive nucleophilic/electrophilic counterparts, and is substantially facilitated in ethylene system with electron-donating and electron-withdrawing groups on each carbon atom. In the donor-acceptor type of compounds, the double bond character reduction is due to the push-pull effect. In azo compounds, the presence of lone pair electrons on the nitrogen atom facilitate isomerization through inversion mechanism.

The isomerization process in olefin generally does not occur spontaneously at room temperature or in daylight. However, the photoisomerization process occurs in the presence of radical generators in the S_1 or T_1 $\pi\pi^*$ state. The process can also occur through photosensitization by singlet-singlet or triplet-triplet energy transfer and intersystem crossing.[84–86] The presence of an intermediate state(S_1-p and T_1-p) corresponding to

the perpendicular structure facilitates the formation of both the isomers in the ground state, which explains the transformation from the most stable isomer into the less stable isomer through photoisomerization.[87] In the case of a non-conjugated C=C bond, the barrier for cis-trans interconversion is very high that involves the Rydberg $\pi\sigma$ state and the $\pi\pi^*$ singlet/triplet states, while in polyene systems, the barrier decreases considerably due to the extended conjugation.[83] Generally, the lifetime in the triplet excited state is beyond 1 ms, but the cis-trans isomerization happens in about 10 ns, and only for some systems, the process is fast which is less than 100 fs.[88–90]

Initially, the photoisomerization process was described by a one-dimensional model[91] involving two states with the twisting motion happening along the central double bond as the primary reaction coordinate. Contrasting this is the new model that involved multiple reaction coordinates and also the degeneracies of multiple states.[82] Taking ethylene as an example, the smallest unsaturated hydrocarbon, the qualitative photoisomerization picture involves at least two coordinates, i.e., twisting and the pyramidalization of one of the ethylenic carbon. This conclusion was made from the ab initio multiple spawning(AIMS) results where the electronic and nuclear Schrödinger equations was solved simultaneously. The invalidity of the conventional one-dimensional model illustrated for ethylene was also found in smaller polyene systems.[92]

Ethylene, being the smallest system, was taken as a prototypical model for cis-trans photoisomerization. Moreover,the stilbene molecule belonging to the olefins group was also used as a model for unravelling the mechanism in polyenes and for establishing a connection with the mechanism suggested for the ethylene molecule. Therefore, numerous studies[93–96] were carried out for stilbene as the model compound where understanding the photodynamics and manipulating the relaxation routes were done that were also applicable for several derivatives of stilbene. The key feature in the photoisomerization of stilbene is the existence of the reactive intermediate popularly known as the phantom state which is identified by the twisted ethylenic C=C bond. Hammond and Saltiel[97] were the first to propose the existence of the phantom state in cis-trans isomerization of stilbene with respect to the photosensitized triplet excitation, which was later extended to the singlet excited states.[95,98,99] The name was retained for singlet excited

states owing to the complexity in detecting and characterizing this state. In the recent non-adiabatic dynamics simulations by Weir et al.[94], where AIMS was employed using SA-CASSCF method, a result contradicting to the already known mechanism was shown. They concluded that the isolated cis-stilbene undergoes isomerization via a one-bond flip mechanism in opposition to the hula-twist mechanism proposed by Fuß et al.[100] and the involvement of the ethylenic hydrogen atoms distinguished the two mechanisms. In their simulations, three relaxation pathways were outlined which include twisting along the central double bond with immediate relaxation via internal conversion, delayed internal conversion and cyclization as the minor pathway. The delayed relaxation is attributed to the excited state population trapped in the phantom state.

Azobenzene is another compound in which extensive studies have been carried out to understand the cis-trans photoisomerization process. Like many other vinylene-linked systems, the most stable conformer is the trans form which undergoes isomerization upon UV light absorption, yielding a small amount of cis form. However, the reverse process of isomerization from the cis to trans occurs upon visible light absorption or thermally due to the stability of the trans conformer.[101–103] These two processes occur at different timescales where photoisomerization is much faster than thermal isomerization. The photoisomerization process in this compound is also known as "one of the cleanest photoreactions" owing to the absence of side products upon prolonged irradiation. The study of the isomerization process in azobenzene has sparked interest for nearly ninety years due to the isolation of cis-isomers.[101,104] The mechanism and the quantum yield were found to profoundly depend on various factors like the excitation wavelength, temperature, pressure, and substituents. For technological purposes, knowing the mechanism is less important compared to knowing the rate of thermal isomerization and the potential to manoeuvre the quantum yield of photoisomerization. However, having the mechanistic information is also significant in designing the azobenzene-derived materials targeted for a specific purpose. The trans form of azobenzene is planar with C_{2h} symmetry,[105,106] ,while the cis form is non-planar with C_2 symmetry[107,108]. Upon light absorption at a certain wavelength, the cis and trans forms are excited to $S_1(n\pi^*)$ and $S_2(\pi\pi^*)$.[109,110] The interconversion between the two forms follows after excitation to

the S_1 or S_2 states. Several pathways of isomerization were found for this system, unlike stilbene, where rotation along the central bond was the only route. There are four mechanisms proposed for the isomerization process in azobenzene: rotation, inversion, concerted inversion , and inversion-assisted rotation.[106,111–113] In the rotation mechanism, there is a large change in the C-N=N-C dihedral angle and the N=N-C is fixed at 120° while in inversion, the dihedral angle is fixed at 0°, and the increase in N=N-C angle is upto 180°. For the concerted inversion isomerization pathway, there is an increase of 180° for both the N=N-C angles. However, the changes in the dihedral angle C-N=N-C and N=N-C bond angle are noticed in the inversion-assisted rotation mechanism where the changes happen simultaneously but are smaller yet significant for the latter one.[101]

1.3 Aim and Scope of the present work

From the above discussion on ESIPT, photoisomerization and non-radiative relaxation pathways, we note that there is a considerable interest in understanding the underlying mechanism at an atomistic scale and in finding the suitable computational method for correlation with the experimental results. In several technological applications, the importance of ESIPT process is indispensable. As mentioned above, ESIPT is without a doubt among the most fundamental chemical reactions by far, as they can be found in inert or biological systems, in gas phase, solution phase and in solid state. However, the simplicity of defining the process as an ultrafast migration of proton from donor to acceptor should not be overestimated as other competitive processes can obstruct or delay the process. Considering the complexity in the excited state from the theoretical point of view where failure of the BO approximation in certain region of PES occurs, traditional treatment of separating the nucleus and electronic motion is inadvisable. Due to the wide variety of systems exhibiting ESIPT and photoisomerization process, which molecular systems are intriguing enough to examine is an issue that arises. Therefore in the present thesis work, we have chosen 1-hydroxy-2-acetonaphthone, a system with unresolved issues related to the photocycle and also a newly designed system, nitrile-substituted 2-(oxazolinyl)-phenols displaying different emission behaviour in the solution

and aggregated phase. Elucidation of the excited state mechanism with state-of-the-art quantum chemical methods keeping balance between the cost and the accuracy is the motivation of our work. In addition to ESIPT, photoisomerization process of vinylene-linked thiophene-pyrrole system is also explored. Non-radiative transition are investigated in all the three systems. In this thesis work, we are able to show the importance of having an efficient computational strategy to accurately describe the process. Non-adiabatic dynamics simulation which is one of the state-of-the-art studies for ultrafast processes is also adopted for the ESIPT systems.

Chapter 2

Theoretical and computational methodologies

This chapter discusses the theoretical concepts and mathematical formulations of the methods used in the study of excited state proton transfer and photoisomerization processes presented in this thesis. It includes the time-independent Schrödinger equation, the fundamental equation in quantum mechanics, which gives information about the stationary state of a system. Various methods including the Hartree-Fock theory which forms the basis of several sophisticated approximations are discussed.

2.1 The time-independent Schrödinger equation

The time-independent Schrödinger equation is the theoretical foundation of quantum mechanics which gives the information about the state of the system and is written as

$$\hat{H}\Psi_i(\mathbf{r}_1, \mathbf{r}_2....\mathbf{r}_n, \mathbf{R}_1, \mathbf{R}_2....\mathbf{R}_N) = E_i\Psi_i(\mathbf{r}_1, \mathbf{r}_2....\mathbf{r}_n, \mathbf{R}_1, \mathbf{R}_2....\mathbf{R}_N), \tag{2.1}$$

where $\hat{H}$ is the Hamiltonian operator for a system of n electrons and N nuclei associated with the total energy E_i of the system for state i. Ψ_i is the total wave function of the system which depends on the electronic coordinates (r) and nuclear coordinates (R). The Hamiltonian operator is the sum of the kinetic energy operator, $\hat{T}$ and potential energy operator, $\hat{V}$. It is expressed in atomic units as follows:[114]

$$\hat{H} = -\sum_{i=1}^{n}\frac{1}{2}\nabla_i^2 - \sum_{A=1}^{N}\frac{1}{2M_A}\nabla_A^2 - \sum_{i=1}^{n}\sum_{A=1}^{N}\frac{Z_A}{\mathbf{r}_{iA}} + \sum_{i=1}^{n}\sum_{j>i}^{n}\frac{1}{\mathbf{r}_{ij}} + \sum_{A=1}^{N}\sum_{B>A}^{N}\frac{Z_A Z_B}{R_{AB}}, \tag{2.2}$$

where M_A represent the mass of the nucleus A, Z_A and Z_B are the atomic number of nuclei A and B respectively. $\mathbf{r}_{ij}$, $\mathbf{r}_{iA}$ and $\mathbf{R}_{AB}$ are the distances between i^{th} and j^{th} electrons, between i^{th} electron and A^{th} nucleus, between A^{th} and B^{th} nuclei, respectively. The first two terms in the above equation are for the kinetic energy operators for the electrons and nuclei, respectively. The third term shows the Coulombic attraction between the electrons and nuclei. While the electron-electron repulsion is given by the fourth term, the fifth term takes care of the nucleus-nucleus repulsion.

2.2 The Born Oppenheimer approximation

The Born Oppenheimer approximation is the cornerstone of all calculations in molecular quantum mechanics. The approximation is based on the simple assumption that the mass of the nucleus being heavier than that of an electron, the nucleus position can be treated as fixed for a certain period of electronic motion. As a result of this separation of the electronic and nuclear motions, the total wave function can be presented as

$$\Psi(\mathbf{r}_1, \mathbf{r}_2....\mathbf{r}_n, \mathbf{R}_1, \mathbf{R}_2....\mathbf{R}_N) = \Psi_{elec}(\mathbf{r}_1, \mathbf{r}_2....\mathbf{r}_n; \mathbf{R}_1, \mathbf{R}_2....\mathbf{R}_N)\Psi_{nucl}(\mathbf{R}_1, \mathbf{R}_2....\mathbf{R}_N), \quad (2.3)$$

where Ψ_{elec} and Ψ_{nucl} are the electronic and nuclear wave functions, respectively. Within the BO approximation, the kinetic energy term of the nuclei can be neglected and the repulsion term between the nuclei can be kept constant. The resulting electronic Hamiltonian is expressed as

$$\hat{H}_{elec} = -\sum_{i=1}^{n} \frac{1}{2}\nabla_i^2 - \sum_{i=1}^{n}\sum_{A=1}^{N} \frac{Z_A}{\mathbf{r}_{iA}} + \sum_{i=1}^{n}\sum_{j>i}^{n} \frac{1}{\mathbf{r}_{ij}}. \quad (2.4)$$

The Schrödinger equation for $\hat{H}_{elec}$ can be written as

$$\hat{H}_{elec}\Psi_{elec} = E_{elec}\Psi_{elec} \quad (2.5)$$

where Ψ_{elec} is the electronic wave function written as follows

$$\Psi_{elec} = \Psi_{elec}(\mathbf{r}_i; R_A). \tag{2.6}$$

Ψ_{elec} describes the electronic motion which is explicitly dependent on the electronic coordinates $\mathbf{r}_i$ and parametrically on the nuclear coordinates $\mathbf{R}_A$. The parametric dependence of the wave function on the nuclear coordinate implies the variation of the electronic wave function for different nuclei arrangements. Therefore, the total energy of the system for fixed nuclei is

$$E_{tot}(\mathbf{R}) = E_{elec}(\mathbf{R}) + \sum_{A=1}^{N} \sum_{B>A}^{N} \frac{Z_A Z_B}{\mathbf{R}_{AB}}. \tag{2.7}$$

2.3 The Hartree Fock theory

The Schrödinger equation for a system of n electrons is analytically unsolvable due to the complex nature of many-body wave function. Using the mean-field approximation, the many-body problem is simplified by writing the n-electron wave function as a product of one-electron orbitals as

$$\Psi(\mathbf{r}_1, \mathbf{r}_2 ... \mathbf{r}_n) = \Phi_1(\mathbf{r}_1)\Phi_2(\mathbf{r}_2)...\Phi_n(\mathbf{r}_n). \tag{2.8}$$

This results in a set of coupled one-electron problems. The orbital in Eq. 2.8 is written as $\Phi_1(r_1) = \Phi_1(1)\sigma_1(1)$, where the spin wave function σ is dependent on the electron's spin orientation. In order to satisfy the Pauli's antisymmetric principle and the indistinguishability of electrons, the wave function for n-electron system is given by a Slater

determinant

$$\Psi(\mathbf{r}_1, \mathbf{r}_2, ...\mathbf{r}_n) = \frac{1}{\sqrt{n!}} \begin{vmatrix} \Phi_1(1)\alpha(1) & \Phi_1(1)\beta(1) & \dots & \Phi_M(1)\beta(1) \\ \Phi_1(2)\alpha(2) & \Phi_1(2)\beta(2) & \dots & \Phi_M(2)\beta(2) \\ \vdots & \vdots & \vdots & \\ \Phi_1(n)\alpha(n) & \Phi_1(n)\beta(n) & \dots & \Phi_M(n)\beta(n) \end{vmatrix}, \tag{2.9}$$

where $\frac{1}{\sqrt{n!}}$ is a normalization factor, $M = \frac{n}{2}$ for even n and $M = \frac{n+1}{2}$ for odd n.

In the Hartree Fock approximation, the ground state of an n-electron system is described by a single Slater determinant. Based on this approximation, the n-electron Schrödinger equation can be rewritten as "n" one-electron Schrödinger equations, and the wave function for each electron satisfies the following equation,

$$\Big(-\frac{1}{2}\nabla_i^2 - \sum_{A=1}^{N} \frac{Z_A}{\mathbf{r}_{iA}} + v^{HF}(i) \Big) \Phi_i(\mathbf{r}) = \varepsilon_i \Phi_i(\mathbf{r}), \tag{2.10}$$

where i = 1, 2....,n. $v^{HF}(i)$ is the average potential exerted by other electrons on the ith electron. The resulting set of equations is referred to as the HF equations, and the iterative self-consistent field procedure is used to solve those.

2.4 Post-Hartree-Fock theory

In the HF theory, the correlation between electrons of opposite spin are neglected which may result in large deviations from experimental results. A variety of approximations collectively called as post-Hartree-Fock methods were devised to incorporate the electron correlation effect. The Møller-Plesset perturbation theory[115] is one of the approaches where the electron correlation is treated as a perturbation to the Fock operator. Other approaches are coupled-cluster methods such as second-order coupled-cluster (CC2)[116] and others, and multi-configurational methods such as the complete active space self-consistent field (CASSCF).[117,118]. Overview of the methods used in my thesis work are presented below.

2.4.1 Møller-Plesset perturbation theory

The correction to the HF method by second order perturbation theory for electron correlation was discussed by Møller and Plesset[115] in the year 1934 and the approach is known as Møller-Plesset perturbation theory. It is based on the idea of splitting the total Hamiltonian into a zeroth order Hamiltonian($\hat{H}^{(0)}$) and the perturbation part($\hat{V}$):

$$\hat{H} = \hat{H}^{(0)} + \hat{V}. \tag{2.11}$$

The zeroth-order problem is defined as

$$\hat{H}^{(0)}\Psi_0^{(0)} = E_0^{(0)}\Psi_0^{(0)} \tag{2.12}$$

where the subscript 0 refers to the ground state. The zeroth-order Hamiltonian is described as the sum of one-electron closed-shell Fock operators

$$\hat{H}^{(0)} = \sum_p \hat{F}(p) = \sum_p \hat{h}(p) + \sum_{p,i}[\hat{J}_i(p) - \hat{K}_i(p)] \tag{2.13}$$

where $\hat{h}(p)$ is the one electron operator comprising of the kinetic and electron-nucleus attraction term, $\hat{J}_i(p)$ and $\hat{K_i}(p)$ are the Coulomb and exchange operator. Here, p and q are used for the general spin orbitals, i and j denote the occupied orbitals, and a and b are for the virtual orbitals. The MP perturbation operator is given by

$$\hat{V} = \hat{H} - \hat{H}^{(0)} = \sum_{p\geq q}\frac{1}{\mathbf{r}_{pq}} - \sum_{p,i}[\hat{J}_i(p) - \hat{K}_i(p)]. \tag{2.14}$$

The operators $\hat{J}_i(p)$ and $\hat{K}_i(p)$ are expressed in terms of spin orbitals Φ_i as follows

$$\hat{J}_i(1)\Phi_j(1) = \left[\int d\mathbf{r}_2\Phi_i^*(2)\frac{1}{\mathbf{r}_{12}}\Phi_i(2)\right]\Phi_j(1) \tag{2.15}$$

and

$$\hat{K}_i(1)\Phi_j(1) = \left[\int d\mathbf{r}_2\Phi_i^*(2)\frac{1}{\mathbf{r}_{12}}\Phi_j(2)\right]\Phi_i(1). \tag{2.16}$$

The average of the perturbation over the unperturbed wave function gives the first order correction to the energy $E^{(0)}$:

$$E_{MP}^{(1)} = \langle \Phi^{(0)} | \hat{V} | \Phi^{(0)} \rangle = V_{00} = -\frac{1}{2} \sum_{ij} \langle ij||ij \rangle, \tag{2.17}$$

where $\langle ij||ij \rangle$ is an antisymmetrized two-electron integral over the occupied spin orbitals ϕs and generally defined as[119]

$$\langle ij||kl \rangle = \langle ij|kl \rangle - \langle ij|lk \rangle = \int d\mathbf{r}_1 \; d\mathbf{r}_2 \; \phi_i^*(\mathbf{r}_1) \phi_j^*(\mathbf{r}_2) \mathbf{r}_{12}^{-1} (1 - \hat{P}_{12}) \phi_k(\mathbf{r}_1) \phi_l(\mathbf{r}_2). \tag{2.18}$$

Here $\hat{P}_{12}$ is an operator which interchanges the coordinates of two electrons. Therefore, MP1 energy is simply the HF energy indicating that the HF is correct upto first order of MP theory

$$E(\text{HF}) = E(\text{MP1}) = \sum_{i}^{occ} \epsilon_i - \frac{1}{2} \sum_{ij}^{occ} \langle ij||ij \rangle. \tag{2.19}$$

The second order correction of energy is given as

$$E_{MP}^{(2)} = \frac{1}{4} \sum_{ij}^{occ} \sum_{ab}^{vir} \langle ij||ab \rangle a_{ij}^{ab} \tag{2.20}$$

with

$$a_{ij}^{ab} = (\epsilon_i + \epsilon_j - \epsilon_a - \epsilon_b)^{-1} \langle ab||ij \rangle \tag{2.21}$$

Eq. 2.20 is obtained considering only the double excitations as single excitations do not contribute to the correlation energy as a consequence of the Brillouin's theorem[120]. In addition, the triple and other higher excitations are excluded from correlation because of the Slater-Condon rules.[121].

The spin-scaling approaches for MP2 was first proposed by Grimme in the year 2003[122] in order to obtain an efficient and precise variants of MP2 method. It is based on splitting the correlation energy into parallel and antiparallel spin components . The weight of these two contributions are scaled by semiempirical parameters and is called

as spin-component-scaled (SCS) variant of MP2. The other variant was proposed by Head-Gordon and coworkers[123] in the subsequent year and is termed as scaled-opposite spin (SOS) where the opposite spin contribution is increased to a small extent while the parallel spin component is neglected.

2.5 Density functional theory

The wave function for each electron depends on four variables, i.e., three spatial coordinates and one spin coordinate, therefore making the wave function complicated for many-electron systems. In DFT, the complexity is reduced where the many-body wave function is replaced by the electron density, $\rho(\mathbf{r})$, which depends on only three spatial coordinates. It is based on two theorems by Hohenberg and Kohn[124]. While the first theorem states that the properties of a molecule in the electronic ground state are obtained from the ground-state electron density, the second theorem states that the energy obtained from the ground-state electron density follows the variational theorem. $\rho(\mathbf{r})$ for a system of n electrons is the square of the wave function integrated over n-1 electron coordinates written as

$$\rho\left(\mathbf{r}\right) = n \int \left|\Psi\left(\mathbf{r}, \mathbf{r}_2, \ldots, \mathbf{r}_n\right)\right|^2 d^3\mathbf{r}_2, ..., d^3\mathbf{r}_n. \tag{2.22}$$

Therefore, the total energy of the system is a functional of electron density as

$$E = E\left[\rho\left(\mathbf{r}\right)\right]. \tag{2.23}$$

Following the Kohn-Sham approach,[125] the energy functional has the following form

$$E\left[\rho\left(\mathbf{r}\right)\right] = T\left[\rho\left(\mathbf{r}\right)\right] + V_{\mathrm{ne}}\left[\rho\left(\mathbf{r}\right)\right] + V_{\mathrm{ee}}\left[\rho\left(\mathbf{r}\right)\right] + E_{\mathrm{xc}}\left[\rho\left(\mathbf{r}\right)\right], \tag{2.24}$$

where T is the kinetic energy of the non-interacting electrons which have the same density as that of the interacting electrons and can be expressed in terms of the Kohn-Sham

orbitals, ψ_i^{KS}, as follows

$$T\left[\rho\left(\mathbf{r}\right)\right] = -\frac{1}{2}\sum_{i=1}^{n}\left\langle\psi_i^{\mathrm{KS}}|\nabla_i^2|\psi_i^{\mathrm{KS}}\right\rangle. \tag{2.25}$$

V_{ne} is the nuclear-electron attraction term expressed as

$$V_{\mathrm{ne}}\left[\rho\left(\mathbf{r}\right)\right] = \sum_{I}^{N}\int\frac{Z_I}{|\mathbf{r}-\mathbf{r}_I|}\rho\left(\mathbf{r}\right)d\mathbf{r}, \tag{2.26}$$

and V_{ee} is the electron-electron repulsion term,

$$V_{\mathrm{ee}}\left[\rho\left(\mathbf{r}\right)\right] = \frac{1}{2}\int\int\frac{\rho\left(\mathbf{r}_1\right)\rho\left(\mathbf{r}_2\right)}{|\mathbf{r}_1-\mathbf{r}_2|}d\mathbf{r}_1 d\mathbf{r}_2. \tag{2.27}$$

The last term in Eq.2.24 is the exchange-correlation functional which takes into account all other aspects of the true system. It comprises of two terms: the correction to the kinetic energy which is the difference between the fictitious non-interacting system and the true system, and the difference between the classical and quantum-mechanical electron-electron repulsion, written as

$$E_{\mathrm{XC}}[\rho\left(\mathbf{r}\right)] = \Delta\langle T[\rho\left(\mathbf{r}\right)]\rangle + \Delta\langle V_{\mathrm{ee}}[\rho\left(\mathbf{r}\right)]\rangle. \tag{2.28}$$

The Kohn-Sham equations shown in Eq. 2.29 are analogous to the Hartree-Fock equations and are iteratively solved to find the orbitals that minimize the energy.

$$\hat{h}_i^{\mathrm{KS}}\psi_i^{\mathrm{KS}} = \varepsilon_i^{\mathrm{KS}}\psi_i^{\mathrm{KS}}. \tag{2.29}$$

Here, $\hat{h}_i^{\mathrm{KS}}$ is the KS one-electron operator and is defined as

$$\hat{h}_i^{\mathrm{KS}} = -\frac{1}{2}\,\nabla_i^2 - \sum_{A}^{N}\frac{Z_A}{\mathbf{r}_{1A}} + \int\frac{\rho(\mathbf{r}_2)}{\mathbf{r}_{12}}d\mathbf{r}_2 + V_{\mathrm{XC}}. \tag{2.30}$$

The exchange correlation potential V_{XC} is obtained by taking a functional derivative of E_{XC} with respect to the density as shown below:

$$V_{\mathrm{XC}} = \frac{\delta E_{\mathrm{XC}}[\rho(\mathbf{r})]}{\delta\rho(\mathbf{r})}. \tag{2.31}$$

The advantage of DFT is that it gives the energy of the molecules that includes electron correlation for a similar computational cost as the HF method. However the difficulty is in the approximation of the exchange-correlation functional where no specific form is known leading to the proposals of a series of functionals resulting in different DFT methods. The problem associated with this approach is that there is no way to systematically correct the performance if the chosen functional fails unlike configuration interaction (CI) where there are many possibilities to improve the results.

2.5.1 The exchange-correlation functionals

Various exchange-correlation functionals are described by a ladder of approximations termed as the Jacob's ladder. The higher rungs of the ladder corresponds to approximation that are complicated to construct and use, yet potentially accurate. The rung in the ladder are arranged from bottom to top as follow: (1) local spin density approximation (LDA), (2) generalized gradient approximation (GGA), (3)meta-GGA, (4)the hybrid functional, and (5) the generalized random phase approximation(RPA). These rung are arranged based on the introduction of additional ingredients to the electron density with the expectation that the additional constraints will give accurate exchange-correlation functional. LDA is a non-empirical approximation where no parameter is fitted to the experimental data and only the local density is used. In GGA, the second ingredient is added which is the gradient of the density. The third rung, meta-GGA, includes the orbital kinetic energy density as the third ingredient. Hybrid functionals use the exact-exchange information and RPA use the Kohn-Sham unoccupied orbitals. The fourth and fifth rungs are computationally expensive unlike the first three rung attributed to the double integration over the three dimensional space.

The hybrid functionals are the most commonly used functionals due to the mixture of exchange-correlation functionals and HF exchange term. A hybrid functional is expressed as follows

$$E_{\mathrm{XC}}^{\mathrm{hybrid}} = aE_{\mathrm{X}}^{\mathrm{exact}} + (1-a)E_{\mathrm{X}}^{\mathrm{DFT}} + E_{\mathrm{C}}^{\mathrm{DFT}}, \tag{2.32}$$

where a is the mixing parameter, $E_{\mathrm{X}}^{\mathrm{exact}}$ is the nonlocal HF exchange energy, $E_{\mathrm{X}}^{\mathrm{DFT}}$ is the local DFT exchange energy, and $E_{\mathrm{C}}^{\mathrm{DFT}}$ is the local DFT correlation energy. For example, the Becke's three-parameter Lee-Yang-Parr (B3LYP) exchange-correlation hybrid functional,[126] can be expressed as

$$E_{\mathrm{XC}}^{\mathrm{B3LYP}} = a_0 E_{\mathrm{X}}^{\mathrm{exact}} + (1-a_0)E_{\mathrm{X}}^{\mathrm{LSDA}} + a_{\mathrm{b}}E_{\mathrm{X}}^{\mathrm{B88}} + a_{\mathrm{c}}E_{\mathrm{c}}^{\mathrm{LYP}} + (1-a_{\mathrm{c}})E_{\mathrm{c}}^{\mathrm{LSDA}}, \quad (2.33)$$

where $E_{\mathrm{X}}^{\mathrm{B88}}$ is the gradient corrected exchange energy obtained from the Becke's exchange functional[127], and $E_{\mathrm{c}}^{\mathrm{LYP}}$ is the correlation energy according to the Lee-Yang-Parr correlation functional.[128] The three parameters a_0, a_{b} and a_{c} are the origin of "3" in the acronym and are optimized to 0.20, 0.72 and 0.81, respectively. Due to these fitting variables, the hybrid functionals contain some degree of semi-empirical character. $E_{\mathrm{X}}^{\mathrm{LSDA}}$ and $E_{\mathrm{c}}^{\mathrm{LSDA}}$ are the energies corresponding to the local spin density approximation to the exchange and correlation functionals. Other varieties of hybrid functionals such as PBE0[129], HSE[130] and O3LYP.[131] are reported in the literature.

Hybrid DFT functionals such as B3LYP are used extensively, however, these functionals have been found to be unsuccessful to describe closely-lying excited states,[132] polarizability of extended conjugated systems,[133–135] and excitation energies for charge transfer states,[136–139]. This is due to the deviation of the exchange potential from the correct form, $-\frac{1}{r_{12}}$, at long range. To overcome this error, Tsuneda and coworkers[140,141] split the Coulomb interaction into the short-range and long-range parts using the error function (erf) as

$$\frac{1}{r_{12}} = \frac{1-erf\,(\mu r_{12})}{r_{12}} + \frac{erf\,(\mu r_{12})}{r_{12}}, \quad (2.34)$$

where r_{12} is the interelectron coordinate, μ is a range separated parameter which can be determined empirically[141–146] or by minimizing the deviations from the conditions set for KS functionals[147]. The first term corresponds to the short-range and is treated using exact exchange while the second term corresponding to the long-range is treated using local or semilocal exchange. The generalized form of the above equation with the

introduction of two extra parameters α and β by Yanai et al.[141] is written as

$$\frac{1}{r_{12}} = \frac{1-[\alpha\ +\beta\ erf\,(\mu r_{12})]}{r_{12}} + \frac{\alpha\ +\beta\ erf\,(\mu r_{12})}{r_{12}}, \tag{2.35}$$

where $0 \leq\ \alpha+\beta \leq 1$, $0 \leq\ \alpha\ \leq 1$, $0 \leq\ \beta\ \leq 1$. The parameter α and $\alpha+\beta$ represent the HF-exchange in the short-range term and long-range term respectively. Several range-separated hybrid functionals have been developed over the years such as LC-ωPB[148], M11[145] , CAM-B3LYP[141], ωB97X-V[149] and many more.

2.6 Time-dependent density functional theory

TDDFT is an extension of the basic ideas of the Hohenberg-Kohn theorem for ground-state to problems involving time-dependent external potentials.[124] It is used for the investigation of the excited-state properties or the general time-dependent phenomena. Similar to the DFT, the time-dependent DFT equation is formulated by considering the fictitious non-interacting systems. It is based on two theorems formulated by Runge and Gross[150] in the year 1984. The first theorem states the existence of a one-to-one correspondence between the time-dependent external potential, $v_{ext}(r,t)$ and the electronic one-body density, $\rho(r,t)$ for many-body systems evolving from a fixed initial state. The second theorem is based on the variational principle where the exact TD density can be obtained by applying the least action principle to the Frenkel- Dirac action defined as[151]:

$$A\,[\rho] = \int_{t_0}^{t_1} dt \Big\langle \Psi[\rho](t) \Big| i\hbar\frac{\partial}{\partial t} - \hat{H}(t) \Big| \Psi[\rho](t) \Big\rangle - i\hbar\,\langle \Psi[\rho](t_f) | \delta\Psi[\rho](t_f) \rangle \tag{2.36}$$

where $\Psi[\rho](t)$ is the exact time-dependent wave function functional of the time-dependent density, $\delta\Psi[\rho](\mathrm{t})$ is the first-order differential of the wave function, $\hat{H}$ is the time-dependent Hamiltonian, and t_0 and t_f are the initial and final times. In cases where the external potential is weak, the changes of the system from its ground state is small, therefore extracting density information using perturbative approach is preferable. The most

commonly used perturbation method is based on response theory where the density-density response function which relates the variations in exact TD density to variations of the TD external potentials is constructed.

At $t < t_0$, the time-dependent potential is assumed to be zero. At time t_0, a time-dependent potential, v_1 ($\mathbf{r}$, t) is turned on thus affecting the density of the system and is written as

$$\rho(\mathbf{r},t) = \rho_0(\mathbf{r}) + \rho_1(\mathbf{r},t) + \rho_2(\mathbf{r},t) + \rho_3(\mathbf{r},t) + ... \tag{2.37}$$

where ρ_0, $\rho_1(\mathbf{r},t)$ and $\rho_2(\mathbf{r},t)$ are the ground state density, first-order response and second-order response etc. The higher order terms can be neglected for weak external perturbations and only the linear term is considered. The linear response term can be written as

$$\rho_1(\mathbf{r},t) = \int dt_1 \int d^3r_1 \chi(\mathbf{r},t,\mathbf{r}_1,t_1) v_1(\mathbf{r}_1,t_1), \tag{2.38}$$

where χ represents the linear density-density response function of the system. The linear change in the density of an interacting system can be calculated within the time-dependent Kohn-Sham framework by considering fictitious non-interacting system and is given by the following equation

$$\rho_1(\mathbf{r},t) = \int dt_1 \int d^3r_1 \chi_s(\mathbf{r},t,\mathbf{r}_1,t_1) v_{s1}(\mathbf{r}_1,t_1), \tag{2.39}$$

where χ_s term is the density-density response function for the noninteracting KS electrons. The symbol $v_{s1}(\mathbf{r},t)$ is the linear change of the effective potential, $v_s(\mathbf{r},t)$, of the time-dependent KS system, and it can be written as

$$v_{s1}[\rho](\mathbf{r},t) = v_1(\mathbf{r},t) + \int d^3r_1 \frac{\rho(\mathbf{r}_1,t)}{|\mathbf{r}-\mathbf{r}_1|} + \int dt_1 \int d^3r_1 \frac{\delta v_{XC}[\rho](\mathbf{r},t)}{\delta\rho(\mathbf{r}_1,t_1)} \rho_1(\mathbf{r}_1,t_1). \tag{2.40}$$

where $v_1(\mathbf{r},t)$ is the external potential and second term is the linearized time-dependent Hartree potential. The functional derivative of the XC potential with respect to the density is known as the exchange kernel and is evaluated at the ground state density.

By using equations 2.40, 2.39 and 2.38, we obtain the Dyson equation of TDDFT as

$$\chi(\mathbf{r},t,\mathbf{r}_1,t_1) = \chi_s(\mathbf{r},t,\mathbf{r}_1,t_1) + \int d\tau \int d^3x \int d\tau_1 \int d^3x_1 \chi_s(\mathbf{r},t,\mathbf{x},\tau) \left\{\frac{\delta(\tau-\tau_1)}{|\mathbf{x}-\mathbf{x}_1|} + f_{XC}(\mathbf{x},\tau,\mathbf{x}_1,\tau_1)\right\}\chi(\mathbf{x}_1,t_1,\mathbf{r}_1,t_1). \tag{2.41}$$

The above equation is successfully applied for the calculation of the properties of many-body systems that are weakly perturbed. Casida approach has been one of the widely used formalism out of the other variants of linear-response.[152]

2.7 Algebraic diagrammatic construction scheme for the polarization propagator

The algebraic diagrammatic construction (ADC) scheme of the polarization propagator for the electronically excited states is based on many-body Green's function theory.[153] Since a unique Green's function cannot be defined in many-body systems, another alternative is made and that is in the identification of building blocks called propagators that can solve certain classes of problems. The polarization propagator describes the time-dependent fluctuations of the ground-state electron density and implicitly contains the information about the excited-states of the molecule. The compact diagonal representation of the polarization propagator $\Pi(\omega)$ is as follows

$$\Pi(\omega) = \mathbf{x}^\dagger(\omega-\Omega)^{-1}\mathbf{x}, \tag{2.42}$$

where Ω is the diagonal matrix of vertical excitation energies ω and $\mathbf{x}$ is the spectroscopic amplitudes. The non-diagonal representation according to ADC schemes is given by

$$\Pi(\omega) = \mathbf{f}^\dagger(\omega-\mathbf{M})^{-\mathbf{1}}\mathbf{f}, \tag{2.43}$$

where $\mathbf{M}$ is a non-diagonal matrix representation of an effective Hamiltonian and $\mathbf{f}$ is the matrix of the effective transition moments. From the diagrammatic perturbation theory, these two terms can be expanded with respect to the perturbation-theoretical

order in the fluctuation potential as follows

$$\mathbf{M} = \mathbf{M}^{(0)} + \mathbf{M}^{(1)} + \mathbf{M}^{(2)} + \dots$$
$$\mathbf{f} = \mathbf{f}^{(0)} + \mathbf{f}^{(1)} + \mathbf{f}^{(2)} + \dots$$

ADC(n), where n denotes the order, takes into account all the terms that are required for the perturbation theoretically consistent description of $\Pi(\omega)$. The explicit algebraic expression of $\mathbf{M}$ and $\mathbf{f}$ can be obtained by the perturbation-theoretical order analysis of $\Pi(\omega)$. Having known the algebraic expression of $\mathbf{M}$, the excitation energies are obtained by diagonalization of the matrix $\mathbf{M}$. The solution of the Hermitian eigenvalue problem

$$\mathbf{MY} = \mathbf{Y}\Omega; \mathbf{Y}^\dagger\mathbf{Y} = 1, \tag{2.44}$$

provides the excitation energies ω_n. The eigenvectors $\mathbf{y}$ are linked to the spectroscopic amplitudes $\mathbf{x}$ via

$$\mathbf{x} = \mathbf{y}^\dagger\mathbf{f}. \tag{2.45}$$

Another route for deriving ADC expression without the knowledge of propagator is called intermediate state representation(ISR). The correlated excited-state basis $\{\Psi_J^0\}$ can be generated from the correlated ground-state wavefunction, $\{\Psi_0\}$ by using excitation operators $\hat{C}_J \equiv \{\hat{c}_a^\dagger\hat{c}_k, \hat{c}_a^\dagger\hat{c}_b^\dagger\hat{c}_k\hat{c}_l, \dots\}$ that represents single, double, etc... excitations as

$$\Psi_J^0 = \hat{C}_J\Psi_0. \tag{2.46}$$

The Gram-Schmidt orthogonalization of the correlated excited-basis $\{\Psi_J^0\}$ yields intermediate state (IS) basis $\{\tilde{\Psi}_J\}$ and the previously mentioned effective quantities $\mathbf{M}$ and $\mathbf{f}$ can be written using the IS basis as follows

$$(\mathbf{M})_{IJ} = \langle\tilde{\Psi}_I|\hat{H} - E_0^N|\tilde{\Psi}_J\rangle \tag{2.47}$$

and

$$(\mathbf{f})_{J,pq} = \langle \tilde{\Psi}_J | \hat{c}_p^\dagger \hat{c}_q | \Psi_0 \rangle. \tag{2.48}$$

The limitation of ADC is in the single-reference nature of the MP theory for electronic ground state as the accuracy of the excited state calculation relies on the reasonable description of the ground state by MP theory. Therefore, ADC schemes are not preferable for molecules with multi-reference character.

2.8 Multi-configurational method

A single electron configuration is considered in the HF method and therefore, the HF wave function does not account for the static electron correlation. This is called a single-reference (SR) method. The method fails to describe the system near regions of conical intersections. If a linear combination of all the possible Slater determinants is used in the configuration interaction expansion, the obtained energies are exact. However, the cost of such calculations is huge, and therefore, methods such as MCSCF are used to describe the CI regions.

The MCSCF wavefunction, Ψ_{MCSCF}, is a linear combination of many electron configurations represented as configuration state functions[154] (denoted as Φ) as

$$\Psi_{\mathrm{MCSCF}} = \sum_m C_n \left| \Phi_n \right\rangle .$$

Here m is the number of CSFs and C_m are the coefficients. In the MCSCF method, both the expansion coefficients and the molecular orbitals, i.e., expansion coefficients connecting MOs to the basis functions, are optimized. The CASSCF[117] is the most widely used MCSCF method. Here, the set of CSFs are divided into an active and an inactive set of orbitals. While the inactive space consists of doubly-occupied in occupied and unoccupied in virtual spaces, respectively, the remaining electrons and orbitals make the active space. Typically, a CASSCF calculation with an active space consisting of X electrons distributed among Y number of orbitals is denoted as CAS(X,Y) calculation.

However, the selection of an active space is non-trivial, and requires an understanding of the system, and the process under consideration. As CASSCF method does not consider dynamical correlation, this is usually included by methods such as CASPT2.[118]

2.9 Non-adiabatic dynamics

As discussed in the Sec. 2.2, the BO approximation forms the basis of the electronic structure calculations. However, its applicability fails in the region of quasi-degenerate states. The following discussion is taken from a review article by Barbatti[155]. In such cases, time evolution of the nuclear wave packet branches along several closely-lying states. This type of phenomenon is called non-adiabatic effect and is commonly observed in photochemical reactions. However, the challenge is the time-dependent theoretical treatment of such effects in molecular systems, ranging from accurate description of the excited states to the time propagation of their properties. A full quantum mechanical treatment of large systems showing non-adiabatic effects is essentially impractical, and this has led to development of several semiclassical methods. Trajectory surface hopping(TSH)[156,157] method is one of the most successful semiclassical approaches in considering the non-adiabatic effects.[158–160] This method is based on the assumption that the time evolution of a wave packet through closely-lying potential energy surfaces can be approximated by an ensemble of independent semiclassical trajectories which are randomly distributed among the branched surfaces. In this method, the time evolution of the nucleus on the BO surface is treated classically, and the switching of the population to nearby states due to the non-adiabatic effects is taken care of by a stochastic algorithm. Tully and Preston's[156] TSH formulation first assumes that the evolution of nuclei is on a general trajectory $\mathbf{R}^c(t)$ that will be later identified as classical trajectory. The time-dependent wave function for the electrons is written in an electronic basis as

$$\varphi\left(r, \mathbf{R}^c, t\right) = \sum_j c_j(t)\Phi_j(r; \mathbf{R}^c(t)), \tag{2.49}$$

where r denotes all the electronic coordinates. The substitution of Eqn. 2.49 in the time-dependent electronic Schrödinger equation

$$\left(i\hbar\frac{\partial}{\partial t} - H_{elec}\right)\varphi\left(r, \mathbf{R}^c, t\right) = 0 \tag{2.50}$$

results in the set of differential equations for the coefficients $c_k(t)$:

$$i\hbar\frac{\mathrm{d}c_k}{\mathrm{d}t} + \sum_j \left(-H^c_{kj} + i\hbar\mathbf{F}^c_{kj}.\mathbf{v}^c\right)c_j = 0. \tag{2.51}$$

The above equation is labelled as a semiclassical time-dependent Schrödinger equation (SC-TDSE) where H^c_{kj} are the matrix elements $\langle\Phi_k|H_{elec}|\Phi_j\rangle_r$, F^c_{kj} is the nonadiabatic coupling vector between states k and j and $\mathbf{v}^c$ is the nuclear velocity vector. The superscript c in the above equation show that the evaluation is for a specific nuclei position $\mathbf{R}^c$ at time t.

In TSH, the propagation of a nucleus m with mass M_m on a single electronic state j is carried out by solving the Newton's equations of motion as

$$\frac{\mathrm{d}^2\mathbf{R}^c_m}{\mathrm{d}t^2} - \frac{f^c_m}{M_m} = 0, \tag{2.52}$$

where the force is proportional to the gradient of the potential energy

$$f^c_m = -\nabla_{R_m}H^c_{jj}. \tag{2.53}$$

One of the most common methods for computing transition probabilities between states k and j is the Fewest-switches algorithm proposed by Tully[157] where the number of hopping event within one time step is minimized. The hopping probability is given as

$$P_{j\to k} = \frac{\text{Population increment in } k \text{ due to flux from } j \text{ during } \Delta t}{\text{Population of } k}. \tag{2.54}$$

The population in the k state, $c_k(t)$, is obtained from the diagonal elements of the density matrix, which is defined as

$$\rho_{jk}(t) = c_j c_k^*. \tag{2.55}$$

The hopping event is determined to be successful if two conditions are satisfied and these are as follows:

1. A random number in the [0,1] interval should satisfy

$$\sum_{n=1}^{k-1} P_{j\to n}(t) < r_t \leq \sum_{n=1}^{k} P_{j\to n}(t); \tag{2.56}$$

2. The energy gap between the initial and final states should satisfy the following equation[155]

$$V_k(\mathbf{R}^c(t)) - V_j(\mathbf{R}^c(t)) \leq \frac{\left(\sum_m^{N_{\text{at}}} \mathbf{v}_m^c . \mathbf{F}_{\text{kj}}^{c,m}\right)^2}{2\sum_m^{N_{\text{at}}} M_m^{-1} \left(\mathbf{F}_{\text{kj}}^{c,m}\right)^2}. \tag{2.57}$$

The above equation was derived with the condition satisfying the law of conservation of energy. However, if only Eqn 2.56 is satisfied, the hopping is termed as frustrated hopping, where the total energy after hopping is larger than the previous one.

The shortcoming of Tully's FSSH is the non-decaying amplitude of the off-diagonal elements in the electronic density matrix during the dynamics. This is due to the propagation of SC-TDSE along a single trajectory $\mathbf{R}^c$ which is determined by the gradients for a particular electronic state j . In this approach, the amplitudes of all other states are constrained to that of trajectory $\mathbf{R}^c$. As a result, the method becomes inconsistent leading to the difference between the fraction of trajectories in each state and the average electronic population. The correction to this decoherence effect in FSSH was implemented by Granucci et *al.*[161] based on Truhlar's scheme of nonlinear decay of mixing model,[162,163] where the time-dependent coefficients in the state k and j are modified

at every time step as follows:

$$c_k^{new} = c_k \exp\left(\frac{-\Delta t}{\tau_{kj}}\right) \forall (k \neq j) \tag{2.58}$$

and

$$c_j^{new} = \frac{c_j}{|c_j|}\left[1 - \sum_{k \neq j} |c_k^{new}|\right]^{\frac{1}{2}}. \tag{2.59}$$

The decoherence time is given by

$$\tau_{kj} = \frac{\hbar}{|V_{\mathrm{kk}} - V_{\mathrm{jj}}|}\left(1 + \frac{\alpha}{E_{\mathrm{kin}}}\right), \tag{2.60}$$

where E_{kin} is a nuclear kinetic energy, Δt is the time interval and α is an empirical decoherence parameter taken as 0.1 Hartree.

The initial conditions for the dynamics simulation are selected to reflect the type of study. For photochemical reactions, the position and momentum of nuclei produced by the laser pulse are essential parameters. In such cases, starting with the ground state molecule that gets promoted to the excited state is preferable. This is mostly done by considering the harmonic potential energy around the ground state minimum and the distribution of nuclei position and momenta was obtained by Wigner distribution.[164] After the initial conditions generation, the absorption spectra can be simulated using nuclear ensemble approach and the dynamics can be simulated. Imposing certain conditions such as excitation energy window and large transition probability in order to fit the experimental data results in fewer geometries starting from multiple electronic state.

Chapter 3

Excited state processes in 1-hydroxy-2-acetonaphthone at ADC(2) and CASSCF levels

In this chapter, a comprehensive picture of the excited st
2-acetonaphthone(HAN) including the proton transfer and re
electronic structure calculations at ADC(2) and CASPT2/
simulations at ADC(2) levels are discussed. Our studies sho
process in the S_1 state is barrierless. The dynamics simula
proton transfer time of 43 fs and the improbable non-radi
within 600 fs simulation time. Reproduced from " *The Journa*
2021, *125*, 8015" with permission from American Chemical

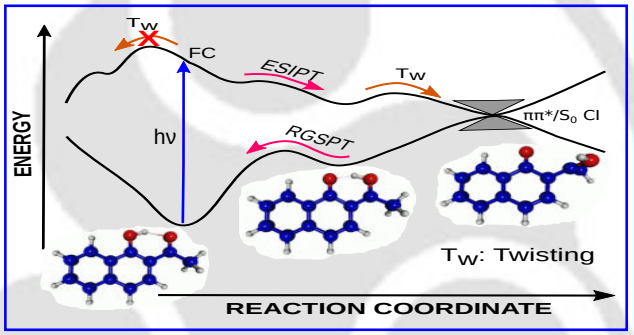

3.1 Introduction

1-hydroxy-2-acetonaphthone(HAN) belonging to the ESIPT-active family is used in probing the micro-environment, chemical, and biological caging effects.[165,166] There are many studies, both experimental and computational, on HAN due to its unusual photophysical properties. The most controversial topic has been the issue of ESIPT in HAN. In contrast to typical ESIPT systems that exhibit Stokes shift $\sim$ 10000 cm^{-1}, HAN showed a comparatively small ($\sim$ 6000 cm^{-1}) shift causing doubt about its existence. Douhal et al.[167] studied fluorescence excitation and emission spectra in a supersonic expansion. Tautomerization from the naphthol to the quinomethide form in the excited state was concluded in their study. In addition, it was also concluded that instead of only one coordinate being active during the proton transfer, multiple coordinates take part in the process. The dual fluorescence spectra were later explained[168] by having asymmetric double-well potential energy surfaces (PESs) in both ground and excited states. On the other hand, a study by Catalán et al. concluded that HAN is devoid of any ESIPT[169]. Lu et al.[170] studied the excited state dynamics in the gas phase using femtosecond time-resolved multiphoton ionization and showed that HAN exhibited biexponential decay, one of those being the rapid ESIPT of $\sim$ 60-85 ps time scale. Lochbrunner et al.[171], using Raman and transient absorption studies, obtained the ESIPT time scale to be $\sim$ 30 fs. In fluorescence and time-resolved photoelectron studies, Catálan and Paz[172] reported that HAN exhibits two stable enol forms in the first π-π^* excited state which can easily be converted into each other by twisting about the methyl group. They concluded that the presence of the two enol forms gave rise to a split-doublet in the fluorescence excitation spectra. In one of the most recent studies, Kim et al.[173] examined the excited state dynamics of HAN by time-resolved fluorescence studies in acetonitrile. It was observed that the excited normal form got deexcited with a 80 fs time constant, while the ESIPT time constant is $<$ 25 fs.

Keeping in mind the above results, many computational studies have also been carried out at different levels of theories to explain the mechanisms of various photophysical processes. Szeghalmi et al.[174] carried out complete active space self-consistent

field (CASSCF) studies along with a resonance Raman spectroscopic study and concluded that ESIPT occurs due to an increase in the electron charge on the carbonyl oxygen and a decrease in hydroxyl oxygen. The possibility of a stable keto structure in the ground state has been a topic of various studies.[175–177]. Regarding this, Tobita et al.[178] suggested that the rotated form of keto viz trans-keto conformer is formed in the ground state via internal conversion of the twisted protonated form after relaxation from the S_1 state. Their results coincide with that of Organero et al.[176]. Ortiz Sánchez et al.[177] performed density functional theory (DFT) and time-dependent DFT (TDDFT) based studies and showed that two minima corresponding to the enol and trans-keto conformer are present in the ground state with enol being the most stable form. It was concluded that the proton-transfer is not possible in the ground state. In S_1, the energy barrier was quite low at the TD-DFT level, enabling the ultrafast ESIPT process. A one-dimensional ab initio potential energy curve was constructed and quantum dynamical studies using this curve resulted in a very fast, $\sim$ 25 fs, ESIPT process. This result is in good agreement with the experimental result of Lochbrunner et al.[171] Two recent computational studies by Yang et al.[179] and Ning et al.[180] based on the TDDFT method have provided more information on these systems. Yang et al.[179] carried out the calculation with the inclusion of the solvents and concluded that the keto-rotamer is possible in the S_1 state after proton transfer due to a smaller barrier. They also showed that the keto-rotamer formed by twisting of the -$COCH_3$ group is the most stable form in the S_1 state, in accordance with the results of Organero et al.[181] Ning et al.[180] performed an adiabatic molecular dynamics simulation with the TDDFT method. The results confirmed the occurrence of proton transfer in HAN by calculating the proton transfer time to be 37 fs, in accordance to the experimental report by Kim and coworkers.[173]

From the above discussion, it is clear that there are still issues to be resolved regarding the photocycle of HAN. Questions regarding the exact proton transfer time and relaxation pathways from the excited states are still to be resolved. In this scenario, computational studies are of great help and in particular, static and dynamical studies with wave function based methods such as second-order coupled-cluster(CC2),[116] the second order algebraic diagrammatic construction (ADC(2)),[153,182] or if possible, multiconfigurational methods such as CASSCF[117,118] methods, add to our understanding

which has been highlighted in many recent studies.[183–187] To the best of our knowledge, the static and dynamic studies reported earlier were confined only to the proton transfer process and the various relaxation pathways have not been explored. The present study is carried out with the objective of illustrating various excited state processes including proton transfer and two different pathways of deactivation in HAN at ADC(2) and complete active space second-order perturbation theory (CASPT2) levels of theories. The ADC(2) method[153,182] was selected in our study due to its success in explaining the various excited state processes in other molecules.[29,185–187] As shown in the literature, wave function-based methods are efficient and produce accurate dynamical results.[187,188] For ADC(2), a particular advantage is its usage with the resolution of identity (RI) approach which immensely reduces the computational time.[189–191] In particular, we use the empirically scaled opposite spin (SOS)[123,192] correction variant of ADC(2) in our studies. The combined static electronic structure and dynamical calculations are performed to provide new insights into the excited state processes with the SOS-ADC(2) method and the results are compared to the literature results.

3.2 Computational Details

In all of the calculations, core electrons were kept frozen. Optimized ground state geometries of various enol and keto conformers were obtained at the second-order Møller-Plesset perturbation theory[115] level with SOS corrections scheme and the RI approximation (RI-SOS-MP2). Similarly, first excited state geometries of all the conformers are optimized at RI-SOS-ADC(2) level of theory. Normal mode analyses are performed at the same levels of theory. Absence of imaginary frequencies indicated that the optimized structures are true minima. Vertical excitation energies (VEEs) were calculated at the optimized ground state geometries at RI-SOS-ADC(2) level. For studying the proton transfer, potential energy curves along the proton transfer coordinate were computed in S_0 and S_1 states at SOS-ADC(2) level. For studying the deactivation paths, potential energy curves along the twisting coordinates were constructed. In the keto region, relaxed scans were performed in the S_1 state, and this was followed by rigid scans in the S_0 state at the S_1 optimized geometries. In addition, the S_1/S_0 MECI structure was

located in this region at CASSCF level of theory. In the enol Franck-Condon region, the curves were constructed by constrained optimization at SOS-ADC(2) level. Further, single point calculations at the multi-state multireference CASPT2 (MS-MR-CASPT2) level were also performed at SOS-ADC(2) optimized geometries. The intruder state issue was handled with a level shift of 0.5 a.u. in the CASPT2 calculation. MP2 and ADC(2) calculations were carried out with correlation-consistent polarized valence double zeta (cc-pVDZ)[193,194] basis set. On the other hand, CASPT2 and CASSCF studies used 6-31G(d) and 6-31G(d,p) basis sets. Multireference calculations were carried out using the MOLPRO 2012 program suite[195]. All other electronic structure calculations were conducted using the TURBOMOLE 7.1 program.[196]

Semi-classical dynamics simulations were performed in the gas phase with the NEWTON-X software[197,198] interfaced with TURBOMOLE 7.1. In the adiabatic dynamics study, 200 initial conditions were generated from a harmonic-oscillator Wigner distribution of the normal modes of the ground state optimized geometry. Trajectories were simulated up to 120 fs with a time step of 0.5 fs. The time period chosen here was sufficient to describe the proton transfer time. Dynamics was initiated in the S_1 state by employing RI-SOS-ADC(2)/cc-pVDZ. Statistical analysis of all the trajectories was performed to obtain detailed insights into the time evolution of proton transfer. In our study, the proton transfer time was taken as the time when the transferred proton was equidistant from the donating and the accepting atoms. Henceforth, RI-SOS-MP2 and RI-SOS-ADC(2) will be denoted as MP2 and ADC(2), respectively.

3.3 Results and discussion

3.3.1 S_0 optimized geometries

In our study, four possible enol and four possible keto structures are considered. Optimized structures of all the possible enol and keto conformers in the S_0 state are shown in Fig. 3.1 and their Cartesian coordinates are given in the Appendix 4. Vibrational frequencies of all these structures, as shown in Table A8, are real. In Fig. 3.1, few atoms in **E-a** that are involved in the proton transfer and the deactivation processes are

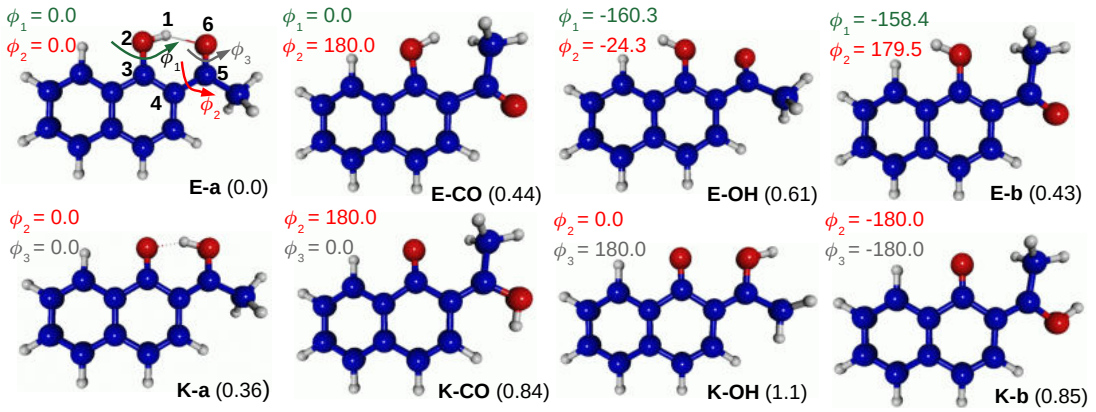

FIGURE 3.1: Optimized structures of different enol and keto conformers of HAN in the S_0 state. Relative energies of the conformers with respect to that of **E-a** are given in parentheses. Torsional angles ϕ_1, ϕ_2, ϕ_3 (in degrees) are marked (The positive and negative values of dihedral angles indicate the clockwise and anti-clockwise rotations, respectively). All results are obtained at MP2/cc-pVDZ level of theory.

labeled. It is to be noted here that all of the enol isomers presented here and two keto isomers were explored by Organero et al.[176,181] using restricted Hartree-Fock (RHF), MP2 and configuration interaction singles (CIS) methods. These isomers are denoted as **E-a**, **E-CO**, **E-OH**, **E-b**, **K-a**, and **K-CO**in our study. The **K-b** form was found in the TDDFT study by Ning et al.[180] All of these isomers are formed from the intramolecular hydrogen-bonded structure of **E-a** and **K-a** by torsional rotations about $\angle H_1$-O_2-C_3-$C_4(\phi_1)$, $\angle C_3$-C_4-C_5-$O_6(\phi_2)$, and $\angle C_4$-C_5-O_6-$H_1(\phi_3)$. Additionally, the structure **K-OH** in which the hydrogen atom connected to O_6 points away from the naphthalene ring is also considered in our work. The most stable structure in the ground state corresponds to **E-a** which agrees with the previous computational studies.[176,177,180,181] The energy of **E-a** is taken as the reference and energies of all the other structures shown in Fig. 3.1 are relative to the energy of this structure. **E-a** is completely planar and its stability is due to an intramolecular hydrogen bond(H-bond) between the oxygen of the carbonyl group and the hydrogen of the hydroxyl group. The other isomers **E-CO**, **E-OH** and **E-b** are devoid of any intramolecular hydrogen bonds. Considering **E-a** as the reference point for rotations, **E-CO** is formed by a 180° twist along ϕ_2 and this is 0.44 eV higher in energy. **E-OH**, formed by rotations of -160.3° and -24.3° along ϕ_1 and ϕ_2, respectively, is higher by 0.61 eV. Torsional rotations along the same two coordinates by -158.4° and 179.50°, respectively, led to the formation of **E-b** at 0.43 eV. The stability

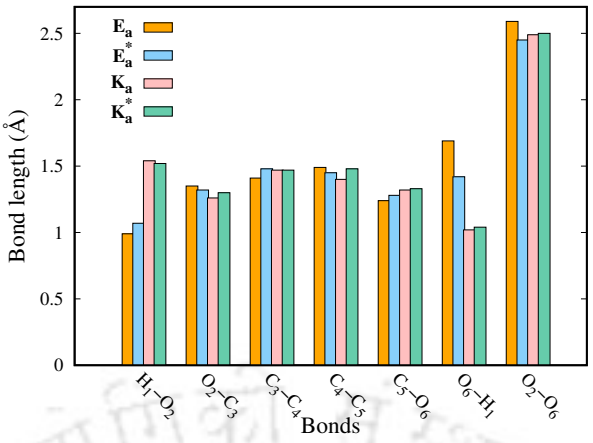

FIGURE 3.2: Comparison of selected geometrical parameters of **E-a** and **K-a** in S_0 and S_1 states.

of these conformers are in the following order: **E-a** > **E-b** > **E-CO** > **E-OH** which is in agreement with the CIS results of Organero et al.[176]

Among the proton transferred forms, **K-a** is found to be the most stable structure in S_0, and is 0.36 eV higher than **E-a**. This is in contrast to the studies by Organero et al.[176,181] and Ortiz-Sanchez et al.[177] in which the structure **K-a** in the ground state was not located. Instead, **K-CO** structure was obtained as a local minimum in the ground state. For the keto-conformers, **K-a** is taken as the reference point for rotation. **K-CO** is obtained by a twisting of 180.0° along ϕ_2 and is located at 0.84 eV. **K-OH** is 1.1 eV higher in energy than **E-a**. This structure is a result of a torsional rotation of 180° along ϕ_3. **K-b**, on the other hand, is almost similar in energy to **K-CO** and is formed by rotations of -180.0°along both ϕ_2 and ϕ_3. The energy of **K-CO** is in close agreement with the result of Organero et al.[176] in which a difference of 0.96 eV is reported. Since **E-a** and **K-a** are involved in proton transfer processes, structural differences between these two are compared by measuring the bond lengths which are involved in the intramolecular hydrogen bonds. Fig. 3.2 shows a comparison of these bond lengths. These parameters are also tabulated in Table A3. It is observed that O_2-C_3 and C_4-C_5 bond lengths are shortened from **E-a**(1.35 Å and 1.49 Å) to **K-a**(1.26 Å and 1.40 Å) by 0.09 Å each. In addition, the lengthening of C_3-C_4 and C_5-O_6 bonds by 0.06 Å and 0.08 Å, respectively, is observed from **E-a**(1.41 Å and 1.24 Å) to **K-a**(1.47 Å and 1.32 Å).The remaining C-C bonds in the naphthalene moiety show only

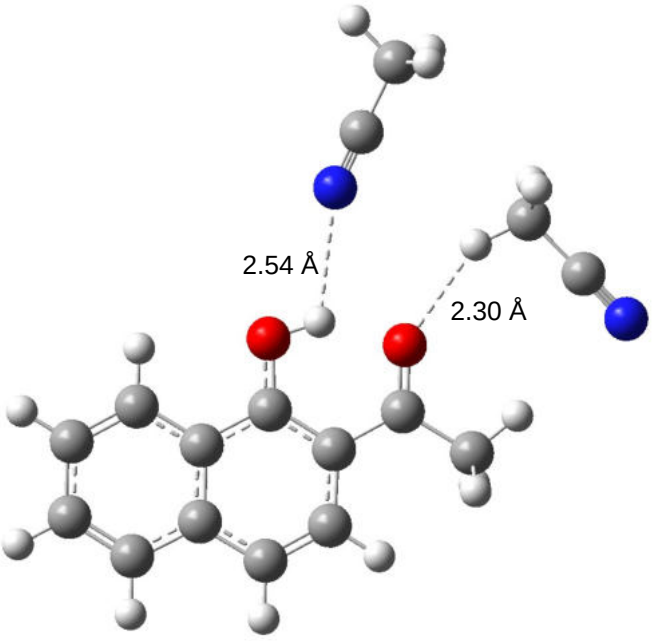

FIGURE 3.3: Optimized ground state structure of the complex between HAN and two acetonitrile molecules.

minor variations between **E-a** and **K-a** structures. These observations clearly explain the stability of **E-a** over **K-a** on the basis of aromaticity which is lost in **K-a**.

3.3.2 VEEs and frontier molecular orbitals(FMOs)

VEEs of **E-a** were obtained using the cc-pVDZ basis set. VEE to the lowest $^1\pi\pi^*$ excited state ($E_g{}^1$) was found to be 3.94 eV, showing a deviation of ∼0.5 eV from the experimental result of 3.4 eV.[173] We note here that this discrepancy between the experimental and computational results can arise due to various reasons. At first, we checked the effect of the basis set. The $E_g{}^1$ values were found to be 3.86 eV, 3.85 eV and 3.82 eV using cc-pVTZ, aug-cc-pVDZ and aug-cc-pVTZ basis sets, respectively. It is worth mentioning here that deviations of about 0.3 to 0.57 eV from the experimentally reported values are reported for systems similar to HAN such as salicylic acid, malonaldehyde and ortho-hydroxy benzaldehyde,[40,41] and for other systems as well[199–201] at the CC2/ADC(2) level of theory. Besides the basis set effect, another source for this deviation is the noninclusion of a solvent. Absorption properties are greatly influenced by solute-solvent interactions which usually stabilize the excited state resulting

in a red-shift of the spectrum. To check the effect of acetonitrile solvent used in Ref. 23, we considered the implicit, and a combination of the implicit and an explicit solvent model. Pure implicit/continuum solvent approaches use the bulk properties of a solvent to polarize a solute. On the other hand, proper solute-solvent interactions are taken into account by explicitly having a large number of solvent molecules in the system. But this approach become computationally prohibitive if a large number of solvent molecules are used, and therefore, in quantum mechanical studies, a fewer number of solvent molecules are considered. For modeling the implicit solvents, we have used the conductor-like screening model (COSMO)[202,203] in a state-specific approach as implemented in TURBOMOLE7.1. Explicit solvation is considered by having two acetonitrile molecules suitably placed around HAN as shown in the Fig. 3.3. The resultant vertical excitation energies are 3.70 and 3.65 eV using implicit and combined implicit-explicit models, respectively. This shows a very good improvement over the gas phase results. We would like to mention here that approximately 1-2 solvation shells are required to be considered quantum mechanically for convergence of excitation energies, in addition to having a bulk which is usually treated using molecular mechanics(MM). Considering the above results, we consider that the results obtained using ADC(2) are improved further with a more accurate solvent model with a QM/MM type study. Nevertheless, keeping in mind the computational cost for dynamical simulation, both static and dynamical studies are carried out using the cc-pVDZ basis set in the gas phase.

VEE values calculated for the ground state optimized structures of all the conformers are tabulated in Table 3.1. For each conformer, energies of only the first three lowest lying excited states are shown with the corresponding oscillator strengths (f_{osc}s) and their state characters. Molecular orbitals that contribute the most to the excitations to the S_1 state are displayed in Fig. 3.4. S_1 states of **E-a**, **E-b**, **E-CO** and **K-a** are of π-π^* nature, and these states are primarily composed of the highest occupied molecular orbitals (HOMO) $\rightarrow$ lowest unoccupied molecular orbital (LUMO) single excitations. It is also observed from Fig. 3.4 that these orbitals have significant spatial overlaps with each other which is reflected in their comparatively larger oscillator strength values. On the other hand, S_1 states of **E-OH**, **K-CO**, **K-OH** and **K-b** are formed by promotions of electrons from the HOMO-3 to LUMOs which involve comparatively lesser spatial

TABLE 3.1: VEEs of the first three excited states of **E-a**, **E-CO**, **E-OH**, **E-b**, **K-a**, **K-CO**, **K-OH** and **K-b** structures. Oscillator strengths (f_{osc}s) for the respective transitions and orbitals involved in the transitions with the character of the corresponding excited states are also shown. H and L denote HOMO and LUMO, respectively. All of the results are obtained at ADC(2)/cc-pVDZ level of theory. The experimental absorption maximum is at 365 nm.[173]

Geometry	State	VEE (eV)	f_{osc}	Transition	Character
E-a	S_1	3.94	0.105	$H \rightarrow L$	$\pi\pi^*$
	S_2	4.32	0.000	H-3 $\rightarrow L$	$n\pi^*$
	S_3	4.61	0.047	$H \rightarrow L$+1	$\pi\pi^*$
E-CO	S_1	4.08	0.050	$H \rightarrow L$	$\pi\pi^*$
	S_2	4.19	0.000	H-3 $\rightarrow L$	$n\pi^*$
	S_3	4.81	0.081	$H \rightarrow L$+1	$\pi\pi^*$
E-OH	S_1	3.97	0.004	H-3 $\rightarrow L$	$n\pi^*$
	S_2	4.09	0.035	$H \rightarrow L$+1	$\pi\pi^*$
	S_3	4.61	0.073	$H \rightarrow L$	$\pi\pi^*$
E-b	S_1	4.08	0.024	$H \rightarrow L$	$\pi\pi^*$
	S_2	4.09	0.008	H-3 $\rightarrow L$	$n\pi^*$
	S_3	4.72	0.077	$H \rightarrow L$	$\pi\pi^*$
K-a	S_1	3.56	0.237	$H \rightarrow L$	$\pi\pi^*$
	S_2	4.05	0.000	H-3 $\rightarrow L$	$n\pi^*$
	S_3	4.57	0.077	H-2 $\rightarrow L$	$\pi\pi^*$
K-CO	S_1	3.70	0.000	H-3 $\rightarrow L$	$n\pi^*$
	S_2	3.91	0.256	$H \rightarrow L$	$\pi\pi^*$
	S_3	4.56	0.083	H-1 $\rightarrow L$	$\pi\pi^*$
K-OH	S_1	3.46	0.000	H-3 $\rightarrow L$	$n\pi^*$
	S_2	3.94	0.254	$H \rightarrow L$	$\pi\pi^*$
	S_3	4.57	0.098	H-1 $\rightarrow L$	$\pi\pi^*$
K-b	S_1	3.69	0.000	H-3 $\rightarrow L$	$n\pi^*$
	S_2	3.85	0.231	$H \rightarrow L$	$\pi\pi^*$
	S_3	4.57	0.079	H-1 $\rightarrow L$	$\pi\pi^*$

overlaps. This is reflected in the smaller magnitudes of f_{osc}s. These S_1 states are of n-π^* nature.

3.3.3 Excited state minima

All of the eight conformers are optimized again in their S_1 states. We denote the S_1 structures with asterisks. Out of the eight, only seven structures are found to be stable at the ADC(2) level. **K-b*** was found to have negative excitation energy, indicating multireference character. Vibrational frequencies of all the seven optimized conformers in the S_1 state are real and are presented in Table A9. Relative energies of these

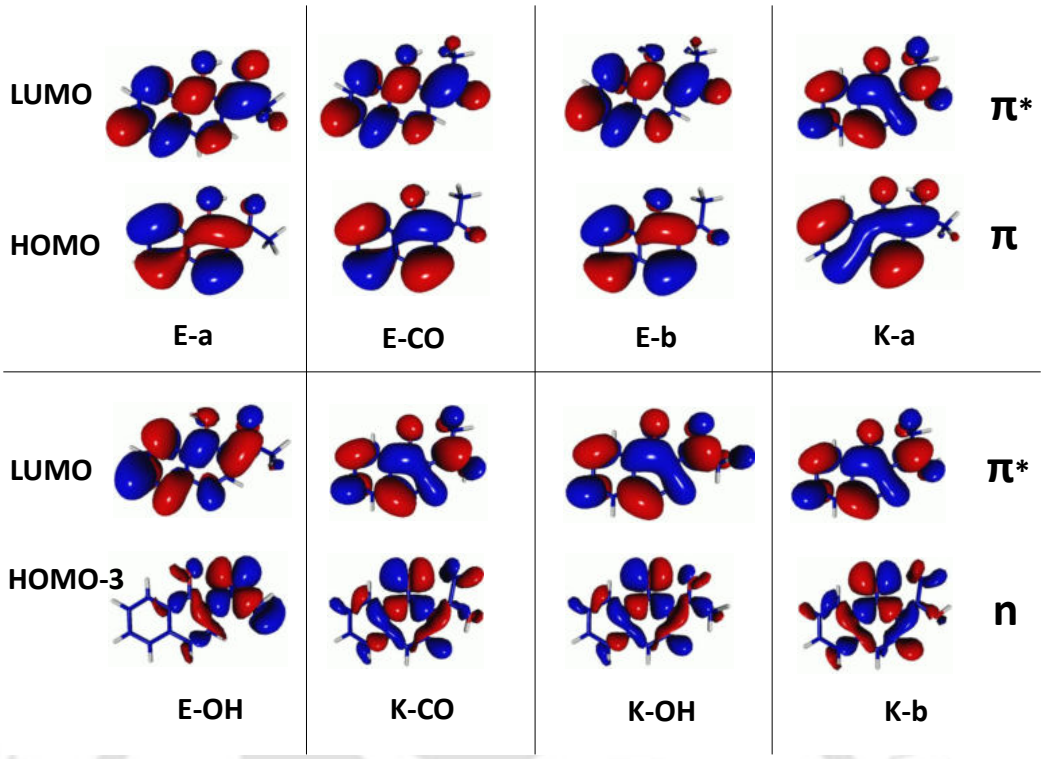

FIGURE 3.4: Molecular orbitals corresponding to the $S_0 \rightarrow S_1$ transition.

optimized structures with the corresponding dihedral angles (in degrees) are presented in Fig. 3.5. As observed in Fig. 3.5, **K-a*** ($\pi\pi^*$) is the most stable structure in S_1 which agrees with TDDFT results by Ortiz-Sanchez et al.[177] and Ning et al.[180]. Organero et al.[181] performed CIS calculation and reported **K-CO*** to be the global minima in the S_1. In the present study, the next stable structure corresponds to **E-a*** which is of $\pi\pi^*$ character. **E-a*** is found to be the most stable structure than the other enol conformers as in the S_0 state. The stability of this form is attributed to the increase in the π conjugation of the system upon photoexcitation.[181] The energy of these four enol conformers are in the following order: **E-b*** > **E-CO*** > **E-OH*** > **E-a*** which differs from that of Organero et al.[181]. **E-CO*** and **E-b*** are higher in energy by $\sim$ 0.66 eV from the **E-a*** and hence, we consider these inaccessible in the present study.[177] **E-OH*** which is in the $n\pi^*$ state is found to be lower in energy than the excitation energy of **E-a** and is 0.19 eV higher than **E-a***. Since **E-OH*** lies below the Franck-Condon (FC) energy, this form is expected to be accessible through a rotation along ϕ_1 by -131.84° from the FC geometry. The existence of this form suggests the possibility of a non-ESIPT deactivation channel which is discussed in a later section.

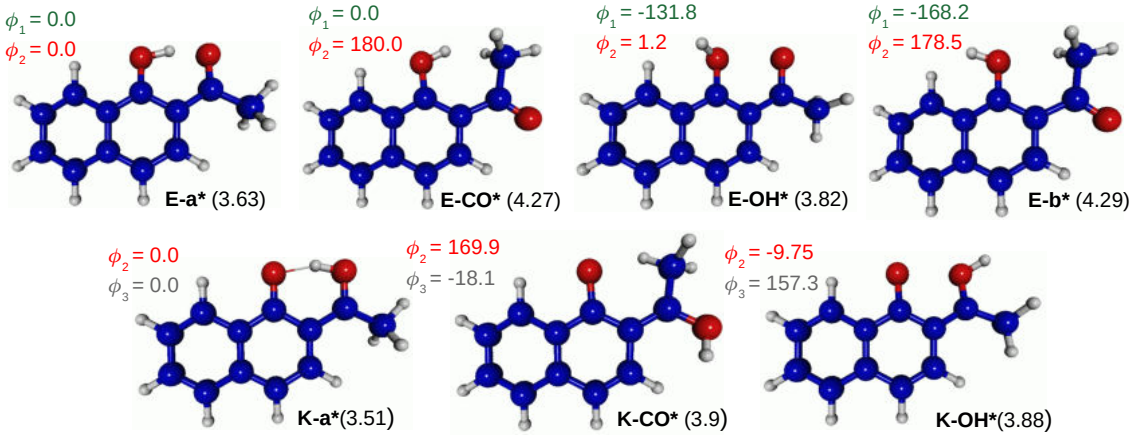

FIGURE 3.5: Optimized structures of different enol and keto conformers of HAN in the S_1 state. Relative energies (in eV) of the conformers with respect to that of **E-a** are given in parentheses. Values of ϕ_1, ϕ_2, ϕ_3 are in degrees. All results are obtained at ADC(2)/cc-pVDZ level of theory.

The energy difference between **K-a*** and **E-a*** is found to be 0.12 eV. Our results are in close agreement with those of Tobita et al.[178] where an energy gap of 0.10 eV was reported. Ortiz-Sanchez et al.[177], Ning et al.[180], and Organero et al.[181] reported the two forms to be almost isoenergetic with a small gap of about 0.03 eV. S_1 states of **K-CO*** and **K-OH*** are of $n\pi^*$ types. These two are found to be 0.39 eV and 0.37 eV higher than **K-a***, respectively, and are accessible via intramolecular rotations of **K-a*** along ϕ_2: 169.9° and ϕ_3: -18.1°, and ϕ_2: -9.75°, and ϕ_3: 157.3°. Similar to **E-a***, the stability of **K-a*** over the other two conformers is attributed to the presence of intramolecular hydrogen bonding. Considering the proton transfer process, the difference in the bond lengths **E-a*** and **K-a*** conformers are compared in Fig. 3.2 and the data is also presented in Table A3. The differences in the C-C bond lengths of the naphthalene ring between **E-a*** and **K-a*** are very small indicating a negligible loss of aromaticity in the proton transfer process. In the **E-a** form, there is a lengthening of the covalent bond H_1-O_2 from 0.99 Å in the S_0 to 1.07 Å in the S_1. In addition, the hydrogen bond O_6 ...H_1 and distance between the two oxygen atoms O_2...O_6 are shortened from 1.69 Å and 2.59 Å in the S_0 to 1.42 Å and 2.45 Å in the S_1, respectively. Furthermore, the bond angle $\angle O_2$-H_1-O_6 is increased from 149.2° to 159.3° upon excitation. Zhao and Han[204] determined the strength of H-bond upon photoexcitation by monitoring the spectral shift of the vibrational modes. In our study, this concept was used and the two

vibrational modes which are involved in the intramolecular H-bond are analyzed. The O-H and C=O stretching frequencies of **E-a** in the S_0 state are found to be 3422 cm^{-1} and 1731 cm^{-1}, respectively. Red shifts of 1310 cm^{-1} and 53 cm^{-1} are observed upon excitation to S_1 where these two vibrational modes are located at 2112 cm^{-1} and 1679 cm^{-1}, respectively. Changes in the bond lengths, bond angles, and the spectral shifts between S_0 and S_1 states indicate that the intramolecular H-bond is strengthened in the S_1 state. This in turn can ease the proton transfer process in the S_1 state which is discussed in the next section. Emissions from **E-a*** and **K-a*** are found to be at 3.25 and 2.64 eV, respectively. Emission from **K-a*** is in good agreement with the experimental value of 2.66 eV, hence confirming the occurrence of proton transfer.

3.3.4 Proton transfer process: Statics and dynamics

A detailed insight into the excited state chemistry can be obtained from the PESs along the involved coordinates. Static potential energy curves were generated along the proton transfer coordinate in both the S_0 and S_1 states using MP2 and ADC(2) methods, respectively. The curves were constructed by constrained optimizations, where the H_1-O_2 bond was fixed for a set of values starting from 0.95 Å to 1.8 Å. The increment in the H_1-O_2 bond was varied from 0.01 to 0.1 Å. The relaxed potentials are shown in Fig. 3.6. Transition state structures for the tautomerization process in the S_0 and S_1 states were also obtained. These are characterized by imaginary frequencies of 893 and $340i$ cm^{-1}, respectively. A barrier of 0.38 eV was obtained in the S_0 and an almost barrierless(0.01 kcal/mol) pathway was found in the S_1 state. A barrierless path in the S_1 state suggested an ultrafast proton transfer process, in accordance with the experimental results of Lochbrunner et al.[171] and Kim et al.[173] The above results are in agreement with TDDFT results of Ning et al.[180] where a small barrier of 0.01 eV was reported for the S_1 and 0.31 eV for S_0 state. The two curves also illustrate the exothermicity and endothermicity natures of proton transfers in the S_1 and S_0 states, respectively. It is also observed from the figure that the reverse proton transfer is more facile in the ground state due to a smaller barrier of 0.02 eV.

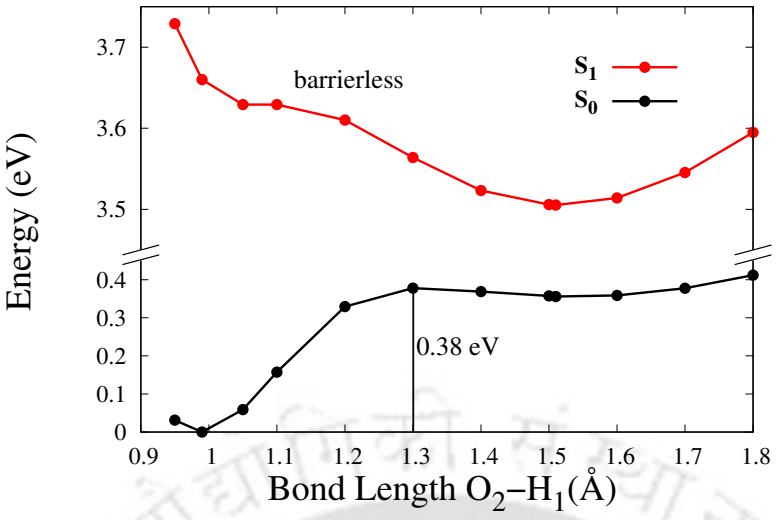

FIGURE 3.6: Relaxed potential energy profiles of **E-a** along the proton transfer coordinate in S_0 and S_1 states.

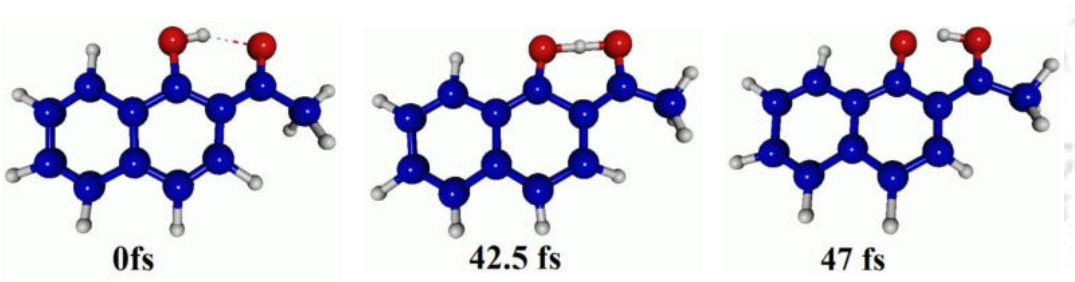

FIGURE 3.7: Snapshots of a typical trajectory representing the time evolution of proton transfer process of HAN in the S_1 state.

In addition to exploration of the above static potential energy curves, on-the-fly adiabatic dynamics simulation was also carried out using the NEWTON-X software. The dynamics was initiated at the FC geometry of the first excited state of **E-a**. Fig. 3.7 displays snapshots of a typical trajectory of HAN at three different time intervals; the **E-a*** structure at 0 fs, an intermediate structure at 42.5 fs where the proton is nearly equidistant (1.2 Å) from the donating and accepting groups, and the formation of **K-a*** at 47 fs. Fig. 3.8 shows the time evolution of proton transfer process where the intersection point of the two curves gives the proton transfer time. Our result shows the average proton transfer time to be around 43 fs which is slightly higher than the experimentally reported values of 25 fs. It is worth mentioning that the TDDFT

dynamics by Ning et al.[180] resulted in a proton transfer time of 37 fs.

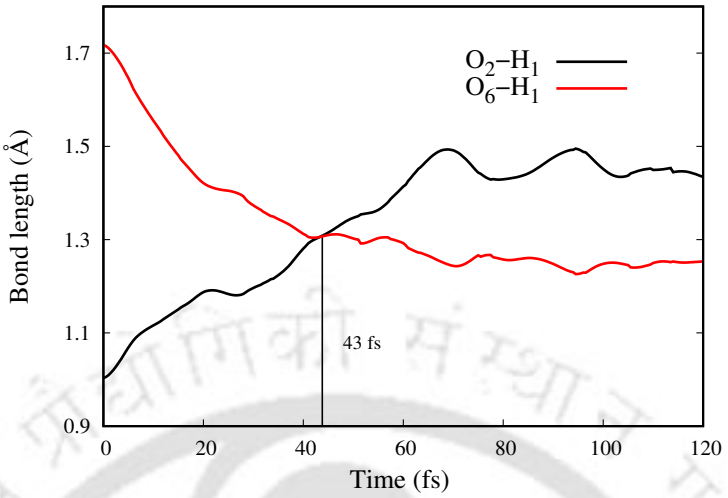

FIGURE 3.8: Time evolutions of O_2-H_1 and O_6-H_1 bond lengths averaged over 200 trajectories.

3.3.5 Non-radiative deactivation pathways

It is well known that torsional motion plays an important role in non-radiative decay process in many typical ESIPT active systems. In HAN, a low quantum yield was reported experimentally by Tobita et al.[178] and their prediction of the existence of a non-radiative pathway prompted us to explore the PESs along the twisting coordinate. In our study, two relaxation pathways were considered: one from the **E-a*** region and the other from the **K-a*** region.

3.3.6 Deactivation from E-a*

As mentioned in a previous section, energetically **E-OH*** is below the FC energy of **E-a*** hinting at the possibility of non-radiative relaxation from the enol region. Estimation of the barrier for the conversion from **E-a*** to **E-OH*** was carried out by a set of relaxed scan calculations along ϕ_1 from 0 to -130° at ADC(2) level. As shown in Fig. 3.9, a barrier of 0.65 eV is obtained from the energy difference between ϕ_1= 0° and -67°. To check the results further, single point calculations using the state-averaged

CASSCF method (equal state weights and three roots), was performed at the ADC(2) S_1 optimized geometries. In these calculations, an active space of 12 electrons in 9 orbitals was chosen. The active space orbitals are shown in the Fig. A1. This was followed by MS-MR-CASPT2 calculation using the above mentioned CASSCF reference wave function with 6-31G(d,p) basis set for generating potential energy curves of the two low-lying excited states along ϕ_1. As shown in Fig. A2, torsional rotation along ϕ_1 results in increasing the energy along S_1 and simultaneously, decreasing the energy along S_2. This leads to a gap of 0.09 eV at -67° indicating the presence of a conical intersection. Consistent with the ADC(2) results, the MS-MR-CASPT2 potential energy profile also shows a barrier of 0.28 eV. The presence of a large energy barrier excludes the possibility of the isomerization process, and thus, ruling out the non-radiative deactivation from the enol Franck-Condon region.

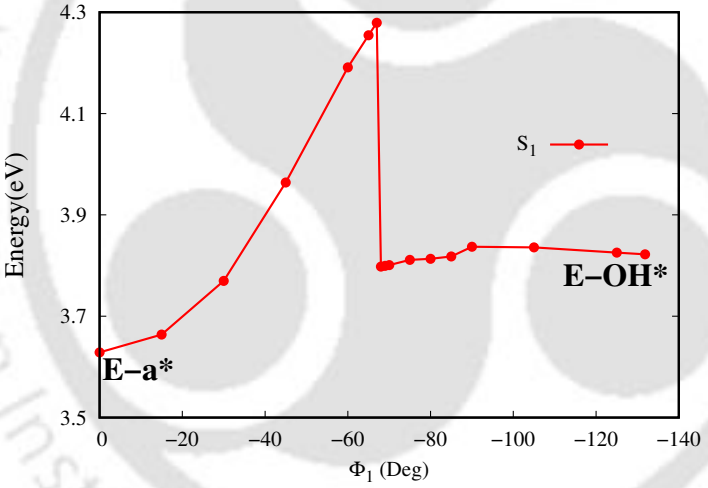

FIGURE 3.9: Potential energy curve along the torsional coordinate ϕ_1, starting from the **E-a*** geometry at ADC(2)/cc-pVDZ level in the S_1 state.

3.3.7 Deactivation from K-a*

To understand the deactivation pathway from the proton-transferred form **K-a***, a set of relaxed scans was carried out along the ϕ_2 angle. The potential energy profile in the S_0 state is obtained from the single point energies of the corresponding optimized S_1 geometries. As shown in Fig. 3.10, a small energy barrier of 0.01 eV is obtained in the

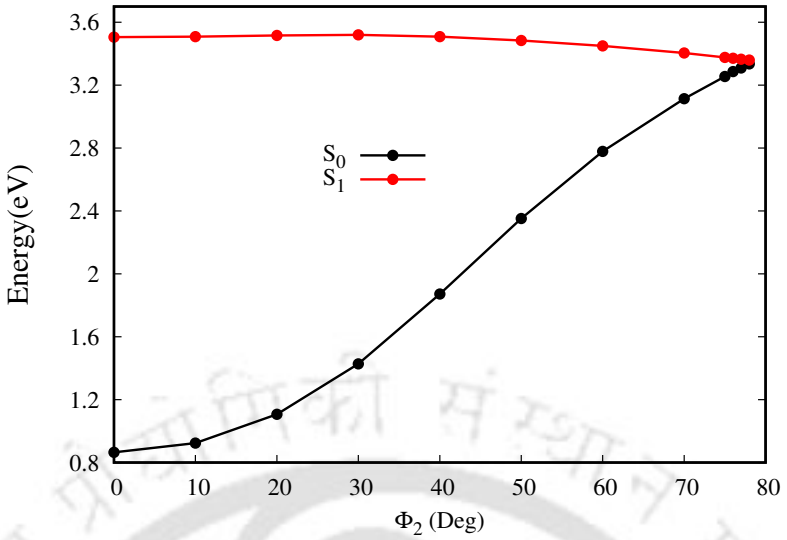

FIGURE 3.10: Potential energy curves along the torsional coordinate ϕ_2, starting from the **K-a*** geometry. In S_1, relaxed scans are performed at the ADC(2)/cc-pVDZ level. For S_0, single point calculations at MP2/cc-pVDZ level are carried out at the S_1 optimized geometries.

S_1 state estimated from the difference between energies at ϕ_2= 0° and 30°. Following the barrier, a gradual decrease in energy occurs in the S_1 state. Because of the single-reference character of the ADC(2) method, the potential energy profile in the S_1 state could not be obtained beyond 78°. From Fig. 3.10, we can see that the S_0 energy increases sharply and advances towards the S_1 state till it reaches a point of closest approach at 78°. The gap between the S_0 and S_1 states is found to be 0.02 eV at this point. This small gap suggested the presence of a conical intersection which can act as a funnel for the molecule to relax non-radiatively. Since ADC(2) cannot accurately describe the topography of the PES in the vicinity of the crossing seam between S_0 and S_1, the CASSCF method was employed to optimize the MECI geometry. Starting from the ADC(2) geometry at $\phi_2 = 78°$, a two-state averaged CASSCF calculation with equal weights was performed. In this CASSCF study, the active space contained 10 electrons in 8 orbitals. These active space orbitals are presented in Fig. A3, which includes five π and three π^* orbitals. Further, CASSCF energies were corrected for inclusion of dynamical correlation using the MS-MR-CASPT2 method. CASSCF optimization was performed with 6-31G(d) basis set and single-point MS-MR-CASPT2 calculations with 6-31G(d,p) basis set. A MECI geometry between S_1 and S_0 was obtained at ϕ_2=

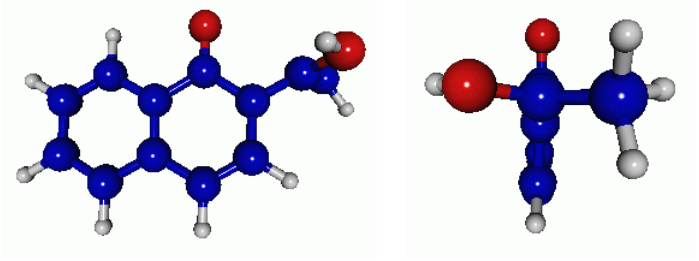

FIGURE 3.11: Front and lateral view of the optimised S_1/S_0 MECI geometry in the keto region at SA-2-CASSCF(10,8)/6-31G(d) level.

96.6°, and this geometry is displayed in Fig. 3.11 The energy difference between the two states at the MS-MR-CASPT2 level is 0.14 eV. These results indicate that the relaxation process through internal conversion is feasible. To study this deactivation pathway, non-adiabatic dynamical studies were carried out at the ADC(2)/cc-pVDZ level using NEWTON-X. Fifty trajectories were computed for a maximum simulation time of 600 fs. Out of these, only six trajectories completed the full duration of dynamics. Analysis of the trajectories showed a small change of 5° in the ϕ_2 angle. In addition, the energy difference between the S_1 and S_0 states remained larger than 1.0 eV over the whole propagation time. These results indicate that the molecule does not approach the crossing seam within 600 fs. A larger simulation time with a larger number of trajectories is probably required for studying this deactivation path. In addition, multi-reference methods like CASSCF are better suited to study these type of deactivation processes. We aim to take the present preliminary results further with multi-reference dynamical studies to understand all the deactivation pathways of HAN.

3.4 Conclusions

In our study, the photochemistry of HAN has been investigated using state-of-the-art computational methods. A combination of electronic structure calculations at ADC(2) and multireference levels, and dynamics simulations at ADC(2) level were carried out. From these calculations, the ESIPT and relaxation processes were sketched providing a detailed insight into the photochemistry of HAN. Upon photoexcitation, the molecule

reaches the FC enol region which then relaxes to the keto region through an ultrafast process of proton transfer with a proton transfer time of 43 fs. From this point, the molecule can relax to the ground state through two channels: (a) through fluorescence from the keto minimum; and (b) through internal conversion via intramolecular rotation along the C=C bond. The latter relaxation pathway is feasible owing to a small barrier along the torsional path, and the presence of the crossing seam associated with the corresponding reaction coordinate. Non-adiabatic dynamics simulations based on the surface-hopping method suggested that the non-radiative relaxation cannot take place within 600 fs simulation time. Our results which are based on highly correlated methods deliver a better understanding of the photophysical and photochemical processes of HAN. Dynamical studies using multireference methods are underway and will shed more light on the deactivation pathways. The method employed here can also serve the purpose of further exploration of the photochemistry of similar systems.

Chapter 4

Nitrile-substituted 2-(oxazolinyl)-phenols in gas and implicit solvents

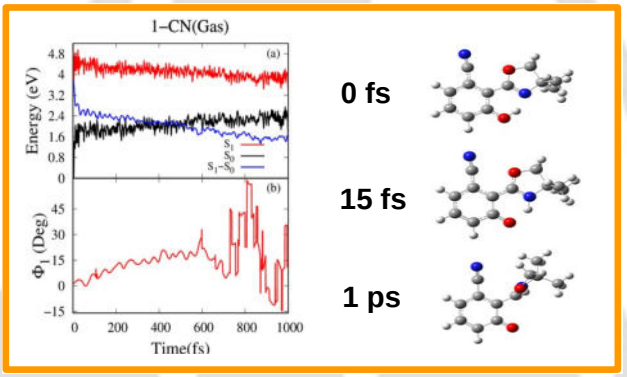

In this chapter, the ground and excited state properties of two nitrile-substituted 2-(oxazolinyl)-phenols in the gas phase, and in two implicit solvents (cyclohexane and methanol) are reported. Computational studies comprising of static calculations at density functional theory (DFT) and ab initio, and non-adiabatic dynamics at DFT levels are performed. The implicit solvent has little influence on the proton transfer (PT) time scale in the S_1 state and an average PT time of ∼11-15 fs is predicted. Following PT, non-radiative decay channels are explored and these channels are found to be more probable in the gas and cyclohexane than in methyl alcohol. Reproduced from "*Chemical Physics Letters*, **2022**, 806, 139969" with permission from Elsevier.

4.1 Introduction

Brightly emissive organic compounds are of significant interest in the field of material science due to their numerous practical applications in biological sensing,[205,206] display technologies,[207,208] and molecular probes.[209,210] Molecules undergoing ESIPT are exemplary candidates for such applications, and coupling of ESIPT with aggregation-induced emission has received widespread attention in recent times.

Conjugated organic compounds built from the simplest benzene unit are commonly employed in developing efficient luminescent systems. However, the large size of conjugated systems lead to decrease in solubility resulting in aggregation. In aggregated form, the intermolecular π-π interactions and charge transfer (CT) lead to non-radiative deactivation through conical intersection (CI) giving rise to emission quenching. To overcome the drawbacks associated with π-conjugated systems, in recent times, researchers have focused on developing small-sized fluorophores. Fluorophores with low molecular weight and single-benzene based fluorophore designs are limited.[211] Recently, Göbel et al. synthesized four nitrile-substituted ortho-hydroxy-2-phenyloxazolines regiomers based on single-benzene ESIPT.[212] These four regiomers showed different emission properties in solvent and crystalline phases. In particular, 2-(4,4-Dimethyl-4,5-dihydrooxazol-2-yl)-3-hydroxybenzonitrile (1-CN) and 3-(4,4-Dimethyl-4,5-dihydrooxazol-2-yl)-4-hydroxybenzonitrile (2-CN), with nitrile groups at ortho and meta positions, respectively, were found to be weakly emissive in solvent phase. In addition, changes in the position of the CN substituent from ortho to meta (1-CN vs 2-CN) resulted in the blue shift of both absorption and emission maxima. The weak emissive nature can arise from access to conical intersections (CI) and twisted intramolecular CT.

Understanding the underlying mechanisms at the atomistic scale is essential for improving material's performance. Computational studies at this stage are of great help to elucidate the structural differences between the systems, and to understand the differences in photophysical properties. Liu et al.[213] investigated the ESIPT mechanism of 4-(4,4-Dimethyl-4,5-dihydrooxazol-2-yl)-3- hydroxybenzonitrile (3-CN) at TDDFT level of theory. Very recently, a computational study was carried out by Li et al.[214] to explore

the difference in fluorescence quantum yield between 1-CN and 3-CN. Time-dependent DFT (TDDFT) studies were performed at B3LYP/TZVP level of theory in acetonitrile solvent using integral equation formalism polarizable continuum model (IEF-PCM).[215] A large spin-orbit coupling and a small energy gap resulted in large intersystem crossing in 1-CN. Keeping the above experimental and computational results in mind, we have chosen both 1-CN and 2-CN to explore the proton transfer time and the effect of non-radiative transition on the quantum yields. For this, static and dynamical simulation studies were carried out at TDDFT level in gas and in implicit solvents (cyclohexane (CyHex) and methyl alcohol (MeOH)). In addition, the second-order algebraic diagrammatic construction ADC(2)[153,182], and multiconfigurational methods such as complete active space self-consistent field (CASSCF)[117] and multistate complete active space second-order perturbation theory (MS-CASPT2)[118] are also included in our static calculations. In recent times, ADC(2) method has been used to analyze and understand the excited state processes[200,201,216–219]. In the next section, details of computational methods are given. The results are presented and analyzed in the Results & Discussion section. We summarize our findings in the Conclusion section.

4.2 Computational Details

The enol and keto geometries of 1-CN and 2-CN were optimized in the S_0 state using DFT at the B3LYP/cc-pVDZ[193] level. The solvent effects of CyHex and MeOH were taken into account using IEF-PCM. Frequency calculations were performed for all the optimized structures, and absence of imaginary frequencies confirmed that the obtained structures are true minima in the potential energy surface. VEE calculations were performed at the optimized S_0 geometries at TDDFT level. To verify the suitability of chosen functional, VEEs were also calculated at ADC(2) level of theory. In case of ADC(2), the scaled opposite-spin (SOS)[123,192] variant with the resolution of identity (RI)[190,220] approximation was employed in our studies. For further verification, we also calculated VEEs using the recently developed domain-based local pair natural orbital similarity transformation based equation of motion coupled cluster singles and doubles (DLPNO-STEOM-CCSD) method.

In the S_1 state, TDDFT was used for structure optimizations of enol and keto forms. Similar to the S_0 state, results of frequency calculations in S_1 showed no imaginary frequencies. For studying the PT and non-radiative deactivation paths, potential energy curves (PEC) were generated along PT and twisting coordinates, respectively. For PT, constrained optimizations were performed by fixing O-H bond length in both S_0 and S_1 states. For constructing the PECs along the twisting coordinates, relaxed scans in S_1 were performed. The corresponding energies in the S_0 state were obtained by performing single-point calculations at the above S_1 optimized geometries. DFT and TDDFT studies were performed using Gaussian 16[221]. The SOS-ADC(2) calculations were conducted using the TURBOMOLE 7.1 program.[196] DLPNO-STEOM-CCSD single point calculations were carried out using the ORCA package.[222] Characterization of the excited states were carried out using the TheoDORE package.[223–225]

Multireference calculations were carried out for locating (i) the MECI geometry, and (ii) for constructing the linear interpolations in internal coordinate (LIIC) paths connecting the keto minima in S_1 to the corresponding MECI structures for estimating the barrier heights. For MECI geometry optimization, the CASSCF method was employed using a state-averaged approach over the first two singlet states of equal weights, denoted as SA2-CASSCF. The active space comprised of eight electrons in seven orbitals. To account for the dynamic electron correlation, MS-CASPT2 studies were performed with a level shift parameter of 0.3 a.u. to mitigate the intruder state effect. For LIIC calculations, CASSCF studies used active spaces comprising of ten electrons in nine orbitals averaged over three singlet states, denoted as SA3-CASSCF. All the multireference calculations were carried out using the MOLPRO[195] suite of programs.

On-the-fly semi-classical dynamics simulation was performed using the NEWTON-X[197,198] interfaced with Gaussian 16. 500 initial conditions were generated from a Wigner distribution of the ground state harmonic oscillator for simulations of absorption spectra for 1-CN and 2-CN in gas, CyHex and MeOH. The initial conditions for dynamics simulations were then chosen from energy windows of ± 0.1 at corresponding absorption maxima. Velocity-verlet algorithm[226,227] implemented in NEWTON-X was chosen for integrating the nuclear motion. Born-Oppenheimer electronic energies and

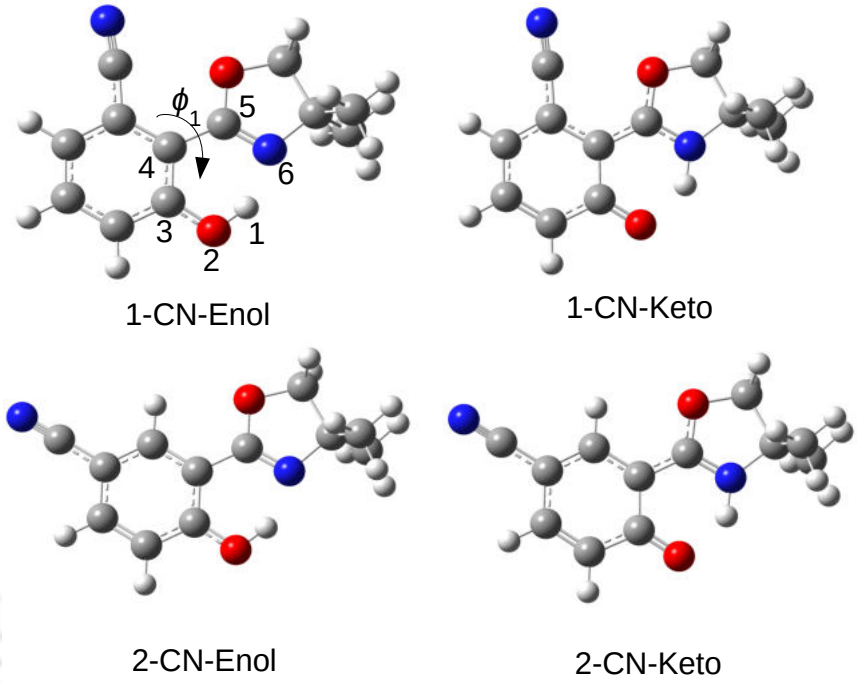

FIGURE 4.1: Optimized structures of enol and keto forms of 1-CN and 2-CN in the S_0 state in gas phase.

gradients were computed for each time step at TD-B3LYP/cc-pVDZ level of theory. A total number of 50 trajectories with a maximum duration of 100 fs was computed for analyzing the PT time in the gas, CyHex and MeOH phases. A time step of 0.025 fs was set for integrating the quantum equations while the classical equations for nuclear motion were integrated with 0.5 fs time step. The maximum duration was later extended to 1000 fs for a subset of 25 trajectories for predicting the non-adiabatic relaxation time.

4.3 Results and Discussion

4.3.1 Ground State Optimized Geometries

The ground-state optimized structures of the enol and keto conformers of 1-CN and 2-CN in the gas phase are shown in Figure 4.1. A few atoms involved in PT and torsional rotation are labeled for 1-CN in Figure 4.1. Similar structures of the conformers are obtained in CyHex and MeOH solvents. Cartesian coordinates of all the optimized geometries are listed in Tables B1 and B2. In general, the PT process in S_1 originates at the FC point of the ground state global minimum structure. Therefore, it is important

TABLE 4.1: Relative energies(in eV) of the Enol and Keto forms of 1-CN and 2-CN in Gas, CyHex and MeOH in the S_0 and S_1 states computed at B3LYP/cc-pVDZ and TD-B3LYP/cc-pVDZ levels of theory. The enol ground state energy in MeOH is taken as reference. Keto* represents the stable structure in the S_1 state.

	1-CN			2-CN		
Medium	Enol	Keto	Keto*	Enol	Keto	Keto*
Gas	0.26	0.54	3.52	0.26	0.56	3.03
CyHex	0.15	0.37	3.36	0.15	0.37	3.48
MeOH	0.00	0.14	3.09	0.00	0.10	3.26

to locate the global minimum in S_0. In the present study, the enol conformers are found to be the most stable in the ground states. Table 4.1 shows the relative energies of the conformers in gas and solvent phases relative to the energy of enol form in MeOH. For both enol and keto conformers in 1-CN and 2-CN, the stabilities are in the following order: MeOH > CyHex > Gas. For both the systems, the differences in energies between the enol and keto forms were found to be in the range of 0.1-0.3 eV. The stability of enol structure over keto is attributed to the aromaticity of the phenolic ring and the planarity of the pseudo ring found in the enol form.[228] In solvents, however, the energy differences were found to be smaller. The smallest energy differences of 0.14 and 0.10 eV are obtained in MeOH for 1-CN and 2-CN, respectively. To check the effect of basis sets, optimizations were also carried out using aug-cc-pVDZ and cc-pVTZ basis sets. The results are tabulated in Table B4. Trends similar to the results for cc-pVDZ basis sets were observed with the above two larger basis sets for both 1-CN and 2-CN. The above results show that use of cc-pVDZ is sufficient for the ground state studies. The permanent dipole moments of enol and keto forms of 1-CN in the gas phase are found to be 3.03 D and 4.77 D, respectively. The values increase to 3.32(3.65) and 5.46(6.36) in the CyHex(MeOH) solvents. This shows that both enol and keto conformers are more polar in solvents. Similar results are obtained for the 2-CN conformers. The polarization of these compounds in solvent phases lead to more stabilization as compared to that in the gas phase which corroborates with the aforementioned relative stabilities of the conformers.

The selected bond parameters of both regiomers in the gas and solvent phases are listed in Table 4.2 and Table A5, respectively. The optimized bond lengths are found to be closer to the reported crystal data. Small differences of 0.01-0.02 Å in the bond length

TABLE 4.2: Summary of selected bond lengths(Å), bond angle(in degree) of the optimized structures of Enol and Keto in the S_0 and S_1 states calculated at B3LYP/cc-pVDZ level of theory in the gas phase. The conformers in the S_1 state are denoted with asterisks.

	1-CN			2-CN		
Geometrical parameters	Enol	Keto	Keto*	Enol	Keto	Keto*
H_1-O_2	1.01	1.54	1.90	1.01	1.60	3.03
H_1-N_6	1.65	1.08	1.03	1.70	1.07	1.02
O_2-C_3	1.33	1.27	1.30	1.33	1.27	1.26
C_3-C_4	1.43	1.46	1.47	1.42	1.47	1.45
C_4-C_5	1.46	1.42	1.42	1.46	1.42	1.51
C_5-N_6	1.29	1.32	1.36	1.29	1.32	1.40
$\angle C_3$-C_4-C_5-N_6	0.5	3.4	21.4	0.0	2.6	76.0

of 1-CN-enol were found between the gas and solvent phase geometries. This shows that implicit solvent models have little influence on the geometry of enol in the ground state, and this is due to the lack of explicit solute-solvent intermolecular interactions. As in the case of relative energies mentioned above, the geometrical parameters with larger basis sets are also similar to the results of the smaller basis sets, validating the chosen method. The selected geometrical parameters of both the compounds obtained at larger basis sets are listed in Tables B6 - B7. Looking into the subtle differences in the H_1-N_6 bond of enol in different environments, we found that the H-bond length is shorter in MeOH which is indicative of a stronger H-bond in polar solvents. Values of inter ring dihedral angles ϕ_1=$\angle C_3$-C_4-C_5-N_6 in the enol forms of 1-CN and 2-CN are found to be in close agreement with the reported crystal data, showing a nearly planar quasi six-membered ring structure for atoms 1-6 in both gas and solvent phases. Minor deviations from planarity are observed for the keto forms.

4.3.2 Vertical Excitation Energies

VEEs are computed for the ground state optimized geometries at various levels of theory. In order to find the reliable method that gives an accurate description of the excited state energies, VEEs were calculated at TDDFT and RI-SOS-ADC(2) levels, and comparisons were made with the experimentally reported values of absorption maxima. At TDDFT level, a set of functionals such as B3LYP,[128,229] CAM-B3LYP,[141] PBE0,[230] M06-2X,[231]

TABLE 4.3: VEEs (in eV) with oscillator strength(inside the parentheses) for the first three singlet excited states of 1-CN and 2-CN. Results in Gas, CyHex and MeOH obtained at TD-B3LYP/cc-pVDZ level of theory are shown.

State	1-CN			2-CN		
	Gas	CyHex	MeOH	Gas	CyHex	MeOH
S_1	4.01(0.146)	3.97(0.198)	3.97(0.195)	4.22(0.103)	4.24(0.135)	4.31(0.126)
S_2	4.77(0.188)	4.68(0.224)	4.63(0.182)	5.00(0.036)	4.93(0.046)	4.88(0.042)
S_3	5.18(0.002)	5.13(0.007)	5.08(0.001)	5.41(0.411)	5.29(0.611)	5.23(0.487)
Expt (S_1)		3.85	3.86		4.05	4.09

ωB97XD, were included in our study. For 1-CN, the first excitation energies (E_g^1) obtained using B3LYP, CAM-B3LYP, PBE0, M06-2X, ωB97XD functionals in MeOH are 3.97, 4.23, 3.61, 4.31, and 4.23 eV, respectively Similarly, the values are 4.31, 4.58, 3.94, 4.64, 4.59 eV for 2-CN in MeOH. These results are obtained with cc-pVDZ basis set. The corresponding oscillator strengths are $\approx$ 0.2 and 0.1 for 1-CN and 2-CN, respectively. Among these functionals, B3LYP produces the best values of E_g^1 with deviations of 0.11 and 0.22 eV, for 1-CN and 2-CN, respectively, from the experimental absorption maxima. Our results are also in agreement with the computed values of VEE of 1-CN at B3LYP/TZVP level of theory[214]. Therefore, B3LYP functional was chosen for further studies. Further, the effect of basis set on E_g^1 was also explored by calculating excitations using larger basis sets such as def2-TZVP[232], cc-pVTZ[193] and aug-cc-pVTZ[194]. With the increase in the size of the basis sets, a small decrease ($\approx$ 0.02 eV) in the E_g^1 was observed. These values are collected in Table B8. Considering the little effect of larger basis sets and also the computational cost, we have employed cc-pVDZ throughout our studies. In order to assess the performance of the selected functional to describe excited state properties, the RI-SOS-ADC(2) method was also employed in computing the VEEs. The RI-SOS-ADC(2)/cc-pVDZ calculations were carried out at the B3LYP ground state optimized geometries. In RI-SOS-ADC(2) studies, solvent effect was taken into account using conductor-like screening model (COSMO)[202,203]. The RI-SOS-ADC(2) results are presented in Table B9. The table shows that RI-SOS-ADC(2) results are blue-shifted by 0.28 and 0.31 eV, for 1-CN and 2-CN, respectively, in MeOH. TDDFT results for the E_g^1 values are found to differ by 0.09-0.17 eV from the RI-SOS-ADC(2) results. DLPNO-STEOM-CCSD E_g^1 values for 1-CN and 2-CN are found to be 3.90 and 4.04 eV, respectively. A hybrid functional like B3LYP without any long-range correction is

known to underestimate the energies of CT states. Therefore, to check the suitability of B3LYP for the S_1 states, the TheoDORE package was used to compute a descriptor named CT number (ω_{CT}) to verify whether a state is of CT or locally excited (LE) type. A value of 1e for ω_{CT} indicates CT character, and a value close to zero shows the state to be a LE state. Small ω_{CT} values of 0.29 (0.23) and 0.34 (0.26) for the S_1 states are obtained for 1-CN and 2-CN in the gas phase at B3LYP (RI-SOS-ADC(2)) levels, respectively. These small numbers suggest that S_1 states are of mostly LE types with little CT character. On the basis of the reasonable agreement of the E_g^1 and CT values obtained using B3LYP and RI-SOS-ADC(2) methods, we proceeded with the computationally efficient TDDFT method.

The VEEs of the first three singlet excited states for enol forms of 1-CN and 2-CN computed in the gas phase, and in CyHex and MeOH solvents at B3LYP/cc-pVDZ level of theory are shown in Table. 4.3. The E_g^1 for 1-CN is 3.97 eV in both CyHex and MeOH solvents showing the insensitivity of the absorption energies to the change in the solvent polarity. On the other hand, the computed values for 2-CN are 4.24 and 4.31 eV in CyHex and MeOH solvents, respectively, showing the small blue-shifting of the E_g^1 in MeOH. The E_g^1s in CyHex and MeOH for 1-CN and 2-CN show a good agreement with the experimental absorption maxima. In the gas phase, the E_g^1s are found to be 4.01 and 4.22 eV for 1-CN and 2-CN, respectively. Small differences between the E_g^1 values in the gas and solvent phases are due to the lack of explicit solute-solvent interactions in the implicit solvent models. The f_{osc}s for the $S_0 \rightarrow S_1$ transition for both 1-CN and 2-CN are in the range of 0.103-0.198, indicating that S_1 states are spectroscopically bright. The natural transition orbitals (NTO) involved in transitions to the first three singlet excited states are shown in Figure. 4.2, for both the compounds in the gas phase. The figure shows that the first three excited states of 1-CN possess LE characters. For S_1, the hole NTO is of π type located over the phenol moiety with little contribution from the oxazole ring. On the other hand, the hole NTO for the S_2 state is delocalised over the whole molecule. The electron NTOs are of π^* character which is similar to the the lowest unoccupied molecular orbital (LUMO). The S_3 state is of nπ^* type. For 2-CN, both S_1 and S_3 states in the gas phase are represented each by a single set of NTO. These two states are classified as $\pi\pi^*$ and nπ^* types, respectively. On the other hand,

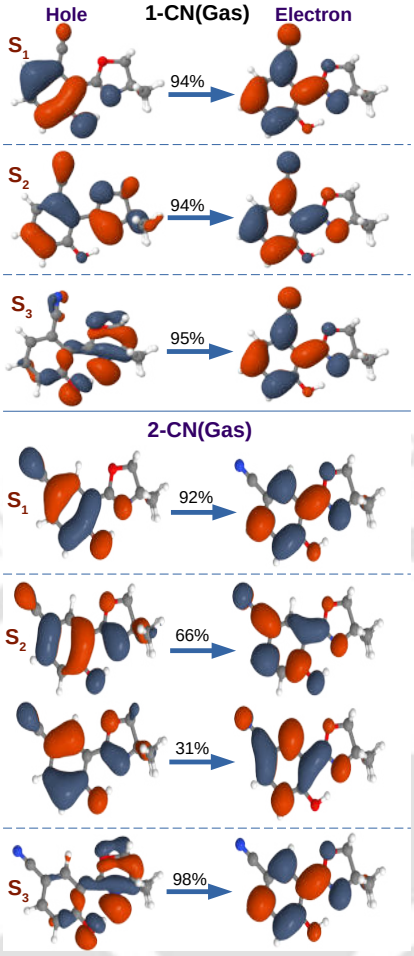

FIGURE 4.2: Natural transition orbitals for the first three singlet excited-states of 1-CN and 2-CN in the gas phase calculated at TD-B3LYP/cc-pVDZ level of theory.

two NTO pairs are involved in the $S_0 \rightarrow S_2$ transition and both are of $\pi\pi^*$ types. The results in CyHex and MeOH solvents are presented in Figures B1-B4. The characters and the energy ordering of the excited states in solvents for 1-CN remain the same as in the gas phase. However, the S_3 states of 2-CN in both the solvents involve two sets of NTOs.

4.3.3 S_1 state minima

Optimizations of the enol structures at TD-B3LYP/cc-pVDZ level in the S_1 state led directly to the corresponding keto structures, for both 1-CN and 2-CN. These observations hint at the presence of barrierless pathways for proton transfer processes in the S_1 states. Cartesian coordinates of the optimized structures in S_1 are tabulated in Table B2. As shown in Table 4.1, for 1-CN, the energy ordering of the keto structures in gas

and solvent phases in the S_1 states remains the same as in the S_0 state, showing the stabilisation effect of the polar solvent. However, the optimization of 2-CN keto structure in the gas phase resulted in a twisted keto conformer (ϕ_1= 75.9°), unlike the the structures obtained in the solvent phases for which the dihedral angles were ≈ 16-20°. The optimized keto structures in the S_1 states show remarkable changes in H_1–O_2 length and ϕ_1 in comparison to the S_0 optimized keto structures. For 1-CN, there is a lengthening of the H_1–O_2 H-bond from 1.54, 1.60 and 1.67 Å in S_0 to 1.89, 1.89 and 1.90 Å in S_1 in the gas, CyHex and MeOH, respectively. Similar findings were also noted for 2-CN, in which an increase of ∼ 0.25 Å in H_1–O_2 bond upon photoexcitation to S_1 states in CyHex and MeOH is found. Deviations from planarity are observed in both the gas and solvent phases in the S_1 states where ϕ_1 changes from 3.4, 3.1 and 2.3° in the S_0 to 21.4, 20.7 and 16.3 degrees in S_1 for 1-CN in gas, CyHex and MeOH, respectively. For 2-CN, the values change from 2.3 and 1.5 in S_0 to 19.9 and 15 degrees in S_1 in CyHex and MeOH, respectively. The above observations clearly indicate the weakening of the H-bond in the S_1 states suggesting less probability of reverse PT in the S_1 as compared to the S_0 states in all the phases.

For 1-CN, the computed emission maxima (λ_{em}) in CyHex and MeOH are found to be 2.57 and 2.64 eV, respectively, which agree well with the experimental values of 2.58 and 2.66 eV. Similarly, in case of 2-CN, the values are 2.69 and 2.84 eV, showing a good match with the experimental values of 2.65 and 2.79 eV, respectively. Emission energies were also calculated at RI-SOS-ADC(2)/cc-pVDZ level for B3LYP optimized geometries. As shown in Table B9, the λ_{em} values are in agreement with the experimental results. The permanent dipole moment of keto form of 1-CN in the gas phase are found to be 5.37 D which increases to 5.83 and 6.74 D in the CyHex and MeOH solvents, respectively. Similarly, the value for 2-CN increases from 7.68 in CyHex to 8.98 in MeOH. As obtained in the ground state, the increased values of dipole moments in MeOH indicate the stabilization of compounds by the polar solvent.

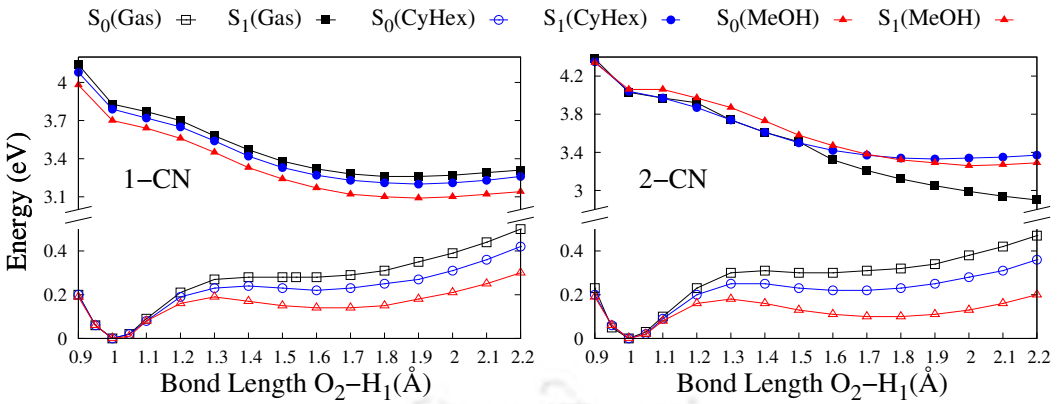

FIGURE 4.3: Relaxed potential energy profiles of 1-CN and 2-CN along the proton transfer coordinate in gas, CyHex and MeOH phases in the S_0 and S_1 states. The energies are relative to the S_0 optimized enol structures in respective phases.

4.3.4 Potential Energy Curves and Conical Intersections

The construction of a potential energy profile along a coordinate of interest has been a good approach to understand the mechanisms of various processes in both the ground and excited states. In the present study, the effect of solvent on the proton transfer and non-radiative deactivation routes was assessed by constructing PECs along these coordinates. Relaxed scan calculations were carried out along the PT reaction coordinates by fixing H_1-O_2 length for a set of values from 0.9 to 2.2 Å. As shown in Figure 4.3, the 1-CN and 2-CN PECs along the PT coordinate in the S_0 states follow the same energy ordering as that obtained in the full geometry optimizations. In the S_0 states of 1-CN, the energy curves are shallow around the keto minima, i.e., around the region of 1.5 -1.6 Å. Similar trends were also found in the S_0 states energy profiles of 2-CN with small differences in the barrier heights. These observations hint at the instabilities of the keto forms in the S_0 states which may result in the fast reverse PT. As observed in the same figure, the forward PT process from enol to keto forms are found to be more favorable in the S_1 states than in the ground states due to the absence of barriers suggesting the PT process to be ultrafast. The implicit solvent does not have any effect on the barrier height in the S_1 state. The order of energies of the S_1 states in gas, CyHex and MeOH phases for 1-CN was found to be the same as that in the ground state. In contrast to the 1-CN energy profile, the energetic ordering of S_1 states for three phases in 2-CN does not remain the same as in S_0 and curves overlap each other.

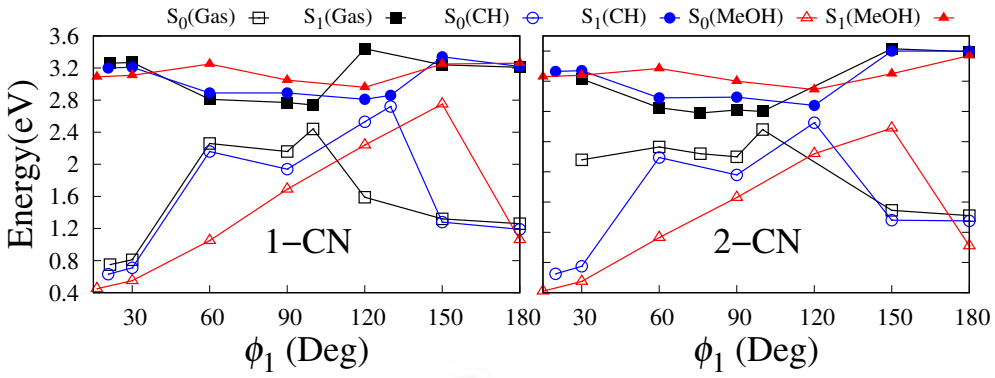

FIGURE 4.4: PECs along the torsional coordinate ϕ_1, starting from the Keto* geometry. In S_1, relaxed scans are performed at TD-B3LYP/cc-pVDZ level. For the S_0, single point calculations at B3LYP/cc-pVDZ level are carried out at the S_1 optimized geometries. The energies are relative to the energies of corresponding S_0 optimized structures.

The weak emissive nature of these compounds in the solution is expected to be due to the presence of non-radiative channels. Identification of the possible non-radiative relaxation channel is made by generating PECs along the twisting coordinate ϕ_1 starting from the keto structures. The TDDFT results for 1-CN and 2-CN are shown in Figure 4.4. The S_0 curves of 1-CN show considerable energy barriers of 2.44, 2.72 and 2.75 eV at 100, 130 and 150°, respectively, in gas, CyHex and MeOH phases. On the other hand, the curves along ϕ_1 in the S_1 states show small barriers of 0.01 eV in the gas and CyHex phases, and 0.16 eV in MeOH solvent. The energy gaps between S_0 and S_1 at the points of closest approach are found to be 0.31, 0.14 and 0.5 eV, in gas, CyHex and MeOH, respectively. Similar to the 1-CN PECs, large energy barriers of 2.56, 2.65 and 2.58 eV at 100, 120 and 150° are found for 2-CN in gas, CyHex and MeOH phases, respectively. In the S_1 states, however, the pathway to reach MECI point in the gas phase is barrierless while small barriers of 0.01 and 0.1 eV are found in CyHex and MeOH solvents. The energy gaps between S_0 and S_1 in gas and CyHex are same, i.e., 0.24 eV and 0.72 eV in MeOH. These results show that the possibility of non-radiative transition is more in the gas and CyHex solvent phases for both 1-CN and 2-CN.

Single-reference methods like TDDFT fail in locating the minimum energy crossing point due to the multiconfigurational character of the CI region. However, the S_1 geometry near the crossing seam with a small energy difference between the two involved

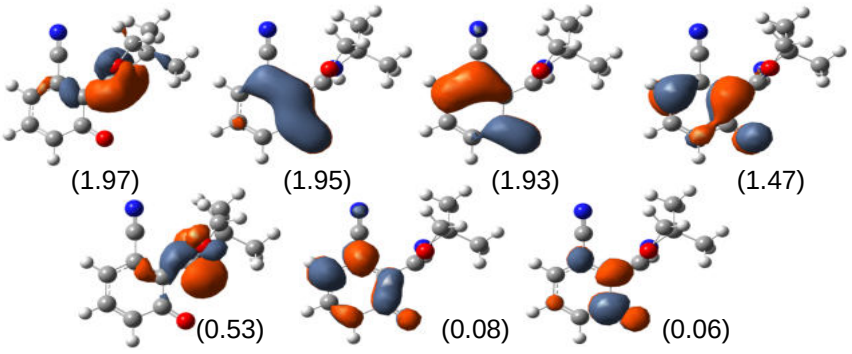

FIGURE 4.5: Active space orbitals selected for MS-CASPT2//SA2-CASSCF/6-31G(d,p) calculations for optimizing the MECI structure in 1-CN. Mean occupation numbers of the orbitals are shown in parenthesis.

states can be used as starting guess structure for multireference calculation in finding out the MECI structure. In our study, TDDFT geometries with small S_1-S_0 energy gaps were used as guess structures to start multireference calculations.

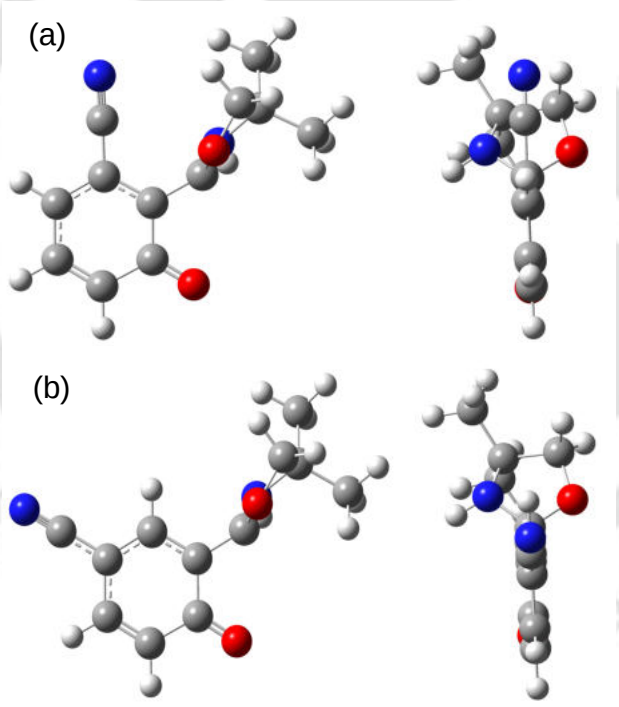

FIGURE 4.6: 1-CN and 2-CN: Front and lateral views of the S_1/S_0 minimum energy conical intersection geometries in the keto region obtained at SA2-CASSCF(8,7)/6-31G(d,p) level.

For CASSCF, the chosen active spaces for 1-CN and 2-CN comprised of π and π^* orbitals located on the two rings, and these are shown in Figures 4.5 and B5, respectively. MECI structures for 1-CN and 2-CN are shown in Figure 4.6. The figure shows that the structures are twisted by 114.7 and 116.13° along ϕ_1. At MS-CASPT2 level, the energy

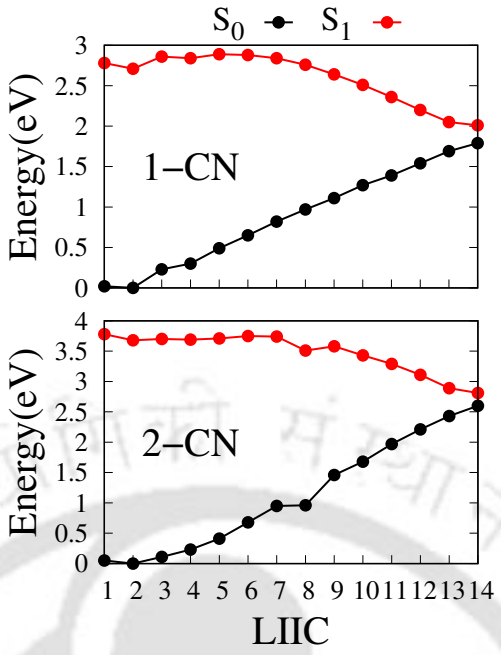

FIGURE 4.7: PECs along the LIIC path linking the S_1 keto minimum and the MECI structure at MS-CASPT2//SA3-CASSCF/6-31G(d,p) level of theory. The energies are relative to the energies of corresponding S_0 optimized structures.

differences between the S_0 and S_1 states for 1-CN and 2-CN are 0.18 eV and 0.28 eV, respectively. Additionally, energies along the LIIC paths connecting Keto* to the MECI structures were computed at MS-CASPT2//SA3-CASSCF/6-31G(d,p) level. Although the barriers obtained through LIIC studies are sometimes overestimated in comparison to the true barriers, the energy profiles from LIIC and relaxed scan calculations generally show qualitative agreement, and the LIIC results are considered reliable.[233,234] As mentioned in Computational Methods, a (10e,9o) active space, different to that used for MECI optimization, was used for constructing the LIIC paths. The active space orbitals are shown in Figures B6 and B7, for 1-CN and 2-CN, respectively. The reaction paths obtained along the LIICs are shown in Figure 4.7. The energy profiles in S_1 states show small barriers of 0.18 and 0.07 eV for 1-CN and 2-CN, respectively. These results suggest the accessibility of the non-radiative pathways through the twisting motion along ϕ_1. The possibilities of non-radiative deactivations from the enol regions were not explored in this study due to the barrierless ESIPT energy profiles suggesting ESIPT pathway to be more favored from the FC region, as observed in other ESIPT systems with almost barrierless ESIPT energy profiles.[185,217]

4.3.5 Dynamics Simulations

Dynamic simulations were performed to gain further insights into the photophysics of the systems. The time scale for the PT process was not reported in the literature. Hence, our aim was to predict the PT time which was expected to be ultrafast from the static results. On the other hand, small barriers to reach the MECI regions indicates the possibility of non-radiative relaxation through torsional motion along ϕ_1 which might take longer time. The PT time was considered to be the time where the hydrogen atom is equidistant from both donor and acceptor atoms. The average PT time for 1-CN and 2-CN are found to be 11.5 and 14.8 fs, respectively, in the gas phase(cf. Figure. 4.8). The timescales were found to increase slightly to 11.8(15.5) and 15.9(15.1) fs for 1-CN(2-CN) in CyHex and MeOH, respectively. The time evolution of the average distances for 1-CN and 2-CN in CyHex and MeOH are shown in Figure 4.8. These small differences in the PT times between phases of different polarities are in accordance with the static results which show barrierless ESIPT pathways in all the three phases. In order to check the reliability of the results presented above, 50 more trajectories were computed for 1-CN in CyHex solvent. Statistical analysis of 100 trajectories showed a minor increase in the PT time to 13 fs. Within 100 fs simulation time, the energy gaps between S_0 and S_1 states remained above 2.4 eV.

Time evolution of ϕ_1, essential for analyzing the non-radiative pathways, showed only a minor change, of the order of 2-5 degrees, for both 1-CN and 2-CN. Hence, the possibility of non-radiative deactivation within 100 fs period is ruled out. Therefore, we extended our simulation time in the gas and CyHex phases to 1 ps to investigate the timescale for non-radiative relaxation pathways. Considering the computational cost, only 25 trajectories were considered for 1 ps simulation. In this case, only few trajectories completed up to the maximum simulation time without any error for both the systems. The error can be due to the multireference characters of these regions where TDDFT fails. Despite the incomplete simulations of few trajectories at TDDFT level, analysis of all 25 trajectories were performed to get idea about the internal conversion processes in both the systems in the gas and CyHex phases.

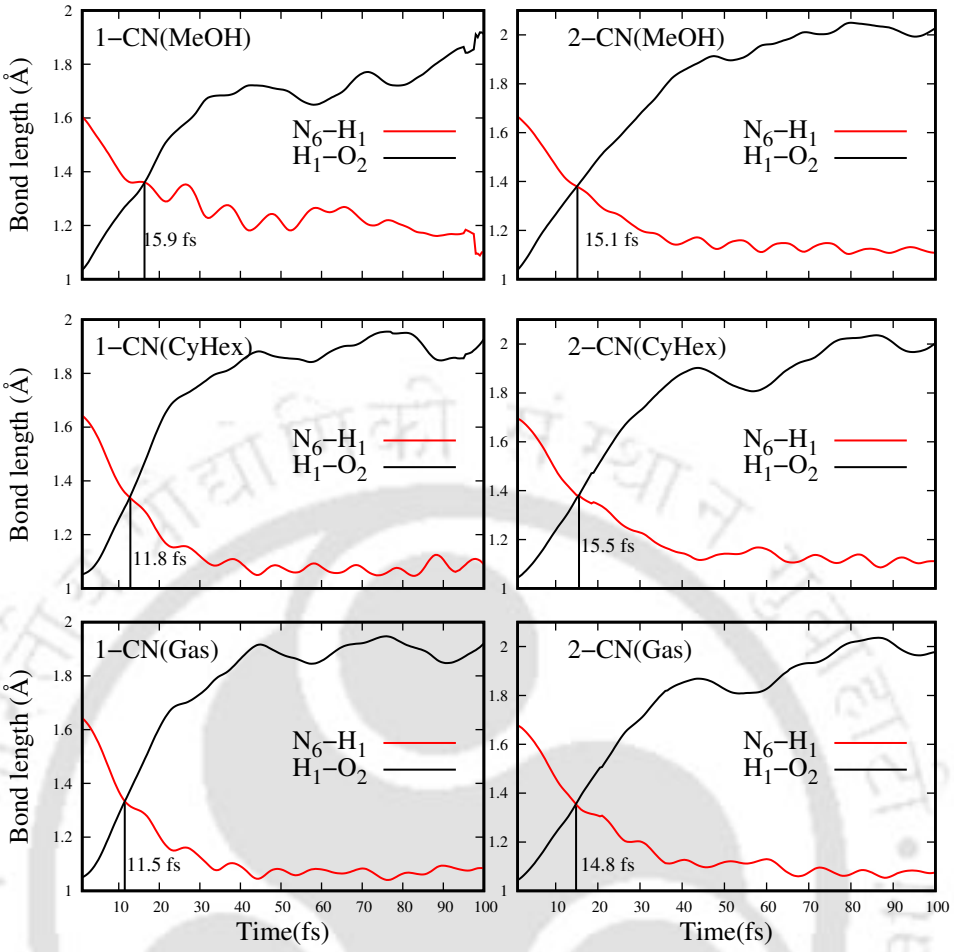

FIGURE 4.8: Time evolution of the two internal coordinates involved in proton transfer process averaged over 50 trajectories for 1-CN and 2-CN in the Gas, CyHex and MeOH solvents.

Figure 4.9 shows the results in the gas phase. Here, the average values of the potential energies of S_0 and S_1, the gaps between these two states and the dihedral angles are shown as a function of time. The energy gap reduced gradually to 1.3 and 1.2 eV for 1-CN and 2-CN within 1 ps simulation time with large torsional motions from 500 fs onwards (cf. Figure 4.9). Figure 4.10 shows the structural evolution of 1-CN and 2-CN for typical trajectories, at the FC region (0 fs), at 100 fs and the twisted structure at the end of the simulation time (1 ps).

Results in CyHex are shown in Figure 4.11. For 2-CN, results similar to gas phase are observed where the energy gap decreases to 1.6 eV and the value of ϕ_1 increases considerably to 60° within the maximum simulation time. However, for 1-CN, there is a small change in ϕ_1 (22°), and the gap does not decrease further below 2.1 eV within

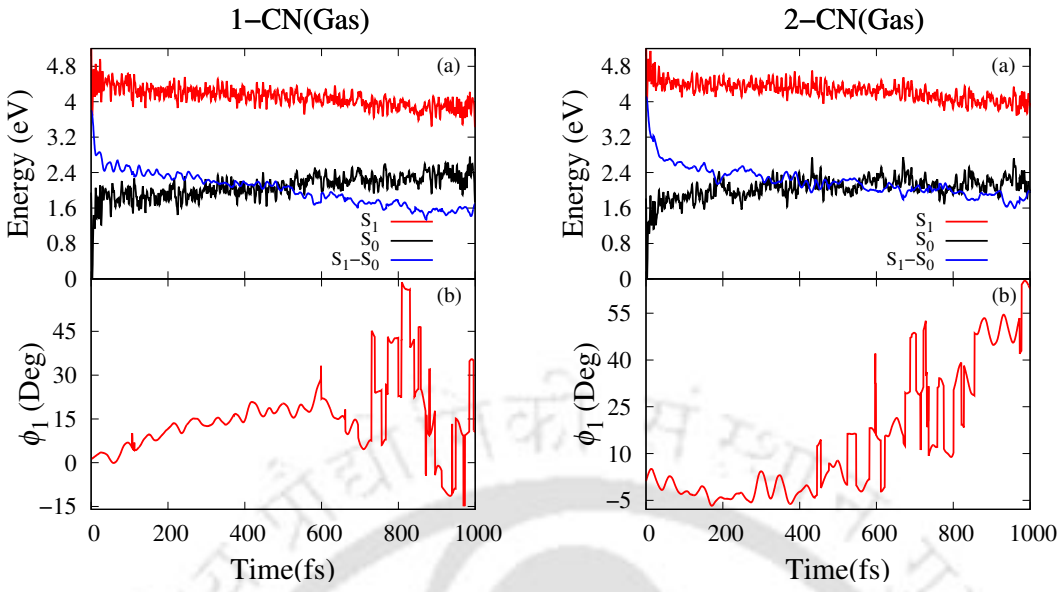

FIGURE 4.9: Time evolution of (a) the S_0 and S_1 states, and their differences and (b) dihedral angle ϕ_1 averaged over 25 trajectories for 1 ps in the gas phase.

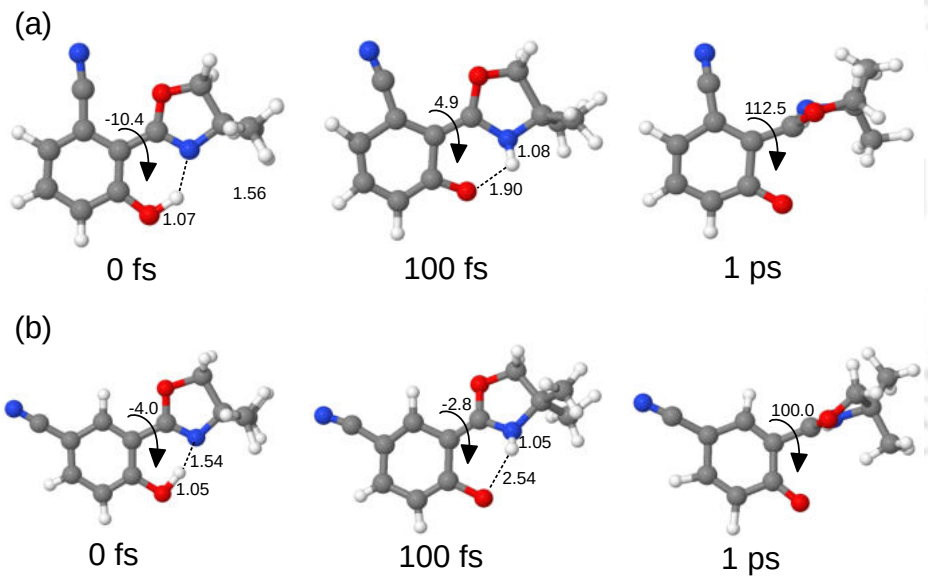

FIGURE 4.10: Snapshots of (a) 1-CN and (b) 2-CN at three different time points of one typical trajectory in the gas phase. Values of key geometrical parameters are indicated in the figure. The bond lengths are in Å and the angles are in degrees. (The positive and negative values of dihedral angles indicate the clockwise and anti-clockwise rotations, respectively.)

1 ps. All the above observations indicate that non-radiative deactivations happen at a much longer timescale than the 1 ps considered here. The non-radiative relaxation dynamics in the MeOH solvent was not carried out as the dynamics is expected to take longer time than that in the gas and CyHex, as predicted from the static results. The decrease in the energy gap and the increase in ϕ_1 over a period of 1 ps suggests that

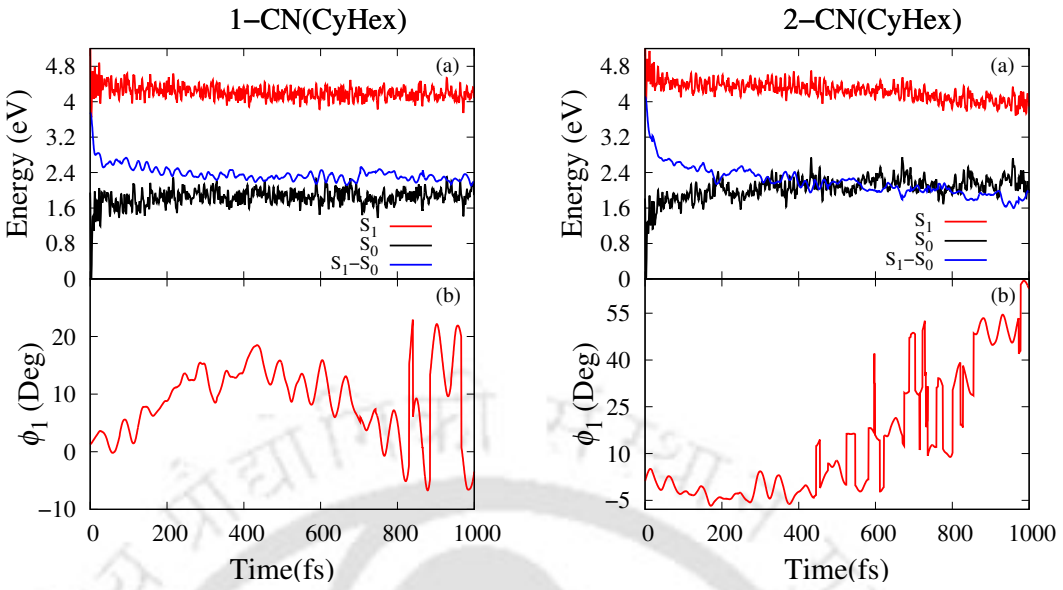

FIGURE 4.11: Time evolution of (a) the potential energies in the S_0 and S_1 states, and their differences, and (b) dihedral angle ϕ_1 averaged over 25 trajectories for 1 ps in CyHex.

the first approach to MECI region happens at around 500 fs. Due to limited timescale and fewer trajectories considered in our study, and also of the failure of TDDFT in the vicinity of CI, the actual lifetimes could not be determined. The time scale is predicted to be much longer than 1 ps timescale considered here.

4.4 Conclusions

In summary, we performed computational studies to understand excited state processes of 1-CN and 2-CN in gas, CyHex and MeOH. We have employed a variety of computational methods including DFT, RI-SOS-ADC(2) and MS-CASPT2//CASSCF in simulating the photoinduced processes. For both the compounds, we found enol and keto conformers to be the most stable structures in the S_0 and S_1 states, respectively, except in the gas phase for 2-CN in which the optimization led to a twisted form. The potential energy scans along the PT coordinates showed the process to be barrierless in gas and solvent environments. We also explored the possible non-radiative deactivation pathways following the PT processes. The identification of the MECIs at multireference

level along the twisting coordinate between the two rings showed easily accessible relaxation pathways. Our dynamics simulations confirmed the predictions of static results for ultrafast PT times and the presence of non-radiative pathways. The exact lifetime of non-radiative transition could not be ascertained due to a small number of trajectories considered and 1 ps TDDFT dynamics showing that our investigation is not conclusive to explain the full photocycle. However, our results predict that the first approach towards the CI to start around 500 fs. These results can serve as a tool to further investigate the dynamics at multireference level. Further studies including explicit solvation which can take into account the solvent-solute interactions are under progress. In addition, solid phase studies which will provide insight into the aggregated induced emission enhancement properties of these systems are also undergoing.

Chapter 5

E/Z photoisomerization in 1-(2-Pyrrolyl)-2-(2-thienyl)ethylene

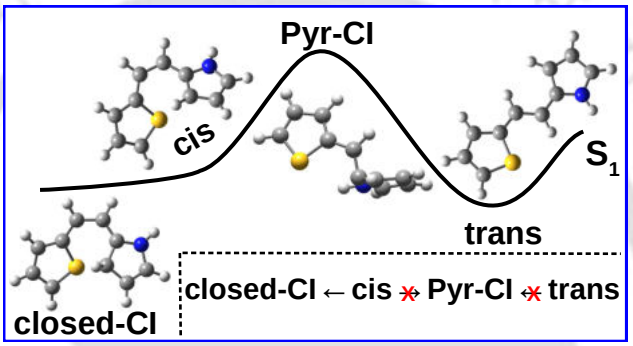

In this chapter, possible photo-induced processes in vinylene-linked thiophene pyrrole system are presented. Computational studies are carried out at the RI-MP2/RI-ADC(2)/cc-pVTZ level to explore different isomerization pathways. Minimum energy conical intersection structures are categorized into two types: closed ring and twisted-pyramidalized structures. Relaxation through the former MECIs is possible only from the *cis* isomers. However, the latter MECIs are inaccessible due to high energy barriers along the linear interpolation in internal coordinate paths. Reproduced from " *The Journal of Physical Chemistry A*, **2023**, 127, 5673" with permission from American Chemical Society.

5.1 Introduction

Photoisomerization is a process in which a molecule isomerizes from one form to another upon light absorption. In nature, this process happens in rhodopsin where the retinal chromophore which forms the backbone of rhodopsin undergoes isomerization and is responsible for the vision.[72,73] This process has drawn considerable attention because of the pivotal role it plays in the field of nano-technological applications which include organic molecular devices like molecular switches and molecular electronics.[235] There are numerous mechanisms suggested for the photoisomerization process which include one-bond twist[236], hula-twist[237,238], bicycle pedal,[239] and so on. It was found that in most of the cases the isomerization process between the *cis* and *trans* form is not favorable in the ground state due to a high rotational barrier, unlike in the excited state where the barrier is comparatively smaller resulting in a facile conversion. Due to this topography, the process is ultrafast in the excited state.[240–242] The photoisomerization process in stilbene molecule has attracted considerable attention and it has been studied extensively both experimentally and computationally[94,96,241,243–246] because of its strong absorption in the near UV region and its intriguing features. Stilbene can undergo isomerization in both directions, i.e, from *trans*-to-*cis* and vice versa.[247] Typically in a vinylene-linked system such as stilbene, it has been observed that upon photoexcitation, the molecule relaxes via rotation along the central double bond. The system at first reaches the perpendicularly twisted geometry in the excited state, identified as the phantom state,[95,98,248] in the vicinity of the CI structure. At this point, the energy gap between the two states becomes small and the system is expected to undergo internal conversion through the nearby CI structure which acts as a funnel for relaxation to the ground state. Starting from the CI structure, either the initial structure can be produced or the molecule can undergo further twisting yielding different products in the ground state. In the case of stilbene, the formation of the *cis* form and the *trans* forms in the ground state occurs almost in equal ratio irrespective of the initial structure.[247] However, the process of isomerization differs in the *cis*-to-*trans* isomerization compared to the *trans*-to-*cis* one. In stilbene, the *trans* conformer is found to have a longer lifetime, on the order of tens of picoseconds compared to the ultrafast relaxation of the *cis* conformer

in hundreds of femtoseconds.[98] The presence of a nearly planar minimum energy *trans* structure in the excited state is the reason for this delay, which is in contrast to the unstable *cis* structure. In addition to these two forms, the cyclization product has also been found to form in the ground state in a smaller fraction, showing one more pathway through which the molecule releases its excess energy.[95,247] The effect of substitution on the ethylenic bond and in the benzene ring of stilbene has also been explored by many groups.[249–252] There are a few studies involving five-membered rings such as thiophene and furan resembling the stilbene structure. In 2004, Nakamura et al.[253,254] explored the role of CI in the photochromic cycloreversion reactions of dithienylethenes.[253,255] Recently, Faraji et al.[255] provided theoretical insights into the isomerization mechanism of a non-symmetric dithienylethene. Photoisomerization pathways in fluorinated di(3-furyl)ethene[256] was also investigated recently. However, to the best of our knowledge, the replacement of the benzene rings in stilbene by pyrrole and thiophene rings resulting in 1-(2-pyrrolyl)-2-(2-thienyl)ethylene system, and its effect on the photoisomerization and relaxation mechanisms have not been studied. Keeping this in mind, the main objective of our work is to illustrate the underlying excited state reaction mechanisms of the vinylene-linked thiophene-pyrrole system by carrying out quantum chemical calculations using wave function-based methods. In our studies, we have employed both single and multi-reference methods, including ADC(2)[153,182] method due to its success in describing various excited state properties[257–260] and the CASSCF method[117]. Since the chosen systems have not been explored experimentally, our results were compared with the few literature reports on vinylene-linked systems such as ethylene and stilbene.

In the next section, the computational methods used are mentioned. Results and discussion are presented in the following section, including general features of the S_0 optimized structures, vertical excitation, results of optimization in the S_1 state, and finally, the obtained MECI structures and linking of the Franck-Condon (FC) structures to these MECIs through energy profiles along the LIIC paths. Conclusions are drawn in the final section.

5.2 Computational Details

The structures of different conformers in the S_0 were optimized at second-order Møller-Plesset perturbation theory(MP2)[115] level. In order to confirm that the obtained stationary points are true minima, numerical frequency analysis was carried out at the same level of theory. The calculations for vertical excitation energies and optimizations in the S_1 were carried out using the ADC(2) method. The empirically scaled opposite-spin(SOS)[123,192,261] variant of ADC(2) was used in our case due to improved accuracy of the excitation energies. The cc-pVTZ basis set[193] was used throughout for MP2 and ADC(2) calculations. The MP2 and ADC(2) calculations were carried out taking advantage of the resolution of identity(RI) approximation[190,220] and the frozen core approximation as implemented in Turbomole version 7.1.[196] Potential energy profiles were generated along the LIIC paths connecting the FC regions of various conformers to the MECIs by performing single point calculations for the interpolated points at the same level of theory. The points along the LIIC were generated by interpolation using the pysisyphus package.[262]

The MECIs structures were located at the CASSCF/6-31G(d,p) level with an active space comprising 12 electrons in 11 orbitals and averaged over two states with equal weights, represented as SA-2-CASSCF(12,11) hereafter. CASSCF CI optimizations were performed using the method of Bearpark et al.[263] as implemented in the MOLPRO package.[195] To account for the dynamic correlation effect, single-point energy calculations were performed for the MECI structures at the multistate complete active space second-order perturbation theory (MS-CASPT2)[118] level. The OpenMolcas package[264] was used for the MS-CASPT2 calculations. The TheoDORE program[223–225] was used for generation of natural transition orbitals (NTO) and analysis of the excited state properties.

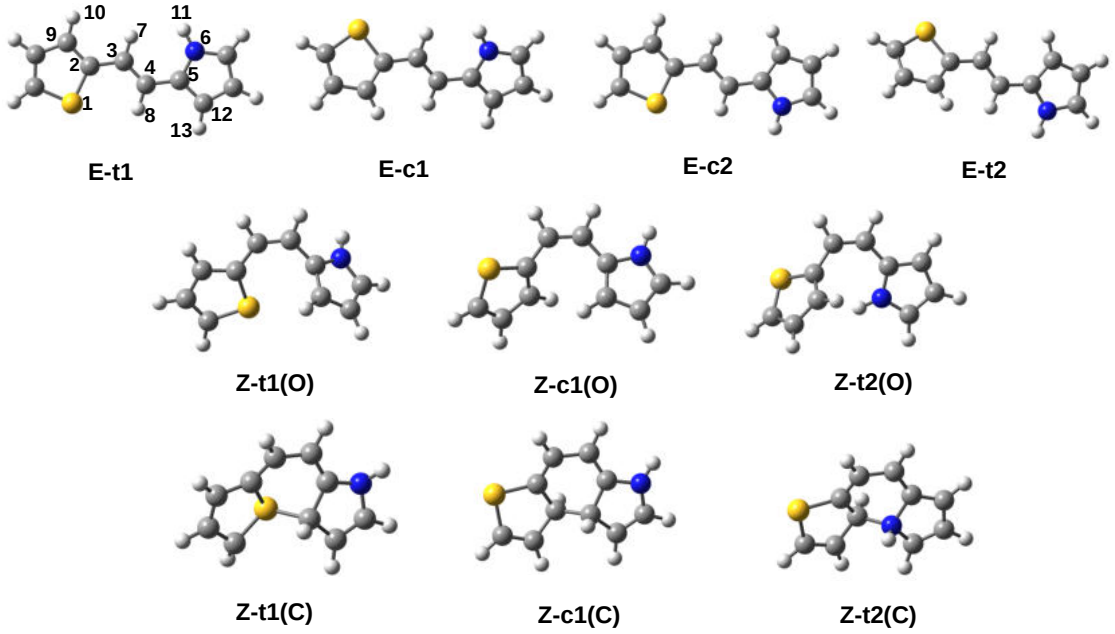

FIGURE 5.1: Ground state optimized structures of isomers obtained at the MP2/cc-pVTZ level of theory

5.3 Results and Discussion

5.3.1 Ground state *cis* and *trans* configurations

A total of ten structures were considered in the ground state: four *trans* (**E**) conformers and six *cis* (**Z**). All 10 conformers of the vinylene-linked thiophene-pyrrole systems were optimized without any geometrical constraints. The results of frequency calculations showed no imaginary values, indicating that the structures are true minima. The optimized structures of all the conformers are shown in Figure 5.1, and the Cartesian coordinates are tabulated in Tables C1-C7. The first structure in Figure 5.1 also shows the atom-numbering scheme of selected atoms employed in the present work to perform the analysis. As shown, in addition to being **E** or **Z**, these conformers also differ from each other with respect to orientations of heteroatoms. Accordingly, the notations **t** and **c** are used to indicate whether the heteroatoms are in the opposite or same direction. For comparison purposes, three dihedral angles are defined as follows: ϕ_1=$\angle$$S_1$-$C_2$-$C_3$-$C_4$, ϕ_2=$\angle$$C_2$-$C_3$-$C_4$-$C_5$ and ϕ_3=$\angle$$C_3$-$C_4$-$C_5$-$N_6$ which denote rotations of the thiophene ring with respect to the other part, the twisting along the central C=C and the rotation

TABLE 5.1: Relative energies (in eV) of all of the considered isomers of vinylene-linked thiophene-pyrrole in the S_0 and S_1 states. Results were obtained at the RI-MP2/cc-pVTZ and RI-ADC(2)/cc-pVTZ levels of theory. The energies were taken relative to the energy of **E-t1**.

	$E(S_0)$	$E(S_1)$
Z-t1(O)	0.18	3.66
Z-c1(O)	0.18	3.67
Z-t2(O)	0.05	
Z-t1(C)	3.37	
Z-c1(C)	0.97	
Z-t2(C)	2.81	
E-t1	0.00	3.82
E-c1	0.05	3.85
E-c2	0.03	3.78
E-t2	0.08	3.83

of the pyrrole ring, respectively. The relative energies of these ground state structures are presented in Table 5.1, with reference to the most stable conformer in the S_0 state.

The four **E** structures are relatively close in energy and differ by only 0.03-0.08 eV from each other. The most stable structure in the S_0 state is the **E-t1**, in which the sulfur and nitrogen atoms in the heterocyclic rings are in opposite directions. Considering **E-t1** as the reference structure, the other three **E** rotational isomers are obtained by rotations along the single bond that connects the thiophene or pyrrole rings to the vinylene double bond. A few important geometrical parameters are presented in Table. 5.2. Conformer **E-t1** was found to be planar: ϕ_1 and ϕ_3 are 0° and ϕ_2 is 180°, indicating that no rotation of the thiophene or the pyrrole ring occurred. The rotamer **E-t2** was formed by rotation of -160 ° and -168.5° along ϕ_1 and ϕ_3, respectively, and is 0.08 eV higher in energy. Similarly, **E-c1** and **E-c2** resulted by rotations of -161° and 180° along ϕ_1 and ϕ_3, respectively (changes along the other angles are very small).

The *cis* isomers are classified into two types, i.e., the open (denoted as **O**) and closed (denoted as **C**) forms, based on the inter-ring distance (R) measured between two closely-lying non-hydrogen atoms. From the atom-numbering scheme in Fig. 5.1, this corresponds to 1-6, 1-12, 9-6 and 9-12 atom-atom distances. A structure is denoted as **C**/**O** inside the parenthesis for R less/greater than 2 Å.[255] **Z-t2(O)** is the most stable conformer among the cis-forms. This conformer is non-planar, with the thiophene ring twisted by -122° along ϕ_1. The other two open forms of cis-isomers denoted as **Z-t1(O)** and **Z-c1(O)** are 0.13 eV higher in energy than **Z-t2(O)**. The three closed-form

TABLE 5.2: Selected geometrical parameters(in Å or deg) for the optimized structures in the S_0 and S_1 states. (The positive and negative values of dihedral angles indicate the clockwise and anti-clockwise rotations, respectively.) The results were obtained at the RI-MP2/cc-pVTZ and RI-ADC(2)/cc-pVTZ levels of theory. In column 1, X=C/S and Y=N/C.

	Z-t1(O)	**Z-c1(O)**	**Z-t2(O)**	**Z-t1(C)**	**Z-c1(C)**	**Z-t2(C)**	**E-t1**	**E-c1**	**E-c2**	**E-t2**
C_2-C_3(S_0)	1.46	1.47	1.47	1.37	1.35	1.36	1.45	1.46	1.45	1.46
C_2-C_3(S_1)	1.39	1.39					1.39	1.39	1.39	1.39
C_3-C_4(S_0)	1.35	1.35	1.35	1.46	1.47	1.42	1.35	1.35	1.35	1.35
C_3-C_4(S_1)	1.42	1.43					1.43	1.43	1.42	1.42
C_4-C_5(S_0)	1.46	1.46	1.45	1.35	1.35	1.38	1.45	1.45	1.45	1.45
C_4-C_5(S_1)	1.41	1.40					1.40	1.40	1.40	1.40
X-Y(S_0)	3.24	3.28	3.17	1.80	1.52	1.49				
X-Y(S_1)	2.82	2.75								
ϕ_1(S_0)	-6.3	142.5	-122.2	-3.0	178.3	176.2	0.0	-161.0	0.0	-160.0
ϕ_1(S_1)	-13.4	163.0					0.0	-175.0	0.0	-178.8
ϕ_2(S_0)	-6.4	-5.5	4.8	-26.5	-18.8	-15.9	180.0	-177.8	180.0	-177.1
ϕ_2(S_1)	-35.6	-35.4					-180.0	-165.0	-180.0	-177.8
ϕ_3(S_0)	132.5	167.1	4.7	174.5	177.8	-3.2	0.0	6.4	180.0	-168.5
ϕ_3(S_1)	167.9	169.0					0.0	7.3	-180.0	-179.1

conformers are found to be higher in energy by 1-3 eV. It is to be noted that the difference in energy between the most stable forms of *cis* and *trans* conformers is found to be 0.05 eV which is almost in the same range to that found between *cis* and *trans*-stilbene.[265] Due to this small difference, ground state thermal conversion is expected to happen.

5.3.2 Excitation Energies

The VEEs at the ground state optimized geometries of all the conformers for the three lowest singlet excited states S_1, S_2, and S_3 are listed in Table 5.3. The corresponding oscillator strengths (f_{osc}) are presented in parentheses. VEEs for the S_1 state are computed to be 4.15-4.27 eV for the *trans* forms and 4.31-4.60 eV for the *cis*(**O**) forms. It is worth mentioning that the obtained VEE values for the pyrrole-thiophenes are similar to the absorption maxima of *trans* and *cis* stilbene in cyclohexane solvent centered at 4.17 and 4.49 eV.[266] The S_1 state FC energies of the *cis*(O) conformers are higher in energy by 0.04-0.45 eV compared to the corresponding energies of *trans* FC structures. Due to this excess energy, photoconversion from *cis* to *trans* is expected to be more facile than from *trans* to *cis*. VEEs of *cis*(C) forms are found to be in the range of 2.09-4.06 eV. Transitions to the S_1 states are accompanied by large values of f_{osc}(between 0.176-1.035), except for the closed form conformers **Z-t1(C)** and **Z-c1(C)**. This indicates that S_1 is a spectroscopically bright state. The character of these excited states

TABLE 5.3: Vertical excitation energies (VEE in eV) with oscillator strength(in parentheses) for the first three singlet excited states obtained at the RI-ADC(2)/cc-pVTZ level of theory.

	S_1	S_2	S_3
Z-t1(O)	4.39 (0.345)	5.24 (0.146)	5.48 (0.172)
Z-c1(O)	4.31 (0.511)	5.33 (0.048)	5.54 (0.046)
Z-t2(O)	4.60 (0.475)	5.51 (0.085)	5.65 (0.073)
Z-t1(C)	2.09 (0.050)	3.53 (0.006)	4.31 (0.165)
Z-c1(C)	4.06 (0.112)	4.97 (0.012)	5.27 (0.142)
Z-t2(C)	2.52 (0.176)	3.81 (0.078)	4.37 (0.074)
E-t1	4.22 (1.001)	5.30 (0.082)	5.57 (0.038)
E-c1	4.27 (1.035)	5.33 (0.057)	5.56 (0.030)
E-c2	4.15 (0.960)	5.29 (0.081)	5.57 (0.017)
E-t2	4.22 (0.983)	5.31 (0.050)	5.57 (0.019)

were determined from the NTOs which are shown in Figure. 5.2 for **E-t1** and **Z-t2(O)**. The NTOs for the others are presented in Figures C1-C8. NTO analysis reveals the $\pi\pi^*$ character of the S_1 state of **E-t1** where the hole and electron NTOs are of π and π^* type delocalized over the whole molecule. As shown in Figure 5.2, the transfer of electron density occurs from C=C to the adjacent C-C bond thus creating a node in the C=C bond. As a result, rotation along the central bond is allowed suggesting the feasibility of the isomerization process in the S_1 state. The S_2 and S_3 states lie ≈ 1 eV above S_1, and are very close in energy. Similar to S_1, these two are also $\pi\pi^*$ type, however, show small f_{osc} values. As the NTOs show, both the hole and electron are mostly located in the thiophene ring for the S_2 state. In comparison, for the S_3 state, while the hole is over the pyrrole ring only, the electron is over the whole molecule. The S_1 state of **Z-t2(O)** is represented by a single set of NTOs, while the S_2 and S_3 states are represented by two sets of NTOs. Similar characters of the three excited states were noticed for **E-c1**, **E-c2** and **E-t2** with small variations in the sets of involved NTO pairs and the corresponding eigenvalues. However, all of the states are of $\pi\pi^*$ character. NTOs for **Z-t1(C)**, **Z-c1(C)**, and **Z-t2(C)** are shown in Figures C6-C8. In the case of **Z-t1(C)**, while both S_1 and S_2 were described by only one set of NTOs, S_3 showed two pairs. For **Z-c1(C)** and **Z-t2(C)**, each of the excitations was found to be dominated by one pair of NTOs. Further, both the holes and electrons were found to be localized almost around the same region for these isomers.

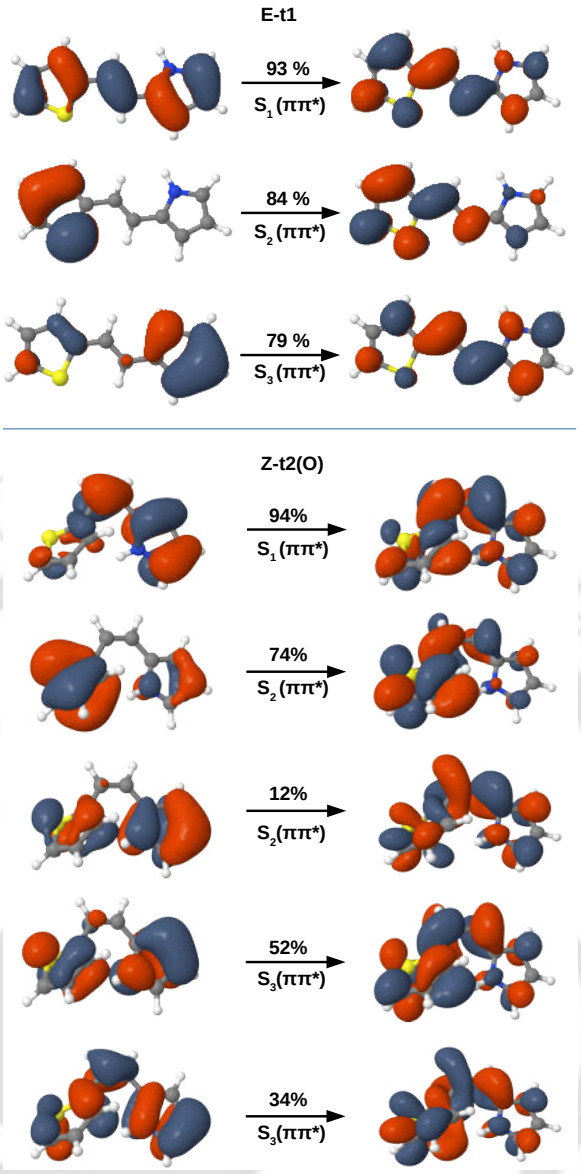

FIGURE 5.2: Dominant NTOs involved in the transitions from S_0 to S_1, S_2, and S_3 states for **E-t1** and **Z-t2(O)**

5.3.3 S_1 state minima

In the S_1 state, minima corresponding to **Z-t2(O)** and the three **Z** closed form structures in S_0 were not obtained at the RI-ADC(2) level of theory. The optimized structures in the S_1 state are shown in Figure C9, and the corresponding Cartesian coordinates are listed in Tables C1-C6. As shown in Table 5.1, the two *cis* conformers are found to be close in energy with a small energy difference of 0.01 eV. It is observed that upon photoexcitation the length of the central double bond increases and the alternate single bond lengths decrease in the S_1 state with respect to the corresponding bond lengths in

S_0. The lengths of C_3-C_4 bond for **Z-t1(O)** and **Z-c1(O)** increased from 1.35 Å each to 1.42 Å and 1.43 Å, respectively. Similarly, the C_2-C_3/C_4-C_5 distances decreased from 1.46 Å each to 1.39/1.41 Å and from 1.47/1.46 Å to 1.39/1.40 Å, for **Z-t1(O)** and **Z-c1(O)** conformers in the S_1 state, respectively. Systems undergoing photoisomerization like stilbene, azobenzene and other diarylethene were also found to show these general traits.[256,267,268] For this reason, the isomerization process along the central bond is expected to be easier in the excited state than in the ground state due to the loss of the double bond character.[269] The two **Z**-conformers, **Z-t1(O)** and **Z-c1(O)**, retain their non-planarity in the S_1 state as well along ϕ_2, but the angles are further twisted by $\approx 30°$ which may be ascribed to electrostatic repulsion between the nearby atoms and also of the weakening of the central double bond. Since the twisted stilbene structure in the S_1 state plays an important role in generating the potential energy profiles for the *cis-trans* isomerization process, in our study, an attempt was made to optimize the perpendicularly twisted and pyramidalized structures in the S_1 state, which is referred to as the phantom state for stilbene.[256] However, these optimizations were unsuccessful and this always resulted in one of the structures already mentioned above.

All of the *trans* structures were found to be almost isoenergetic (the energy differences were 0.01-0.07 eV). Among these structures, **E-c2** was found to be the most stable structure which lies 3.75 eV above its ground state structure(cf. Table 5.1), and 0.4 eV below the FC region. This structure was found to retain its planarity in the S_1 state. Similarly, as presented in Table 5.2, the other two isomers **E-t1** and **E-t2** remain planar in S_1 with $\phi_2 \approx -180°$. For **E-c1**, however, a deviation from planarity was observed, with a torsional angle of -165° in the S_1 state along ϕ_2. The lengthening of the central ethylenic double bond and the shortening of the adjacent single bond were also noted in the case of *trans* isomers, as was the case for the *cis* conformers mentioned above. Radiative transitions from these structures are possible deactivation paths as the transitions are accompanied by large oscillator strengths.

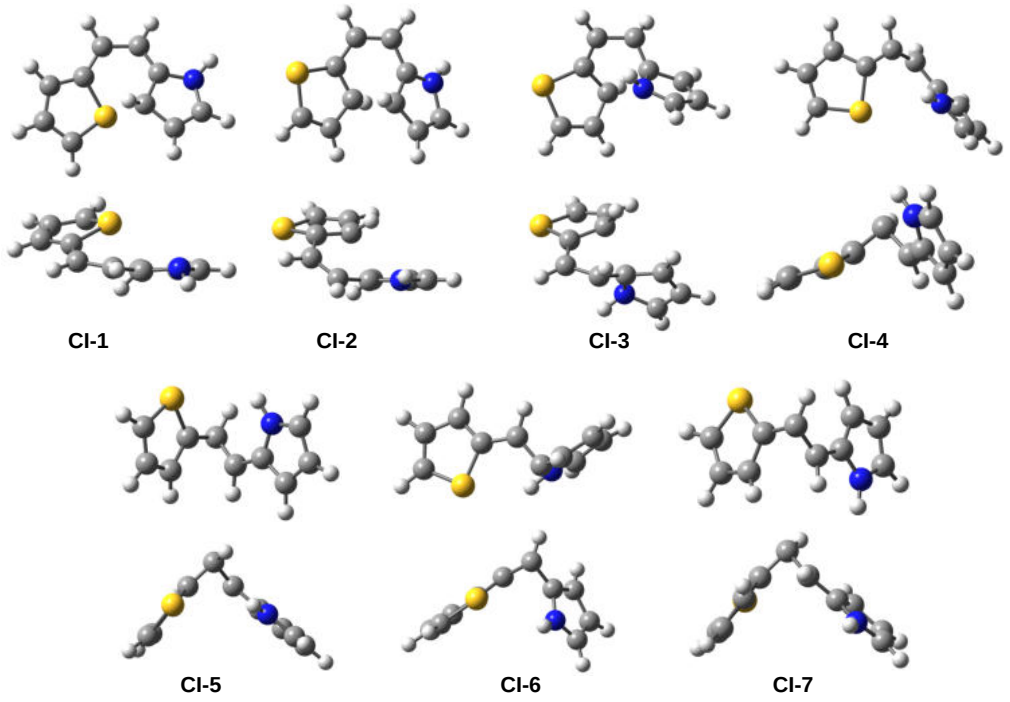

FIGURE 5.3: Conical intersection structures obtained at the SA-CASSCF/6-31G(d,p) level of theory.

5.3.4 MECIs and LIICs

The important role of CIs in the excited state relaxation mechanism has long been known. Due to the multireference character of CI, single-reference methods fail to accurately describe the CI seam. The use of the CASSCF method is widely accepted for exploring CIs in photochemistry. In the present study, seven MECIs located between the S_1 and S_0 states at the SA-2-CASSCF(12,11)/6-31G(d,p) level, similar to the two types of MECIs located for vinylene-linked systems,[94,267,270,271] are considered. The similarities are in the cyclization and the isomerization coordinates. For the first case, the guess structures are taken from the optimized geometries of *cis* forms and in the second case, perpendicularly twisted and pyramidalized structures are considered. The MECI structures are shown in Figure 5.3, and the Cartesian coordinates are given in Tables C8-C11. The active spaces chosen in our studies for **CI-1** and **CI-2** optimization comprising π and π^* orbitals are shown in Figure 5.4. Single-point energy calculations were carried out for these seven MECI structures at the MS-CASPT2 level. The energy

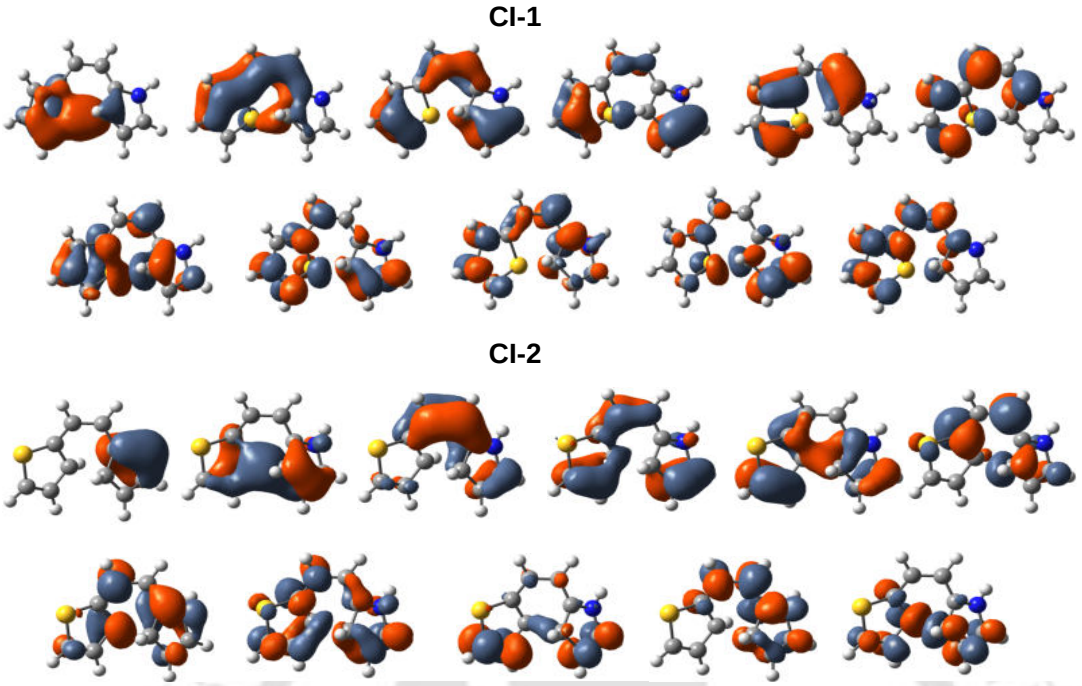

FIGURE 5.4: Orbitals used in the active space for **CI-1** and **CI-2** optimizations computed at the SA-2-CASSCF(12,11) /6-31G(d,p) level of theory.

differences between the S_0 and S_1 states at the CASSCF and MS-CASPT2 levels of theory are presented in the Table C2. As the table shows, the energy gap between the two states increased to be in the range of 0.3-0.7 eV at the MS-CASPT2 level. The increase in the energy gap at the MS-CASPT2 level has been observed in many cases[272–275] after the inclusion of dynamic correlation. It has also been found that the geometries optimized at these two levels are qualitatively similar in many cases.[274,276,277] Therefore, in the present study, we considered the CASSCF MECIs for further explorations. In the **Z** region, three MECIs were found, labeled as **CI-1**, **CI-2**, **CI-3**. The relative energies and selected geometrical parameters are presented in Table 5.4. These include the twisting angles of the thiophene/pyrrole (labelled as ϕ_1 and ϕ_3), twisting along the central C=C bond (ϕ_2), and pyramidalization angles (τ_1 and τ_2). In our study, τ_1 and τ_2 were measured according to the recipe specified by Tsutsumi et al.[250] The **CI-1** structure is closer to the S_0 **Z-t1(C)** conformer in terms of the bond length and dihedral angle around the two rings, except for the S_1-C_{12} bond, which is longer by 0.28 Å. The **CI-2** structure is similar to that of **Z-c1(O)** and **Z-c1(C)**, with a decrease of 1.31 Å and an increase of 0.45 Å for C_9-C_{12} from **Z-c1(O)** and **Z-c1(C)**, respectively. The **CI-3** structure differs from those of the other two MECIs: it is slightly pyramidalized

TABLE 5.4: Relative energies (in eV) computed at the RI-ADC(2)/cc-pVTZ level of theory and optimized geometrical parameters (in Å or deg) obtained at the CASSCF level of theory for all the optimized MECI structures. The energies are taken relative to **E-t1**.

	CI-1	**CI-2**	**CI-3**	**CI-4**	**CI-5**	**CI-6**	**CI-7**
E(eV)	4.24	4.00	4.78	4.51	4.36	4.19	4.47
X-Y	2.08	1.97	2.79				
C_2-C_3	1.39	1.39	1.35	1.38	1.39	1.45	1.38
C_3-C_4	1.44	1.38	1.48	1.47	1.46	1.45	1.46
C_4-C_5	1.36	1.45	1.42	1.42	1.43	1.51	1.44
ϕ_1	-9.8	141.1	161.2	67.8	120.4	8.77	-118.5
ϕ_2	-25.5	-11.1	-36.2	-101.0	-93.9	106.0	95.3
ϕ_3	163.5	139.5	-58.2	-7.7	6.1	-82.7	179.1
τ_1	179.3	-178.7	177.4	-118.2	123.2	-175.5	-124.5
τ_2	179.0	171.8	142.2	178.6	-170.5	109.9	170.2

at the ethylenic carbon close to the pyrrole ring, which is reflected in the value of τ_2. As presented in Table 5.4, value of τ_2 in this case is $\approx$ 142°, deviating by about 36° from the value for **Z-t2(O)**(τ_2=178.3 °). **CI-1** and **CI-2** are lower in energy by 0.33 and 0.48 eV from the FC energies of **Z-t1(O)** and **Z-c1(O)**, respectively. On the other hand, **CI-3** is 0.13 eV higher in energy than FC **Z-t2(O)**(see Table C4). The relatively higher energy of **CI-3** could be ascribed to the pyramidalized ethylenic carbon atom and also the pyramidalized ring structure.[256] Since **CI-1** and **CI-2** are lower in energy than **Z-t1(O)** and **Z-c1(O)** at their FC point, it is expected that **Z-t1(O)** and **Z-c1(O)** will undergo relaxation directly from the FC region to the MECIs by small distortions in the geometrical parameters. The geometric proximity of the two MECIs with the **Z-t1(O)** and **Z-c1(O)** structures and the location of MECIs below the FC region led us to generate points along the LIICs connecting the two structures. In the current work, the potential energy profiles were generated along the LIIC pathways, as we believed that restricting calculations to a single coordinate like a torsion is inadequate in outlining the photoisomerization and the relaxation pathways through the obtained MECIs where multiple coordinates were involved in the photodynamics. Single point energy calculations were carried out at the RI-ADC(2) level for the interpolated structures in the S_1 state. The potential energy profiles obtained along the two generated pathways are shown in Figures 5.5 and 5.6, respectively. Along these two reaction paths, the energy drops gradually from the FC region with no barrier to reach the MECIs suggesting the accessibility of the obtained MECIs for non-radiative relaxation to the ground state. Another pathway from **Z-t2(O)** to **CI-3** was also generated in which a large barrier of

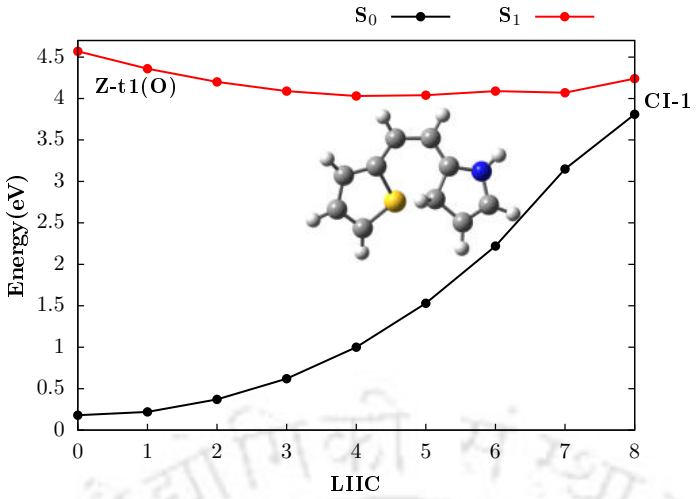

FIGURE 5.5: Potential energy profiles along the generated LIIC pathways connecting **Z-t1(O)** to the **CI-1** structure at the RI-ADC(2)/cc-pVTZ level of theory. The energies were calculated with reference to the **E-t1** in the ground state. The structure inside the plot corresponds to MECI structure **CI-1**.

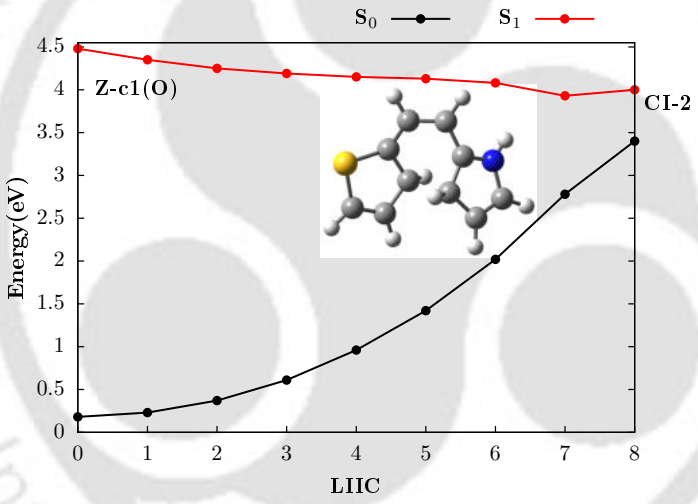

FIGURE 5.6: Potential energy profiles along the generated LIIC pathways connecting **Z-c1(O)** to the **CI-2** structure at the RI-ADC(2)/cc-pVTZ level of theory. The energies were calculated with reference to the **E-t1** in the ground state. The structure inside the plot corresponds to MECI structure **CI-2**.

3.7 eV was found along the path joining the FC region to the MECI; this pathway is presented in Figure 5.7.

In most cases of photoisomerization,[243,247,265,278–280] significant barriers are found in the singlet excited state for the isomerization from the *trans* form to the *cis* form but the barrier gets reduced for the transformation from the *cis* side. For the present system, among the *cis* forms, only one feasible pathway with a small barrier of 0.04 eV was observed for the photoisomerization of **Z-t1(O)** to **E-c2**. The potential energy

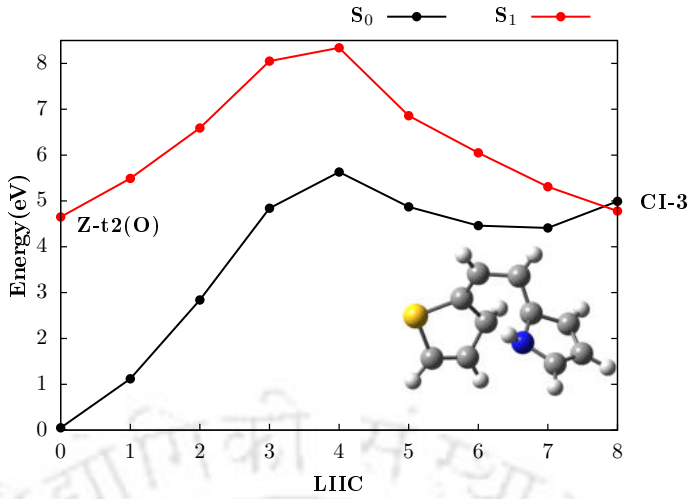

FIGURE 5.7: Potential energy profiles along the generated LIIC pathways connecting **Z-t2(O)** to the **CI-3** structure at the RI-ADC(2)/cc-pVTZ level of theory. The energies were calculated with reference to the **E-t1** in the ground state. The structure inside the plot corresponds to MECI structure **CI-3**.

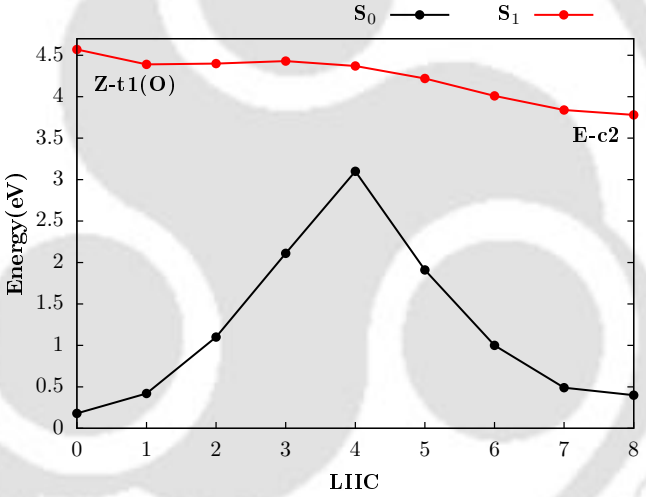

FIGURE 5.8: Potential energy profiles along the generated LIIC pathways connecting **Z-t1(O)** to the **E-c2** structure at the RI-ADC(2)/cc-pVTZ level of theory. The energies were calculated with reference to the **E-t1** in the ground state.

profiles along the LIIC pathway connecting these two structures are shown in Figure 5.8. Since most of the pathways in S_1 show large barriers for photoisomerization from *cis* to *trans* and vice versa, the process is expected to happen in the ground state from the MECI. LIICs connecting the two MECIs, **CI-1** and **CI-2**, to the geometries in S_0 in both *trans* and *cis* configurations were generated. For this, ground state energy calculations were carried out at these interpolated points and the results are shown in Figure 5.9. From **CI-1**, the conversion to the *trans* structures was found to have a significant barrier making the process unfeasible. For isomerization to the *cis* forms, only two pathways

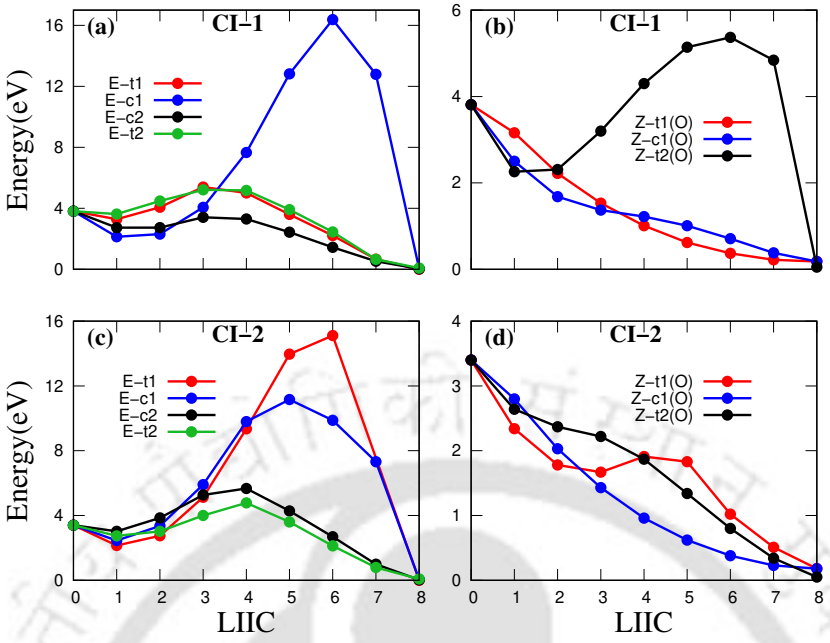

FIGURE 5.9: Potential energy profiles along the generated LIIC pathways connecting **CI-1** and **CI-2** to all the Z and E conformers in the ground state at RI-MP2/cc-pVTZ level of theory.

that resulted in the formation of **Z-t1(O)** and **Z-c1(O)** were considered possible due to their barrierless channels. For the transformation from **CI-2** to the *trans* forms, large barriers were found. However, for *cis* forms, two barrierless pathways were found forming **Z-c1(O)** and **Z-t2(O)** (as shown in Figure 5.9). Therefore, while the formation of *trans* forms from these two MECIs is unlikely, formation of *cis* is possible.

The other four MECIs are found to be perpendicularly twisted along the central double bond and pyramidalized at one of the ethylenic carbon atoms (denoted as Pyr-CI), which resembles the hula-twist CIs[100,281] found in stilbene and ethylene.[270] In all these CIs, the two ethylenic C-H bond lengths are very similar indicating that these Pyr-CIs have no similarity to the hydrogen-migration character CIs.[270] These MECIs are formed by coupling of the covalent and charge transfer states which is similar to that of ethylene and stilbene Pyr-CI. The twisted-pyramidalized CI for ethylene was found to be lower in energy than the true minimum, while the CI in stilbene lies above the minimum. Since in both the cases, the CIs lie below the FC region, relaxation through the obtained CIs was considered feasible. These four CIs are labelled as **CI-4**, **CI-5**, **CI-6** and **CI-7**. **CI-4** was found to be the least stable, which could be due to the steric

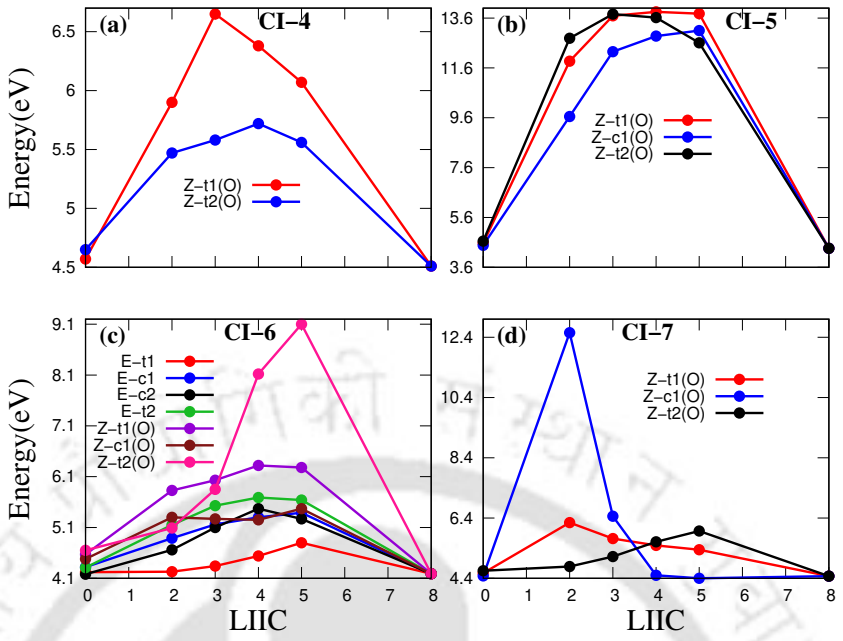

FIGURE 5.10: Potential energy profiles along the generated LIIC pathways connecting (a) **Z-t1(O)** and **Z-t2(O)** to **CI-4**, (b) **Z-t1(O)**, **Z-c1(O)** and **Z-t2(O)** to **CI-5**, (c) **E-t1**, **E-c1**, **E-c2**, **E-t2**, **Z-t1(O)**, **Z-c1(O)**, and **Z-t2(O)** to **CI-6**, and (d) **Z-t1(O)**, **Z-c1(O)** and **Z-t2(O)** to **CI-7** in the S_1 state at RI-ADC(2)/cc-pVTZ level of theory.

hindrance caused by the unfavorable arrangement of the two rings. In **CI-4**, **CI-5** and **CI-7** structures, pyramidalization happens at the carbon atom that is attached to the thiophene ring. The τ_1 values are -118.2, 123.2 and -124.5° for **CI-4**, **CI-5** and **CI-7**, respectively. On the other hand, **CI-6** has a pyramidalized carbon atom adjacent to the pyrrole ring with a τ_2 value of 109.9°. Single point calculations were carried out at the RI-ADC(2) level for the obtained MECI structures to compare their relative energies with the FC energies. The S_1 FC energies of all the **E** conformers are found to be energetically lower than **CI-5** and **CI-7**. Therefore, LIIC paths were generated connecting only the *cis* conformers to these two MECIs. For **CI-4**, LIICs connecting **Z-t1(O)** and **Z-t2(O)** to **CI-4** were generated as they lie above **CI-4**. **CI-6** lies above the **E-c2** FC region by 0.01 eV, therefore, interpolation paths were constructed from all the conformers to **CI-6**. In all the cases, the potential energy profiles along LIICs show large barriers of >0.5 eV(as shown in Figure 5.10). This suggests that these MECIs are inaccessible for non-radiative relaxation at the RI-ADC(2) level.

5.4 Conclusions

Computational exploration of various possible pathways in the relaxation mechanism of a vinylene-linked thiophene-pyrrole system has been carried out using wave-function based methods. The existence of different conformers was inspected in the ground state and the first excited state at the RI-MP2 and RI-ADC(2) levels, respectively. Most of the *cis* conformers are found to be unstable in the excited state suggesting the feasibility of the non-radiative relaxation from these forms. MECI structures that are close to the *cis* conformers were found. In addition, perpendicularly twisted and pyramidalized MECI structures, similar to those reported in literature for diarylethene systems, were also located. Based on these two types of MECIs, LIICs pathways were generated connecting the FC structures to the MECIs. The probability of non-radiative deactivation from the *cis* conformers to the former MECI is more than that from the *trans* conformer because of the similarity between initial and final structures leading to barrierless pathways. However, the potential energy profiles connecting both the *trans* and *cis* FC geometries to the second set of MECIs show large barriers. Therefore, we conclude that the obtained twisted and pyramidalized MECIs are inaccessible in this case. Molecular dynamics studies are under progress, and results will be reported soon.

Chapter 6

Summary and conclusions

Excited state studies have developed over time as a result of several fascinating occurrences that have attracted diverse applications in the field of material science and also in the comprehension of natural phenomena. Computational studies are of great help in understanding the mechanism that would not have been possible to explain from the experimental results. In this thesis, we have unravelled various excited state pathways using state-of-the-art computational tools.

In *chapter 3*, we present the results of static and dynamics studies of the excited state proton transfer and the non-radiative relaxation pathways in HAN molecule in the gas phase. The proton transfer process is more feasible in the S_1 than in the S_0 state. The molecule undergoes non-radiative relaxation after proton transfer by twisting along one of the torsional coordinates. From the dynamics simulation, an average proton transfer time of 43 fs is found. The non-radiative relaxation time is observed to be beyond the simulation time of 600 fs.

In *chapter 4*, effect of implicit solvents on the photoinduced processes in 1-CN and 2-CN are presented. Additionally, the mechanisms behind these two regiomers' weakly emissive properties in the solvent phases are investigated. The solvent has little effect on the proton transfer process, however, the effect on the non-radiative relaxation is more pronounced. An average proton transfer time of 10-15 fs is found from the dynamics simulation.

In *chapter 5*, photoisomerization pathways in vinylene-linked thiophene-pyrrole system are explored and those are compared with the reported results in ethylene and stilbene, which are prototype systems for photoisomerization. Only one plausible photoisomerization pathway from the *cis* to the *trans* conformer in the S_1 state is found.

The photocyclization from the *cis* conformers are also investigated and it is found to proceed through two minimum energy conical intersection structures.

In the thesis, single-reference methods like DFT, TDDFT and ADC(2) and multi-reference methods such as CASSCF and CASPT2 are employed for the exploration of photoinduced process in three different systems. Understanding the proton transfer process and the relaxation mechanisms has been greatly aided by the generation of potential energy profiles along a small number of chosen coordinates. The profiles along the LIIC points are constructed for scenarios where multiple coordinates are involved such as connecting FC geometries to MECIs and geometries involved in photoisomerization. The time evolution of the excited state processes have been elucidated using ADC(2) and DFT methods. The simulation time of selected few trajectories are extended for longer timescale to investigate the probable time for non-radiative relaxation. However, due to the inherent flaw of single reference methods in describing regions near conical intersections, it would be worthwhile to investigate the time evolution of non-radiative process with a multireference approach in future studies. In addition, explicit inclusion of the solvent is known to have a significant impact on the excited state processes, therefore the studies of the aforementioned systems can be extended to include the solvent in the static and dynamics simulations.

References

[1] Schinke, R. *Photodissociation dynamics: spectroscopy and fragmentation of small polyatomic molecules*; Cambridge university press, 1995.

[2] Domcke, W.; Yarkony, D. R.; Köppel, H. *Conical intersections: theory, computation and experiment*; World Scientific, 2011; Vol. 17.

[3] Robin, M. *Higher Excited States of Polyatomic Molecules V3*; Elsevier, 2012; Vol. 3.

[4] Gutzler, R.; Garg, M.; Ast, C. R.; Kuhnke, K.; Kern, K. Light–matter interaction at atomic scales. *Nat. Rev. Phys.* **2021**, *3*, 441–453.

[5] Weller, A. Uber die Fluoreszenz der Salizylsuure und verwandter Verbindungen. *Naturwissenschaften* **1955**, *42*, 175–176.

[6] Shendre, S.; Sharma, V. K.; Dang, C.; Demir, H. V. Exciton dynamics in colloidal quantum-dot LEDs under active device operations. *ACS Photonics* **2018**, *5*, 480–486.

[7] Yin, C.; Zhen, X.; Zhao, H.; Tang, Y.; Ji, Y.; Lyu, Y.; Fan, Q.; Huang, W.; Pu, K. Amphiphilic semiconducting oligomer for near-infrared photoacoustic and fluorescence imaging. *ACS Appl. Mater. Interfaces* **2017**, *9*, 12332–12339.

[8] Stricker, L.; Fritz, E.-C.; Peterlechner, M.; Doltsinis, N. L.; Ravoo, B. J. Arylazopyrazoles as light-responsive molecular switches in cyclodextrin-based supramolecular systems. *J. Am. Chem. Soc.* **2016**, *138*, 4547–4554.

[9] Sobolewski, A. L.; Domcke, W. Photophysics of intramolecularly hydrogen-bonded aromatic systems: ab initio exploration of the excited-state deactivation mechanisms of salicylic acid. *Phys. Chem. Chem. Phys.* **2006**, *8*, 3410–3417.

[10] Zhao, J.; Ji, S.; Chen, Y.; Guo, H.; Yang, P. Excited state intramolecular proton transfer (ESIPT): from principal photophysics to the development of new chromophores and applications in fluorescent molecular probes and luminescent materials. *Phys. Chem. Chem. Phys.* **2012**, *14*, 8803–8817.

[11] Shimomura, O.; Johnson, F. H. Properties of the bioluminescent protein aequorin. *Biochemistry* **1969**, *8*, 3991–3997.

[12] Chalfie, M.; Tu, Y.; Euskirchen, G.; Ward, W. W.; Prasher, D. C. Green fluorescent protein as a marker for gene expression. *Science* **1994**, *263*, 802–805.

[13] Tsien, R. Y. The green fluorescent protein. *Ann. Rev. Biochem.* **1998**, *67*, 509–544.

[14] Zhang, K.; Corrie, J. E.; Munasinghe, V. R. N.; Wan, P. Mechanism of photosolvolytic rearrangement of p-hydroxyphenacyl esters: evidence for excited-state intramolecular proton transfer as the primary photochemical step. *J. Am. Chem. Soc.* **1999**, *121*, 5625–5632.

[15] Taylor, C. A.; El-Bayoumi, M. A.; Kasha, M. Excited-state two-proton tautomerism in hydrogen-bonded N-heterocyclic base pairs. *Proc. Natl. Acad. Sci.* **1969**, *63*, 253–260.

[16] Gelabert, R.; Moreno, M.; Lluch, J. M. Charge-transfer $\pi\pi^*$ excited state in the 7-azaindole dimer. A hybrid configuration interactions singles/time-dependent density functional theory description. *J. Phys. Chem. A* **2006**, *110*, 1145–1151.

[17] Zhong, D.; Douhal, A.; Zewail, A. H. Femtosecond studies of protein–ligand hydrophobic binding and dynamics: human serum albumin. *Proc. Natl. Acad. Sci.* **2000**, *97*, 14056–14061.

[18] Sedgwick, A. C.; Wu, L.; Han, H.-H.; Bull, S. D.; He, X.-P.; James, T. D.; Sessler, J. L.; Tang, B. Z.; Tian, H.; Yoon, J. Excited-state intramolecular proton-transfer ESIPT based fluorescence sensors and imaging agents. *Chem. Soc. Rev.* **2018**, *47*, 8842–8880.

[19] Li, Y.; Dahal, D.; Abeywickrama, C. S.; Pang, Y. Progress in tuning emission of the excited-state intramolecular proton transfer (ESIPT)-based fluorescent probes. *ACS Omega* **2021**, *6*, 6547–6553.

[20] Chen, L.; Fu, P.-Y.; Wang, H.-P.; Pan, M. Excited-State Intramolecular Proton Transfer ESIPT for Optical Sensing in Solid State. *Adv. Opt. Mat.* **2021**, *9*, 2001952.

[21] Stoerkler, T.; Pariat, T.; Laurent, A. D.; Jacquemin, D.; Ulrich, G.; Massue, J. Excited-State Intramolecular Proton Transfer Dyes with Dual-State Emission Properties: Concept, Examples and Applications. *Molecules* **2022**, *27*, 2443.

[22] Huang, J.-D.; Lin, F.; Cheng, S.; Ma, H. Theoretical Insights into the Luminescence and Sensing Mechanisms of N,N′Bis(salicylidene)-[2-(3′,4′diaminophenyl)benzthiazole] for Copper(II). *J. Phys. Chem. A* **2023**, *127*, 966–972.

[23] Tang, Z.; Wang, S.; Liu, S.; Zhao, J. Theoretical study of excited state intramolecular proton transfer behavior for 2-phenyl, 3-hydroxybenzo [g] quinolones and its derivative in the aprotic and protic solvents. *Chem. Phys. Lett.* **2023**, *811*, 140215.

[24] Frutos-Puerto, S.; Colín, M. J.; Corchado, J. C.; Sánchez, M. L.; Martín, M. E.; Aguilar, M. A. Photophysical and photochemical properties of 3-hydroxyflavone in ethanol solution: implicit vs explicit solvent models. *J. Mol. Liq.* **2023**, 121783.

[25] Gu, H.; Wang, W.; Wu, W.; Wang, M.; Liu, Y.; Jiao, Y.; Wang, F.; Wang, F.; Chen, X. Excited-state intramolecular proton transfer (ESIPT) based fluorescent probes for biomarker detection: design, mechanism, and application. *Chemical Communications* **2023**, 2056–2071.

[26] Sekiya, H.; Sakota, K. Excited-state double-proton transfer in a model DNA base pair: resolution for stepwise and concerted mechanism controversy in the 7-azaindole dimer revealed by frequency-and time-resolved spectroscopy. *J. Photochem. Photobiol. C: Photochem. Rev.* **2008**, *9*, 81–91.

[27] Ortiz-Sánchez, J. M.; Gelabert, R.; Moreno, M.; Lluch, J. M.; Anglada, J. M.; Bofill, J. M. Bipyridyl Derivatives as Photomemory Devices: A Comparative Electronic-Structure Study. *Chem. Eur. J.* **2010**, *16*, 6693–6703.

[28] Yu, X.-f.; Yamazaki, S.; Taketsugu, T. Concerted or stepwise mechanism? CASPT2 and LC-TDDFT study of the excited-state double proton transfer in the 7-azaindole dimer. *J. Chem. Theory Comput.* **2011**, *7*, 1006–1015.

[29] Crespo-Otero, R.; Kungwan, N.; Barbatti, M. Stepwise double excited-state proton transfer is not possible in 7-azaindole dimer. *Chem. Sci.* **2015**, *6*, 5762–5767.

[30] Zhao, J.; Yao, H.; Liu, J.; Hoffmann, M. R. New excited-state proton transfer mechanisms for 1, 8-dihydroxydibenzo [a, h] phenazine. *J. Phys. Chem. A* **2015**, *119*, 681–688.

[31] Zhao, J.; Dong, H.; Zheng, Y. Theoretical insights into the excited state double proton transfer mechanism of deep red pigment alkannin. *J. Phys. Chem. A* **2018**, *122*, 1200–1208.

[32] Zhao, J.; Dong, H.; Yang, H.; Zheng, Y. Exploring and elaborating the novel excited state dynamical behavior of a bisflavonol system. *Org. Chem. Front.* **2018**, *5*, 2710–2718.

[33] Zhou, P.; Han, K. Unraveling the detailed mechanism of excited-state proton transfer. *Acc. Chem. Res.* **2018**, *51*, 1681–1690.

[34] Vendrell, O.; Gelabert, R.; Moreno, M.; Lluch, J. M. Operation of the proton wire in green fluorescent protein. A quantum dynamics simulation. *J. Phys. Chem. B* **2008**, *112*, 5500–5511.

[35] Stetina, T. F.; Sun, S.; Lingerfelt, D. B.; Clark, A.; Li, X. The role of excited-state proton relays in the photochemical dynamics of water nanodroplets. *J. Phys. Chem. Lett.* **2019**, *10*, 3694–3698.

[36] Kasha, M. Proton-transfer spectroscopy. Perturbation of the tautomerization potential. *J. Chem. Soc., Faraday Trans. 2* **1986**, *82*, 2379–2392.

[37] Lüdemann, H.-C.; Hillenkamp, F.; Redmond, R. W. Photoinduced hydrogen atom transfer in salicylic acid derivatives used as matrix-assisted laser desorption/ionization (MALDI) matrices. *J. Phys. Chem. A* **2000**, *104*, 3884–3893.

[38] Yahagi, T.; Fujii, A.; Ebata, T.; Mikami, N. Infrared spectroscopy of the OH stretching vibrations of jet-cooled salicylic acid and its dimer in S_0 and S_1. *J. Phys. Chem. A* **2001**, *105*, 10673–10680.

[39] Sobolewski, A. L.; Domcke, W. Intramolecular hydrogen bonding in the S1 ($\pi\pi^*$) excited state of anthranilic acid and salicylic acid: TDDFT calculation of excited-state geometries and infrared spectra. *J. Phys. Chem. A* **2004**, *108*, 10917–10922.

[40] Aquino, A. J.; Lischka, H.; Hättig, C. Excited-state intramolecular proton transfer: a survey of TDDFT and RI-CC2 excited-state potential energy surfaces. *J. Phys. Chem. A* **2005**, *109*, 3201–3208.

[41] Aquino, A. J.; Plasser, F.; Barbatti, M.; Lischka, H. Ultrafast excited-state proton transfer processes: energy surfaces and on-the-fly dynamics simulations. *Croat. Chem. Acta* **2009**, *82*, 105–114.

[42] Pozdnyakov, I. P.; Pigliucci, A.; Tkachenko, N.; Plyusnin, V. F.; Vauthey, E.; Lemmetyinen, H. The photophysics of salicylic acid derivatives in aqueous solution. *J. Phys. Org. Chem.* **2009**, *22*, 449–454.

[43] Raeker, T.; Hartke, B. Full-dimensional excited-state intramolecular proton transfer dynamics of salicylic acid. *J. Phys. Chem. A* **2017**, *121*, 5967–5977.

[44] Joshi, H.; Tripathi, H.; Pant, T.; Pant, D. Hydrogen-bonding effect on the dual emission of salicylic acid. *Chem. Phys. Lett.* **1990**, *173*, 83–86.

[45] Pant, D.; Joshi, H.; Bisht, P.; Tripathi, H. Dual emission and double proton transfer in salicylic acid. *Chem. Phys.* **1994**, *185*, 137–144.

[46] Denisov, G.; Golubev, N.; Schreiber, V.; Shajakhmedov, S. S.; Shurukhina, A. Excited state intramolecular proton transfer and dual emission of the cyclic homo- and heterodimers of 2-hydroxy and 2, 6-dihydroxy benzoic acids. *J. Mol. Struct.* **1996**, *381*, 73–81.

[47] Weller, A. Innermolekularer protonenübergang im angeregten zustand. *Z Elektrochem.* **1956**, *60*, 1144–1147.

[48] Weller, A. Fast reactions of excited molecules. *Prog. React. Kinet.* **1961**, *1*, 187.

[49] Bisht, P. B.; Petek, H.; Yoshihara, K.; Nagashima, U. Excited state enol-keto tautomerization in salicylic acid: A supersonic free jet study. *J. Chem. Phys.* **1995**, *103*, 5290–5307.

[50] Bisht, P. B.; Okamoto, M.; Hirayama, S. Effect of High Pressure on Enol- Keto Tautomerization in Salicylic Acid: A Study by Steady-State Absorption and Fluorescence Measurements. *J. Phys. Chem. B* **1997**, *101*, 8850–8855.

[51] Lahmani, F.; Zehnacker-Rentien, A. Effect of substitution on the photoinduced intramolecular proton transfer in salicylic acid. *J. Phys. Chem. A* **1997**, *101*, 6141–6147.

[52] Sobolewski, A. L.; Domcke, W. Ab initio study of excited-state intramolecular proton dislocation in salicylic acid. *Chem. Phys.* **1998**, *232*, 257–265.

[53] de Melo, J. S. S.; Rondão, R.; Burrows, H. D.; Melo, M. J.; Navaratnam, S.; Edge, R.; Voss, G. Spectral and photophysical studies of substituted indigo derivatives in their keto forms. *Chem. Phys. Chem.* **2006**, *7*, 2303–2311.

[54] Moreno, M.; Ortiz-Sánchez, J. M.; Gelabert, R.; Lluch, J. M. A theoretical study of the photochemistry of indigo in its neutral and dianionic (leucoindigo) forms. *Phys. Chem. Chem. Phys.* **2013**, *15*, 20236–20246.

[55] Yamazaki, S.; Sobolewski, A. L.; Domcke, W. Molecular mechanisms of the photostability of indigo. *Phys. Chem. Chem. Phys.* **2011**, *13*, 1618–1628.

[56] Cui, G.; Thiel, W. Nonadiabatic dynamics of a truncated indigo model. *Phys. Chem. Chem. Phys.* **2012**, *14*, 12378–12384.

[57] Iwakura, I.; Yabushita, A.; Kobayashi, T. Why is indigo photostable over extremely long periods? *Chem. Lett.* **2009**, *38*, 1020–1021.

[58] Pina, J.; Sarmento, D.; Accoto, M.; Gentili, P. L.; Vaccaro, L.; Galvao, A.; Seixas de Melo, J. S. Excited-state proton transfer in indigo. *J. Phys. Chem. B* **2017**, *121*, 2308–2318.

[59] Lan, Z. Photo-induced nonadiabatic dynamics of aromatic molecules via conical intersections: electronic-structure and time-dependent quantum dynamics calculations. Ph.D. thesis, Technical University of Munich, 2007.

[60] Zewail, A. H. *Femtochemistry: Ultrafast Dynamics of the Chemical Bond (World Scientific Series in 20th Century Chemistry)*; World Scientific, 1994.

[61] Manz, J., Wöste, L., Eds. *Femtosecond Chemistry*; Wiley, 1994.

[62] Hund, F. Zur deutung der molekelspektren. i. *Z. Physik* **1927**, *40*, 742–764.

[63] von Neuman, J.; Wigner, E. Uber merkwürdige diskrete Eigenwerte. Uber das Verhalten von Eigenwerten bei adiabatischen Prozessen. *Physik Z* **1929**, *30*, 467–470.

[64] Domcke, W.; Yarkony, D.; Köppel, H. *Conical intersections: electronic structure, dynamics & spectroscopy*; World Scientific, 2004; Vol. 15.

[65] Domcke, W.; Yarkony, D. R. Role of conical intersections in molecular spectroscopy and photoinduced chemical dynamics. *Ann. Rev. Phys. Chem.* **2012**, *63*, 325–352.

[66] Nevesely, T.; Wienhold, M.; Molloy, J. J.; Gilmour, R. Advances in the E→ Z isomerization of alkenes using small molecule photocatalysts. *Chem. Res.* **2021**, *122*, 2650–2694.

[67] Corpas, J.; Mauleón, P.; Gomez Arrayas, R.; Carretero, J. C. E/Z Photoisomerization of Olefins as an Emergent Strategy for the Control of Stereodivergence in Catalysis. *Adv. Synth. Catal.* **2022**, *364*, 1348–1370.

[68] Muriel, W. A.; Morales-Cueto, R.; Rodríguez-Córdoba, W. Unravelling the solvent polarity effect on the excited state intramolecular proton transfer mechanism of the 1-and 2-salicylideneanthrylamine. A TD-DFT case study. *Phys. Chem. Chem. Phys.* **2019**, *21*, 915–928.

[69] Avadanei, M.; Pina, J.; Serpa, C.; Tigoianu, R.; Cozan, V. Photochromic cycle of two N-salicylidene-pX-anilines revealed by the dynamics over 10 orders of magnitude. *J. Mol. Liq.* **2019**, *283*, 617–629.

[70] Li, S.; Han, G.; Zhang, W. Concise synthesis of photoresponsive polyureas containing bridged azobenzenes as visible-light-driven actuators and reversible photopatterning. *Macromolecules* **2018**, *51*, 4290–4297.

[71] Weis, P.; Wu, S. Light-switchable azobenzene-containing macromolecules: from UV to near infrared. *Macromol. Rapid Commun.* **2018**, *39*, 1700220.

[72] Bismuth, O.; Friedman, N.; Sheves, M.; Ruhman, S. Photochemistry of a retinal protonated schiff-base analogue mimicking the opsin shift of bacteriorhodopsin. *J. Phys. Chem. B* **2007**, *111*, 2327–2334.

[73] Wand, A.; Rozin, R.; Eliash, T.; Jung, K.-H.; Sheves, M.; Ruhman, S. Asymmetric toggling of a natural photoswitch: Ultrafast spectroscopy of Anabaena sensory rhodopsin. *J. Am. Chem. Soc.* **2011**, *133*, 20922–20932.

[74] Fregoni, J.; Granucci, G.; Coccia, E.; Persico, M.; Corni, S. Manipulating azobenzene photoisomerization through strong light–molecule coupling. *Nat. Commun.* **2018**, *9*, 4688.

[75] Castiglioni, F.; Danowski, W.; Perego, J.; Leung, F. K.-C.; Sozzani, P.; Bracco, S.; Wezenberg, S. J.; Comotti, A.; Feringa, B. L. Modulation of porosity in a solid material enabled by bulk photoisomerization of an overcrowded alkene. *Nat. Chem.* **2020**, *12*, 595–602.

[76] Baker, L. A.; Staniforth, M.; Flourat, A. L.; Allais, F.; Stavros, V. G. Gas-solution phase transient absorption study of the plant sunscreen derivative methyl sinapate. *Chem. Photo. Chem.* **2018**, *2*, 743–748.

[77] Abiola, T. T.; Whittock, A. L.; Stavros, V. G. Unravelling the photoprotective mechanisms of nature-inspired ultraviolet filters using ultrafast spectroscopy. *Molecules* **2020**, *25*, 3945.

[78] Kuramochi, H.; Takeuchi, S.; Yonezawa, K.; Kamikubo, H.; Kataoka, M.; Tahara, T. Probing the early stages of photoreception in photoactive yellow protein with ultrafast time-domain Raman spectroscopy. *Nat. Chem.* **2017**, *9*, 660–666.

[79] Kiefer, H. V.; Gruber, E.; Langeland, J.; Kusochek, P. A.; Bochenkova, A. V.; Andersen, L. H. Intrinsic photoisomerization dynamics of protonated Schiff-base retinal. *Nat. Commun.* **2019**, *10*, 1210.

[80] Kazaryan, A.; Lan, Z.; Schafer, L. V.; Thiel, W.; Filatov, M. Surface hopping excited-state dynamics study of the photoisomerization of a light-driven fluorene molecular rotary motor. *J. Chem. Theory Comput.* **2011**, *7*, 2189–2199.

[81] Conyard, J.; Addison, K.; Heisler, I. A.; Cnossen, A.; Browne, W. R.; Feringa, B. L.; Meech, S. R. Ultrafast dynamics in the power stroke of a molecular rotary motor. *Nat. Chem.* **2012**, *4*, 547–551.

[82] Levine, B. G.; Martínez, T. J. Isomerization through conical intersections. *Ann. Rev. Phys. Chem.* **2007**, *58*, 613–634.

[83] Dugave, C.; Demange, L. Cis- trans isomerization of organic molecules and biomolecules: implications and applications. *Chem. Rev.* **2003**, *103*, 2475–2532.

[84] Hampp, N.; Bräuchle, C.; Dürr, H.; Bouas-Laurent, H. Photochromism, Molecules and Systems. 1990.

[85] Durr, H.; Bouas-Laurent, H. *Photochromism: molecules and systems*; Elsevier, 2003.

[86] Bartocci, G.; Galiazzo, G.; Marri, E.; Mazzucato, U.; Spalletti, A. Role of adiabatic pathways in the photoisomerization of aromatic olefins. *Inorganica Chim. Acta* **2007**, *360*, 961–969.

[87] Horspool, W. M.; Lenci, F. *CRC Handbook of Organic Photochemistry and Photobiology, Volumes 1 & 2*; CRC press, 2003.

[88] Arai, T. *Organic Molecular Photochemistry*; CRC Press, 2020; pp 131–167.

[89] Rao, V. J. *Organic Molecular Photochemistry*; CRC Press, 2020; pp 169–209.

[90] Ramamurthy, V.; Schanze, K. S. *Organic molecular photochemistry*; CRC Press, 2020.

[91] Turro, N. J. *Modern molecular photochemistry*; University science books, 1991.

[92] Glover, W. J.; Mori, T.; Schuurman, M. S.; Boguslavskiy, A. E.; Schalk, O.; Stolow, A.; Martínez, T. J. Excited state non-adiabatic dynamics of the smallest polyene, trans 1, 3-butadiene. II. Ab initio multiple spawning simulations. *J. Chem. Phys.* **2018**, *148*, 164303.

[93] Liu, Y.; Xia, S.-H.; Zhang, Y. Photochemical and photophysical properties of cis-stilbene molecule by electronic structure calculations and nonadiabatic surface-hopping dynamics simulations. *Chem. Phys.* **2020**, *539*, 110957.

[94] Weir, H.; Williams, M.; Parrish, R. M.; Hohenstein, E. G.; Martínez, T. J. Nonadiabatic dynamics of photoexcited cis-stilbene using Ab initio multiple spawning. *J. Phys. Chem. B* **2020**, *124*, 5476–5487.

[95] Williams, M.; Forbes, R.; Weir, H.; Veyrinas, K.; MacDonell, R. J.; Boguslavskiy, A. E.; Schuurman, M. S.; Stolow, A.; Martinez, T. J. Unmasking the cis-stilbene phantom state via vacuum ultraviolet time-resolved photoelectron spectroscopy and ab initio multiple spawning. *J. Phys. Chem. Lett.* **2021**, *12*, 6363–6369.

[96] Nakatani, K.; Sato, H.; Fukuda, R. A catalyzed E/Z isomerization mechanism of stilbene using para-benzoquinone as a triplet sensitizer. *Phys. Chem. Chem. Phys.* **2022**, *24*, 1712–1721.

[97] Hammond, G. S.; Saltiel, J.; Lamola, A. A.; Turro, N. J.; Bradshaw, J. S.; Cowan, D. O.; Counsell, R. C.; Vogt, V.; Dalton, C. Mechanisms of photochemical reactions in solution. XXII. 1 Photochemical cis-trans isomerization. *J. Am. Chem. Soc.* **1964**, *86*, 3197–3217.

[98] Kovalenko, S.; Dobryakov, A.; Ioffe, I.; Ernsting, N. Evidence for the phantom state in photoinduced cis–trans isomerization of stilbene. *Chem. Phys. Lett.* **2010**, *493*, 255–258.

[99] Sajadi, M.; Dobryakov, A.; Garbin, E.; Ernsting, N.; Kovalenko, S. Time-resolved fluorescence spectra of cis-stilbene in hexane and acetonitrile. *Chem. Phys. Lett.* **2010**, *489*, 44–47.

[100] Fuß, W.; Kosmidis, C.; Schmid, W. E.; Trushin, S. A. The Photochemical cis–trans Isomerization of Free Stilbene Molecules Follows a Hula-Twist Pathway. *Angew. Chem. Int.* **2004**, *43*, 4178–4182.

[101] Bandara, H. D.; Burdette, S. C. Photoisomerization in different classes of azobenzene. *Chem. Soc. Rev.* **2012**, *41*, 1809–1825.

[102] Koch, M.; Saphiannikova, M.; Guskova, O. Cyclic Photoisomerization of Azobenzene in Atomistic Simulations: Modeling the Effect of Light on Columnar Aggregates of Azo Stars. *Molecules* **2021**, *26*, 7674.

[103] Airinei, A.; Isac, D. L.; Fifere, N.; Maftei, D.; Rusu, E. Computational and experimental investigation of photoresponsive behavior of 4, 4′-dihydroxyazobenzene diglycidyl ether. *Results in Chemistry* **2023**, *5*, 100709.

[104] Hartley, G. S. The cis-form of azobenzene. *Nature* **1937**, *140*, 281–281.

[105] Brown, C. t. A refinement of the crystal structure of azobenzene. *Acta. Crystallogr.* **1966**, *21*, 146–152.

[106] Crecca, C. R.; Roitberg, A. E. Theoretical study of the isomerization mechanism of azobenzene and disubstituted azobenzene derivatives. *J. Phys. Chem. A* **2006**, *110*, 8188–8203.

[107] Mostad, A.; Rømming, C.; Hammarström, S. Lousberg, RJJC, U. Weiss. *Acta Chem. Scand* **1971**, *25*, 3561–3568.

[108] Gagliardi, L.; Orlandi, G.; Bernardi, F.; Cembran, A.; Garavelli, M. A theoretical study of the lowest electronic states of azobenzene: the role of torsion coordinate in the cis–trans photoisomerization. *Theor. Chem. Acc.* **2004**, *111*, 363–372.

[109] Hamm, P.; Ohline, S.; Zinth, W. Vibrational cooling after ultrafast photoisomerization of azobenzene measured by femtosecond infrared spectroscopy. *J. Chem. Phys.* **1997**, *106*, 519–529.

[110] Lednev, I.; Ye, T.-Q.; Matousek, P.; Towrie, M.; Foggi, P.; Neuwahl, F.; Umapathy, S.; Hester, R.; Moore, J. N. Femtosecond time-resolved UV-visible absorption spectroscopy of trans-azobenzene: dependence on excitation wavelength. *Chem. Phys. Lett.* **1998**, *290*, 68–74.

[111] Rau, H.; Lueddecke, E. On the rotation-inversion controversy on photoisomerization of azobenzenes. Experimental proof of inversion. *J. Am. Chem. Soc.* **1982**, *104*, 1616–1620.

[112] Magee, J. L.; Shand Jr, W.; Eyring, H. Non-adiabatic reactions. Rotation about the double bond. *J. Am. Chem. Soc.* **1941**, *63*, 677–688.

[113] Curtin, D. Y.; Grubbs, E. J.; McCarty, C. G. Uncatalyzed syn-anti Isomerization of Imines, Oxime Ethers, and Haloimines1. *J. Am. Chem. Soc.* **1966**, *88*, 2775–2786.

[114] Szabo, A.; Ostlund, N. S. *Modern quantum chemistry: introduction to advanced electronic structure theory*; Courier Corporation, 2012.

[115] Møller, C.; Plesset, M. S. Note on an Approximation Treatment for Many-Electron Systems. *Phys. Rev.* **1934**, *46*, 618–622.

[116] Christiansen, O.; Koch, H.; Jørgensen, P. The second-order approximate coupled cluster singles and doubles model CC2. *Chem. Phys. Lett.* **1995**, *243*, 409–418.

[117] Roos, B. O.; Taylor, P. R.; Sigbahn, P. E. A complete active space SCF method (CASSCF) using a density matrix formulated super-CI approach. *Chem. Phys.* **1980**, *48*, 157–173.

[118] Andersson, K.; Malmqvist, P. A.; Roos, B. O.; Sadlej, A. J.; Wolinski, K. Second-order perturbation theory with a CASSCF reference function. *J. Phys. Chem.* **1990**, *94*, 5483–5488.

[119] Szabo, A.; Ostlund, N. S. *Modern quantum chemistry: introduction to advanced electronic structure theory*; Courier Corporation, 2012.

[120] Brillouin, L. Les problèmes de perturbations et les champs self-consistents. *J. phys. radium* **1932**, *3*, 373–389.

[121] Piela, L. *Ideas of quantum chemistry*; Elsevier, 2013.

[122] Grimme, S. Improved second-order Møller–Plesset perturbation theory by separate scaling of parallel-and antiparallel-spin pair correlation energies. *J. Chem. Phys.* **2003**, *118*, 9095–9102.

[123] Jung, Y.; Lochan, R. C.; Dutoi, A. D.; Head-Gordon, M. Scaled opposite-spin second order Møller–Plesset correlation energy: An economical electronic structure method. *J. Chem. Phys.* **2004**, *121*, 9793–9802.

[124] Hohenberg, P.; Kohn, W. Inhomogeneous Electron Gas. *Phys. Rev.* **1964**, *136*, B864–B871.

[125] Kohn, W.; Sham, L. J. Self-Consistent Equations Including Exchange and Correlation Effects. *Phys. Rev.* **1965**, *140*, A1133–A1138.

[126] Stephens, P. J.; Devlin, F. J.; Chabalowski, C. F.; Frisch, M. J. Ab Initio Calculation of Vibrational Absorption and Circular Dichroism Spectra Using Density Functional Force Fields. *J. Phys. Chem.* **1994**, *98*, 11623–11627.

[127] Becke, A. D. Density-functional exchange-energy approximation with correct asymptotic behavior. *Phys. Rev. A* **1988**, *38*, 3098–3100.

[128] Lee, C.; Yang, W.; Parr, R. G. Development of the Colle-Salvetti correlation-energy formula into a functional of the electron density. *Physical review B* **1988**, *37*, 785.

[129] Perdew, J. P.; Ernzerhof, M.; Burke, K. Rationale for mixing exact exchange with density functional approximations. *J. Chem. Phys.* **1996**, *105*, 9982–9985.

[130] Krukau, A. V.; Vydrov, O. A.; Izmaylov, A. F.; Scuseria, G. E. Influence of the exchange screening parameter on the performance of screened hybrid functionals. *J. Chem. Phys.* **2006**, *125*, 224106.

[131] Cohen, A. J.; Handy, N. C. Dynamic correlation. *Mol. Phys.* **2001**, *99*, 607–615.

[132] Levine, B. G.; Ko, C.; Quenneville, J.; MartÍnez, T. J. Conical intersections and double excitations in time-dependent density functional theory. *Mol. Phys.* **2006**, *104*, 1039–1051.

[133] Cai, Z.-L.; Sendt, K.; Reimers, J. R. Failure of density-functional theory and time-dependent density-functional theory for large extended π systems. *J. Chem. Phys.* **2002**, *117*, 5543–5549.

[134] Grimme, S.; Parac, M. Substantial Errors from Time-Dependent Density Functional Theory for the Calculation of Excited States of Large π Systems. *Chem. Phys. Chem.* **2003**, *4*, 292–295.

[135] Mewes, S. A.; Plasser, F.; Dreuw, A. Universal Exciton Size in Organic Polymers is Determined by Nonlocal Orbital Exchange in Time-Dependent Density Functional Theory. *J. Chem. Phys.* **2017**, *8*, 1205–1210.

[136] Dreuw, A.; Weisman, J. L.; Head-Gordon, M. Long-range charge-transfer excited states in time-dependent density functional theory require non-local exchange. *J. Chem. Phys.* **2003**, *119*, 2943–2946.

[137] Dreuw, A.; Head-Gordon, M. Failure of Time-Dependent Density Functional Theory for Long-Range Charge-Transfer Excited States: The Zincbacteriochlorin-Bacteriochlorin and Bacteriochlorophyll-Spheroidene Complexes. *J. Am. Chem. Soc.* **2004**, *126*, 4007–4016.

[138] Magyar, R. J.; Tretiak, S. Dependence of Spurious Charge-Transfer Excited States on Orbital Exchange in TDDFT: Large Molecules and Clusters. *J. Chem. Theory Comput.* **2007**, *3*, 976–987.

[139] Kümmel, S. Charge-Transfer Excitations: A Challenge for Time-Dependent Density Functional Theory That Has Been Met. *Adv. Ener. Mat.* **2017**, *7*, 1700440.

[140] Tawada, Y.; Tsuneda, T.; Yanagisawa, S.; Yanai, T.; Hirao, K. A long-range-corrected time-dependent density functional theory. *J. Chem. Phys.* **2004**, *120*, 8425–8433.

[141] Yanai, T.; Tew, D. P.; Handy, N. C. A new hybrid exchange–correlation functional using the Coulomb-attenuating method (CAM-B3LYP). *Chem. Phys. Lett.* **2004**, *393*, 51–57.

[142] Rohrdanz, M. A.; Martins, K. M.; Herbert, J. M. A long-range-corrected density functional that performs well for both ground-state properties and time-dependent density functional theory excitation energies, including charge-transfer excited states. *J. Chem. Phys.* **2009**, *130*, 054112.

[143] Henderson, T. M.; Izmaylov, A. F.; Scalmani, G.; Scuseria, G. E. Can short-range hybrids describe long-range-dependent properties? *J. Chem. Phys.* **2009**, *131*, 044108.

[144] Iikura, H.; Tsuneda, T.; Yanai, T.; Hirao, K. A long-range correction scheme for generalized-gradient-approximation exchange functionals. *J. Chem. Phys.* **2001**, *115*, 3540–3544.

[145] Peverati, R.; Truhlar, D. G. Improving the accuracy of hybrid meta-GGA density functionals by range separation. *J. Phys. Chem. Lett.* **2011**, *2*, 2810–2817.

[146] Chai, J.-D.; Head-Gordon, M. Systematic optimization of long-range corrected hybrid density functionals. *J. Chem. Phys.* **2008**, *128*, 084106.

[147] Santra, G.; Calinsky, R.; Martin, J. M. Benefits of Range-Separated Hybrid and Double-Hybrid Functionals for a Large and Diverse Data Set of Reaction Energies and Barrier Heights. *J. Phys. Chem. A* **2022**, *126*, 5492–5505.

[148] Vydrov, O. A.; Heyd, J.; Krukau, A. V.; Scuseria, G. E. Importance of short-range versus long-range Hartree-Fock exchange for the performance of hybrid density functionals. *J. Chem. Phys.* **2006**, *125*, 074106.

[149] Mardirossian, N.; Head-Gordon, M. ωB97X-V: A 10-parameter, range-separated hybrid, generalized gradient approximation density functional with nonlocal correlation, designed by a survival-of-the-fittest strategy. *Phys. Chem. Chem. Phys.* **2014**, *16*, 9904–9924.

[150] Runge, E.; Gross, E. K. U. Density-Functional Theory for Time-Dependent Systems. *Phys. Rev. Lett.* **1984**, *52*, 997–1000.

[151] Huix-Rotllant, M.; Ferré, N.; Barbatti, M. Time-dependent density functional theory. *Quantum Chemistry and Dynamics of Excited States: Methods and Applications* **2020**, 13–46.

[152] Ullrich, C. A. *Time-Dependent Density-Functional Theory: Concepts and Applications*; OUP Oxford, 2011.

[153] Schirmer, J. Beyond the random-phase approximation: A new approximation scheme for the polarization propagator. *Phys. Rev. A* **1982**, *26*, 2395–2416.

[154] Lischka, H.; Nachtigallova, D.; Aquino, A. J.; Szalay, P. G.; Plasser, F.; Machado, F. B.; Barbatti, M. Multireference approaches for excited states of molecules. *Chem. Rev.* **2018**, *118*, 7293–7361.

[155] Barbatti, M. Nonadiabatic dynamics with trajectory surface hopping method. *Wiley Interdiscip. Rev. Comput. Mol. Sci.* **2011**, *1*, 620–633.

[156] Tully, J. C.; Preston, R. K. Trajectory surface hopping approach to nonadiabatic molecular collisions: the reaction of H^+ with D2. *J. Chem. Phys.* **1971**, *55*, 562–572.

[157] Tully, J. C. Molecular dynamics with electronic transitions. *J. Chem. Phys.* **1990**, *93*, 1061–1071.

[158] Toniolo, A.; Ciminelli, C.; Persico, M.; Martínez, T. Simulation of the photodynamics of azobenzene on its first excited state: Comparison of full multiple spawning and surface hopping treatments. *The Journal of chemical physics* **2005**, *123*, 234308.

[159] Barbatti, M.; Granucci, G.; Persico, M.; Ruckenbauer, M.; Vazdar, M.; Eckert-Maksić, M.; Lischka, H. The on-the-fly surface-hopping program system Newton-X: Application to ab initio simulation of the nonadiabatic photodynamics of benchmark systems. *J. Photochem. Photobiol. A: Chem.* **2007**, *190*, 228–240.

[160] Wang, L.; Qiu, J.; Bai, X.; Xu, J. Surface hopping methods for nonadiabatic dynamics in extended systems. *Wiley Interdiscip. Rev. Comput. Mol. Sci.* **2020**, *10*, e1435.

[161] Granucci, G.; Persico, M.; Zoccante, A. Including quantum decoherence in surface hopping. *J. Chem. Phys.* **2010**, *133*, 134111.

[162] Zhu, C.; Jasper, A. W.; Truhlar, D. G. Non-Born–Oppenheimer trajectories with self-consistent decay of mixing. *J. Chem. Phys.* **2004**, *120*, 5543–5557.

[163] Shu, Y.; Zhang, L.; Mai, S.; Sun, S.; González, L.; Truhlar, D. G. Implementation of Coherent Switching with Decay of Mixing into the SHARC program. *J. Chem. Theory Comput.* **2020**, *16*, 3464–3475.

[164] Barbatti, M.; Aquino, A. J.; Lischka, H. The UV absorption of nucleobases: semi-classical ab initio spectra simulations. *Phys. Chem. Chem. Phys.* **2010**, *12*, 4959–4967.

[165] Mandal, S.; Rao, V. G.; Ghatak, C.; Pramanik, R.; Sarkar, S.; Sarkar, N. Photophysics and Photodynamics of 1′-Hydroxy-2′-acetonaphthone (HAN) in Micelles and Nonionic Surfactants Forming Vesicles: A Comparative Study of Different Microenvironments of Surfactant Assemblies. *J. Phys. Chem. B* **2011**, *115*, 12108–12119.

[166] Organero, J. A.; Martin, C.; Cohen, B.; Douhal, A. Chemical and Biological Caging Effects on the Relaxation of a Proton-Transfer Dye. *Langmuir* **2008**, *24*, 10352–10357.

[167] Douhal, A.; Lahmani, F.; Zehnacker-Rentien, A. Excited-state intramolecular proton transfer in jet-cooled 1-hydroxy-2-acetonaphthone. *Chem. Phys.* **1993**, *178*, 493–504.

[168] Douhal, A.; Lahmani, F.; Zewail, A. H. Proton-transfer reaction dynamics. *Chem. Phys.* **1996**, *207*, 477–498.

[169] Catalan, J.; del Valle, J. C. Toward the photostability mechanism of intramolecular hydrogen bond systems. The photophysics of 1-hydroxy-2-acetonaphthone. *J. Am. Chem. Soc.* **1993**, *115*, 4321–4325.

[170] Lu, C.; Hsieh, R.-M. R.; Lee, I.-R.; Cheng, P.-Y. Ultrafast dynamics of gas-phase excited-state intramolecular proton transfer in 1-hydroxy-2-acetonaphthone. *Chem. Phys. Lett.* **1999**, *310*, 103 – 110.

[171] Lochbrunner, S.; Szeghalmi, A.; Stock, K.; Schmitt, M. Ultrafast proton transfer of 1-hydroxy-2-acetonaphthone: Reaction path from resonance Raman and transient absorption studies. *J. Chem. Phys.* **2005**, *122*, 244315.

[172] Catalán, J.; de Paz, J. L. G. On the Inoperativeness of the ESIPT Process in the Emission of 1-Hydroxy-2-acetonaphthone: A Reappraisal. *J. Phys. Chem. A* **2008**, *112*, 904–914.

[173] Kim, J.; Heo, W.; Joo, T. Excited state intramolecular proton transfer dynamics of 1-hydroxy-2-acetonaphthone. *J. Phys. Chem. B* **2015**, *119*, 2620–2627.

[174] Szeghalmi, A. V.; Engel, V.; Zgierski, M. Z.; Popp, J.; Schmitt, M. The excited-state geometry of 1-hydroxy-2- acetonaphthone: a resonance Raman and quantum chemical study. *J. Raman Spectro.* **2006**, *37*, 148–160.

[175] Catalán, J.; Palomar, J.; Paz, J. D. Double- or single-well potential for GSIPT in 1-hydroxy-2-acetonaphthone? *Chem. Phys. Lett.* **1997**, *269*, 151–155.

[176] Organero, J. A.; García-Ochoa, I.; Moreno, M.; Lluch, J. M.; Santos, L.; Douhal, A. A theoretical insight into the internal H-bond and related rotational motion and proton transfer processes of 1-hydroxy-2-acetonaphthone in the S_0 state. *Chem. Phys. Lett.* **2000**, *328*, 83–89.

[177] Ortiz-Sánchez, J. M.; Gelabert, R.; Moreno, M.; Lluch, J. M. Electronic and quantum dynamical insight into the ultrafast proton transfer of 1-hydroxy-2-acetonaphthone. *J. Chem. Phys.* **2007**, *127*, 084318.

[178] Tobita, S.; Yamamoto, M.; Kurahayashi, N.; Tsukagoshi, R.; Nakamura, Y.; Shizuka, H. Effects of Electronic Structures on the Excited-State Intramolecular Proton Transfer of 1-Hydroxy-2-acetonaphthone and Related Compounds. *J. Phys. Chem. A* **1998**, *102*, 5206–5214.

[179] Yang, D.; Zheng, R.; Wang, Y.; Lv, J. Theoretical Confirmation of the Excited State Intramolecular Proton Transfer and Twisting Process of 1-hydroxy-2-acetonaphthone in Solution: A TDDFT Study. *Commun. Comput. Chem.* **2015**, *3*, 1–10.

[180] Ning, C.; Xiao, C.; Lu, R.; Zhou, P. Whether the excited state intramolecular proton transfer of 1-hydroxy-2-acetonaphthone will happen? *J. Lumin.* **2020**, *217*, 116825.

[181] Organero, J. A.; Moreno, M.; Santos, L.; Lluch, J. M.; Douhal, A. Photoinduced Proton Transfer and Rotational Motion of 1-Hydroxy-2-acetonaphthone in the S_1 State: A Theoretical Insight into Its Photophysics. *J. Phys. Chem. A* **2000**, *104*, 8424–8431.

[182] Trofimov, A. B.; Schirmer, J. An efficient polarization propagator approach to valence electron excitation spectra. *J. Phys. B: At., Mol. Opt. Phys.* **1995**, *28*, 2299–2324.

[183] Piteša, T.; Alešković, M.; Becker, K.; Basarić, N.; Došlić, N. Photoelimination of Nitrogen from Diazoalkanes: Involvement of Higher Excited Singlet States in the Carbene Formation. *J. Am. Chem. Soc.* **2020**, *142*, 9718–9724.

[184] Omidyan, R.; Abedini, F.; Shahrokh, L.; Azimi, G. Excited State Deactivation Mechanism in Protonated Uracil: New Insights from Theoretical Studies. *J. Phys. Chem. A* **2020**, *124*, 5089–5097.

[185] Dommett, M.; Crespo-Otero, R. Excited state proton transfer in 2′-hydroxychalcone derivatives. *Phys. Chem. Chem. Phys.* **2017**, *19*, 2409–2416.

[186] Daengngern, R.; Kungwan, N. Dynamics simulations of photoinduced proton transfer reactions of 2-(2′-hydroxyphenyl)benzoxazole in the gas phase and its hydrated clusters. *Chem. Phys. Lett.* **2014**, *609*, 147–154.

[187] Daengngern, R.; Kungwan, N.; Wolschann, P.; Aquino, A. J. A.; Lischka, H.; Barbatti, M. Excited-State Intermolecular Proton Transfer Reactions of 7-Azaindole(MeOH)n(n= 1–3) Clusters in the Gas phase: On-the-Fly Dynamics Simulation. *J. Phys. Chem. A* **2011**, *115*, 14129–14136.

[188] Plasser, F.; Crespo-Otero, R.; Pederzoli, M.; Pittner, J.; Lischka, H.; Barbatti, M. Surface hopping dynamics with correlated single-reference methods: 9H-adenine as a case study. *J. Chem. Theory Comput.* **2014**, *10*, 1395–1405.

[189] Hä, C.; Weigend, F. CC2 excitation energy calculations on large molecules using the resolution of the identity approximation. *J. Chem. Phys.* **2000**, *113*, 5154.

[190] Hättig, C. Geometry optimizations with the coupled-cluster model CC2 using the resolution-of-the-identity approximation. *J. Chem. Phys.* **2003**, *118*, 7751–7761.

[191] Hättig, C. *Response Theory and Molecular Properties (A Tribute to Jan Linderberg and Poul Jørgensen)*; Elsevier, 2005; pp 37–60.

[192] Hellweg, A.; Grün, S. A.; Hättig, C. Benchmarking the performance of spin-component scaled CC2 in ground and electronically excited states. *Physical Chemistry Chemical Physics* **2008**, *10*, 4119.

[193] Dunning, T. H. Gaussian basis sets for use in correlated molecular calculations. I. The atoms boron through neon and hydrogen. *J. Chem. Phys.* **1989**, *90*, 1007–1023.

[194] Kendall, R. A.; Dunning, T. H.; Harrison, R. J. Electron affinities of the first-row atoms revisited. Systematic basis sets and wave functions. *J. Chem. Phys.* **1992**, *96*, 6796–6806.

[195] Werner, H.-J.; Knowles, P. J.; Knizia, G.; Manby, F. R.; Schütz, M. Molpro: a general-purpose quantum chemistry program package. *WIREs Comput Mol Sci* **2012**, *2*, 242–253.

[196] TURBOMOLE V7.1 2016, a development of University of Karlsruhe and Forschungszentrum Karlsruhe GmbH, 1989-2007, TURBOMOLE GmbH, since 2007; available from `http://www.turbomole.com`.

[197] Barbatti, M.; Ruckenbauer, M.; Plasser, F.; Pittner, J.; Granucci, G.; Persico, M.; Lischka, H. Newton-X: a surface-hopping program for nonadiabatic molecular dynamics. *Wiley Interdisciplinary Reviews: Computational Molecular Science* **2013**, *4*, 26–33.

[198] NEWTON-X: A package for Newtonian dynamics close to the crossing seam. Version 2, 2016, www.newtonx.org.

[199] Shi, B.; Nachtigallová, D.; Aquino, A. J.; Machado, F. B.; Lischka, H. High-level theoretical benchmark investigations of the UV-vis absorption spectra of paradigmatic polycyclic aromatic hydrocarbons as models for graphene quantum dots. *J. Chem. Phys.* **2019**, *150*, 124302.

[200] Barboza, C. A.; Gawrys, P.; Banasiewicz, M.; Suwinska, K.; Sobolewski, A. L. Photophysical transformations induced by chemical substitution to salicylaldimines. *Phys. Chem. Chem. Phys.* **2020**, *22*, 6698–6705.

[201] Barboza, C. A.; Gawrys, P.; Banasiewicz, M.; Kozankiewicz, B.; Sobolewski, A. L. Substituent effects on the photophysical properties of tris (salicylideneanilines). *Phys. Chem. Chem. Phys.* **2021**, *23*, 1156–1164.

[202] Klamt, A.; Schüürmann, G. COSMO: a new approach to dielectric screening in solvents with explicit expressions for the screening energy and its gradient. *J. Chem. Soc., Perkin Trans. 2* **1993**, 799–805.

[203] Lunkenheimer, B.; Köhn, A. Solvent effects on electronically excited states using the conductor-like screening model and the second-order correlated method ADC (2). *J. Chem. Theory Comput.* **2013**, *9*, 977–994.

[204] Zhao, G.-J.; Han, K.-L. Hydrogen bonding in the electronic excited state. *Acc. Chem. Res.* **2012**, *45*, 404.

[205] Fery-Forgues, S. Fluorescent organic nanocrystals and non-doped nanoparticles for biological applications. *Nanoscale* **2013**, *5*, 8428–8442.

[206] Geng, J.; Li, K.; Ding, D.; Zhang, X.; Qin, W.; Liu, J.; Tang, B. Z.; Liu, B. Lipid-PEG-Folate Encapsulated Nanoparticles with Aggregation Induced Emission Characteristics: Cellular Uptake Mechanism and Two-Photon Fluorescence Imaging. *Small* **2012**, *8*, 3655–3663.

[207] Gierschner, J.; Varghese, S.; Park, S. Y. Organic single crystal lasers: A materials view. *Adv. Opt. Mater.* **2016**, *4*, 348–364.

[208] Li, X.; Xu, Y.; Li, F.; Ma, Y. Organic light-emitting diodes based on an ambipolar single crystal. *Org. Electron.* **2012**, *13*, 762–766.

[209] Karton-Lifshin, N.; Segal, E.; Omer, L.; Portnoy, M.; Satchi-Fainaro, R.; Shabat, D. A unique paradigm for a Turn-ON near-infrared cyanine-based probe: noninvasive intravital optical imaging of hydrogen peroxide. *J. Am. Chem. Soc.* **2011**, *133*, 10960–10965.

[210] Löwe, C.; Weder, C. Oligo (p-phenylene vinylene) excimers as molecular probes: deformation-induced color changes in photoluminescent polymer blends. *Advanced Materials* **2002**, *14*, 1625–1629.

[211] Kim, J.; Oh, J. H.; Kim, D. Recent advances in single-benzene-based fluorophores: physicochemical properties and applications. *Org. Biomol. Chem.* **2021**, *19*, 933–946.

[212] Göbel, D.; Duvinage, D.; Stauch, T.; Nachtsheim, B. J. Nitrile-Substituted 2-(oxazolinyl)-phenols: minimalistic excited-state intramolecular proton transfer (ESIPT)-based fluorophores. *J. Mater. Chem. C* **2020**, *8*, 9213–9225.

[213] Gai-Mei, L.; Wei-Jia, M.; Yan, W.; Yan, Y.; Xin-Jian, S. Computational Insights into the Excited State Intramolecular Proton Transfer Reactions in Ortho-hydroxylated Oxazolines. *Chinese J. Struct. Chem.* **2021**, *40*, 540–548.

[214] Li, Q.; Wan, Y.; Zhou, Q.; Li, Y.; Li, B.; Zhu, L.; Wan, Y.; Yin, H.; Shi, Y. Exploring the effect of nitrile substituent position on fluorescence quantum yield of ESIPT-based oxazoline derivatives: A TDDFT investigation. *Spectrochim. Acta - A: Mol. Biomol. Spectrosc.* **2022**, *272*, 120953.

[215] Cances, E.; Mennucci, B.; Tomasi, J. A new integral equation formalism for the polarizable continuum model: Theoretical background and applications to isotropic and anisotropic dielectrics. *J. Chem. Phys.* **1997**, *107*, 3032–3041.

[216] Barboza, C. A.; Morawski, O.; Olas, J.; Gawrys, P.; Banasiewicz, M.; Suwinska, K.; Shova, S.; Kozankiewicz, B.; Sobolewski, A. L. Unravelling the ambiguity of the emission pattern of donor-acceptor salicylaldimines. *J. Mol. Liq.* **2021**, *343*, 117532.

[217] Mawa, I.; Panda, A. N. Insights into the Excited-State Processes in 1-Hydroxy-2-acetonaphthone at ADC (2) and CASSCF Levels. *J. Phys. Chem. A* **2021**, *125*, 3015–3024.

[218] Ehrmaier, J.; Huang, X.; Rabe, E. J.; Corp, K. L.; Schlenker, C. W.; Sobolewski, A. L.; Domcke, W. Molecular Design of Heptazine-Based Photocatalysts: Effect of Substituents on Photocatalytic Efficiency and Photostability. *J. Phys. Chem. A* **2020**, *124*, 3698–3710.

[219] Iravani, M.; Omidyan, R. Photochromism of 2-(2-Hydroxyphenyl) Benzothiazole (HBT) and Its Derivatives: A Theoretical Study. *J. Phys. Chem. A* **2018**, *122*, 3182–3189.

[220] Hättig, C.; Weigend, F. CC2 excitation energy calculations on large molecules using the resolution of the identity approximation. *J. Chem. Phys.* **2000**, *113*, 5154.

[221] Frisch, M. J. et al. Gaussian16 Revision C.01. 2016; Gaussian Inc. Wallingford CT.

[222] Neese, F.; Wennmohs, F.; Becker, U.; Riplinger, C. The ORCA quantum chemistry program package. *J. Chem. Phys.* **2020**, *152*, 224108.

[223] Plasser, F. TheoDORE: A toolbox for a detailed and automated analysis of electronic excited state computations. *J. Chem. Phys.* **2020**, *152*, 084108.

[224] Plasser, F.; Wormit, M.; Dreuw, A. New tools for the systematic analysis and visualization of electronic excitations. I. Formalism. *J. Chem. Phys.* **2014**, *141*, 024106.

[225] Plasser, F.; Thomitzni, B.; Bäppler, S. A.; Wenzel, J.; Rehn, D. R.; Wormit, M.; Dreuw, A. Statistical analysis of electronic excitation processes: Spatial location, compactness, charge transfer, and electron-hole correlation. *J. Comput. Chem.* **2015**, *36*, 1609–1620.

[226] Verlet, L. Computer Experiments on Classical Fluids. I. Thermodynamical Properties of Lennard-Jones Molecules. *Phys. Rev.* **1967**, *159*, 98–103.

[227] Swope, W. C.; Andersen, H. C.; Berens, P. H.; Wilson, K. R. A computer simulation method for the calculation of equilibrium constants for the formation of physical clusters of molecules: Application to small water clusters. *J. Chem. Phys.* **1982**, *76*, 637–649.

[228] Forés, M.; Duran, M.; Solà, M.; Adamowicz, L. Excited-State Intramolecular Proton Transfer and Rotamerism of 2-(2'-hydroxyvinyl) benzimidazole and 2-(2'-hydroxyphenyl) imidazole. *J. Phys. Chem. A* **1999**, *103*, 4413–4420.

[229] Becke, A. D. Density-functional thermochemistry. III. The role of exact exchange. *J. Chem. Phys.* **1993**, *98*, 5648–5652.

[230] Adamo, C.; Barone, V. Toward reliable density functional methods without adjustable parameters: The PBE0 model. *J. Chem. Phys.* **1999**, *110*, 6158–6170.

[231] Zhao, Y.; Truhlar, D. G. The M06 suite of density functionals for main group thermochemistry, thermochemical kinetics, noncovalent interactions, excited states, and transition elements: two new functionals and systematic testing of four M06-class functionals and 12 other functionals. *Theor. Chem. Acc.* **2008**, *120*, 215–241.

[232] Weigend, F.; Ahlrichs, R. Balanced basis sets of split valence, triple zeta valence and quadruple zeta valence quality for H to Rn: Design and assessment of accuracy. *Phys. Chem. Chem. Phys.* **2005**, *7*, 3297–3305.

[233] Chaiwongwattana, S.; Sapunar, M.; Ponzi, A.; Decleva, P.; Došlić, N. Exploration of excited state deactivation pathways of adenine monohydrates. *J. Phys. Chem. A* **2015**, *119*, 10637–10644.

[234] Zhao, L.; Liu, J.; Zhou, P. New insight into the photoisomerization process of the salicylidene methylamine under vacuum. *J. Phys. Chem. A* **2016**, *120*, 7419–7426.

[235] Irie, M. Photochromism: memories and switches introduction. *Chem. Res.* **2000**, *100*, 1683–1684.

[236] Saltiel, J. Perdeuteriostilbene. The triplet and singlet paths for stilbene photoisomerization. *J. Am. Chem. Soc.* **1968**, *90*, 6394–6400.

[237] Liu, R. S.; Mead, D.; Asato, A. E. Photochemistry of polyenes. 23. Application of the HT-n mechanism of photoisomerization to the photocycles of bacteriorhodopsin. A model study. *J. Am. Chem. Soc.* **1985**, *107*, 6609–6614.

[238] Liu, R. S.; Hammond, G. S. The case of medium-dependent dual mechanisms for photoisomerization: one-bond-flip and hula-twist. *Proc. Natl. Acad. Sci. USA* **2000**, *97*, 11153–11158.

[239] Liu, R.; Asato, A. E. The primary process of vision and the structure of bathorhodopsin: a mechanism for photoisomerization of polyenes. *Proc. Natl. Acad. Sci. USA* **1985**, *82*, 259–263.

[240] Wei-Guang Diau, E. A new trans-to-cis photoisomerization mechanism of azobenzene on the S_1 (n, π^*) surface. *J. Phys. Chem. A* **2004**, *108*, 950–956.

[241] Takeuchi, S.; Ruhman, S.; Tsuneda, T.; Chiba, M.; Taketsugu, T.; Tahara, T. Spectroscopic tracking of structural evolution in ultrafast stilbene photoisomerization. *Science* **2008**, *322*, 1073–1077.

[242] Kihara, Y.; Tani, S.; Higashi, Y.; Teramoto, T.; Nagasawa, Y. Ultrafast Excited State Dynamics of Forward and Reverse trans-cis Photoisomerization of Red-Light-Absorbing Indigo Derivatives. *J. Phys. Chem. B* **2022**, *126*, 3539–3550.

[243] Harabuchi, Y.; Keipert, K.; Zahariev, F.; Taketsugu, T.; Gordon, M. S. Dynamics simulations with spin-flip time-dependent density functional theory: Photoisomerization and photocyclization mechanisms of cis-stilbene in $\pi\pi^*$ states. *J. Phys. Chem. A* **2014**, *118*, 11987–11998.

[244] Taketsugu, T.; Harabuchi, Y. Ab initio molecular dynamics study on photoisomerization reactions: applications to azobenzene and stilbene. *Frontiers of Quantum Chemistry* **2018**, 431–453.

[245] Nakamura, T.; Takeuchi, S.; Taketsugu, T.; Tahara, T. Femtosecond fluorescence study of the reaction pathways and nature of the reactive S 1 state of cis-stilbene. *Phys. Chem. Chem. Phys.* **2012**, *14*, 6225–6232.

[246] Han, J.; Zheng, Q.; Jin, C.; Wang, S.; Liu, Y.; Zhao, Y.; Zhu, J. Comparative Study on Properties, Structural Changes, and Isomerization of Cis/Trans-Stilbene under High Pressure. *J. Phys. Chem. C* **2022**, *126*, 16859–16866.

[247] Minezawa, N.; Gordon, M. S. Photoisomerization of stilbene: A spin-flip density functional theory approach. *J. Phys. Chem. A* **2011**, *115*, 7901–7911.

[248] Wang, C.; Waters, M. D.; Zhang, P.; Suchan, J.; Svoboda, V.; Luu, T. T.; Perry, C.; Yin, Z.; Slavíček, P.; Wörner, H. J. Different timescales during ultrafast stilbene isomerization in the gas and liquid phases revealed using time-resolved photoelectron spectroscopy. *Nat. Chem.* **2022**, *14*, 1126–1132.

[249] Quick, M.; Dobryakov, A.; Ioffe, I.; Berndt, F.; Mahrwald, R.; Ernsting, N.; Kovalenko, S. Rotamer-specific photoisomerization of difluorostilbenes from transient absorption and transient Raman spectroscopy. *J. Phys. Chem. B* **2018**, *122*, 1049–1059.

[250] Tsutsumi, T.; Harabuchi, Y.; Yamamoto, R.; Maeda, S.; Taketsugu, T. On-the-fly molecular dynamics study of the excited-state branching reaction of α-methyl-cis-stilbene. *Chem. Phys.* **2018**, *515*, 564–571.

[251] Krishnan, S. B.; Clark, R. J.; Lin, X.; Dmitrenko, O.; Hilinski, E. F.; Kuhn, L. R.; Alabugin, I. V.; Saltiel, J. α-Methylstilbene Isomers: Relationship of Structure to Photophysics and Photochemistry. *J. Phys. Chem. A* **2022**, *126*, 8976–8987.

[252] Mlakić, M.; Mandić, L.; Basarić, N.; Mihaljević, B.; Pavošević, F.; Škorić, I. Substituents affect the mechanism of photochemical EZ isomerization of diarylethene triazoles via adiabatic singlet excited state pathway or via triplet excited state. *J. Photochem. Photobiol. A: Chem.* **2022**, *422*, 113567.

[253] Asano, Y.; Murakami, A.; Kobayashi, T.; Goldberg, A.; Guillaumont, D.; Yabushita, S.; Irie, M.; Nakamura, S. Theoretical study on the photochromic cycloreversion reactions of dithienylethenes; on the role of the conical intersections. *J. Am. Chem. Soc.* **2004**, *126*, 12112–12120.

[254] Guillaumont, D.; Kobayashi, T.; Kanda, K.; Miyasaka, H.; Uchida, K.; Kobatake, S.; Shibata, K.; Nakamura, S.; Irie, M. An ab Initio MO Study of the

Photochromic Reaction of Dithienylethenes. *J. Phys. Chem. A* **2002**, *106*, 7222–7227.

[255] Salazar, E.; Reinink, S.; Faraji, S. Providing theoretical insight into the role of symmetry in the photoisomerization mechanism of a non-symmetric dithienylethene photoswitch. *Phys. Chem. Chem. Phys.* **2022**, *24*, 11592–11602.

[256] Sudarkova, S. M.; Ioffe, I. N. E/Z photoisomerization pathway in pristine and fluorinated di (3-furyl) ethenes. *Phys. Chem. Chem. Phys.* **2022**, *24*, 23749–23757.

[257] Mahato, B.; Panda, A. N. Effects of Heterocyclic Ring Fusion and Chain Elongation on Chiroptical Properties of Polyaza [9] helicene: A Computational Study. *J. Phys. Chem. A* **2022**, *126*, 1412–1421.

[258] Dreuw, A.; Wormit, M. The algebraic diagrammatic construction scheme for the polarization propagator for the calculation of excited states. *WIREs Comput Mol Sci* **2015**, *5*, 82–95.

[259] Bohnwagner, M. V.; Burghardt, I.; Dreuw, A. Regular and red-shifted fluorescence of the donor–acceptor compound 5-(1 H-pyrrole-1-yl) thiophenecarbonitrile (TCN) is efficiently quenched by internal modes of thiophene. *Phys. Chem. Chem. Phys.* **2017**, *19*, 13951–13959.

[260] Mawa, I.; Panda, A. N. Excited state processes in nitrile-substituted 2-(oxazolinyl)-phenols in gas and implicit solvents: A computational study. *Chem. Phys. Lett.* **2022**, *806*, 139969.

[261] Tajti, A.; Tulipan, L.; Szalay, P. G. Accuracy of spin-component scaled ADC (2) excitation energies and potential energy surfaces. *J. Chem. Theory Comput.* **2019**, *16*, 468–474.

[262] Steinmetzer, J.; Kupfer, S.; Gräfe, S. pysisyphus: Exploring potential energy surfaces in ground and excited states. *Int. J. Quantum Chem.* **2021**, *121*, e26390.

[263] Bearpark, M. J.; Robb, M. A.; Schlegel, H. B. A direct method for the location of the lowest energy point on a potential surface crossing. *Chem. Phys. Lett.* **1994**, *223*, 269–274.

[264] Fdez. Galván, I.; Vacher, M.; Alavi, A.; Angeli, C.; Aquilante, F.; Autschbach, J.; Bao, J. J.; Bokarev, S. I.; Bogdanov, N. A.; Carlson, R. K., et al. OpenMolcas: From source code to insight. *J. Chem. Theory Comput.* **2019**, *15*, 5925–5964.

[265] Han, W.-G.; Lovell, T.; Liu, T.; Noodleman, L. Density functional studies of the ground-and excited-state potential-energy curves of stilbene cis–trans isomerization. *Comput. Phys. Comm.* **2002**, *3*, 167–178.

[266] Taniguchi, M.; Lindsey, J. S. Database of absorption and fluorescence spectra of > 300 common compounds for use in photochemCAD. *Photochem. Photobiol.* **2018**, *94*, 290–327.

[267] Ioffe, I.; Granovsky, A. Photoisomerization of stilbene: The detailed XMCQDPT2 treatment. *J. Chem. Theory Comput.* **2013**, *9*, 4973–4990.

[268] Cembran, A.; Bernardi, F.; Garavelli, M.; Gagliardi, L.; Orlandi, G. On the mechanism of the cis- trans isomerization in the lowest electronic states of azobenzene: S_0, S_1, and T_1. *J. Am. Chem. Soc.* **2004**, *126*, 3234–3243.

[269] Beveridge, D. L.; Jaffe, H. The Electronic Structure and Spectra of cis-and trans-Stibene1. *J. Am. Chem. Soc.* **1965**, *87*, 5340–5346.

[270] Quenneville, J.; Martinez, T. J. Ab initio study of cis- trans photoisomerization in stilbene and ethylene. *J. Phys. Chem. A* **2003**, *107*, 829–837.

[271] Harabuchi, Y.; Yamamoto, R.; Maeda, S.; Takeuchi, S.; Tahara, T.; Taketsugu, T. Ab initio molecular dynamics study of the photoreaction of 1, 1′-dimethylstilbene upon $S_0 \rightarrow S_1$ excitation. *J. Phys. Chem. A* **2016**, *120*, 8804–8812.

[272] Karsili, T. N.; Marchetti, B.; Ashfold, M. N.; Domcke, W. Ab initio study of potential ultrafast internal conversion routes in oxybenzone, caffeic acid, and ferulic acid: Implications for sunscreens. *J. Phys. Chem. A* **2014**, *118*, 11999–12010.

[273] Wang, Y.-T.; Liu, X.-Y.; Cui, G.; Fang, W.-H.; Thiel, W. Photoisomerization of Arylazopyrazole Photoswitches: Stereospecific Excited-State Relaxation. *Angew. Chem. Int.* **2016**, *128*, 14215–14219.

[274] Kochman, M. A.; Durbeej, B. Theoretical Study of Ground-and Excited-State Charge Transfer in Fulvene-Based Donor–Acceptor Systems. *J. Phys. Chem. A* **2019**, *123*, 6660–6673.

[275] Gao, A.; Wang, M. Ultrafast Photoisomerization of N-(2-Methoxybenzylidene) aniline: Nonadiabatic Surface-Hopping Study. *J. Phys. Chem. A* **2021**, *125*, 7151–7160.

[276] Winslow, M.; Cross, W. B.; Robinson, D. Comparison of Spin-Flip TDDFT-Based Conical Intersection Approaches with XMS-CASPT2. *J. Chem. Theory Comput.* **2020**, *16*, 3253–3263.

[277] Su, Q.; Li, Y.; Wang, B.; Liu, M.; Wang, H.; Wang, W.; Liu, F. Combining the advantages of alkene and azo E–Z photoisomerizations: mechanistic insights into ketoimine photoswitches. *J. Phys. Chem. A* **2017**, *121*, 2588–2596.

[278] Pang, J.; Deng, Z.; Sun, S.; Huang, G.; Zhang, G.; Islam, A.; Dang, L.; Phillips, D. L.; Li, M.-D. Unprecedentedly Ultrafast Dynamics of Excited States of C=C Photoswitching Molecules in Nanocrystals and Microcrystals. *J. Phys. Chem. Lett.* **2020**, *12*, 41–48.

[279] Zhao, J.; Wang, X.; Liu, Z.; Zhang, Y.; Gan, L. Theoretical study of the cis–trans isomerization mechanism of azobenzene containing carboxy groups. *Comp. Theo. Chem.* **2022**, *1217*, 113901.

[280] Schnack-Petersen, A. K.; Pápai, M.; Møller, K. B. Azobenzene photoisomerization dynamics: Revealing the key degrees of freedom and the long timescale of the trans-to-cis process. *J. Photochem. Photobiol. A: Chem.* **2022**, *428*, 113869.

[281] Nenov, A.; Cordes, T.; Herzog, T. T.; Zinth, W.; de Vivie-Riedle, R. Molecular driving forces for Z/E isomerization mediated by heteroatoms: the example hemithioindigo. *J. Phys. Chem. A* **2010**, *114*, 13016–13030.

Appendices

Appendix A

TABLE A1: Cartesian coordinates of enol conformers in the S_0 state optimized with RI-MP2/cc-pVDZ.

Atom	x	y	z	Atom	x	y	z
	E-a				**E-OH**		
C	-3.8488117	-2.2897211	0.0035615	C	0.8570834	-3.6805070	-0.7356338
C	-2.4602153	-2.2935771	0.0001988	C	0.8281949	-2.8880772	0.4019270
C	-1.7236406	-1.0669313	-0.0017044	C	0.7059490	-1.4637153	0.3083837
C	-2.4459276	0.1662890	-0.0001383	C	0.5905532	-0.8561195	-0.9848145
C	-3.8763808	0.1536218	0.0033205	C	0.6529174	-1.6973315	-2.1463188
C	-4.5621536	-1.0538788	0.0051348	C	0.7781427	-3.0740197	-2.0251047
H	0.2636349	-1.9950707	-0.0064095	H	0.7983356	-1.0964707	2.4637728
H	-4.4004312	-3.2375524	0.0049729	H	0.9530108	-4.7691729	-0.6488829
H	-1.9081372	-3.2418814	-0.0011907	H	0.9051249	-3.3434807	1.3972610
C	-0.2855022	-1.0460683	-0.0051165	C	0.7033664	-0.6335780	1.4743880
C	-1.7148061	1.4129934	-0.0020164	C	0.4445453	0.5789332	-1.0833388
H	-4.4139012	1.1063766	0.0046815	H	0.6389343	-1.2633416	-3.1537611
H	-5.6586309	-1.0599924	0.0077897	H	0.8307002	-3.6973467	-2.9254577
C	-0.3069201	1.4148543	-0.0053580	C	0.4624446	1.3778518	0.0681112
C	0.3925786	0.1544389	-0.0068894	C	0.5925319	0.7381426	1.3470431
H	1.4873912	0.1497044	-0.0095156	H	0.6034289	1.3565705	2.2502564
O	-2.4538489	2.5394687	-0.0002874	O	0.2708666	1.1681559	-2.3037954
H	-1.7991159	3.2794241	-0.0018851	H	-0.0257068	0.4791089	-2.9145237
C	0.4200658	2.7127680	-0.0073387	C	0.3385238	2.8831595	-0.0137205
C	1.9425899	2.7147786	-0.0110182	C	-0.1863649	3.6108721	1.2271881
H	2.3335550	2.1944299	0.8809834	H	-1.0878507	3.1203874	1.6341563
H	2.3295395	2.1933784	-0.9041295	H	0.5822692	3.6228445	2.0215975
H	2.2913344	3.7584101	-0.0123696	H	0.5822692	3.6228445	2.0215975
O	-0.1859969	3.7950912	-0.0058870	O	0.6466122	3.5097287	-1.0174803
Atom	x	y	z	Atom	x	y	z
	E-CO				**E-b**		
C	1.0541339	-0.8132321	-3.6574557	C	0.2383733	-3.7709251	0.0156165
C	1.7981695	-0.8586748	-2.4861588	C	1.2514001	-2.8225307	0.0320203
C	1.2295963	-0.4479269	-1.2396362	C	0.9535275	-1.4226875	0.0241765
C	-0.1225125	0.0129751	-1.2142636	C	-0.4156081	-1.0015498	0.0204481
C	-0.8754232	0.0530539	-2.4317764	C	-1.4431515	-2.0010689	-0.0277917
C	-0.2952655	-0.352555	-3.6267989	C	-1.1242007	-3.3526073	-0.0250903
H	3.0169926	-0.8391547	-0.0307321	H	3.0380287	-0.7536753	0.0002685
H	1.5018273	-1.130928	-4.6067615	H	0.481738	-4.8398743	0.0203463
H	2.8369464	-1.2117637	-2.5008855	H	2.3031593	-3.1347639	0.0452764
C	1.9789928	-0.4857353	-0.0141471	C	1.9898711	-0.4312789	0.0049388
C	-0.708991	0.4316514	0.0409501	C	-0.7177506	0.4128754	0.0446743
H	-1.909937	0.4060949	-2.4082919	H	-2.4998904	-1.7162425	-0.1045954
H	-0.8790146	-0.3185857	-4.5544475	H	-1.9241556	-4.1010476	-0.0681501
C	0.0340131	0.3897804	1.2283024	C	0.3036587	1.3654736	0.0090389
C	1.3970575	-0.081959	1.1655384	C	1.667224	0.9088558	-0.0193842
H	1.9567119	-0.1059779	2.1047891	H	2.4471698	1.6752914	-0.0435011
O	-2.0092669	0.848484	-0.0849501	O	-2.0307741	0.8222854	0.0834123
H	-2.3455343	1.1103335	0.7790649	H	-2.552893	0.0917144	0.4427697
C	-0.4412317	0.7932413	2.6048624	C	0.1108631	2.8717575	0.0131374
C	-1.8622796	1.3182772	2.8277546	C	-1.2821309	3.4864514	0.0453459
H	-2.0410456	2.2417419	2.2448716	H	-1.8806612	3.1465638	-0.8157853
H	-2.615249	0.5565617	2.5492338	H	-1.8219929	3.1750229	0.95474
H	-1.9810727	1.5511612	3.8964705	H	-1.1677866	4.5814611	0.0248381
O	0.3120291	0.7048738	3.5679706	O	1.100566	3.5962802	-0.011684

TABLE A2: Cartesian coordinates of keto conformers in the S_0 state optimized at RI-MP2/cc-pVDZ.

Atom	x	y	z	Atom	x	y	z
	K-a				**K-OH**		
C	-3.859586	-2.3521613	0.0035489	C	-0.3151592	-1.0799158	-0.0939885
C	-2.4936818	-2.3496687	0.0001689	C	-1.7304582	-1.0762608	-0.0522871
C	-1.7430293	-1.0953041	-0.001447	C	-2.4161773	0.1633008	0.0212837
C	-2.4327792	0.1490306	0.0005315	C	-1.6855019	1.3712898	0.0521752
C	-3.918131	0.1821881	0.0042134	C	-0.2844617	1.3539198	0.0100116
C	-4.620815	-1.1065053	0.0056442	C	0.4037882	0.1229736	-0.0633087
C	-1.7099589	1.367128	-0.0009652	C	-3.9229895	0.2307462	0.0694277
C	-0.3122915	1.3552338	-0.0044842	C	-4.6555368	-1.0866101	0.0286273
C	0.3840857	0.1222145	-0.0065468	C	-3.8630568	-2.3245469	-0.0458558
C	-0.3230894	-1.0840856	-0.0050342	C	-2.5012112	-2.3224782	-0.0833554
O	-4.5322131	1.2812572	0.0059779	O	-4.486646	1.3213795	0.137313
C	-6.0190477	-1.0871098	0.0090704	C	-6.0344841	-1.1283094	0.0598947
O	-6.6978564	0.045217	0.0110198	C	-6.8902724	-2.3767482	0.0223514
C	-6.8846808	-2.3259065	0.01096	O	-6.7538558	0.021921	0.1320113
H	-1.9356664	-3.2935845	-0.0013566	H	-1.9545846	-3.2720408	-0.13824
H	1.4808186	0.1122971	-0.0093283	H	1.4999845	0.1063663	-0.0962835
H	0.2180276	-2.0387692	-0.0066141	H	0.2170595	-2.0381369	-0.1508059
H	-2.2713914	2.3069471	0.000709	H	-2.240628	2.3131014	0.109449
H	0.2456484	2.299065	-0.0056461	H	0.2770969	2.2955257	0.0340705
H	-4.399541	-3.3057511	0.0046998	H	-4.3768977	-3.2898431	-0.0711334
H	-6.6848949	-2.9424964	-0.8823492	H	-6.3192133	-3.3099889	-0.0496685
H	-6.6806432	-2.9427334	0.9031462	H	-7.5113399	-2.4208977	0.9378007
H	-7.9433498	-2.025423	0.0135261	H	-7.573543	-2.3229897	-0.8471482
H	-5.9838888	0.7718247	0.0094034	H	-7.6911576	-0.2227566	0.140307

Atom	x	y	z	Atom	x	y	z
	K-CO				**K-b**		
C	1.2449501	0.0010132	3.5548005	C	-3.219003	-2.7377327	-0.8974453
C	1.2410455	0.0005779	2.138435	C	-2.5016084	-2.2865098	0.2187174
C	2.4792305	-0.0002226	1.4443675	C	-1.7613332	-1.0801928	0.1651229
C	3.6925494	-0.000848	2.1678719	C	-1.7565213	-0.331455	-1.041752
C	3.6814757	-0.0008079	3.569069	C	-2.4815651	-0.7918997	-2.1632728
C	2.4524467	0.0001668	4.2656111	C	-3.2091182	-1.987391	-2.0941117
C	2.5366674	-0.0011296	-0.0600683	H	-1.0255569	-1.192595	2.2453697
C	1.2239372	-0.0003487	-0.7777818	H	-3.7878353	-3.6737409	-0.8399729
C	-0.0133393	0.0017962	0.0159915	H	-2.5082579	-2.8689242	1.1488931
C	-0.0116862	0.0023766	1.3787327	C	-1.0055066	-0.5953941	1.3252931
O	3.6280545	-0.0038196	-0.6367422	C	-0.9882124	0.9563049	-1.1568838
C	1.1959492	-0.0021004	-2.1615226	H	-2.4581327	-0.192364	-3.0790403
C	2.3892899	0.0038206	-3.0828356	H	-3.7703314	-2.3404725	-2.9674926
O	0.0438077	-0.0099475	-2.8800432	C	-0.2426649	1.3895802	0.0618243
H	-0.9589997	0.0054211	1.9314783	C	-0.2927068	0.5642855	1.276332
H	2.4416122	0.0004587	5.3622656	H	0.2635957	0.9070476	2.1538796
H	0.2888737	0.0022741	4.0936772	O	-0.994371	1.5956334	-2.2146868
H	4.632465	-0.0019489	1.606621	H	1.6117562	3.730553	1.0368197
H	4.626455	-0.0013142	4.1252551	C	0.4895186	2.5574617	0.0502154
H	-0.9918519	0.0062893	-0.4837032	C	0.6348505	3.50567	-1.1181711
H	-0.7090419	-0.0195354	-2.2706992	H	1.0690024	2.9902478	-1.9896824
H	3.0271868	0.8808813	-2.8898528	H	-0.3482993	3.8838277	-1.4407931
H	3.0205938	-0.8821108	-2.9080104	H	1.2809072	4.3592354	-0.8395639
H	2.0289418	0.0150366	-4.1236021	O	1.1476246	2.897082	1.1957022

TABLE A3: Summary of selected bond lengths(Å), bond angle(in degree) of the optimized structures of **E-a** and **K-a** in the S_0 and S_1 states calculated at RI-SOS-MP2 and RI-SOS-ADC(2) levels with cc-pVDZ basis set.

Structures	H_1-O_2	O_2-C_3	C_3-C_4	C_4-C_5	C_5-O_6	O_6-H_1	O_2-O_6	$\angle O_2$-H_1-O_6
E-a	0.99	1.35	1.41	1.49	1.24	1.69	2.59	149.2
K-a	1.54	1.26	1.47	1.4	1.32	1.02	2.49	153.8
E-a*	1.07	1.32	1.48	1.45	1.28	1.42	2.45	159.3
K-a*	1.52	1.3	1.47	1.48	1.33	1.04	2.5	157.1

TABLE A4: Cartesian coordinates of enol conformers in the S_1 state optimized with RI-ADC(2)/cc-pVDZ.

Atom	x	y	z	Atom	x	y	z
	E-a*				**E-OH***		
C	-3.8868769	-2.3204406	0.003543	C	0.8663636	-3.7161244	-0.781827
C	-2.4799019	-2.31998	0.0001871	C	0.7204941	-2.9587917	0.3771344
C	-1.7435043	-1.1055357	-0.0015628	C	0.6079938	-1.5390373	0.3186965
C	-2.4653159	0.1760277	0.0001358	C	0.6304656	-0.8861613	-0.9591697
C	-3.8919806	0.149701	0.0034842	C	0.8110987	-1.6807051	-2.138366
C	-4.58107	-1.0731008	0.0050611	C	0.9202289	-3.0640185	-2.0473372
H	0.2381868	-2.0099764	-0.0067084	H	0.4829718	-1.2284331	2.4853684
H	-4.4438051	-3.2638017	0.0049527	H	0.9523471	-4.8074611	-0.7226168
H	-1.9289776	-3.2696874	-0.0010213	H	0.6952778	-3.4501216	1.3585382
C	-0.3248516	-1.0681593	-0.0052129	C	0.4865909	-0.7317115	1.5069633
C	-1.7365903	1.3951254	-0.0014648	C	0.4878199	0.5387032	-1.0163776
H	-4.4408554	1.0974483	0.0046693	H	0.8936819	-1.1913802	-3.1154181
H	-5.6779932	-1.0663642	0.0075886	H	1.0616844	-3.6578509	-2.958732
C	-0.2548866	1.4112221	-0.0054461	C	0.3615292	1.3254766	0.1529956
C	0.397197	0.1638225	-0.0069653	C	0.3849453	0.6376052	1.4341491
H	1.4924391	0.123338	-0.0097262	H	0.2939327	1.2160225	2.358622
O	-2.3683256	2.5553666	0.00034	O	0.5163753	1.2013774	-2.2371588
H	-1.5754317	3.2680648	-0.001699	H	-0.1101649	0.7483799	-2.8247393
C	0.4239384	2.6924579	-0.0071823	C	0.1877933	2.734102	0.0577858
C	1.9407137	2.7664223	-0.0113145	C	0.0527408	3.7369379	1.1753514
H	2.3715641	2.2748857	0.8812686	H	0.1439705	3.2688677	2.1660766
H	2.3668894	2.273402	-0.9053031	H	0.8354694	4.512373	1.0693688
H	2.2361932	3.8271363	-0.0129353	H	-0.92749	4.2467392	1.1037468
O	-0.2504864	3.7839797	-0.0052994	O	0.1128155	3.3782955	-1.1763585
Atom	x	y	z	Atom	x	y	z
	E-CO*				**E-b***		
C	1.0717102	-0.8280451	-3.700205	C	0.2449198	-3.8146585	0.0311617
C	1.8199329	-0.8697649	-2.5007553	C	1.272135	-2.8407664	0.0442053
C	1.2591629	-0.461932	-1.2619031	C	0.9816443	-1.4536736	0.0282755
C	-0.1482568	0.0224667	-1.2138186	C	-0.4434723	-0.9949194	0.0269736
C	-0.8766206	0.0530938	-2.43766	C	-1.4482676	-2.0048531	-0.0441195
C	-0.2772445	-0.362984	-3.6492188	C	-1.1139626	-3.3785623	-0.0288995
H	3.0111946	-0.8366767	-0.0251479	H	3.0373395	-0.7463568	-0.0352621
H	1.5156863	-1.1453703	-4.6495269	H	0.4845059	-4.8829177	0.0459717
H	2.859211	-1.2231137	-2.5116799	H	2.3245325	-3.1525689	0.0566856
C	1.9710594	-0.487727	-0.0412933	C	1.9805646	-0.4518434	-0.0131924
C	-0.7243529	0.4346161	0.0197693	C	-0.7353407	0.4016518	0.0705579
H	-1.9132536	0.4035662	-2.4377063	H	-2.5107938	-1.7436836	-0.141013
H	-0.8711873	-0.3244891	-4.5706086	H	-1.9213747	-4.1189998	-0.0781925
C	0.0195621	0.4030531	1.2680754	C	0.2986086	1.4085293	0.0128983
C	1.3658984	-0.0685136	1.1766339	C	1.6476605	0.9310404	-0.0248479
H	1.9401044	-0.0986554	2.1079451	H	2.4396883	1.6853812	-0.05229
O	-2.0188328	0.8564406	-0.0700411	O	-2.0266227	0.835069	0.1558515
H	-2.3272789	1.114973	0.808151	H	-2.5829208	0.0722102	0.3734563
C	-0.4412126	0.797602	2.6213191	C	0.115135	2.8910442	0.0194337
C	-1.8659418	1.320572	2.8499426	C	-1.2769827	3.5150589	0.0496003
H	-2.0546972	2.2505033	2.2785617	H	-1.8862547	3.1696415	-0.8023316
H	-2.6262395	0.5625382	2.5774631	H	-1.8150323	3.2315816	0.9698515
H	-1.9783227	1.5481454	3.9206663	H	-1.1536016	4.6086006	0.0080025
O	0.3195659	0.7114386	3.5945404	O	1.1124765	3.6197758	-0.0077109

TABLE A5: Cartesian coordinates of keto conformers in the S_1 state optimized at RI-ADC(2)/cc-pVDZ.

Atom	x	y	z	Atom	x	y	z
	K-a*				**K-OH***		
C	-3.8896255	-2.2925703	0.0040416	C	-0.2996566	-1.067626	-0.0848489
C	-2.4468393	-2.3106374	-0.0000437	C	-1.7225679	-1.1174698	-0.0371531
C	-1.717634	-1.1144221	-0.0018894	C	-2.4544152	0.1151132	0.0255956
C	-2.4442544	0.1503252	0.0003088	C	-1.7416375	1.3600913	0.0344535
C	-3.8808402	0.1734643	0.0042199	C	-0.354453	1.3695989	-0.014938
C	-4.6026556	-1.1041933	0.0058484	C	0.3794088	0.1476441	-0.0763764
C	-1.6982165	1.3726569	-0.001121	C	-3.8847195	0.0699239	0.0691432
C	-0.3102999	1.3510977	-0.004165	C	-4.6127759	-1.1523685	0.0628441
C	0.4162488	0.1073157	-0.0064133	C	-3.8257433	-2.3792384	0.012396
C	-0.2759887	-1.0907932	-0.0054347	C	-2.4532114	-2.3618792	-0.0372359
O	-4.5516803	1.2843955	0.0064411	O	-4.5460885	1.2993233	0.1059498
C	-6.0864733	-1.1002244	0.0091477	C	-6.0215656	-1.154516	0.0925099
O	-6.7340204	0.0583121	0.010152	C	-6.9290496	-2.3482947	-0.0249161
C	-6.9210529	-2.3481017	0.0112475	O	-6.6315534	0.0604333	0.3364729
H	-1.9280941	-3.2770766	-0.0017786	H	-1.8945163	-3.3054651	-0.069189
H	1.512456	0.1159389	-0.0089138	H	1.4750581	0.1681323	-0.1145475
H	0.2634251	-2.046998	-0.0075095	H	0.2584518	-2.0119002	-0.1310463
H	-2.2523636	2.3169693	0.0001083	H	-2.3029762	2.2997562	0.0833908
H	0.2469935	2.2960195	-0.0048282	H	0.1834727	2.3253824	-0.0060968
H	-4.4181618	-3.25375	0.0058228	H	-4.3466565	-3.3422176	0.0371587
H	-6.7212721	-2.9725079	-0.8818535	H	-6.400157	-3.2392387	-0.3945964
H	-6.7169659	-2.9723779	0.9034578	H	-7.3991456	-2.5931332	0.9486823
H	-7.9854856	-2.0643513	0.0137831	H	-7.7489959	-2.1306053	-0.740293
H	-5.9751543	0.7644131	0.0082196	H	-7.5357526	0.0175547	-0.0147115

Atom	x	y	z
	K-CO*		
C	1.2370161	0.0520095	3.572966
C	1.2198879	0.0342308	2.149754
C	2.4668653	0.0060842	1.4419255
C	3.6954297	-0.0176623	2.1816019
C	3.6724557	-0.0046394	3.5701081
C	2.4364785	0.0307796	4.2801658
C	2.4461902	-0.0170428	0.0103106
C	1.2465507	-0.0066137	-0.7595391
C	0.0063435	0.0393779	0.0172851
C	-0.0069714	0.0627229	1.3893168
O	3.6889955	-0.0913917	-0.6204097
C	1.220504	-0.0582711	-2.1680848
C	2.3755829	0.1008202	-3.1148238
O	0.0452512	-0.2525405	-2.859604
H	-0.9622852	0.1205191	1.9256473
H	2.4332805	0.0430079	5.3763389
H	0.2796491	0.0797597	4.109599
H	4.6506952	-0.0432393	1.6453011
H	4.6170988	-0.0221898	4.1272082
H	-0.9494949	0.1238276	-0.5146713
H	-0.6104445	-0.6154335	-2.2464939
H	3.2481251	0.5693344	-2.635854
H	2.6813975	-0.8753872	-3.5399552
H	2.0520115	0.7379164	-3.9587773

TABLE A6: Cartesian coordinates of transition state structures in the S_0 and S_1 states optimized at RI-MP2/cc-pVDZ and RI-ADC(2)/cc-pVDZ levels, respectively.

Atom	x	y	z	Atom	x	y	z
	S_0- TS				S_1- TS		
C	0.222529	-3.7534864	-0.0001129	C	0.23432	-3.7927265	0.0000119
C	1.2498431	-2.809105	-0.0002013	C	1.2637342	-2.8366436	0.0000511
C	0.9607413	-1.4153589	-0.0000599	C	0.9761057	-1.4445532	0.0000189
C	-0.404267	-1.0067613	0.0001757	C	-0.4227982	-0.9988694	0.0000164
C	-1.4435845	-1.9745077	0.0002678	C	-1.4508614	-1.9886325	0.0000427
C	-1.1336198	-3.33442	0.0001245	C	-1.1239552	-3.3520348	0.0001132
H	3.0650121	-0.7619394	-0.0003317	H	3.0448369	-0.7622853	-0.0000485
H	0.464039	-4.82336	-0.0002276	H	0.4683471	-4.8630148	-0.0000267
H	2.2976155	-3.1352483	-0.0003847	H	2.3137639	-3.1574766	0.0000515
C	2.0233818	-0.4197668	-0.0001548	C	1.9918802	-0.4535273	-0.0000153
C	-0.7365987	0.4272029	0.000314	C	-0.7203793	0.3915625	-0.0001164
H	-2.4815218	-1.6265926	0.00045	H	-2.4974988	-1.6660041	0.0000633
H	-1.9361522	-4.0814525	0.0001935	H	-1.9315001	-4.0944624	0.0002003
C	0.3515865	1.3790813	0.0002045	C	0.3593458	1.4084597	0.000022
C	1.7291143	0.917816	-0.0000296	C	1.6846805	0.9411775	0.0000893
H	2.5410148	1.6541705	-0.0001068	H	2.514757	1.6570357	0.0001078
O	-1.9580922	0.8110188	0.0005199	O	-1.9649916	0.8210262	-0.0001842
H	-1.790684	2.1139949	0.0005554	H	-1.8477442	1.9147604	-0.0000902
C	-0.0147473	2.7493983	0.0003174	C	-0.0176463	2.8080123	0.000009
C	0.9896634	3.8789881	0.0002137	C	1.0299429	3.9042946	-0.0000584
H	1.6366705	3.8192758	0.8925419	H	1.6802774	3.8425302	0.8930123
H	1.6363748	3.8193746	-0.8923355	H	1.6798523	3.8427781	-0.8934573
H	0.4535034	4.8398837	0.0003554	H	0.5150199	4.8776655	0.0001985
O	-1.2628779	3.0932591	0.0005172	O	-1.2644219	3.1386459	-0.0000224

TABLE A7: Cartesian coordinates of the conical intersection structure obtained at SA-2-CASSCF(10,8) /6-31G(d) level.

Atom	x	y	z
C	1.641361604	0.932192508	0.217030645
C	1.95980794	-0.383731892	0.256875927
C	0.949542546	-1.405496374	0.104820141
C	-0.381924685	-1.041106686	-0.079817988
C	-0.770846289	0.389077309	-0.118195724
C	0.30660871	1.365165864	0.027316558
C	-1.371485829	-2.026817636	-0.22843724
C	-1.03062238	-3.366570547	-0.193325038
C	0.311709721	-3.741879539	-0.006792782
C	1.287386768	-2.775424252	0.140461332
O	-1.924559021	0.735539849	-0.25515043
C	-0.033638284	2.784186432	-0.024992978
O	-0.216866345	3.459128773	1.125691205
C	0.230775601	3.662386802	-1.197984712
H	2.980383963	-0.688425277	0.402376152
H	0.579583727	-4.782713266	0.021258472
H	2.314883211	-3.059565672	0.283243654
H	-2.38777816	-1.713871533	-0.368767589
H	-1.788365526	-4.120153058	-0.307893031
H	2.413679407	1.672005827	0.331422896
H	-0.438907302	2.860860864	1.82844914
H	1.251754295	4.047485555	-1.1805536
H	0.092470038	3.11549698	-2.121668209
H	-0.440593911	4.51351737	-1.181752301

TABLE A8: Vibrational frequencies of all the enol and keto tautomers in the S_0 state. In addition the vibrational frequencies of transition state structure, denoted as TS, are also given.

	E-a	**E-b**	**E-CO**	**E-OH**	**K-a**	**K-b**	**K-CO**	**K-OH**	TS
1	62.51	27.59	19.6	34.64	58.25	21.01	37.95	26.13	-893.3
2	100.01	70.71	64.28	68.77	79.17	63.3	95.2	69.02	65.6
3	144.23	125.9	134.11	122.89	115.16	106.45	117.38	116.29	109.88
4	190.83	195.54	181.85	174.28	173.39	121.12	183.75	186.22	119.48
5	197.46	211.32	198.14	194.8	188.06	187.82	190.07	195.57	178.03
6	219.33	249.84	242.09	207.43	204.63	192.56	200.29	219.99	213.17
7	273.12	256.47	276.04	265.69	258.89	266.57	255.97	254.66	217.98
8	315.04	278.23	324.6	280.29	307.03	321.83	322.95	326.13	261.69
9	343.31	325.16	337.06	313.96	343.08	329.4	331.34	334.09	311.16
10	408.98	345.84	377.14	349.69	409.78	398.19	367.33	394.19	413.35
11	416.78	374.28	385.3	391.39	436.43	400.87	397.69	396.18	413.35
12	457.3	416.68	418.54	416.25	451.54	413.51	405.74	440.58	454.5
13	489.41	453.72	453.8	459.76	482.68	448.91	443.36	461.24	482.75
14	528.99	484.72	487.87	484.45	532.62	480.34	480.31	480.32	514.09
15	534.23	517.13	518.69	522.15	532.69	495.15	504.42	505.64	534.62
16	568.05	536.87	534.93	542.96	542.03	532.6	520.63	518.47	542.71
17	578.71	565.67	564.09	544.44	575.64	538.02	545.99	546.48	584.97
18	593.2	576.1	580.75	571.1	595.67	552.38	593.53	591.57	597.7
19	603.47	588.8	602.39	584.6	611.4	599.06	600.88	610.44	610.12
20	652.66	611.38	611.44	599.65	686.52	599.18	617.15	617.86	672.92
21	682.21	644.46	642.79	659.48	709.52	674.79	679.91	680.3	701.37
22	732	668.85	668.16	669.25	733.58	729.46	724.71	718.75	730.52
23	755.81	728.51	727.23	727.98	752.39	729.75	732.66	730.86	752.89
24	798.77	747.26	759.4	744.51	795.6	743.66	763.77	731.23	795.05
25	835.63	819.62	818.46	803.4	865.95	793.25	804.28	788.76	839.36
26	861.36	842.39	857.66	839.44	876.67	855.17	868.58	868.24	872.81
27	863.31	865.39	868.69	851.45	907.46	879.48	879.69	879.47	876.02
28	893.28	887.86	885.3	883.37	931.91	889	897.13	898.8	915.16
29	930.2	937.52	950.36	936.91	956.43	925.7	947.2	911.66	929.28
30	954.57	955.74	958.89	938.18	970.05	953.5	956.24	954.59	956.32
31	965.78	972.94	968.89	958.59	1008.83	971.72	970.46	972.2	968.87
32	998.29	985.5	971.05	989.5	1043.32	1004.2	997.65	999.65	1016.88
33	1044.24	1049.67	1044.31	1038.67	1053.39	1053.17	1040.78	1055.26	1051.03
34	1047.81	1051.96	1046.17	1048.55	1075.42	1054.99	1055.45	1056.45	1054.86
35	1098.38	1086.17	1081.84	1092.07	1098.11	1078.09	1081.23	1077.55	1104.02
36	1152.81	1134.64	1130.08	1143.45	1142.56	1125.03	1121.57	1121.59	1154.04
37	1168.03	1162.94	1164.03	1163.93	1167.11	1166.21	1162.24	1168.54	1169.16
38	1175.26	1184.18	1171.33	1186.79	1169.21	1167.78	1168.88	1173.44	1177.48
39	1231.84	1210.22	1221.01	1222.95	1230.73	1235.94	1234.42	1230.35	1235.14
40	1252.51	1228.79	1227.5	1232.64	1262.31	1245.5	1240.76	1239.27	1265.27
41	1276.42	1275.5	1265.1	1265.19	1280.59	1254.56	1265.49	1269.88	1266.8
42	1302.83	1283.13	1270.77	1287.07	1328.55	1291.79	1279.79	1298.6	1299.78
43	1371.63	1301.58	1304.03	1314.94	1359.23	1333.89	1333.44	1331.8	1354.22
44	1407.83	1389.03	1395.59	1391.3	1384.85	1350.86	1352.84	1354.9	1383.37
45	1431.66	1411.94	1401.91	1398.43	1404.21	1368.02	1395.43	1390.23	1406.93
46	1438.72	1422.94	1425.39	1429.05	1453.11	1431.44	1423.74	1427.1	1449.95
47	1463.62	1454.62	1459.54	1450.69	1465.13	1450.77	1440.39	1449.72	1473.08
48	1476.48	1465.25	1478.19	1463.57	1490.71	1488.81	1467.79	1481.51	1488.84
49	1481.1	1472	1500.9	1481.12	1492.78	1490.2	1485.73	1483.59	1493.16
50	1489.96	1488.22	1507.94	1490.92	1499.04	1495.37	1493.45	1494.08	1512.55
51	1517.06	1507.55	1510.16	1510.35	1524.38	1525.24	1523.03	1523.9	1527.49
52	1556.58	1556.68	1554.27	1558.3	1610.67	1621.16	1619.1	1618.83	1602
53	1638.03	1638.43	1634.45	1635.16	1648.21	1654.07	1654.44	1645.19	1643.79
54	1657.41	1656.06	1656.81	1654.77	1677.52	1675.83	1669.29	1657.92	1677.2
55	1697.95	1694.17	1693.92	1691.37	1686.77	1697.73	1689.61	1685.17	1688.85
56	1731.45	1760.2	1758.87	1773.4	1709.19	1751.27	1745.78	1743.25	1703.01
57	3078.11	3088.01	3051.15	3072.03	2836.13	3059.99	3065.48	3092.71	1932.02
58	3165.72	3182.83	3139.24	3158.29	3083.12	3128.39	3165.74	3167.44	3082.54
59	3196.88	3191.79	3190.71	3192.7	3167.61	3193.94	3184.62	3183.25	3168.1
60	3199.28	3198.76	3197.38	3192.84	3196.35	3199.59	3194.56	3195.83	3196.5
61	3207.27	3201.19	3208.18	3200.39	3197.94	3208.05	3201.38	3197.8	3199.88
62	3211.06	3209.37	3210.75	3208.23	3202.89	3222.05	3208.51	3209.07	3203.29
63	3225.12	3216.56	3225.31	3216.49	3210.5	3223.49	3223.19	3211.58	3210.64
64	3235.76	3230.7	3251.73	3230.62	3224.56	3242.44	3241.39	3224.92	3224.07
65	3249.77	3251.43	3254.07	3237.31	3226.21	3246.61	3243.17	3243.4	3225.36
66	3422.36	3839.58	3896.35	3837.19	3242.88	3811.95	3840.24	3823.06	3243.53

TABLE A9: Vibrational frequencies of all the enol and keto tautomers in the S_1 state. In addition the vibrational frequencies of transition state structure, denoted as TS, are also given.

	E-a*	**E-b***	**E-CO***	**E-OH***	**K-a***	**K-CO***	**K-OH***	TS*
1	63.76	44.32	21.68	58.92	46.87	55.82	60.26	-340.4
2	100.85	62.47	66.77	64.41	68.56	113.08	85.11	65.16
3	110.81	87.47	110.77	97.34	107.97	151.22	114.29	100.64
4	130.1	182.32	175.94	134.92	130.14	173	134.59	116.31
5	177	193.49	192.81	151.54	194.61	184.06	181.41	130.18
6	188.96	224.29	217.51	198.69	195.84	212.3	210.45	190.3
7	239.52	241.02	235.29	216.14	235.06	249.61	258.18	208.16
8	259.96	286.8	318.35	267.39	300.24	273.57	295.93	241.82
9	313.62	317.06	324.39	294.22	353	314.86	316.25	306.27
1	0 377.34	350.39	356.24	312.49	358.05	361.24	352.15	378.82
11	391.14	365.72	368.55	353.5	386.94	392.79	388.01	394.27
12	409.21	368.56	368.65	373.38	410.03	417.77	397.92	404.87
13	411.07	394.07	394.89	408.13	435.81	427.69	401.16	413.55
14	463.95	410.84	412.87	452.4	458.61	441.77	467.16	463.16
15	495.51	455.65	462.76	483.13	481.16	480.32	481.83	490.64
16	506.66	464.48	468.65	488.54	509.59	503.3	490.38	509.5
17	520.6	512.39	510.89	518.01	535.21	532.12	499.55	514.04
18	548.11	521.08	523.4	523.85	546.76	584.32	526.85	534.02
19	576.14	533.12	532.68	550.39	593.57	588.64	531.63	575.99
20	582.61	587.74	574.9	579.94	606.85	617.18	568.67	581.6
21	662.79	596.61	597.07	594.13	669.04	677.6	589.32	659.75
22	705.86	648.16	646.59	650.46	712.82	727.24	665.72	702.17
23	715.08	677.16	685.96	716.59	741.26	747.94	704.92	719.75
24	781.7	708.65	708.05	744.62	796.64	793.73	740.38	785.06
25	828.32	752.55	786.88	781.35	845.98	821.54	772.87	831.76
26	856.81	781.46	798.81	838.98	853.63	859.34	840.11	838.13
27	860.81	849.39	853.82	845.06	879.35	881.42	857.85	861.15
28	875.41	850.13	855.07	874.1	893.12	894.87	886.47	878.84
29	891.47	859.95	865.36	925.54	932.26	940.79	921.69	896.26
30	936.13	873.53	887.83	926.31	960.99	954.02	938.46	939.64
31	988.27	877.62	902.62	940.37	987.15	970.33	955.12	988.63
32	1015.82	973.61	956.13	953.9	993.85	975.71	987.31	1007.42
33	1020.62	1000.72	998.36	1012.84	1021.73	1041.77	1033.8	1019.56
34	1073.69	1040.28	1024.8	1043.6	1060.66	1053.48	1037.69	1032.34
35	1102.81	1067.71	1061.47	1070.03	1079.81	1085.35	1052.29	1089.18
36	1121.65	1095.72	1092.47	1111.75	1128.59	1119.8	1098.34	1109.9
37	1155.91	1131.57	1128.3	1144.99	1141.04	1147.4	1145.54	1127.96
38	1182.99	1165.77	1159.57	1157.34	1155.33	1167.39	1166.81	1157.18
39	1213.36	1190.81	1209.11	1174.72	1217	1206.93	1192.87	1236.98
40	1236.89	1245.84	1255.42	1196.63	1228.73	1235.63	1218.92	1244.79
41	1267.46	1268.57	1262.85	1225.84	1250.52	1247.93	1235.11	1254.22
42	1293.54	1293.16	1288.71	1269.92	1298.26	1266.52	1274.56	1293.89
43	1362.67	1315.42	1309.02	1279.03	1333.01	1300.96	1319.92	1352.61
44	1388.92	1397.74	1388.97	1351.44	1377.87	1338.61	1338.01	1392.02
45	1417.25	1407.58	1408.06	1388.96	1400.85	1361.7	1381.22	1410.12
46	1429.54	1420.98	1424.1	1404.6	1406.72	1393.01	1402.31	1433.41
47	1441.22	1457.46	1450.38	1416.68	1439.19	1427.23	1440	1439.01
48	1454.66	1473.01	1489.87	1452.79	1468.36	1457.9	1445.44	1444.77
49	1482.8	1489.17	1506.84	1462.58	1473.6	1478.89	1460.86	1478.34
50	1487.19	1490.02	1507.75	1465.67	1476.57	1490.65	1474.68	1486.34
51	1512.86	1515.72	1512.94	1482.93	1502.69	1515.73	1480.75	1503.8
52	1537.11	1540.97	1526.75	1504.43	1540.36	1538.86	1507.36	1541.55
53	1559.51	1548.63	1554.73	1550.4	1558.89	1598.64	1555.3	1559.44
54	1602.97	1648.14	1651.56	1601.04	1591.6	1619.58	1583.28	1592.31
55	1623.76	1700.03	1675.56	1639.74	1626.35	1657.36	1640.63	1608.84
56	1678.66	1751.43	1704.6	1667.35	1636.11	2456.74	1658.74	1650.79
57	2111.99	3083.71	3040.1	3053.71	2651.8	3034.73	3053.68	1917.4
58	3055.93	3174.85	3123.2	3120.67	3039.83	3112.47	3125.14	3054.07
59	3131.04	3178	3186.05	3192.94	3103.97	3145.22	3188.25	3127.91
60	3185.95	3194.27	3197.47	3198.12	3179.29	3199.57	3188.89	3184.79
61	3195.19	3198.55	3205.94	3202.24	3193.91	3208.42	3193.96	3195.21
62	3203.2	3206	3208.42	3204.15	3202.93	3212.51	3204.33	3203.2
63	3207.9	3214.15	3233.68	3218.52	3206.31	3228.12	3212.79	3207.31
64	3226.46	3236.82	3244.69	3228.69	3219.76	3233.73	3219.64	3224.85
65	3229.14	3248.81	3245.41	3237.73	3224.94	3243.73	3229.78	3228.84
66	3237.66	3810.93	3849.07	3781.97	3240.65	3795.55	3826.54	3237.48

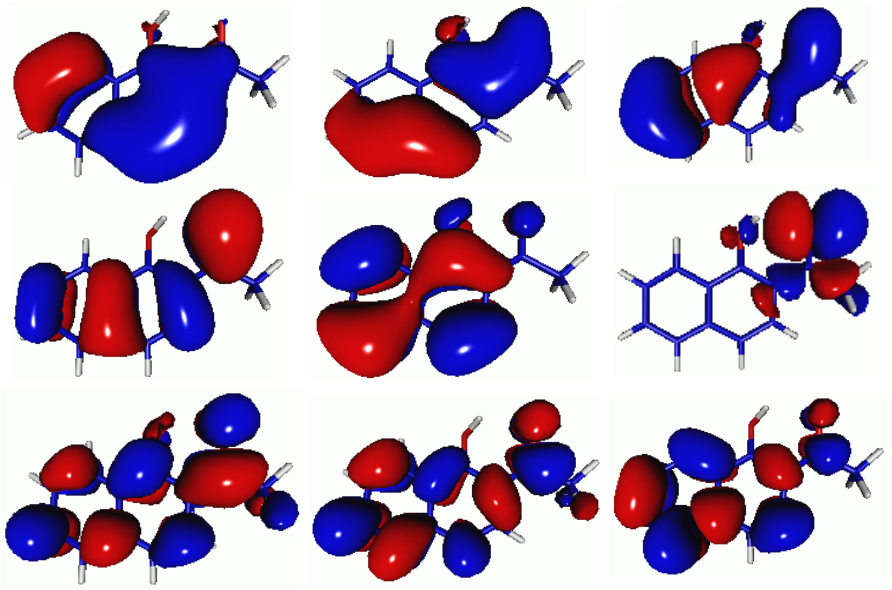

FIGURE A1: The active space orbitals used for generating potential energy curves along the torsional coordinate ϕ_1 at MS-MR-CASPT2//SA-3-CASSCF(12,9)/6-31G(d,p) in the S_1 and S_2 states.

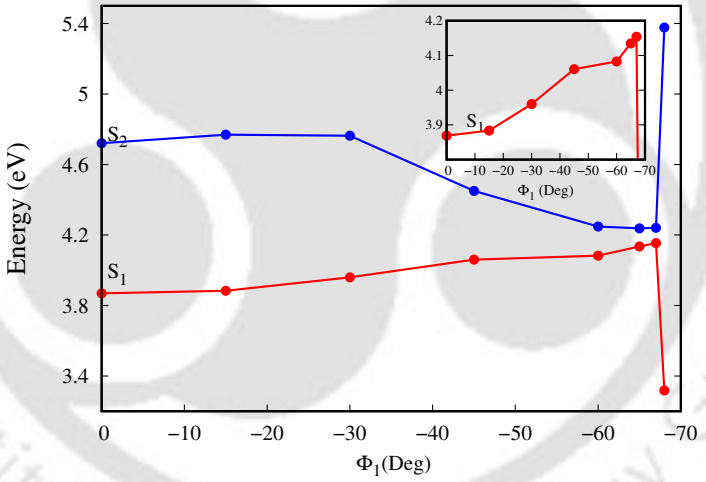

FIGURE A2: Potential energy curve along the torsional coordinate ϕ_1, starting from the **E-a*** geometry at MS-MR-CASPT2//SA-3-CASSCF(12,9) level in the S_1 and S_2 states.

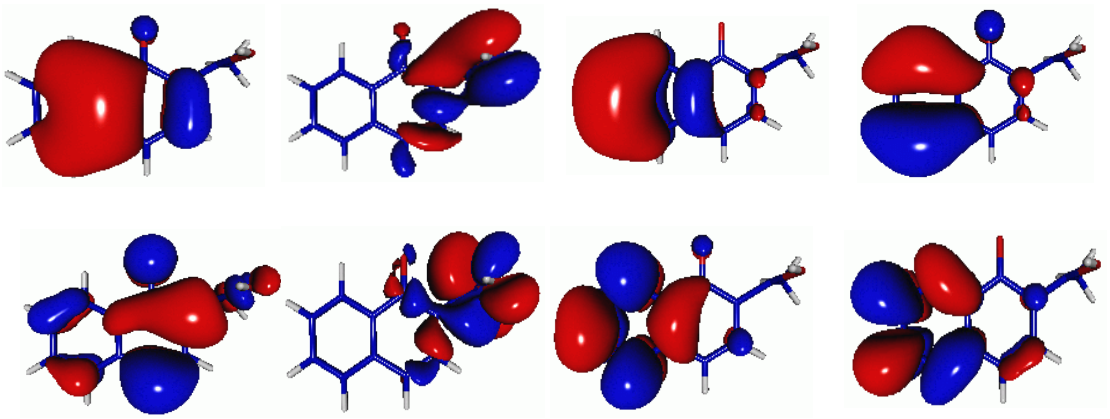

FIGURE A3: The active space orbitals used in SA-2-CASSCF(10,8)/6-31G(d) conical intersection optimisation between S_1 and S_0.

Appendix B

TABLE B1: Cartesian coordinates of enol and keto conformers in the S_0 state optimized at B3LYP/cc-pVDZ level of theory in Gas, CyHex and MeOH.

1-CN-Enol-Gas				2-CN-Enol-Gas			
Atom	x	y	z	Atom	x	y	z
C	-1.605002	1.765255	0.356159	C	-1.911291	1.630041	0.441794
C	-0.30335	1.311924	0.111343	C	-0.581979	1.220033	0.187198
C	-0.023732	-0.04571	0.066404	C	-0.255662	-0.124484	0.122612
C	-1.044901	-0.995614	0.266182	C	-1.242877	-1.112811	0.309523
C	-2.377674	-0.555912	0.515763	C	-2.583271	-0.704845	0.56622
C	-2.638785	0.841972	0.55769	C	-2.900536	0.657985	0.629102
C	-3.404312	-1.581277	0.714173	C	-3.605465	-1.73092	0.7597
N	-3.162781	-2.84958	0.682995	N	-3.374796	-2.997889	0.713465
C	-4.433897	-3.573485	0.90785	C	-4.649246	-3.711824	0.955674
C	-5.449906	-2.409449	1.121838	C	-5.661527	-2.539	1.151078
O	-4.676784	-1.19649	0.940262	O	-4.874863	-1.329019	1.002881
O	-0.708631	-2.285769	0.211162	O	-0.885422	-2.395074	0.239114
C	-4.768996	-4.410721	-0.334628	C	-4.994083	-4.573112	-0.266758
C	-4.306386	-4.464648	2.150259	C	-4.519763	-4.577415	2.216242
H	-1.829301	2.830915	0.393083	H	0.766462	-0.450773	-0.07317
H	0.983693	-0.419114	-0.122479	H	-1.710498	-2.946504	0.395694
H	-1.545193	-2.823292	0.374623	H	-6.118711	-2.521864	2.151688
H	-5.876216	-2.384944	2.135904	H	-6.455357	-2.518812	0.389533
H	-6.266396	-2.39858	0.385291	H	-5.069671	-3.954216	-1.174388
H	-4.851382	-3.771883	-1.227764	H	-5.955172	-5.092847	-0.1186
H	-5.724788	-4.943418	-0.198644	H	-4.214509	-5.331951	-0.434458
H	-3.98127	-5.157152	-0.519431	H	-4.255082	-3.961612	3.089897
H	-4.040658	-3.867019	3.036014	H	-3.733736	-5.336298	2.082242
H	-3.522562	-5.223131	2.001336	H	-5.468112	-5.09728	2.431041
H	-5.256215	-4.986159	2.3543	H	0.190889	1.976363	0.04084
H	0.498861	2.036058	-0.045248	H	-3.930687	0.953438	0.826352
C	-3.943666	1.397551	0.804149	C	-2.240925	3.024153	0.507106
N	-4.949101	1.952518	0.994222	N	-2.504322	4.157736	0.559328

1-CN-Enol-CyHex				2-CN-Enol-CyHex			
Atom	x	y	z	Atom	x	y	z
C	-1.60918	1.765783	0.329202	C	-1.911999	1.629954	0.424475
C	-0.305015	1.311706	0.099505	C	-0.580105	1.219401	0.184111
C	-0.023156	-0.046379	0.076753	C	-0.253594	-0.12587	0.137645
C	-1.04369	-0.995393	0.284032	C	-1.242689	-1.111713	0.32893
C	-2.378879	-0.555761	0.518058	C	-2.585559	-0.702158	0.571297
C	-2.641593	0.841967	0.537567	C	-2.903801	0.660149	0.616355
C	-3.405021	-1.580934	0.723406	C	-3.608261	-1.728532	0.768029
N	-3.156969	-2.847786	0.716983	N	-3.370408	-2.994345	0.739151
C	-4.43174	-3.574656	0.920188	C	-4.647622	-3.712548	0.962306
C	-5.443672	-2.413	1.157695	C	-5.658723	-2.542454	1.175958
O	-4.681672	-1.197976	0.925622	O	-4.88017	-1.328933	0.991585
O	-0.706286	-2.286949	0.2515	O	-0.886969	-2.395407	0.276582
C	-4.761678	-4.376648	-0.347175	C	-4.985446	-4.546251	-0.281435
C	-4.315108	-4.498101	2.138678	C	-4.52736	-4.60468	2.204305
H	-1.834716	2.831626	0.348829	H	0.770458	-0.452587	-0.046989
H	0.986948	-0.418659	-0.100061	H	-1.717849	-2.943232	0.434202
H	-1.546806	-2.821565	0.418397	H	-6.082333	-2.516635	2.190911
H	-5.823791	-2.37492	2.189577	H	-6.475451	-2.531166	0.440026
H	-6.290056	-2.414737	0.45696	H	-5.063397	-3.906405	-1.17426
H	-4.847154	-3.712375	-1.221304	H	-5.944389	-5.0729	-0.146233
H	-5.715315	-4.916238	-0.226134	H	-4.202095	-5.297589	-0.464689
H	-3.97062	-5.114212	-0.552163	H	-4.25948	-4.009352	3.090951
H	-4.042331	-3.926688	3.039262	H	-3.749075	-5.368779	2.055226
H	-3.542212	-5.263531	1.96947	H	-5.481204	-5.119328	2.40576
H	-5.271912	-5.011655	2.328544	H	0.194377	1.973288	0.034449
H	0.496733	2.034843	-0.062527	H	-3.935389	0.957503	0.802832
C	-3.948865	1.398673	0.768018	C	-2.243284	3.023808	0.471183
N	-4.955577	1.956412	0.943924	N	-2.508394	4.157961	0.508286

1-CN-Enol-MeOH				2-CN-Enol-MeOH			
Atom	x	y	z	Atom	x	y	z
C	-1.600677	1.768964	0.356217	C	-1.905717	1.630726	0.44046
C	-0.299758	1.312434	0.113307	C	-0.576501	1.219346	0.18602
C	-0.025781	-0.047263	0.069076	C	-0.2572	-0.127135	0.123018
C	-1.0498	-0.994383	0.267394	C	-1.250346	-1.109702	0.311198
C	-2.381398	-0.553587	0.515767	C	-2.590348	-0.698153	0.56773
C	-2.635312	0.845045	0.556262	C	-2.902485	0.663684	0.629357
C	-3.410743	-1.577983	0.714463	C	-3.615003	-1.724948	0.761781
N	-3.165298	-2.844007	0.68006	N	-3.375493	-2.98962	0.713886
C	-4.434469	-3.575909	0.907104	C	-4.648132	-3.713664	0.955535
C	-5.45495	-2.417308	1.123772	C	-5.666242	-2.547115	1.152563
O	-4.682192	-1.195125	0.943796	O	-4.881522	-1.328131	1.004376
O	-0.721005	-2.289009	0.212935	O	-0.904247	-2.39572	0.243156
C	-4.767076	-4.413293	-0.335378	C	-4.987308	-4.574225	-0.268468
C	-4.2994	-4.46591	2.149054	C	-4.512906	-4.579484	2.214837
H	-1.819236	2.835795	0.391892	H	0.764823	-0.453837	-0.072664
H	0.982649	-0.418857	-0.118982	H	-1.743249	-2.938466	0.402292
H	-1.568719	-2.819253	0.375906	H	-6.119955	-2.530817	2.153486
H	-5.878025	-2.395069	2.138102	H	-6.4578	-2.527642	0.390328
H	-6.268868	-2.406981	0.385874	H	-5.067222	-3.953943	-1.174679
H	-4.852686	-3.774632	-1.228235	H	-5.946618	-5.095325	-0.118026
H	-5.722033	-4.945113	-0.195388	H	-4.205768	-5.33169	-0.434504
H	-3.979191	-5.160289	-0.517732	H	-4.252447	-3.962999	3.089168
H	-4.034447	-3.866817	3.03395	H	-3.725973	-5.337196	2.077962
H	-3.515919	-5.224041	1.99589	H	-5.460617	-5.100508	2.426582
H	-5.24856	-4.987305	2.35313	H	0.201289	1.969983	0.03859
H	0.504481	2.033737	-0.042206	H	-3.931235	0.963858	0.826253
C	-3.938643	1.404318	0.799827	C	-2.230957	3.024311	0.504664
N	-4.942275	1.964687	0.986951	N	-2.491034	4.159608	0.556048

1-CN-Keto-Gas				2-CN-Keto-Gas			
Atom	x	y	z	Atom	x	y	z
C	-1.610884	1.775247	0.231912	C	-1.706459	1.761014	0.282829
C	-0.300721	1.274069	0.026517	C	-0.36424	1.299753	0.07599
C	-0.028137	-0.071063	0.082604	C	-0.046964	-0.03294	0.113684
C	-1.056233	-1.044759	0.35763	C	-1.043056	-1.048631	0.367547
C	-2.405646	-0.516871	0.557078	C	-2.404424	-0.547523	0.571702
C	-2.650665	0.894922	0.492535	C	-2.706225	0.830743	0.526805
C	-3.418276	-1.487377	0.794225	C	-3.410515	-1.520885	0.802868
N	-3.158031	-2.778937	0.89882	N	-3.159883	-2.814642	0.888764
C	-4.393963	-3.576743	0.96662	C	-4.398541	-3.607831	0.96211
C	-5.409231	-2.434864	1.251739	C	-5.404753	-2.460872	1.26628
O	-4.718727	-1.201822	0.909179	O	-4.709478	-1.225334	0.935902
O	-0.780211	-2.285733	0.415818	O	-0.750767	-2.281377	0.40801
C	-4.655182	-4.260411	-0.385044	C	-4.677082	-4.279546	-0.391869
C	-4.330485	-4.597722	2.106354	C	-4.330855	-4.637103	2.094156
H	-1.809503	2.845686	0.188481	H	0.976362	-0.377486	-0.044406
H	0.979323	-0.460902	-0.073077	H	-2.13198	-3.033601	0.69772
H	-2.116021	-2.98369	0.708122	H	-5.674689	-2.414183	2.332723
H	-5.684845	-2.374829	2.316014	H	-6.315854	-2.50229	0.655633
H	-6.317164	-2.486563	0.637443	H	-4.756662	-3.530338	-1.194831
H	-4.733222	-3.51715	-1.193679	H	-5.61829	-4.851417	-0.352778
H	-5.592878	-4.838468	-0.350668	H	-3.864458	-4.975388	-0.65188
H	-3.835024	-4.951919	-0.632857	H	-4.078595	-4.155145	3.050597
H	-4.090257	-4.106969	3.061422	H	-3.56568	-5.399068	1.879265
H	-3.558397	-5.356321	1.904376	H	-5.298039	-5.153326	2.203921
H	-5.295533	-5.11907	2.211309	H	0.415019	2.040894	-0.115375
H	0.506378	1.981872	-0.179264	H	-3.734307	1.159343	0.68602
C	-3.955808	1.462946	0.700333	C	-2.004156	3.160468	0.23702
N	-4.982253	1.988793	0.861992	N	-2.238932	4.30188	0.198028

1-CN-Keto-CyHex				2-CN-Keto-CyHex			
Atom	x	y	z	Atom	x	y	z
C	-1.614243	1.77899	0.233957	C	-1.705994	1.761765	0.289056
C	-0.29963	1.28869	0.031862	C	-0.359924	1.314016	0.081367
C	-0.019162	-0.054901	0.086303	C	-0.034455	-0.016914	0.113091
C	-1.040201	-1.040284	0.355058	C	-1.022861	-1.043978	0.359677
C	-2.394112	-0.522544	0.55319	C	-2.388159	-0.553942	0.565075
C	-2.646988	0.888055	0.489923	C	-2.699463	0.820377	0.52746
C	-3.407666	-1.494529	0.790194	C	-3.398386	-1.529116	0.793693
N	-3.158577	-2.787721	0.891699	N	-3.160744	-2.823982	0.871901
C	-4.398731	-3.581564	0.966175	C	-4.404781	-3.611342	0.958537
C	-5.405242	-2.433484	1.253939	C	-5.402338	-2.455663	1.257089
O	-4.703606	-1.202049	0.911966	O	-4.690051	-1.223023	0.934608
O	-0.753049	-2.277446	0.409737	O	-0.719786	-2.272949	0.392746
C	-4.667931	-4.264372	-0.383726	C	-4.690617	-4.293069	-0.388019
C	-4.334127	-4.599816	2.107864	C	-4.334976	-4.628555	2.100944
H	-1.820781	2.847944	0.191267	H	0.992292	-0.351263	-0.045757
H	0.992512	-0.435128	-0.067585	H	-2.153877	-3.074929	0.687366
H	-2.139427	-3.022798	0.707707	H	-5.68022	-2.404416	2.320342
H	-5.678713	-2.370088	2.317793	H	-6.306866	-2.48546	0.637096
H	-6.31224	-2.476978	0.638672	H	-4.769441	-3.551167	-1.197735
H	-4.742122	-3.521705	-1.193136	H	-5.635425	-4.857274	-0.337849
H	-5.610983	-4.832545	-0.343822	H	-3.883975	-4.99754	-0.642968
H	-3.855428	-4.964709	-0.631484	H	-4.074545	-4.137665	3.050544
H	-4.088279	-4.108387	3.061026	H	-3.5771	-5.398266	1.888325
H	-3.567751	-5.363174	1.902921	H	-5.305692	-5.135028	2.220881
H	-5.302121	-5.114254	2.216369	H	0.415035	2.060789	-0.105458
H	0.502893	2.002571	-0.170052	H	-3.730337	1.13963	0.687341
C	-3.954912	1.452241	0.691663	C	-2.017251	3.157189	0.250246
N	-4.980979	1.981336	0.846456	N	-2.263568	4.296949	0.216835

1-CN-Keto-MeOH				2-CN-Keto-MeOH			
Atom	x	y	z	Atom	x	y	z
C	-1.613069	1.786202	0.254653	C	-1.701813	1.765093	0.311016
C	-0.295279	1.308262	0.051975	C	-0.352453	1.334715	0.097329
C	-0.009468	-0.035682	0.090777	C	-0.019301	0.004568	0.108208
C	-1.024438	-1.033314	0.340755	C	-0.999775	-1.036052	0.335393
C	-2.381076	-0.527945	0.542113	C	-2.367989	-0.560952	0.548208
C	-2.639633	0.88142	0.4955	C	-2.688942	0.80813	0.533547
C	-3.398721	-1.503671	0.772131	C	-3.385602	-1.540504	0.768528
N	-3.163463	-2.797956	0.85181	N	-3.165847	-2.83614	0.82029
C	-4.406896	-3.587488	0.957066	C	-4.414891	-3.61565	0.947028
C	-5.406814	-2.431784	1.238278	C	-5.404626	-2.447222	1.226477
O	-4.68662	-1.199232	0.914199	O	-4.664599	-1.217523	0.93248
O	-0.727231	-2.269411	0.378082	O	-0.684792	-2.262294	0.347004
C	-4.692951	-4.294381	-0.375683	C	-4.718547	-4.336914	-0.37346
C	-4.327041	-4.583692	2.11693	C	-4.328695	-4.597744	2.118602
H	-1.826525	2.854154	0.223984	H	1.011532	-0.316201	-0.05524
H	1.006675	-0.404433	-0.064408	H	-2.18091	-3.124313	0.642152
H	-2.164468	-3.064262	0.674563	H	-5.711242	-2.394572	2.280294
H	-5.694217	-2.368871	2.297287	H	-6.288799	-2.458948	0.57831
H	-6.302594	-2.462276	0.60712	H	-4.797136	-3.621369	-1.206186
H	-4.770141	-3.567855	-1.199085	H	-5.669748	-4.885727	-0.29257
H	-5.640379	-4.851942	-0.311048	H	-3.923231	-5.060774	-0.60855
H	-3.889192	-5.007769	-0.613989	H	-4.06361	-4.077551	3.050945
H	-4.070871	-4.074192	3.057699	H	-3.570895	-5.370881	1.919389
H	-3.564843	-5.351623	1.914267	H	-5.297947	-5.100483	2.259546
H	-5.295332	-5.092095	2.244321	H	0.418562	2.088596	-0.076567
H	0.503725	2.029111	-0.137372	H	-3.72257	1.115274	0.698433
C	-3.949026	1.442484	0.695927	C	-2.026821	3.155817	0.295375
N	-4.971707	1.979591	0.848083	N	-2.282819	4.294793	0.280452

TABLE B2: Cartesian coordinates of keto conformers in the S_1 state optimized at B3LYP/cc-pVDZ level of theory in Gas, CyHex and MeOH.

1-CN-Keto*-Gas				2-CN-Keto*-Gas			
Atom	x	y	z	Atom	x	y	z
C	-1.643149	1.777953	0.103965	C	-1.459801	1.719598	0.633209
C	-0.406761	1.315185	-0.286473	C	-0.570883	1.40042	-0.427406
C	-0.072013	-0.059494	-0.149499	C	-0.66008	0.178045	-1.05514
C	-1.019422	-0.989187	0.293063	C	-1.657469	-0.791759	-0.636543
C	-2.373754	-0.532938	0.619567	C	-2.556448	-0.438959	0.43833
C	-2.624064	0.867523	0.614917	C	-2.455909	0.777193	1.054449
C	-3.364891	-1.508914	0.916511	C	-3.601776	-1.436181	0.858802
N	-3.174748	-2.790331	1.329776	N	-3.362146	-2.580517	1.624769
C	-4.396376	-3.57707	1.036863	C	-4.346655	-3.611373	1.193457
C	-5.415981	-2.420884	1.133678	C	-5.438475	-2.680721	0.620882
O	-4.675829	-1.239696	0.751593	O	-4.728518	-1.555925	0.088083
O	-0.753478	-2.256211	0.402981	O	-1.747709	-1.927753	-1.173157
C	-4.341212	-4.174915	-0.378426	C	-3.750452	-4.508473	0.097627
C	-4.618913	-4.652807	2.099732	C	-4.842646	-4.423844	2.389807
H	-1.891458	2.838697	0.060856	H	0.009696	-0.097512	-1.871764
H	0.904479	-0.438018	-0.452553	H	-2.395879	-2.90668	1.62009
H	-2.232639	-3.162044	1.162559	H	-6.118688	-2.33514	1.420252
H	-5.780585	-2.279965	2.164606	H	-6.019833	-3.131905	-0.193144
H	-6.266641	-2.520207	0.447705	H	-3.370001	-3.902079	-0.73676
H	-4.219317	-3.384712	-1.13553	H	-4.506739	-5.214054	-0.283792
H	-5.266453	-4.730365	-0.601945	H	-2.91371	-5.103798	0.499775
H	-3.494559	-4.873305	-0.47241	H	-5.218984	-3.761621	3.183765
H	-4.593934	-4.217398	3.109555	H	-4.027415	-5.033286	2.811315
H	-3.838302	-5.427576	2.038614	H	-5.649892	-5.111494	2.088817
H	-5.591559	-5.148547	1.951454	H	0.174955	2.137896	-0.72908
H	0.345457	2.01151	-0.661776	H	-3.132569	1.045598	1.868008
C	-3.820686	1.419837	1.160586	C	-1.366126	2.982366	1.283263
N	-4.774812	1.925233	1.605965	N	-1.289351	4.017127	1.818516

1-CN-Keto*-CyHex				2-CN-Keto*-CyHex			
Atom	x	y	z	Atom	x	y	z
C	-1.637415	1.784271	0.118531	C	-1.663754	1.779615	0.275499
C	-0.392219	1.331338	-0.256912	C	-0.392013	1.36816	-0.109456
C	-0.057327	-0.043624	-0.130231	C	-0.073	-0.006318	-0.104322
C	-1.012278	-0.988673	0.285745	C	-1.0262	-1.008442	0.233665
C	-2.374868	-0.534081	0.604041	C	-2.376686	-0.560652	0.616684
C	-2.628159	0.863317	0.612299	C	-2.647756	0.792585	0.682882
C	-3.367658	-1.516275	0.892328	C	-3.369579	-1.554609	0.936357
N	-3.171513	-2.795161	1.289903	N	-3.151076	-2.847396	1.294008
C	-4.400559	-3.583077	1.030872	C	-4.396454	-3.618544	1.057729
C	-5.419441	-2.425799	1.128066	C	-5.407431	-2.464079	1.247982
O	-4.676414	-1.2409	0.743073	O	-4.68968	-1.264405	0.864566
O	-0.739105	-2.246933	0.378914	O	-0.748013	-2.251242	0.190917
C	-4.366929	-4.201937	-0.375767	C	-4.432214	-4.178522	-0.373635
C	-4.606286	-4.642925	2.113044	C	-4.561569	-4.722252	2.102203
H	-1.891948	2.843626	0.07303	H	0.905885	-0.352497	-0.439818
H	0.924041	-0.418455	-0.423385	H	-2.223998	-3.194421	1.005308
H	-2.224509	-3.156906	1.118736	H	-5.712322	-2.359851	2.302579
H	-5.781535	-2.279081	2.15831	H	-6.296019	-2.543594	0.609147
H	-6.270037	-2.523643	0.44258	H	-4.341824	-3.369997	-1.115758
H	-4.255782	-3.424055	-1.147138	H	-5.377808	-4.714183	-0.556432
H	-5.297248	-4.757991	-0.574306	H	-3.60394	-4.886603	-0.533799
H	-3.523894	-4.904099	-0.470491	H	-4.474996	-4.314328	3.120156
H	-4.567768	-4.192645	3.115882	H	-3.788179	-5.495557	1.972991
H	-3.826103	-5.417685	2.050367	H	-5.543545	-5.210536	1.998021
H	-5.581145	-5.139377	1.985118	H	0.356535	2.104736	-0.4035
H	0.358785	2.035983	-0.618762	H	-3.61829	1.136447	1.041747
C	-3.82904	1.416474	1.143859	C	-2.021237	3.157201	0.279991
N	-4.785245	1.929664	1.578226	N	-2.32834	4.284456	0.290723

1-CN-Keto*-MeOH				2-CN-Keto*-MeOH			
Atom	x	y	z	Atom	x	y	z
C	-1.624285	1.790125	0.14104	C	-1.676958	1.773438	0.248442
C	-0.353595	1.358829	-0.174779	C	-0.367483	1.398686	-0.050173
C	-0.016117	-0.01416	-0.062658	C	-0.015855	0.034548	-0.00782
C	-0.985588	-0.981994	0.297692	C	-0.965239	-0.989458	0.293048
C	-2.365807	-0.540667	0.583354	C	-2.348771	-0.578522	0.601285
C	-2.640813	0.853638	0.574403	C	-2.666167	0.773119	0.607601
C	-3.355879	-1.535119	0.857977	C	-3.333404	-1.581985	0.893261
N	-3.156429	-2.822801	1.189705	N	-3.135639	-2.886682	1.202528
C	-4.408328	-3.595453	1.018942	C	-4.40772	-3.627184	1.039993
C	-5.408934	-2.42816	1.177501	C	-5.378423	-2.452365	1.302106
O	-4.662715	-1.237991	0.788805	O	-4.645909	-1.260759	0.905376
O	-0.696201	-2.228585	0.367245	O	-0.647788	-2.219865	0.280983
C	-4.46988	-4.222486	-0.383048	C	-4.542815	-4.175087	-0.390029
C	-4.555362	-4.648876	2.117307	C	-4.53398	-4.737072	2.083601
H	-1.889083	2.84661	0.084569	H	0.994927	-0.289547	-0.261222
H	0.982515	-0.377717	-0.309786	H	-2.221473	-3.263327	0.93255
H	-2.212132	-3.184612	1.011841	H	-5.627655	-2.357379	2.371138
H	-5.729049	-2.293604	2.222173	H	-6.297497	-2.49586	0.705389
H	-6.28396	-2.500305	0.521196	H	-4.485214	-3.362602	-1.131192
H	-4.399112	-3.450918	-1.165505	H	-5.508923	-4.689886	-0.51314
H	-5.419613	-4.76476	-0.51429	H	-3.740018	-4.898107	-0.603755
H	-3.644501	-4.937522	-0.523488	H	-4.380015	-4.34092	3.098212
H	-4.455724	-4.194046	3.113834	H	-3.787757	-5.525571	1.899593
H	-3.785766	-5.428708	2.009162	H	-5.531896	-5.199711	2.031601
H	-5.540586	-5.1354	2.047465	H	0.374699	2.153536	-0.310872
H	0.401412	2.080208	-0.492394	H	-3.669939	1.098409	0.879068
C	-3.874079	1.412411	1.009031	C	-2.063625	3.142128	0.204709
N	-4.851988	1.953414	1.358639	N	-2.392969	4.263198	0.174153

TABLE B3: Cartesian coordinates of the conical intersection structures obtained at SA-2-CASSCF(8,7) /6-31G(d,p) level.

1-CN-CI				2-CN-CI			
Atom	x	y	z	Atom	x	y	z
C	-2.931303	1.205577	-0.223604	C	2.758082	-0.551104	-0.081923
C	-3.834261	0.091857	-0.220544	C	3.404413	0.736814	-0.116585
C	-3.382696	-1.161858	-0.085181	C	2.679036	1.859092	-0.059524
C	-1.956005	-1.44435	0.055743	C	1.21818	1.821724	0.036953
C	-1.040325	-0.314053	0.065113	C	0.585133	0.510374	0.086888
C	-1.563522	0.986207	-0.08534	C	1.36902	-0.642358	0.018482
C	0.405813	-0.564669	0.232082	C	-0.881435	0.415336	0.217815
N	1.293268	-0.269439	-0.801558	N	-1.650316	-0.153635	-0.801614
C	2.64037	-0.194892	-0.231698	C	-2.979036	-0.418287	-0.245493
C	2.270598	0.305384	1.172168	C	-2.556637	-0.754177	1.19199
O	0.965913	-0.198796	1.407975	O	-1.370185	-0.013418	1.40825
O	-1.544191	-2.60423	0.145482	O	0.559647	2.862586	0.061454
C	3.308704	-1.57415	-0.175371	C	-3.874737	0.826309	-0.286862
C	3.497066	0.805418	-1.001531	C	-3.640098	-1.595211	-0.95549
H	-3.30616	2.206486	-0.319979	H	3.137476	2.830246	-0.086113
H	-4.044277	-2.008429	-0.079682	H	-1.63188	0.350939	-1.663353
H	1.190376	-0.838201	-1.615624	H	-2.334996	-1.810635	1.302398
H	2.236077	1.387311	1.211521	H	-3.28884	-0.46535	1.933441
H	2.928265	-0.065822	1.945858	H	-3.415127	1.653936	0.242541
H	2.709778	-2.273017	0.398992	H	-4.839895	0.623407	0.167206
H	4.291224	-1.509093	0.282218	H	-4.049687	1.135824	-1.313314
H	3.435525	-1.978179	-1.175849	H	-2.983022	-2.456756	-0.960885
H	2.992154	1.760891	-1.072259	H	-3.872241	-1.339926	-1.984747
H	3.692601	0.44661	-2.007507	H	-4.570735	-1.867268	-0.466251
H	4.455832	0.948209	-0.511233	H	4.475966	0.772607	-0.190378
H	-4.886655	0.2848	-0.32726	H	0.898384	-1.607252	0.04343
C	-0.683638	2.136818	-0.063548	C	3.554697	-1.745052	-0.150832
N	-0.020371	3.058244	-0.042285	N	4.190097	-2.686281	-0.207652

Medium	1-CN				2-CN			
	Enol		Keto		Enol		Keto	
	avdz	cc-pVTZ	avdz	cc-pVTZ	avdz	cc-pVTZ	avdz	cc-pVTZ
Gas	0.30	0.29	0.56	0.56	0.30	0.29	0.59	0.58
CyHex	0.18	0.17	0.37	0.37	0.18	0.17	0.36	0.37
MeOH	0.00	0.00	0.09	0.11	0.00	0.00	0.05	0.06

TABLE B4: Relative energies(in eV) of the enol and keto forms of 1-CN and 2-CN in Gas, CyHex and MeOH in the S_0 states computed at B3LYP/aug-cc-pVDZ and B3LYP/cc-pVTZ levels of theory. The enol ground state energy in MeOH was taken as reference.

TABLE B5: Summary of selected bond lengths(Å), bond angle(in degree) of the optimized structures of Enol and Keto in the S_0 and S_1 states in MeOH/CyHex calculated at B3LYP/cc-pVDZ level of theory.

Geometrical parameters	1-CN			2-CN		
	Enol	Keto	Keto*	Enol	Keto	Keto*
H_1-O_2	1.01 / 1.01	1.67 / 1.60	1.90 / 1.90	1.01 / 1.01	1.75 / 1.67	2.00 / 1.93
H_1-N_6	1.63 / 1.64	1.05 / 1.06	1.03 / 1.03	1.66 / 1.68	1.04 / 1.05	1.03 / 1.03
O_2-C_3	1.34 / 1.34	1.27 / 1.27	1.28 / 1.29	1.33 / 1.33	1.27 / 1.27	1.27 / 1.27
C_3-C_4	1.42 / 1.43	1.46 / 1.46	1.48 / 1.47	1.43 / 1.43	1.46 / 1.47	1.48 / 1.47
C_4-C_5	1.47 / 1.47	1.43 / 1.42	1.43 / 1.43	1.46 / 1.46	1.43 / 1.42	1.44 / 1.44
C_5-N_6	1.29 / 1.29	1.32 / 1.32	1.35 / 1.35	1.29 / 1.29	1.32 / 1.32	1.36 / 1.36
$\angle C_3$-C_4-C_5-N_6	0.3 / 0.8	2.3 / 3.1	16.3 / 20.7	0.0 / 0.2	1.5 / 2.3	14.9 / 19.9

TABLE B6: Summary of selected bond lengths(Å) and bond angles(in degree) of optimized Enol and Keto forms of 1-CN in the ground state. Results obtained in Gas, CyHex and MeOH phases using aug-cc-pVDZ/cc-pVTZ basis sets with B3LYP functional are shown.

Geometrical parameters	Enol			Keto		
	Gas	CyHex	MeOH	Gas	CyHex	MeOH
H_1-O_2	1.0 / 1.00	1.00 / 1.00	1.00 / 1.00	1.61 / 1.63	1.66 / 1.68	1.72 / 1.73
H_1-N_6	1.67 / 1.68	1.66 / 1.67	1.65 / 1.65	1.06 / 1.05	1.05 / 1.04	1.04 / 1.03
O_2-C_3	1.34 / 1.33	1.34 / 1.34	1.34 / 1.34	1.27 / 1.26	1.27 / 1.26	1.28 / 1.27
C_3-C_4	1.424 / 1.418	1.423 / 1.417	1.42 / 1.42	1.46 / 1.46	1.46 / 1.46	1.46 / 1.45
C_4-C_5	1.47 / 1.46	1.47 / 1.46	1.47 / 1.46	1.42 / 1.41	1.43 / 1.42	1.43 / 1.42
C_5-N_6	1.29 / 1.28	1.29 / 1.28	1.29 / 1.28	1.32 / 1.32	1.32 / 1.32	1.32 / 1.31
$\angle C_3$-C_4-C_5-N_6	0.4 / 0.5	0.5 / 0.7	0.1 / 0.2	2.8 / 3.2	2.3 / 2.6	1.5 / 1.6

TABLE B7: Summary of selected bond lengths(Å) and bond angles(in degree) of optimized Enol and Keto forms of 2-CN in the ground state. Results obtained in Gas, CyHex and MeOH phases using aug-cc-pVDZ/cc-pVTZ basis sets with B3LYP functional are shown.

Geometrical parameters	Enol			Keto		
	Gas	CyHex	MeOH	Gas	CyHex	MeOH
H_1-O_2	1.00 / 1.00	1.00 / 1.00	1.00 / 1.00	1.66 / 1.68	1.72 / 1.74	1.80 / 1.81
H_1-N_6	1.72 / 1.73	1.71 / 1.71	1.69 / 1.69	1.05 / 1.05	1.04 / 1.04	1.03 / 1.03
O_2-C_3	1.34 / 1.33	1.34 / 1.33	1.34 / 1.33	1.27 / 1.26	1.27 / 1.26	1.27 / 1.26
C_3-C_4	1.42 / 1.42	1.42 / 1.42	1.42 / 1.42	1.46 / 1.46	1.46 / 1.46	1.46 / 1.46
C_4-C_5	1.46 / 1.46	1.46 / 1.46	1.46 / 1.46	1.42 / 1.41	1.42 / 1.42	1.43 / 1.43
C_5-N_6	1.29 / 1.28	1.29 / 1.28	1.29 / 1.28	1.32 / 1.32	1.32 / 1.31	1.31 / 1.31
$\angle C_3$-C_4-C_5-N_6	0.0 / 0.0	0.1 / 0.1	0.0 / 0.0	2.1 / 2.2	1.7 / 1.8	0.4 / 0.4

TABLE B8: Vertical excitation energies(in eV) of the first singlet excited states of 1-CN and 2-CN in MeOH solvent calculated with TDDFT methods. DFT functionals and different basis sets used are shown.

	1-CN					
	B3LYP	CAM-B3LYP	PBE0	M06-2X	ωB97XD	EXPT
cc-pvDZ	3.97	4.23	3.61	4.31	4.23	3.86
cc-pVTZ	3.95					
aug-cc-PVTZ	3.94					
def2-TZVP	3.95					
	2-CN					
cc-pVDZ	4.31	4.58	3.94	4.64	4.59	4.09
cc-pVTZ	4.30					
aug-cc-PVTZ	4.29					
def2-TZVP	4.30					

TABLE B9: Vertical excitation and emission energies(in eV) of 1-CN and 2-CN in gas phase, CyHex and MeOH solvents computed at RI-SOS-ADC(2)/cc-pVDZ level of theory at DFT/TDDFT optimized geometries.

	1-CN			2-CN		
Transition	CyHex	Gas	MeOH	CyHex	Gas	MeOH
$S_0 \rightarrow S_1$	4.11	4.16	4.14	4.33	4.34	4.40
$S_1 \rightarrow S_0$	2.51	2.50	2.66	2.61		2.80

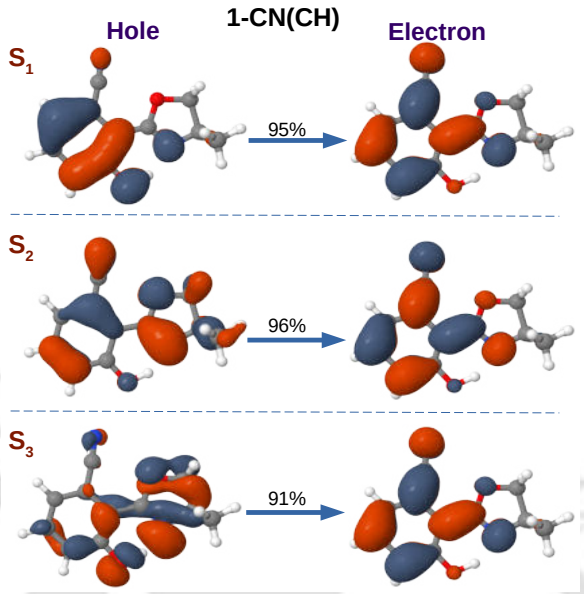

FIGURE B1: NTO for transition to the first three singlet excited states of 1-CN in cyclohexane solvent.

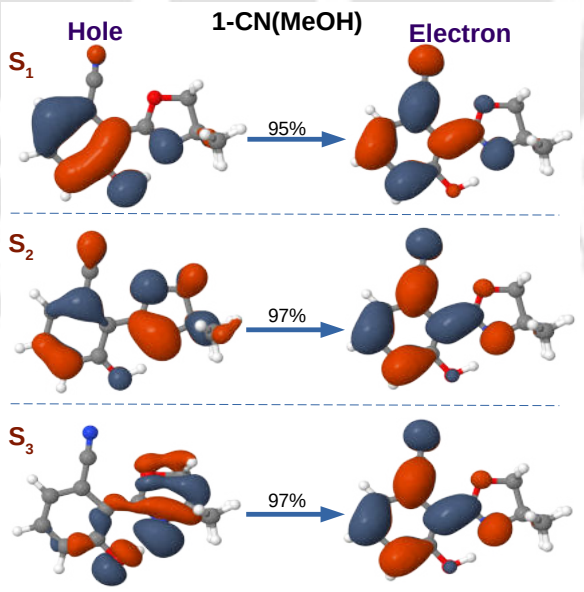

FIGURE B2: NTO for transition to the first three singlet excited states of 1-CN in methanol solvent.

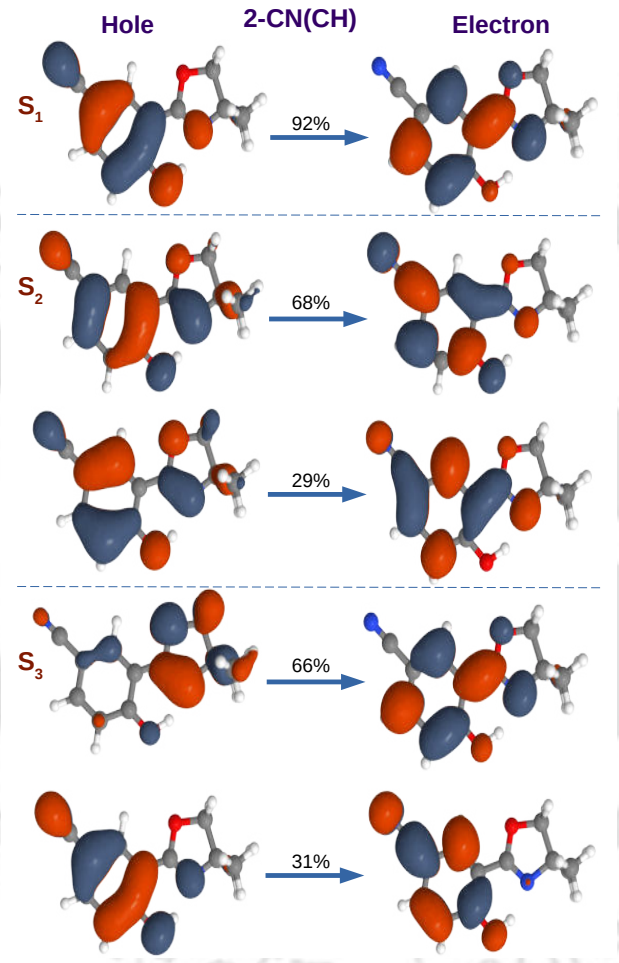

FIGURE B3: NTO for transition to the first three singlet excited states of 2-CN in cyclohexane solvent.

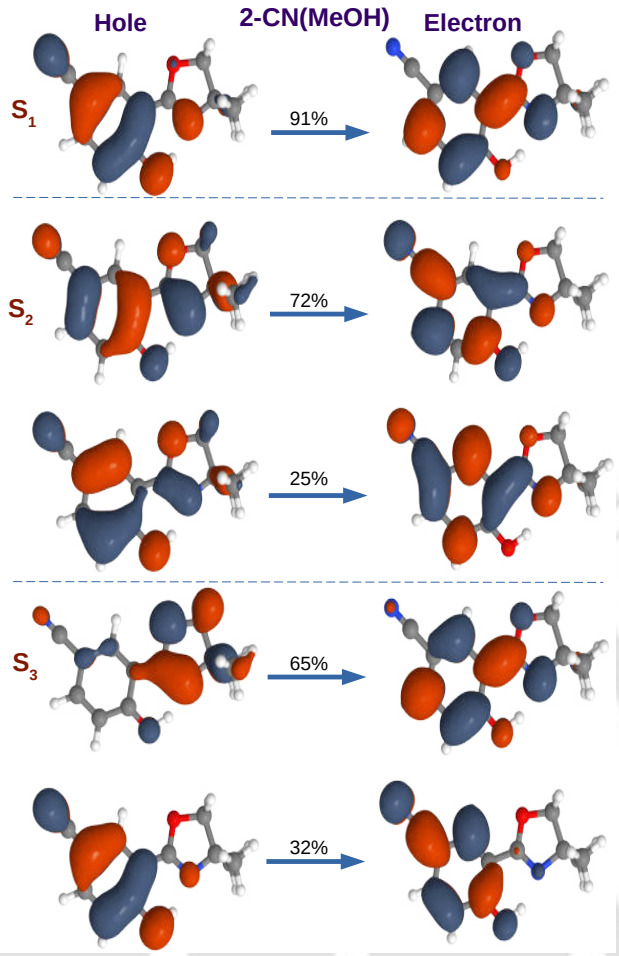

FIGURE B4: NTO for transition to the first three singlet excited states of 2-CN in methanol solvent.

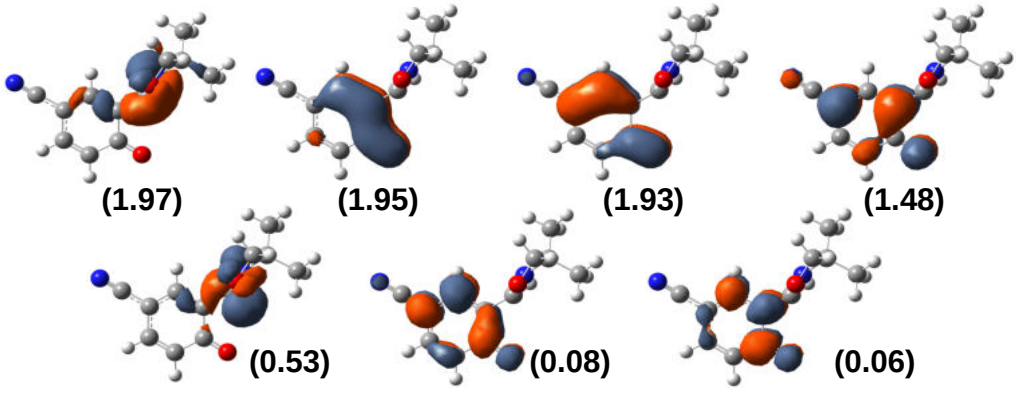

FIGURE B5: The active space orbitals used in SA-2-CASSCF(8,7)/6-31G(d,p) conical intersection optimisation between S_1 and S_0 for 2-CN.

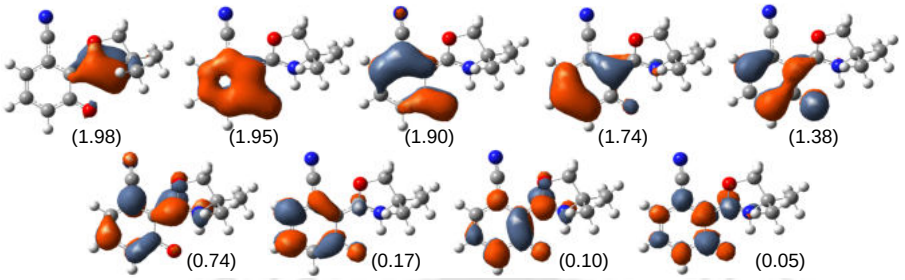

FIGURE B6: Active space orbitals used in MS-CASPT2//SA3-CASSCF/6-31G(d,p) calculations for generating the PEC along the LIIC path connecting the S_1 keto minimum and the MECI structure in 1-CN. Mean occupation numbers of the orbitals are shown in parenthesis.

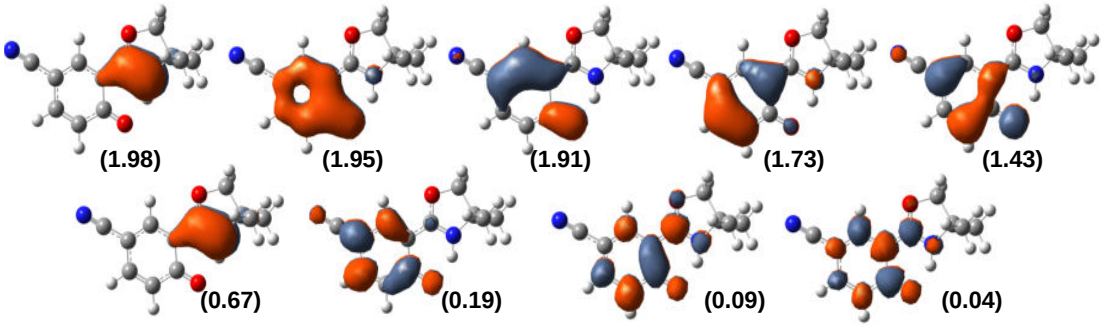

FIGURE B7: Active space orbitals used for MS-CASPT2//SA3-CASSCF(10,9)/6-31G(d,p) calculations in generating the PEC along the LIIC connecting the S_1 keto minimum and the CI structure in 2-CN.

Appendix C

TABLE C1: Cartesian coordinates of **E-t1** in the S_0 and S_1 states optimized at MP2/cc-pVTZ and ADC(2)/cc-pVTZ levels of theory, respectively.

S_0				S_1			
Atom	x	y	z	Atom	x	y	z
C	-0.5215852	0.372788	-0.0217127	C	-0.5213456	0.4246773	-0.0223852
H	-0.2165201	1.4146822	-0.0225182	H	-0.1619041	1.4491837	-0.0211178
C	0.4090485	-0.6051973	0.0203717	C	0.4085511	-0.6485526	0.0206813
H	0.0861457	-1.6404138	0.0205516	H	0.0421916	-1.6672197	0.0192213
C	1.8442432	-0.4261969	0.0671447	C	1.7972959	-0.47716	0.0660011
C	2.8414889	-1.3932077	0.1115894	C	2.8545341	-1.4359593	0.1123713
N	2.4765048	0.7983232	0.0752459	N	2.4204643	0.7697625	0.0737139
C	4.0957417	-0.7283586	0.1469368	C	4.0648003	-0.7442767	0.1460692
H	2.6683968	-2.4568799	0.1173424	H	2.7065105	-2.5031257	0.1189565
C	3.8374638	0.6277042	0.1233405	C	3.771497	0.6297582	0.1212438
H	2.0128219	1.6874652	0.0497054	H	1.9307639	1.6466498	0.0474384
H	5.0716668	-1.1815095	0.1850473	H	5.0566526	-1.1627246	0.1843506
H	4.5028758	1.4737187	0.1366883	H	4.4262218	1.4849537	0.1343356
C	-1.9613353	0.1764258	-0.0684747	C	-1.8987629	0.2606755	-0.0673669
C	-2.9213259	1.1658305	-0.111519	C	-2.9402606	1.2371823	-0.1130454
S	-2.7107668	-1.3956576	-0.0772454	S	-2.6104585	-1.3691018	-0.074113
C	-4.2535922	0.6627999	-0.151374	C	-4.2112268	0.6720737	-0.1500399
H	-2.6698722	2.2172326	-0.1141261	H	-2.7341419	2.2981497	-0.1173593
C	-4.2942248	-0.7061257	-0.1382489	C	-4.2107708	-0.7261256	-0.1350006
H	-5.1366384	1.2833026	-0.1878976	H	-5.1267773	1.2459056	-0.1872793
H	-5.1605368	-1.3467259	-0.1608475	H	-5.0638345	-1.3847261	-0.1566736

TABLE C2: Cartesian coordinates of **E-c1** in the S_0 and S_1 states optimized at MP2/cc-pVTZ and ADC(2)/cc-pVTZ levels of theory, respectively.

S_0				S_1			
Atom	x	y	z	Atom	x	y	z
C	0.5922504	-0.5445564	0.0036532	N	-2.2351878	-1.1531881	-0.2361609
H	0.3665669	-1.6045956	0.057799	C	-1.7858722	0.1680406	-0.1819622
C	-0.4140067	0.3506326	-0.0967643	C	-2.9490963	0.9630358	0.0553766
H	-0.172801	1.4014928	-0.2075585	C	-4.0439966	0.1058887	0.1477035
C	-1.8303589	0.0523203	-0.0832903	C	-3.5736575	-1.2099526	-0.0232566
C	-2.9040906	0.9019238	-0.3213491	C	-0.4398624	0.5066314	-0.3398664
N	-2.3576654	-1.1969715	0.1628043	C	0.555228	-0.4454771	-0.7178079
C	-4.0977988	0.1403935	-0.2130602	C	1.91547	-0.1894048	-0.5810271
H	-2.8203248	1.950281	-0.5565964	S	3.1409642	-1.3154852	-1.1727182
C	-3.7275869	-1.1542449	0.0920933	C	4.4288932	-0.2991505	-0.6116636
H	-1.823495	-2.0065708	0.4194514	C	3.947843	0.8537861	-0.0082469
H	-5.1074961	0.4913219	-0.3419357	C	2.5515113	0.9447848	0.0127792
H	-4.3203099	-2.0356124	0.2668237	H	0.2492481	-1.3785703	-1.1813874
C	2.0078244	-0.1903462	0.0299966	H	-0.1647307	1.5443523	-0.1985645
C	2.6129667	1.0189942	0.3041452	H	-2.9480501	2.0381814	0.1245895
S	3.2070884	-1.3971666	-0.3326457	H	-1.6136395	-1.943771	-0.2752004
C	4.0318363	0.9705423	0.2111514	H	-5.0747519	0.3753654	0.3071211
H	2.0586527	1.9030366	0.583964	H	-4.1042465	-2.1473815	-0.0103411
C	4.4988737	-0.2755903	-0.1226032	H	5.4565539	-0.5859962	-0.7648795
H	4.6787489	1.8157204	0.394822	H	4.6066371	1.6074343	0.4007481
H	5.5211256	-0.5910047	-0.2509007	H	1.9945415	1.7536425	0.4616349

TABLE C3: Cartesian coordinates of **E-c2** in the S_0 and S_1 states optimized at MP2/cc-pVTZ and ADC(2)/cc-pVTZ levels of theory, respectively.

S_0				S_1			
Atom	x	y	z	Atom	x	y	z
C	-0.2111395	0.6545265	0.0002862	C	-0.3756165	-0.5571329	0.1741239
H	0.0751944	1.7007147	0.0011131	H	0.2832666	-1.3779879	0.4352797
C	0.7506921	-0.2921036	-0.0002655	C	0.2050416	0.6782974	-0.2123888
H	0.4544469	-1.3374267	-0.0009213	H	-0.4318583	1.514036	-0.4777547
C	2.1784757	-0.0353319	-6.4E-05	C	1.5950332	0.8428114	-0.258779
C	2.9289357	1.1357007	-0.0008982	C	2.6678655	-0.0652554	0.0308453
N	3.0783542	-1.0810322	0.0011092	N	2.2006408	2.030443	-0.6298895
C	4.3002353	0.7735166	-0.0001126	C	3.8707891	0.6131331	-0.1778572
H	2.5288154	2.1358014	-0.0020895	H	2.5415444	-1.0852327	0.3509465
C	4.3640434	-0.6075344	0.001147	C	3.562128	1.9156128	-0.588542
H	2.820795	-2.0516368	0.0021453	H	1.6941134	2.8583471	-0.8920098
H	5.1455161	1.4407852	-0.000498	H	4.8680461	0.2256519	-0.0523037
H	5.2063045	-1.2773464	0.0020213	H	4.2040976	2.7410466	-0.8456608
C	-1.6435132	0.4115287	-5.8E-05	C	-1.7407747	-0.7950401	0.2433581
C	-2.6351122	1.3701921	0.0008127	C	-2.4484024	-1.9774214	0.6128008
S	-2.3445068	-1.1836586	-0.0016485	S	-2.8998582	0.4884969	-0.1657407
C	-3.9517829	0.8257391	0.0002324	C	-3.8308509	-1.8227637	0.5582906
H	-2.4158001	2.4286112	0.0018484	H	-1.9377575	-2.8854324	0.9009502
C	-3.950305	-0.543744	-0.0010755	C	-4.2403336	-0.5484668	0.1552317
H	-4.8542827	1.4187482	0.0007682	H	-4.537244	-2.6041638	0.8014111
H	-4.7967232	-1.210767	-0.0017568	H	-5.2498699	-0.1889791	0.0376884

TABLE C4: Cartesian coordinates of **E-t2** in the S_0 and S_1 states optimized at MP2/cc-pVTZ and ADC(2)/cc-pVTZ levels of theory, respectively.

S_0				S_1			
Atom	x	y	z	Atom	x	y	z
C	-0.2113822	-0.3776557	0.090681	C	-2.5406967	0.9949527	-0.4941635
H	-0.0019567	-1.4410287	0.0584074	C	-1.9514604	-0.2826756	-0.2400329
C	0.8198389	0.488689	0.1735131	S	-3.2018854	-1.5307968	-0.2726242
H	0.6029078	1.549202	0.26219	C	-4.4356799	-0.3656076	-0.6164538
C	2.2225018	0.1162832	0.1563729	C	-3.9219561	0.9215456	-0.7025154
C	2.8773562	-1.0741115	-0.1394004	C	-0.6175304	-0.5904749	0.0058787
N	3.1992798	1.0355349	0.479604	C	0.4089709	0.3905593	0.0640476
C	4.2697991	-0.8563106	0.0222778	C	1.7425483	0.0196581	0.2696133
H	2.4009626	-1.9874292	-0.4544878	N	2.7787904	0.9342318	0.3529159
C	4.4408672	0.4599159	0.4083371	C	3.9720341	0.2993962	0.55525
H	3.0172846	1.9812628	0.763861	C	3.7231402	-1.0783006	0.6063204
H	5.0591863	-1.5718652	-0.1344639	C	2.3514713	-1.2714049	0.4321641
H	5.3311277	1.0225919	0.6295684	H	-0.3437984	-1.6261464	0.1672507
C	-1.6144294	0.0197681	0.0494994	H	0.1645766	1.4400981	-0.0401067
C	-2.1820735	1.2345288	-0.2779433	H	2.6545624	1.9289794	0.2783396
S	-2.8502293	-1.1304854	0.4676301	H	1.8219705	-2.2083515	0.4113828
C	-3.6011897	1.2363341	-0.1793485	H	4.8930687	0.8496401	0.648077
H	-1.6008658	2.0852991	-0.6030578	H	4.4747696	-1.8356551	0.7542695
C	-4.1059331	0.0216977	0.2114791	H	-5.4613917	-0.6755422	-0.7345779
H	-4.221814	2.0921618	-0.4006987	H	-4.5470314	1.7785768	-0.9121635
H	-5.1373763	-0.254659	0.3556654	H	-1.9644726	1.9073175	-0.5328717

TABLE C5: Cartesian coordinates of **Z-t1(O)** in the S_0 and S_1 states optimized at MP2/cc-pVTZ and ADC(2)/cc-pVTZ levels of theory, respectively.

S_0				S_1			
Atom	x	y	z	Atom	x	y	z
C	0.691869	1.5683513	-0.3251089	C	-0.6986346	1.788369	0.0287672
H	1.2066643	2.5072737	-0.5013387	H	-1.1946365	2.7335023	0.2213741
C	-0.6559029	1.6040638	-0.3861997	C	0.6918288	1.7644777	-0.2705138
H	-1.1033678	2.5778	-0.5616807	H	1.1556845	2.6498936	-0.6978879
C	-1.5887004	0.4813359	-0.2710426	C	1.5250284	0.6919437	0.0126354
C	-1.6805819	-0.7200304	-0.9572117	C	2.4449939	-1.4513316	0.9602461
N	-2.6930176	0.5550129	0.5535147	C	3.3512054	-0.7836541	0.1214325
C	-2.8529518	-1.3893958	-0.5110785	H	2.5925948	-2.3930155	1.4641061
H	-0.9883031	-1.0561024	-1.710375	H	4.3394818	-1.1712612	-0.0826536
C	-3.4558479	-0.5788247	0.4294942	C	-1.4850773	0.6276344	-0.0673284
H	-2.8625669	1.2972474	1.2082306	C	-3.2923666	-0.7208197	0.1753808
H	-3.2194637	-2.3455401	-0.8444109	H	-3.1993592	1.2388782	0.9914546
H	-4.3486962	-0.7167601	1.0144654	C	-2.3527237	-1.4526628	-0.5302346
C	1.6077187	0.4768999	-0.013874	H	-4.2837976	-0.9811219	0.5054462
C	2.9831718	0.6155346	-0.0223503	H	-2.4903151	-2.4570797	-0.8936363
S	1.1678991	-1.1176647	0.5310056	S	0.9635307	-0.6094803	1.1080909
C	3.6790071	-0.5487298	0.4021569	C	2.8597393	0.4094092	-0.3981293
H	3.4655412	1.536695	-0.318471	H	3.4025499	1.0608758	-1.0678694
C	2.8221791	-1.5636879	0.7402883	C	-1.2081656	-0.6446648	-0.6886935
H	4.7544381	-0.6304137	0.4549879	H	-0.3582199	-0.827271	-1.3235909
H	3.070912	-2.5530649	1.0889984	N	-2.7633415	0.5273789	0.4316038

TABLE C6: Cartesian coordinates of **Z-c1(O)** in the S_0 and S_1 states optimized at MP2/cc-pVTZ and ADC(2)/cc-pVTZ levels of theory, respectively.

S_0				S_1			
Atom	x	y	z	Atom	x	y	z
C	-0.3802526	-1.5399922	0.1100377	C	-0.4189464	-1.6881161	-0.1690249
H	-0.8734185	-2.505205	0.1344325	H	-0.9136339	-2.5813562	-0.536972
C	0.9704477	-1.5567503	0.099251	C	0.9617728	-1.7403658	0.1828149
H	1.4256182	-2.5404967	0.1712806	H	1.4157828	-2.6736702	0.4997181
C	1.9252409	-0.4655458	-0.0288701	C	1.7829365	-0.6200951	-0.0016522
C	1.8524812	0.8489596	-0.4801833	C	1.5390486	0.6100382	-0.7222334
N	3.2558938	-0.7075691	0.2567347	N	3.0589036	-0.5087308	0.5056659
C	3.1618789	1.3929877	-0.4523047	C	2.6883759	1.4082564	-0.5944602
H	0.9568631	1.3455798	-0.8089834	H	0.695078	0.7711281	-1.3686419
C	4.0115696	0.4076447	0.0146612	C	3.6090909	0.7093701	0.1767279
H	3.6077296	-1.5748144	0.6209315	H	3.4766754	-1.1878924	1.1175605
H	3.4535345	2.3882127	-0.7425981	H	2.8511985	2.3822197	-1.0242795
H	5.0726997	0.4137346	0.1940959	H	4.600563	0.9766397	0.5011849
C	-1.2705318	-0.3752663	0.1019044	C	-1.1595816	-0.5204118	0.0035381
C	-1.1761404	0.8167833	0.7862835	C	-0.783456	0.6440775	0.7497501
S	-2.7538073	-0.4355309	-0.8067882	S	-2.7072699	-0.2451878	-0.791857
C	-2.2870023	1.6799934	0.5687227	C	-1.7360453	1.6790039	0.6527061
H	-0.3416175	1.0522859	1.4297037	H	0.0267426	0.6240526	1.4622654
C	-3.2222126	1.1352896	-0.2743337	C	-2.8173427	1.3630498	-0.1409399
H	-2.3923626	2.655389	1.0205239	H	-1.6472667	2.6266293	1.1651579
H	-4.1486646	1.5710452	-0.6105899	H	-3.674679	1.9780958	-0.3631168

TABLE C7: Cartesian coordinates of **Z-t2(O)** in the S_0 state optimized at MP2/cc-pVTZ level of theory.

S_0			
Atom	x	y	z
C	0.3916155	1.6901917	0.7480057
H	0.8287979	2.5938402	1.1566484
C	-0.9298483	1.7102388	0.4682081
H	-1.4468696	2.6487319	0.6339764
C	-1.8049303	0.6519368	0.0019157
C	-3.1585781	0.7507872	-0.3071432
N	-1.4525973	-0.6685376	-0.1721176
C	-3.6186729	-0.5383046	-0.6770678
H	-3.7364449	1.6594726	-0.2606051
C	-2.5383734	-1.3955561	-0.5813336
H	-0.5269035	-1.0305963	-0.0245227
H	-4.6156891	-0.8130356	-0.9766916
H	-2.4577898	-2.4522207	-0.77083
C	1.3082239	0.5557217	0.5429161
C	1.6324978	-0.0931635	-0.6292562
S	2.2126383	-0.1097978	1.8720097
C	2.5964717	-1.1297721	-0.4540397
H	1.2016202	0.1848364	-1.58074
C	3.0035401	-1.2520544	0.8495838
H	2.9767473	-1.7454034	-1.2558085
H	3.7186104	-1.9464914	1.2594061

TABLE C8: Cartesian coordinates of conical intersection structures, **CI-1** and **CI-2** at SA-2-CASSCF(12,10)/6-31G(d,p) level of theory.

CI-1				**CI-2**			
Atom	x	y	z	Atom	x	y	z
C	0.2983445	1.9988429	-0.4029795	C	-1.8928512	-0.3537884	-1.1114548
H	0.2559124	2.9741468	-0.8530752	C	-1.0238300	-0.3328420	0.0584709
C	-0.1415820	1.8128465	0.9545947	C	-0.0578215	-1.3986136	-0.1661381
H	-0.0905031	2.6419943	1.6415697	N	-0.3203237	-1.9147498	-1.3303748
C	-0.6022661	0.6091501	1.3976706	C	-1.4461606	-1.2952292	-1.9652808
C	-0.7737280	-0.5802150	0.5272757	C	0.5115464	0.8933729	-0.0444982
N	-0.7598047	0.1859486	2.7486783	C	1.4602858	0.6086703	1.0177684
C	-1.1096328	-1.6692426	1.4653540	C	1.7080312	-0.7267606	1.3186852
H	-1.3543603	-0.4700054	-0.3756964	C	1.0645911	-1.7659863	0.6681686
C	-1.1361718	-1.1555088	2.7112807	C	-0.0579150	2.2423483	0.1464448
H	-1.2690098	0.7872846	3.3591538	C	0.3122565	2.8256146	1.3014049
H	-1.3130379	-2.6846774	1.1930770	S	1.3820555	1.8790830	2.3012027
H	-1.3828782	-1.6627598	3.6231854	H	1.4244704	-2.7758167	0.6504636
C	0.7721727	0.9473405	-1.1744963	H	2.4423741	-0.9738933	2.0710270
C	1.0540218	0.7815156	-2.5361875	H	0.8082935	0.6447997	-1.0548821
S	1.0937646	-0.6529125	-0.3763912	H	-0.7116578	2.7022829	-0.5711618
C	1.2853172	-0.5661071	-2.9088092	H	0.0046005	3.8015541	1.6254681
H	0.9485409	1.5826092	-3.2415286	H	0.2939128	-2.5640630	-1.7722569
C	1.2050304	-1.5029660	-1.9063034	H	-1.3806700	-0.1369642	1.0493287
H	1.5029192	-0.8517191	-3.9229583	H	-1.7724178	-1.6302746	-2.9250367
H	1.5169529	-2.5255654	-1.9234122	H	-2.7487702	0.2712560	-1.2673485

TABLE C9: Cartesian coordinates of conical intersection structure **CI-3** at SA-2-CASSCF(12,10)/6-31G(d,p) level of theory.

CI-3			
Atom	x	y	z
S	0.9962937	1.7637026	2.7656299
C	1.2889506	0.6436302	1.4136636
C	1.2986678	1.3716630	0.1134889
C	0.6974299	2.6880589	0.3070611
C	0.4801972	3.0066054	1.6022447
C	1.2211375	-0.7022440	1.3843288
C	1.0985708	-1.1994200	-0.0050643
C	0.3056238	-0.3411893	-0.8053369
N	-1.0532202	-0.0094220	-0.4907643
C	-1.7970378	-0.0640431	-1.6818581
C	-0.9230602	-0.1664566	-2.7815610
C	0.3585966	-0.2977266	-2.3093359
H	1.9488786	-1.6663024	-0.4785572
H	1.2110985	-1.3326948	2.2548550
H	2.1927048	1.3102445	-0.4853652
H	0.4888828	3.3651496	-0.5003859
H	0.0692556	3.9238149	1.9759198
H	1.2628151	-0.3955902	-2.8746652
H	-1.4344463	-0.4663105	0.3064273
H	-1.2248533	-0.1153236	-3.8092698
H	-2.8447105	0.1530393	-1.6780365

TABLE C10: Cartesian coordinates of conical intersection structures, **CI-4** and **CI-5** at SA-2-CASSCF(12,10)/6-31G(d,p) level of theory.

CI-4				**CI-5**			
Atom	x	y	z	Atom	x	y	z
C	-0.2663836	1.3101371	0.2746732	N	-1.5660039	-0.9528301	-0.6863510
H	-0.5037401	1.8463723	-0.6308075	C	-1.2939228	0.3497404	-0.3577026
C	0.3801224	-0.0013157	0.1358060	C	-2.2258952	0.7300115	0.6063630
H	0.0693822	-0.6925271	-0.6311129	C	-3.0604565	-0.3808129	0.8557898
C	1.4155815	-0.4507137	1.0011706	C	-2.6108921	-1.4077231	0.0496524
C	2.0713136	-1.6787240	1.1023769	C	-0.2948715	1.1535127	-0.9892545
N	1.9820795	0.3846367	1.9281114	C	0.4986467	0.7625822	-2.1547461
C	3.0601327	-1.5480219	2.0983621	C	1.5046899	0.3082117	-1.3156031
H	1.8536228	-2.5478967	0.5151245	S	2.1435787	-1.3703075	-1.2385487
C	2.9710126	-0.2570176	2.5913274	C	3.0701610	-1.0087298	0.2245675
H	1.6814664	1.3235651	2.0577293	C	2.8667693	0.2716528	0.6614356
H	3.7523793	-2.2967483	2.4253692	C	2.0319185	1.0503054	-0.1774410
H	3.5366796	0.2300215	3.3577382	H	0.0784979	0.0793418	-2.8711188
C	-1.3452151	0.7050040	0.8940926	H	-0.2703047	2.1631155	-0.6180399
C	-2.7810443	0.8757028	0.4895746	H	-2.2890807	1.7008354	1.0551256
S	-1.3626844	-0.1002792	2.5307392	H	-0.9979098	-1.5104261	-1.2798416
C	-3.6714034	0.6802970	1.5105629	H	-3.8850401	-0.4314297	1.5366362
H	-3.0269972	1.2811702	-0.4730606	H	-2.9592389	-2.4146414	-0.0465786
C	-3.0927967	0.1306056	2.6744856	H	3.8107884	-1.6977272	0.5754248
H	-4.7288668	0.8515556	1.4260012	H	3.3808882	0.6794308	1.5120755
H	-3.6255547	-0.3043106	3.4950631	H	1.9814777	2.1186536	-0.1349753

TABLE C11: Cartesian coordinates of conical intersection structures, **CI-6** and **CI-7** at SA-2-CASSCF(12,10)/6-31G(d,p) level of theory.

CI-6				**CI-7**			
Atom	x	y	z	Atom	x	y	z
N	1.1569386	1.6715570	-0.4550514	C	-0.4212070	-0.2780456	-0.4687859
C	1.3144310	0.3057430	-0.3207684	H	-0.1386306	-1.0466026	-1.1631944
C	2.6210651	0.1332491	0.2068787	C	0.6061685	0.5012375	0.2209885
C	3.2280516	1.3862681	0.2990435	H	0.4686010	1.5571183	0.3839275
C	2.2820880	2.3252066	-0.1148489	C	1.9199860	0.0111663	0.5454075
C	0.2235131	-0.6516721	-0.7272552	C	4.0150354	0.1234370	1.3230535
C	-0.3692451	-0.3858176	0.5712214	H	2.6822682	1.7215413	1.5305325
C	-1.5457960	0.4317421	0.7635253	C	3.8717533	-1.1123332	0.7804212
S	-2.4869863	0.9879656	-0.6012480	H	2.0888310	-2.0304141	-0.2104023
C	-3.6248361	1.7477191	0.4645954	H	4.8647453	0.5705076	1.7973775
C	-3.3026949	1.5778073	1.7750851	H	4.6231489	-1.8735425	0.7374244
C	-2.0928124	0.8235840	1.9385305	C	-0.9661114	-0.6312137	0.7515044
H	0.6402747	-1.6409820	-0.8511104	C	-1.5977435	-1.6904026	3.0090740
H	0.0701102	-0.7249933	1.5051947	C	-1.5401980	-0.3212050	3.0710489
H	-4.4736144	2.2689363	0.0694927	H	-2.0312501	-2.3388429	3.7428551
H	-3.8826009	1.9654727	2.5912067	H	-1.8298268	0.2273212	3.9482016
H	0.3460843	2.0776529	-0.8626460	N	2.8527401	0.8085521	1.1835954
H	2.3590708	3.3894740	-0.1942989	C	2.5411619	-1.1933379	0.2789970
H	4.2221627	1.6078820	0.6300579	S	-1.1305561	-2.3327083	1.4359357
H	-1.6591030	0.5863814	2.8924625	C	-1.2323794	0.3059338	1.8449251
H	3.0520501	-0.8151448	0.4566359	H	-1.4343706	1.3389662	1.6487830

TABLE C12: Energies of FC geometries and MECIs relative to **E-t1**(S_0) energy.

	Z-t1(O)	**Z-c1(O)**	**Z-t2(O)**	**Z-t1(C)**	**Z-c1(C)**	**Z-t2(C)**	**E-t1**	**E-c1**	**E-c2**	**E-t2**
FC(eV)	4.57	4.48	4.65	5.46	5.03	7.34	4.22	4.32	4.18	4.31
	CI-1	**CI-2**	**CI-3**	**CI-4**	**CI-5**	**CI-6**	**CI-7**			
MECI(eV)	4.24	4.00	4.78	4.51	4.36	4.19	4.47			

TABLE C13: Energy gaps between S_0 and S_1 states (ΔE) calculated at CASSCF and MS-CASPT2 levels.

	CASSCF ΔE (in eV)	MS-CASPT2 ΔE (in eV)
CI-1	0.00	0.55
CI-2	0.01	0.52
CI-3	0.00	0.33
CI-4	0.00	0.49
CI-5	0.00	0.42
CI-6	0.00	0.34
CI-7	0.00	0.72

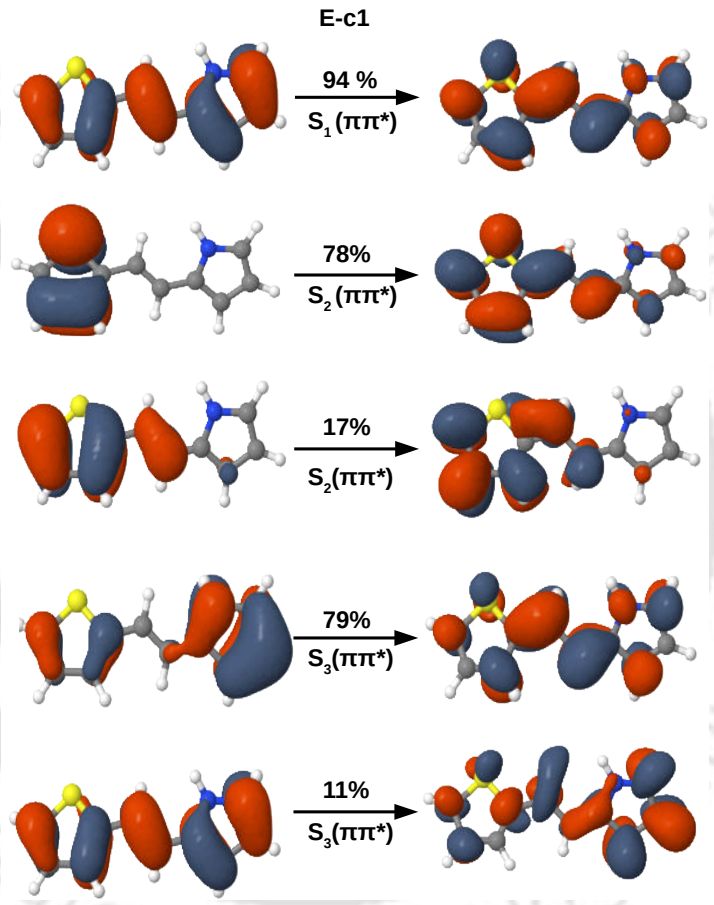

FIGURE C1: Dominant NTOs involved in the transitions from S_0 to S_1, S_2, S_3 for **E-c1**.

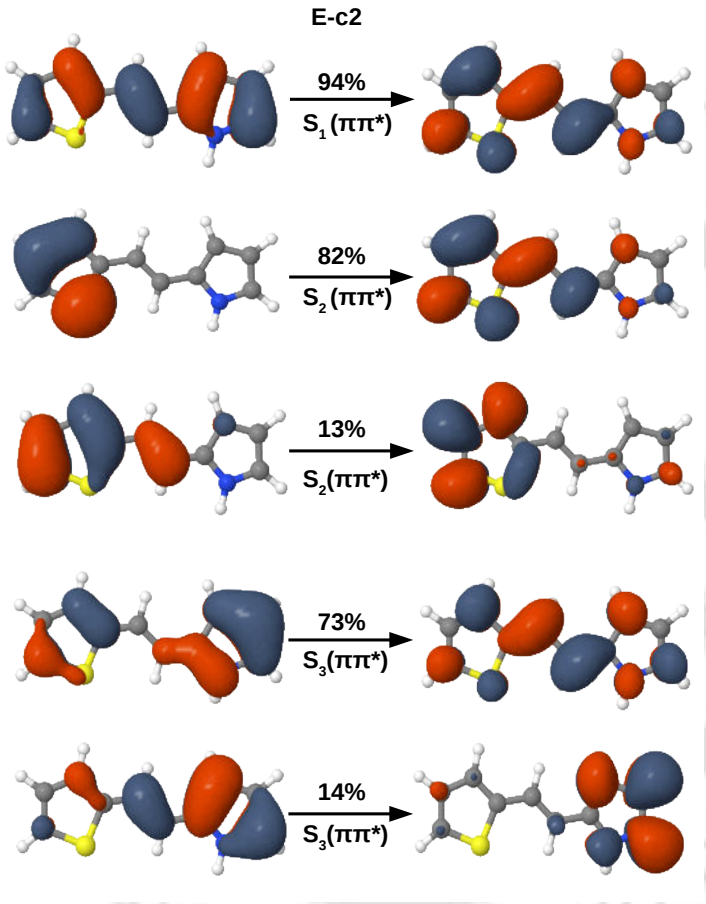

FIGURE C2: Dominant NTOs involved in the transitions from S_0 to S_1, S_2, S_3 for **E-c2**.

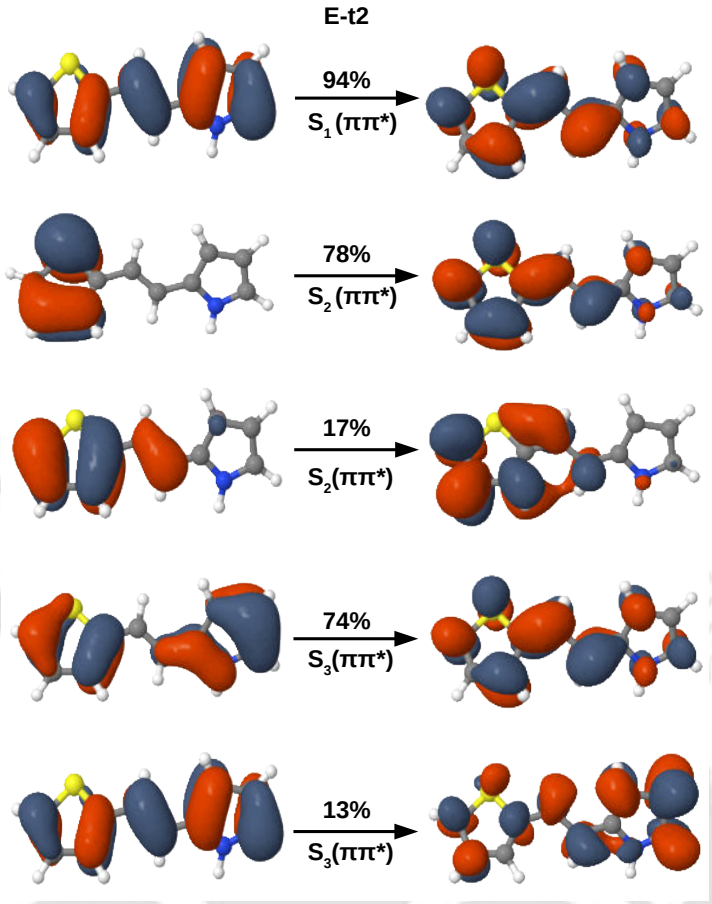

FIGURE C3: Dominant NTOs involved in the transitions from S_0 to S_1, S_2, S_3 for **E-t2**.

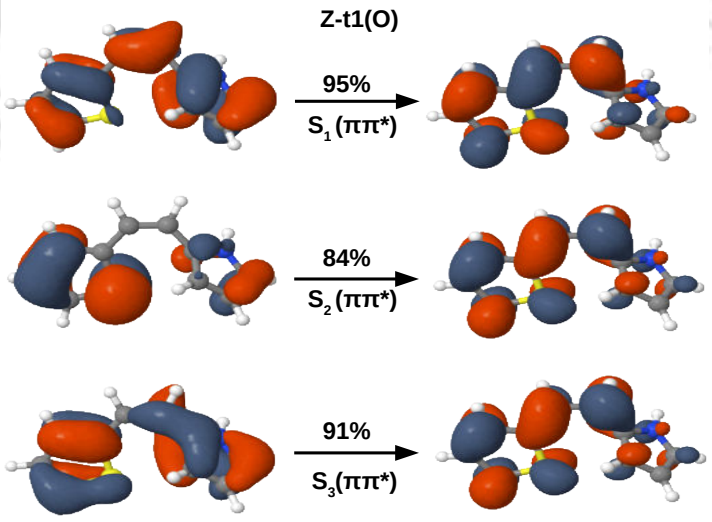

FIGURE C4: Dominant NTOs involved in the transitions from S_0 to S_1, S_2, S_3 for **Z-t1(O)**.

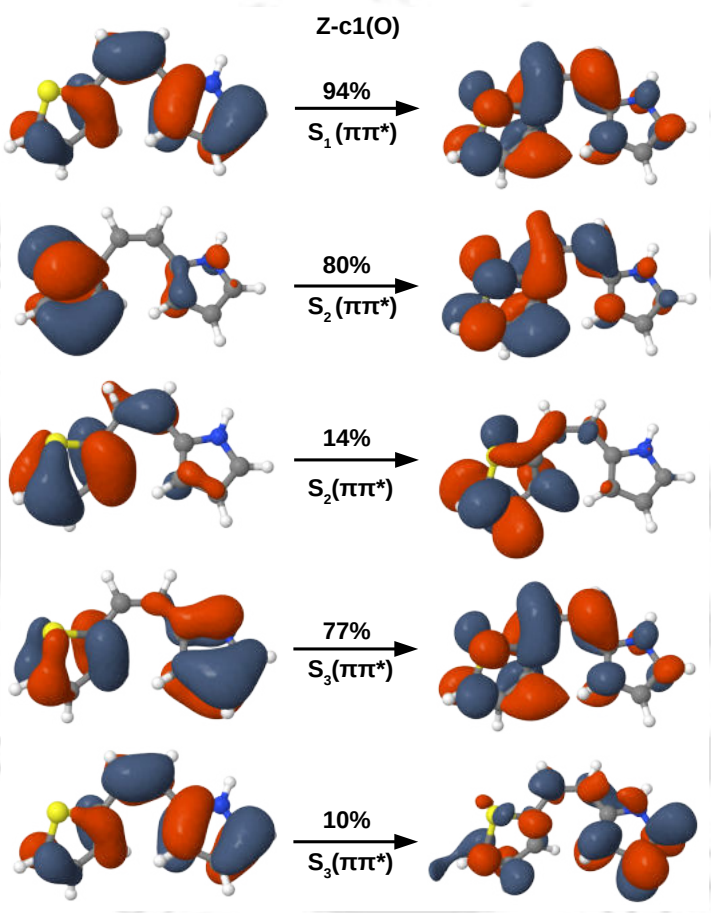

FIGURE C5: Dominant NTOs involved in the transitions from S_0 to S_1, S_2, S_3 for **Z-c1(O)**.

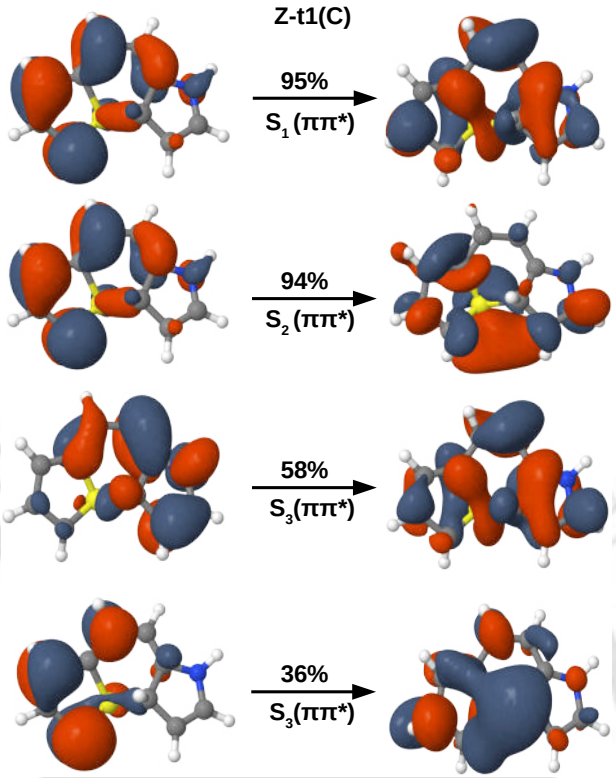

FIGURE C6: Dominant NTOs involved in the transitions from S_0 to S_1, S_2, S_3 for **Z-t1(C)**.

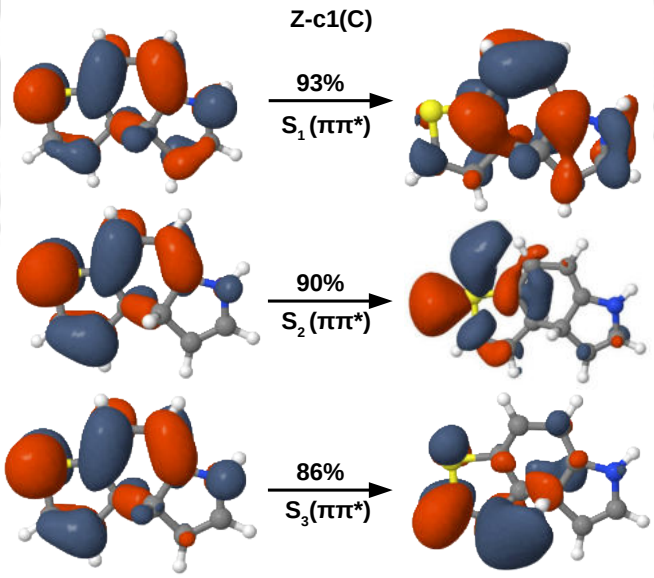

FIGURE C7: Dominant NTOs involved in the transitions from S_0 to S_1, S_2, S_3 for **Z-c1(C)**.

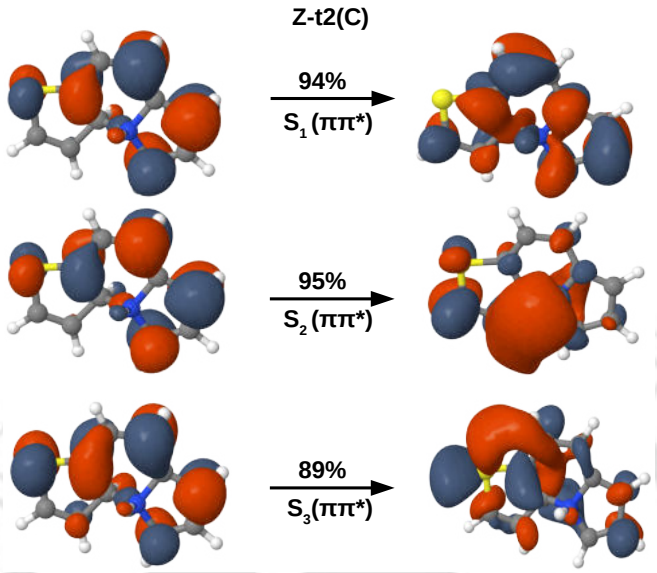

FIGURE C8: Dominant NTOs involved in the transitions from S_0 to S_1, S_2, S_3 for **Z-t2(C)**.

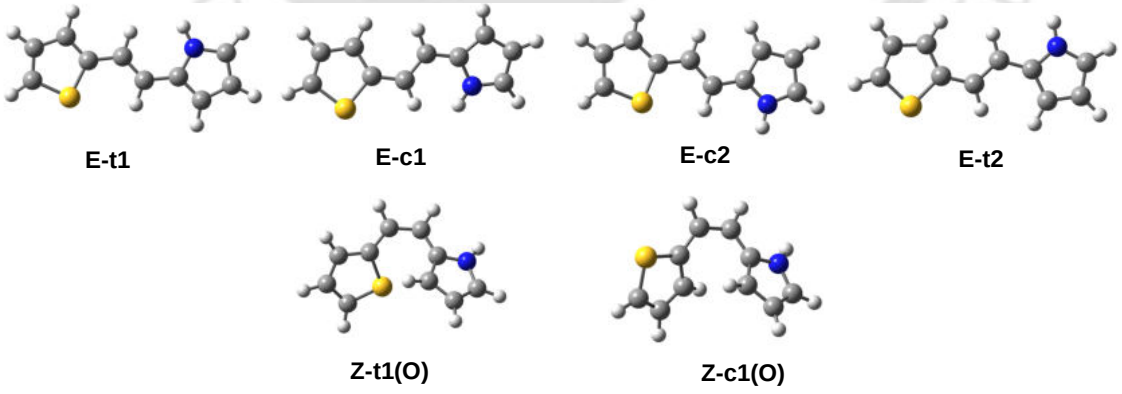

FIGURE C9: Optimized structures of isomers in the S_1 state obtained at RI-ADC(2)/cc-pVTZ level of theory

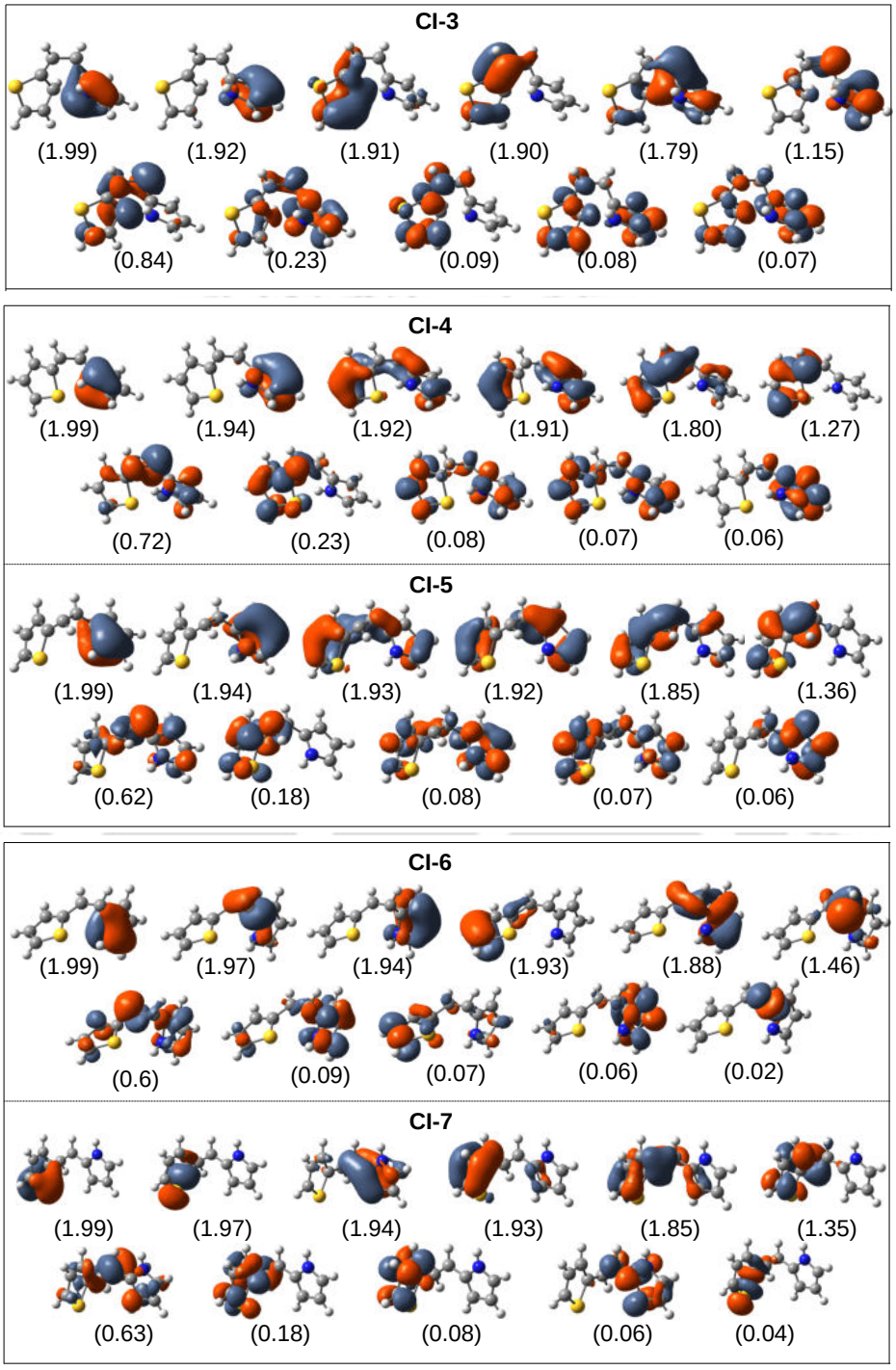

FIGURE C10: Orbitals used in the active space for **CI-3**, **CI-4**, **CI-5**, **CI-6**, **CI-7** optimizations computed at SA-2-CASSCF(12,11)/6-31G(d,p) level of theory.